

ABSTRACT

Title of Document: DEVELOPMENT OF COLORLESS
DISTRIBUTED COMBUSTION FOR GAS
TURBINE APPLICATION

Vaibhav Kumar Arghode, PhD, 2011

Directed By: Dr. Ashwani K. Gupta
Distinguished University Professor
Department of Mechanical Engineering

Colorless Distributed Combustion (CDC) is investigated for gas turbine engine application due to its benefit for ultra-low pollutant emission, improved pattern factor, low noise emission, stable combustion and low pressure drop, alleviation of combustion instabilities and increased life of turbine blades with less air cooling requirements. The CDC is characterized by discrete and direct injection of fuel and air at high velocity and the reaction zone is stabilized due to controlled aerodynamics inside the combustor and wider (radially) shear layer mixing. Mixing between the injected air and product gases to form hot and diluted oxidant is required followed by rapid mixing with the fuel. This results in distributed reaction zone instead of a concentrated flame front as observed in conventional diffusion flames and hence, to avoid hot spot regions and provide reduced NO_x and CO emissions. The focus of this dissertation is to develop and demonstrate CDC for application to stationary gas turbine combustors which generally operate at thermal intensity of $15\text{MW/m}^3\text{-atm}$. However, higher thermal intensity is desirable to reduce hardware costs due to smaller weight and volume of the combustors. Design of high thermal intensity CDC combustor requires careful control of critical parameters, such as, gas recirculation, fuel/oxidizer mixing and residence time characteristics via careful selection of

different air and fuel injection configurations to achieve desirable combustion characteristics. This dissertation examines sequential development of low emission colorless distributed combustor operating from thermal intensity of $5\text{MW/m}^3\text{-atm}$ up to $198\text{MW/m}^3\text{-atm}$. Initially, various fuel and air injection configurations were investigated at a low thermal intensity of $5\text{MW/m}^3\text{-atm}$. Further investigations were performed for a simpler combustor having single air and fuel injection ports for medium thermal intensity range of $28\text{-}57\text{MW/m}^3\text{-atm}$. Among the flow configurations investigated, reverse cross-flow configuration was found to give more favorable results possibly due to higher residence time because of reverse flow geometry and faster mixing with the fuel injection in cross-flow. This configuration was investigated in detail by further reducing the combustor volume to give ultra-high thermal intensity of up to $198\text{MW/m}^3\text{-atm}$. At thermal intensity of $53\text{MW/m}^3\text{-atm}$ NO emissions were 4ppm in non-premixed mode and 1ppm in premixed mode and CO emissions were 30ppm in both the modes. The pressure loss was less than 5% and heat loss was less than 15%. The pressure fluctuations were less than 0.025% suggesting very stable combustion. At ultra-high thermal intensity of $170\text{MW/m}^3\text{-atm}$ NO emissions were 8ppm and 3ppm in non-premixed and premixed modes respectively and CO emissions were about 100ppm in both the modes. Dilution of fuel with nitrogen, carbon dioxide and air resulted in significant reduction in NO emission in non-premixed mode from 8ppm to about 2ppm. Methane was used as fuel for all these investigations. Liquid fuel (ethanol) was also tested and very low NO emission of about 6ppm was obtained in direct injection mode and 2ppm in premixed prevaporized mode. CO emission of about 200ppm was observed in both the modes.

DEVELOPMENT OF COLORLESS DISTRIBUTED COMBUSTION FOR GAS
TURBINE APPLICATION

By

Vaibhav Kumar Arghode

Dissertation submitted to the Faculty of the Graduate School of the
University of Maryland, College Park, in partial fulfillment
of the requirements for the degree of
Doctor of Philosophy
2011

Advisory Committee:
Dr. Ashwani K. Gupta, Chair
Dr. Keith E. Herold
Dr. Kenneth H. Yu (Dean's Representative)
Dr. Kenneth T. Kiger
Dr. Michael R. Zachariah

© Copyright by
Vaibhav K. Arghode
2011

Dedication

I dedicate this dissertation in the honor of my dear parents Dr. Vishwasrao J. Arghode and Dr. Ratnamala V. Arghode for their unwavering love, support and blessings and great faith in my efforts. I owe everything that I have achieved and yet to achieve in my life to them.

Acknowledgements

First and foremost, I am thankful to my dissertation advisor Dr. Ashwani K. Gupta for giving me opportunity to work on a very interesting topic of colorless distributed combustion. I am grateful to him for giving me freedom both in terms of time and financial support to pursue new ideas and for guiding me through the course of this dissertation. He has motivated me to believe in the value of hard work, persistence and dedication to achieve excellence. I would like to express my sincere gratitude to Dr. Gupta for supporting me at critical points during my graduate studies without which this work would not have met its destination.

I would like to thank my dissertation committee members Dr. Kenneth Kiger, Dr. Kenneth Yu, Dr. Michael Zachariah and Dr. Keith Herold for their guidance and valuable suggestions. I am thankful to Dr. Gregory Jackson for providing key physical insights that was helpful in shaping this dissertation.

I am thankful to Mr. Howard Paul Grossenbacher of Aerospace Machine Shop for his help as well as great quality work of facility fabrication.

I express my gratitude to all my compatriots at the Combustion Laboratory for providing great camaraderie and making the work environment enjoyable. I also take this opportunity to thank my friend Tanmay for his encouragement and support during my graduate studies.

I will most cherish the six seasons of cricket that I played on weekends with Warriors Cricket Club; the team has taught me to perform at top level by maintaining

a very humorous, calm and cordial environment. I owe a great deal to the team to help me maintain proper work-life balance during often rigorous work schedules.

I wish to express my sincere gratitude to Office of Naval Research (ONR) program manager, Dr. Gabriel D. Roy, for providing the financial support that made this research possible.

I owe a great deal to my parents who have showered unconditional love and support and have shown great confidence in my abilities. I am grateful to my brother Vishal who has encouraged me and shown me the right path at every critical point during my graduate studies. Last, but not the least, I am thankful to my lovely wife Neha for filling my life with love and affection that was more than helpful in wading through the concluding part of my graduate studies.

Table of Contents

Dedication	ii
Acknowledgements	iii
Table of Contents	v
List of Tables.....	ix
List of Figures	x
Chapter 1 : Introduction	1
1.1 Background and Objective.....	1
1.2 Gas Turbine Combustor Design Considerations.....	4
1.2.1 Low Pollutant Emission.....	5
1.2.2 High Thermal Intensity	6
1.2.3 Stable Combustion.....	6
1.2.4 Low Pressure Loss	7
1.2.5 Wide Stability Limit	7
1.2.6 Desired Pattern Factor.....	8
1.2.6 Fuel flexibility.....	8
1.3 Pollutant Formation	9
1.3.1 NO _x Formation.....	9
1.3.2 CO (UHC) Formation	13
1.3.3 Soot Formation.....	14
1.4 NO _x Abatement Strategies	14
1.4.1 Injection of Diluents	15
1.4.2 Exhaust Clean-up.....	16
1.4.3 Limiting NO _x Formation.....	16
1.5 High Temperature Air Combustion (HiTAC).....	21
(a) HiTAC	23
(b) Ordinary combustion.....	23
1.6 Objective.....	27
Chapter 2 CDC Design Considerations.....	29
2.1 Gas Recirculation.....	30
2.2 Ignition Delay	32
2.3 Fuel/Oxidizer Mixing (Turbulent Mixing Time).....	35
2.4 Fuel/Oxidizer Mixing (Jet Decay in Cross-Flow)	38
2.5 Thermal Intensity and Flow Configuration.....	41
Chapter 3 : Literature Review	52
3.1 Furnace Application.....	60
3.2 Gas Turbine Application.....	72

3.3 Flame Investigations	78
3.4 Thesis Outline	86
Chapter 4 Low Thermal Intensity ($5\text{MW}/\text{m}^3\text{-atm}$)	92
4.1 Experimental Setup ($5\text{MW}/\text{m}^3\text{-atm}$).....	93
4.2 Numerical Setup ($5\text{MW}/\text{m}^3\text{-atm}$).....	98
4.3 Results and Discussion	101
4.3.1 Flowfield Characteristics	101
4.3.2 Residence Time Characteristics and Pressure Loss	103
4.3.3 Global Pictures.....	105
4.3.4 NO and CO Emissions	109
4.4 Effect of Air and Fuel Injection Diameter (configuration “FS1”).....	112
4.4.1 Numerical Results.....	113
4.4.2 Experimental Results	121
4.4 Conclusions.....	123
Chapter 5 Medium Thermal Intensity ($20\text{-}40\text{MW}/\text{m}^3\text{-atm}$).....	125
5.1 Experimental and Numerical Setup ($20, 30$ and $40\text{MW}/\text{m}^3\text{-atm}$).....	125
5.2 Results and Discussion	128
5.3 Experimental and Numerical Set Up ($28\text{MW}/\text{m}^3\text{-atm}$)	137
5.4 Results and Discussion	141
5.4.1 Flowfield Characteristics	141
5.4.2 Global Pictures.....	149
5.4.3 OH^* Distribution	153
5.4.4 NO and CO Emissions	157
5.4.5 Lean Operational Limit.....	160
5.5 Conclusions.....	160
Chapter 6 : High Thermal Intensity ($57\text{-}85\text{MW}/\text{m}^3\text{-atm}$)	163
6.1 Experimental Set Up ($57\text{MW}/\text{m}^3\text{-atm}$).....	163
6.2 Results and Discussion	166
6.2.1 OH^* Distribution	166
6.2.2 NO and CO Emissions	169
6.2.3 Lean Operational Limit.....	170
6.3 Experimental and Numerical Set Up ($85\text{MW}/\text{m}^3\text{-atm}$)	171
6.3.1 Experimental Set Up.....	173
6.3.2 Numerical Set Up.....	174
6.4 Results and Discussion	176
6.4.1 Flowfield Characteristics	176
6.4.2 Global Pictures.....	180
6.4.3 OH^* Distribution	181
6.4.4 NO and CO Emissions	185
6.4.5 Lean Operational Limit.....	190
6.5 Conclusions.....	191
Chapter 7 : Ultra-High Thermal Intensity ($53\text{-}198\text{MW}/\text{m}^3\text{-atm}$).....	193

7.1 Experimental Set Up (53-85MW/m ³ -atm).....	193
7.2 Results and Discussion	201
7.2.1 Flowfield Characteristics	201
7.2.2 Global Pictures.....	203
7.2.3 OH* Distribution	204
7.2.4 Emissions of NO and CO.....	206
7.2.5 Dynamic Pressure Fluctuations.....	208
7.2.6 Pressure Loss, Heat Loss and Lean Limit.....	209
7.3 Experimental Set Up (156-198MW/m ³ -atm).....	211
7.4 Results and Discussion	213
7.4.1 NO and CO emissions.....	213
7.4.2 Fuel Dilution Effects.....	213
7.5 Operation with Liquid Fuel (170MW/m ³ -atm).....	216
7.7 Effect of Thermal Intensity.....	218
7.7 Conclusions.....	224
Chapter 8 : Summary	226
 Chapter 9 : Conclusions and Recommendations for Future Work	 232
9.1 Conclusions.....	232
9.1.1 Effect of Flowfield Configuration	232
9.1.2 Effect of Air and Fuel Injection Diameter	233
9.1.3 Fuel/Oxidizer Mixing.....	234
9.1.4 Effect of Thermal Intensity.....	234
9.1.5 Effect of Hydrogen Addition to Methane	235
9.1.6 Effect of Air Preheat Temperature.....	235
9.1.7 Fuel Dilution Effects.....	236
9.1.8 Operation with Liquid Fuel.....	236
9.2 Recommendations for Future Work.....	237
9.2.1 Detailed Species and Temperature Distribution	237
9.2.2 Quantification of Relevant Time Scales	237
9.2.3 Flowfield in Reacting Condition.....	238
9.2.4 Improved Fuel/Oxidizer Mixing.....	238
9.2.5 Characterization of Dynamic Performance.....	238
9.2.6 Scaling of CDC Combustor	239
9.2.7 Liquid Fuel Operation.....	239
9.2.8 Application to Aircraft Engines.....	240
9.2.9 Elevated Pressure Operation	240
9.2.10 Part Load Operation.....	241
Appendix A - List of Papers	242
 A. 1 Journal Papers	 242
A. 2 Conference Papers.....	243
A. 3 Other Journal Papers	244
A. 4 Other Conference Papers	244
Appendix B - Centerline Jet Velocity Decay.....	246

Appendix C - CFD Simulations of Free Jet	248
Appendix D – Scaling of CDC Combustor.....	251
Appendix E – Equilibrium and Perfectly Stirred Reactor Calculations.....	256
Appendix F – Operational Characteristics of Low Emission Combustors.....	261
Appendix G – Experimental Apparatus	276
G.1 Air/Fuel Flowrate Measurement	276
G.2 Air Preheater	278
G.3 Temperature Measurement	278
G.4 Global Imaging	279
G.5 Chemiluminescence Imaging.....	279
G.6 Gas Analyzer.....	280
G.6.1 NO analyzer.....	281
G.6.2 O ₂ analyzer.....	281
G.6.3 CO analyzer.....	281
G.7 Particle Image Velocimetry	282
G.7.1 PIV Laser	282
G.7.2 PIV Camera.....	283
G.7.3 Seeder.....	283
G.8 Dynamic Pressure Sensor.....	284
G.9 Liquid Supply System.....	285
G.10 Ignition and Initial Heating of the Combustor	286
Appendix H – Combustor Assembly	288
References	295
Combustion.....	295
Flameless Oxidation (FLOX)	295
Fuel/Oxidant Direct Injection(FODI)	296
Gas Turbine Combustion	296
High Intensity Low Emission (HILE).....	297
High Temperature Air Combustion (HiTAC).....	297
Hydrogen Addition to Methane Fuel	298
Jet Stirred Reactor (JSR).....	298
Moderate and Intense Low Oxygen Dilution (MILD).....	299
Particle Image Velocimetry	300
Pollutant Emission	300
Princeton Axysymmetric Whirl Combustor (PAWC)	300
Stagnation Point Reverse Flow (SPRF).....	300
Trapped Vortex Combustor (TVC).....	301
Temperature Measurement	302
Turbulent Jets.....	302

List of Tables

Table 1.1 Typical parameters for land based and aeropropulsion gas turbine combustor.....	3
Table 1.2 Contribution to total NO from different mechanisms [Lefebvre, A. H., 1999].	13
Table 4.1 Different cases investigated for the effect of air and fuel injection diameter.	113
Table 6.1 Different cases investigated for the effect of hydrogen addition.....	173
Table 7.1 Parameters for PIV experiment.....	201
Table 7.2 Different cases for the effect of fuel dilution ($\Phi=0.6$, $170\text{MW}/\text{m}^3\text{-atm}$).	214
Table B.1 Correlation constants for centerline velocity decay of a free jet.....	247
Table D.1 Different scaling approach.	252
Table D.2 Parameters of high thermal intensity scaled combustor.	253
Table D.3 Parameters of ultra-high thermal intensity scaled combustor.....	255
Table E.1 Equilibrium calculations for methane air combustion ($T_{in}=300\text{K}$).	257
Table E.2 Equilibrium calculations for methane air combustion ($T_{in}=600\text{K}$).	258
Table E.3 Perfectly stirred reactor calculations for methane air combustion ($T_{in}=300\text{K}$, $T_{res}=20\text{ms}$).	259
Table F.1 Combustor geometries reported in literature.	261
Table F.2 Combustor geometries investigated by Arghode, V. K. and Gupta, A. K.	268

List of Figures

Figure 1.1 (a-c) Gas turbine operation and (d) power generation by fuel.	2
Figure 1.2 Gas turbine combustor.....	3
Figure 1.3 Gas turbine design considerations [Lefebvre, A. H., 1999].	4
Figure 1.4 Pollutant trade-off.....	5
Figure 1.5 Pollutant formation [Lefebvre, A. H., 1999].....	9
Figure 1.6 NO formation via thermal Zeldovich mechanism.	11
Figure 1.7 NO _x abatement strategies [Lefebvre, A. H., 1999].....	14
Figure 1.8 Water/Steam injection [Lefebvre, A. H., 1999].	15
Figure 1.9 Exhaust gas recirculation [Lefebvre, A. H., 1999].....	16
Figure 1.10 Lean premixed/lean premixed prevaporized [Lefebvre, A. H., 1999]. ...	17
Figure 1.11 Catalytic combustion.	19
Figure 1.12 Rich burn-quick quench-lean burn (RQL) concept.	20
Figure 1.13 Conceptual difference between (a) high temperature air combustion (HiTAC) and (b) ordinary combustion [Gupta, A. K., <i>et al.</i> , 2003].	23
Figure 1.14 Effect of air temperature and oxygen concentration on (a) global flame behavior (b) operational regime of propane-air flames [Gupta, A. K., <i>et al.</i> , 2003]. .	24
Figure 1.15 Flame structure for ordinary combustion and high temperature air combustion (HiTAC) for furnaces [Gupta, A. K., <i>et al.</i> , 2003].....	25
Figure 1.16 Conceptual temperature profiles for (a) ordinary combustion and (b) high temperature air combustion (HiTAC) [Gupta, A. K., <i>et al.</i> , 2003].....	26
Figure 2.1 Important factors for designing a CDC combustor.	29
Figure 2.2 Variation of recirculation ratio with (a) air injection temperature and (b) air injection diameter for a free jet (D=3/16inch).	32
Figure 2.3 Set up for Chemkin simulations to obtain oxidizer temperature and O ₂ concentration.....	33
Figure 2.4 (a) Temperature and oxygen concentration variation (b) ignition delay variation with recirculation ratio and (c) ignition delay variation with temperature and oxygen concentration.	35
Figure 2.5 Variation of mixing time and pressure loss with jet velocity.....	38
Figure 2.6 Jet decay in cross-flow (d=D/3, D=3/16inch, fuel=methane).	41
Figure 2.7 (a) Effect of thermal intensity on residence time (b) effect of residence time on NO and CO levels (perfectly stirred reactor, $\phi=0.8$) (c) CO conversion rate variation with residence time (d) effect of gases having low residence time on CO emissions.....	44
Figure 2.8 Geometry and mesh for forward and reverse flow configurations.....	46
Figure 2.9 Jet decay and gas recirculation in confinement.....	47
Figure 2.10 (a) Tracer mass fraction at the combustor exit and (b) residence time frequency distribution for configurations F and R (psr=perfectly stirred reactor).	51
Figure 3.1 Thermal intensity of combustors reported in literature.	54
Figure 3.2 NO _x /CO emissions from combustors reported in literature.	55
Figure 3.3 Length scale of combustors reported in literature.	56
Figure 3.4 Heat load for combustors reported in literature.....	57
Figure 3.5 (a) Air and fuel injection velocity and (b) turbulent mixing time (D/U) for combustors reported in literature.	58

Figure 3.6 (a) Air preheat temperature and (b) operating pressure for combustors reported in literature.....	60
Figure 3.7 Jet in cross flow of high temperature and diluted air.	81
Figure 3.8 Jet in co-flow of flue gases.....	83
Figure 3.9 Effect of fuel mixing.	84
Figure 3.10 Mild combustion furnace.....	86
Figure 3.11 Combustor designs investigated in the present work	90
Figure 4.1 (a) Photograph and (b-m) schematics of different flow configurations for low thermal intensity ($5\text{MW}/\text{m}^3\text{-atm}$) CDC combustor.....	98
Figure 4.2 Grid used for numerical simulation for different flowfield configuration.	101
Figure 4.3 Velocity contour plots for different flowfield configurations.	103
Figure 4.4 (a,b) Residence time characteristics and (c) pressure loss (cold flow) of different flowfield configurations.	105
Figure 4.5 Global pictures for different flowfield configurations.	109
Figure 4.6 NO and CO emissions for different flowfield configurations.	112
Figure 4.7 Velocity contours plots of configuration “FS1” for effect of air and fuel injection diameter.....	114
Figure 4.8 (a,b) Centerline velocity decay of air jet (X is distance along the air jet, $D=3/16\text{inch}$) and (c,d) pressure loss for effect of air and fuel injection diameter. ...	116
Figure 4.9 Centerline methane mass fraction variation for air jet (X is distance along the air jet, $\text{CH}_{4\text{mix}}=0.045$ for perfect mixing, $D=3/16\text{inch}$) for effect of air and fuel injection diameter.....	117
Figure 4.10 Centerline velocity and methane concentration decay for the fuel jet (x is distance along the fuel jet, $D=3/16\text{inch}$) for effect of air and fuel injection diameter.	119
Figure 4.11 Recirculation ratio variation for air jet (X is distance along the air jet, $D=3/16\text{inch}$) for effect of air and fuel injection diameter.....	121
Figure 4.12 NO and CO emissions for effect of fuel and air injection diameter.....	123
Figure 5.1 Schematic diagrams of medium thermal intensity ($20, 30 \& 40\text{MW}/\text{m}^3\text{-atm}$) CDC combustor.	127
Figure 5.2 (a) Grid (b-d) Velocity contour plots and (e-g) pathline (14 pathlines) plots for three thermal intensity cases.	130
Figure 5.3 (a) Centerline velocity decay, (b) Recirculation ratio variation and (c) overall pressure loss for the three thermal intensity cases.....	132
Figure 5.4 Global pictures for (a-c) Diffusion, (d-f) non-premixed CDC and (g-i) premixed CDC for the three thermal intensity cases.	135
Figure 5.5 (a) NO and (b) CO emissions for the three thermal intensity cases.	137
Figure 5.6 Medium thermal intensity ($28\text{MW}/\text{m}^3\text{-atm}$) CDC combustor (a) CAD drawing (b) photograph (c) schematic diagram (d) pilot flame used for initial heating.	138
Figure 5.7 (a) photograph and (b-i) schematic diagrams of different flow configurations examined for medium thermal intensity ($28\text{MW}/\text{m}^3\text{-atm}$) CDC combustor.....	139
Figure 5.8 Grid used for different configurations.	141
Figure 5.9 Velocity magnitude contour plots for different configurations.....	143

Figure 5.10 Velocity decay and gas recirculation for forward flow configuration. .	145
Figure 5.11 (a) Tracer mass fraction at the exit and (b) residence time frequency distribution for configurations “FS2” and “FO” (psr=perfectly stirred reactor).	147
Figure 5.12 (a-b) Velocity decay and (c-d) gas recirculation for reverse flow configurations.	149
Figure 5.13 Global pictures for different configurations (A=Air, F=Fuel, B=Burned gases).....	152
Figure 5.14 OH* distribution for different configurations.	156
Figure 5.15 (a) NO emissions and (b) CO emissions for different configurations...	159
Figure 5.16 Lean operational limit for different configurations.	160
Figure 6.1 (a) photograph and (b-i) schematic diagrams of different configurations for high thermal intensity (57MW/m ³ -atm) CDC combustor.	165
Figure 6.2 OH* distribution for different configurations.	168
Figure 6.3 (a) NO emissions (b) CO emissions for different configurations.....	170
Figure 6.4 Lean operational limit for different configurations.	171
Figure 6.5 (a) photograph and (b-e) schematic diagrams for high thermal intensity (85MW/m ³ -atm) CDC combustor.....	172
Figure 6.6 (a) Grid used for CFD simulation and (b) velocity magnitude contour plot (c) pathline plot (15 pathlines tracked from air injection).	177
Figure 6.7 (a) Air jet centerline velocity decay and (b) Variation of recirculation ratio along the length (X) of the combustor, D=d _{air}	178
Figure 6.8 (a) Tracer mass fraction at the exit and (b) residence time frequency distribution for CDC combustor and comparison with perfectly stirred reactor (psr).	180
Figure 6.9 Global pictures for pure methane fuel for (a-d) non-premixed (e-h) premixed mode (A=Air, B=Burned gases, F=Fuel).	181
Figure 6.10 OH* distribution of non-premixed mode for (a-d) 0wt%H ₂ , (e-h) 4wt%H ₂ , and (i-l) 8wt%H ₂ (A=Air, B=Burned gases, F=Fuel).	183
Figure 6.11 OH* distribution of premixed mode for (a-d) 0wt%H ₂ , (e-h) 4wt%H ₂ , and (i-l) 8wt%H ₂ (A=Air, B=Burned gases, F=Fuel).	185
Figure 6.12 NO and CO emissions for (a-b) perfectly stirred reactor, (c-d) non-premixed mode and (e-f) premixed mode.....	189
Figure 6.13 Lean operational limit with different amount of hydrogen addition to methane fuel.....	191
Figure 7.1 (a) photograph (b) schematic (c) non-premixed and (d) premixed mode for high thermal intensity (53-85MW/m ³ -atm) CDC combustor.	196
Figure 7.2 (a-c) PIV and (d) dynamic pressure sensor set-up for CDC combustor..	200
Figure 7.3 (a-b) Velocity contour plot and (b) vector plot obtained from PIV experiments, T _{air} =300K.....	202
Figure 7.4 Fluctuating velocity contour plots obtained from PIV experiments, T _{air} =300K.	203
Figure 7.5 Global pictures for the CDC combustor.	204
Figure 7.6 OH* chemiluminescence images for CDC combustor for (a-d) non-premixed, (e-h) premixed (A=Air, B=Burned gases, F=Fuel).	206
Figure 7.7 (a) NO and (b) CO emissions in non-premixed and premixed conditions (-p denotes premixed) for T _{air} =300K and 600K.	208

Figure 7.8 Dynamic pressure response for (a) non-premixed and (b) premixed mode.	209
Figure 7.9 (a) Pressure loss and heat loss and (b) lean operational limit for $T_{air}=600K$ in non-premixed mode and (c) pressure loss obtained from CFD simulations.	211
Figure 7.10 (a) Photograph (b) schematic (c) non-premixed and (d) premixed mode for ultra-high thermal intensity ($156-198MW/m^3\text{-atm}$) CDC combustor.	212
Figure 7.11 (a) NO and (b) CO emissions in non-premixed and premixed modes.	213
Figure 7.12 (a) NO and (b) CO emission levels for the effect of fuel dilution.	216
Figure 7.13 (a) NO and (b) CO emission levels with liquid (ethanol) fuel operation in direct injection (DI) and premixed prevaporized (PP) modes.	218
Figure 7.14 Reverse flow configurations investigated for thermal intensity range from $5-198MW/m^3\text{-atm}$.	218
Figure 7.15 (a) NO and (b) CO emissions for premixed flow mode corresponding to thermal intensity range of $5-198MW/m^3\text{-atm}$, equivalence ratio = 0.7.	219
Figure 7.16 (a) Average residence time in reacting condition (b) confinement ratio for thermal intensity range from $5-198MW/m^3\text{-atm}$.	221
Figure 7.17 OH^* distribution at thermal intensity of (a) $57MW/m^3\text{-atm}$ and (b) $85MW/m^3\text{-atm}$.	221
Figure 7.18 Residence time characteristics for the reverse flow combustors investigated.	223
Figure 8.1 Thermal intensity and length scale for various combustors investigated in the present work.	227
Figure 8.2 NO, CO emissions for various combustors investigated in the present work.	227
Figure 8.3 Heat load for various combustors investigated in the present work.	228
Figure 8.4 Selected combustor geometry and operational parameters among the combustors investigated in the present work.	231
Figure B.1 Centerline jet velocity decay plots using different correlations in literature.	246
Figure C.1 Mesh used for simulations (2D axisymmetric, diameter=64D, length=64D, air injection diameter=D, $D=3/16''$).	248
Figure C.2 Effect of (a) grid size and (b) inlet velocity, k-e realizable model, turbulent intensity=5%, inlet velocity $x=128m/s$.	249
Figure C.3 Effect of inlet turbulence intensity and turbulence models.	250
Figure D.1 Scaling of CDC combustor.	252
Figure E.1 (a) Adiabatic flame temperature, (b) NO and CO emissions from equilibrium calculations.	257
Figure E.2 (a) Outlet temperature, (b) NO and CO emissions from perfectly stirred reactor calculations.	259
Figure E.3 (a,b) Effect of pressure and (c,d) effect of temperature on NO and CO emissions from perfectly stirred reactor calculations.	260
Figure G.1 Line Diagram of CDC test facility.	276
Figure G.2 Exit gas sampling system.	280
Figure G.3 Entrained flow seeding system for alumina particles used for PIV experiments.	284
Figure G.4 Liquid fuel supply system.	286

Figure G.5 Ignition system and initial heating for the CDC combustor.....	287
Figure H. 1 Main combustor plates (dimensions in inch).....	288
Figure H. 2 Combustor cover plates (dimensions in inch).	289
Figure H. 3 Quartz and alumina silicate plates (dimensions in inch).	290
Figure H. 4 Photographs of ultra high thermal intensity CDC combustor (156- 198MW/m ³ -atm).....	291
Figure H. 5 Main combustor tube and top and bottom plates.....	292
Figure H. 6 Main combustor tube and top and bottom plates.....	293
Figure H. 7 Scaled ultra-high thermal intensity CDC combustor (93MW/m ³ -atm).	294

Chapter 1 : Introduction

1.1 Background and Objective

The focus of present dissertation is on development of colorless distributed combustion (CDC) for land based gas turbine combustors. Gas turbines operate on Brayton cycle shown in Figure 1.1(a, b) where air is compressed isentropically (1-2) then heat is added at constant pressure (2-3) then the high temperature and high pressure gases are expanded isentropically in turbine (3-4) followed by heat rejection (4-1). The primary objective of a gas turbine combustor is to increase the temperature of gases at constant pressure as shown in path 2-3 in Figure 1.1(a). Gas turbine combustors operate at elevated pressure (see Figure 1.1(a)) and the inlet temperature of gases is governed by the pressure ratio in the compressor (see Figure 1.1(c)). Generally, the operational pressure of a land based gas turbine combustor is about 15atm and inlet temperature is about 700K.

Gas turbines could be powered by both liquid as well as gaseous fuels however; natural gas is one of the major fuels used for gas turbines in a land based power plant. Now about 90% of newer power plants are fueled by natural gas [National Energy Policy, 2001]. Figure 1.1(d) shows the share of natural gas for power generation and from the figure it can be observed that natural gas constitutes about 23% of electricity generated in USA. The major constituent of natural gas is methane and hence for the present investigation methane is used as fuel to simulate operation of gas turbine combustor with natural gas. Liquid fuels such as jet-A, which are derivatives of petroleum fuels are mostly used for aircraft engines.

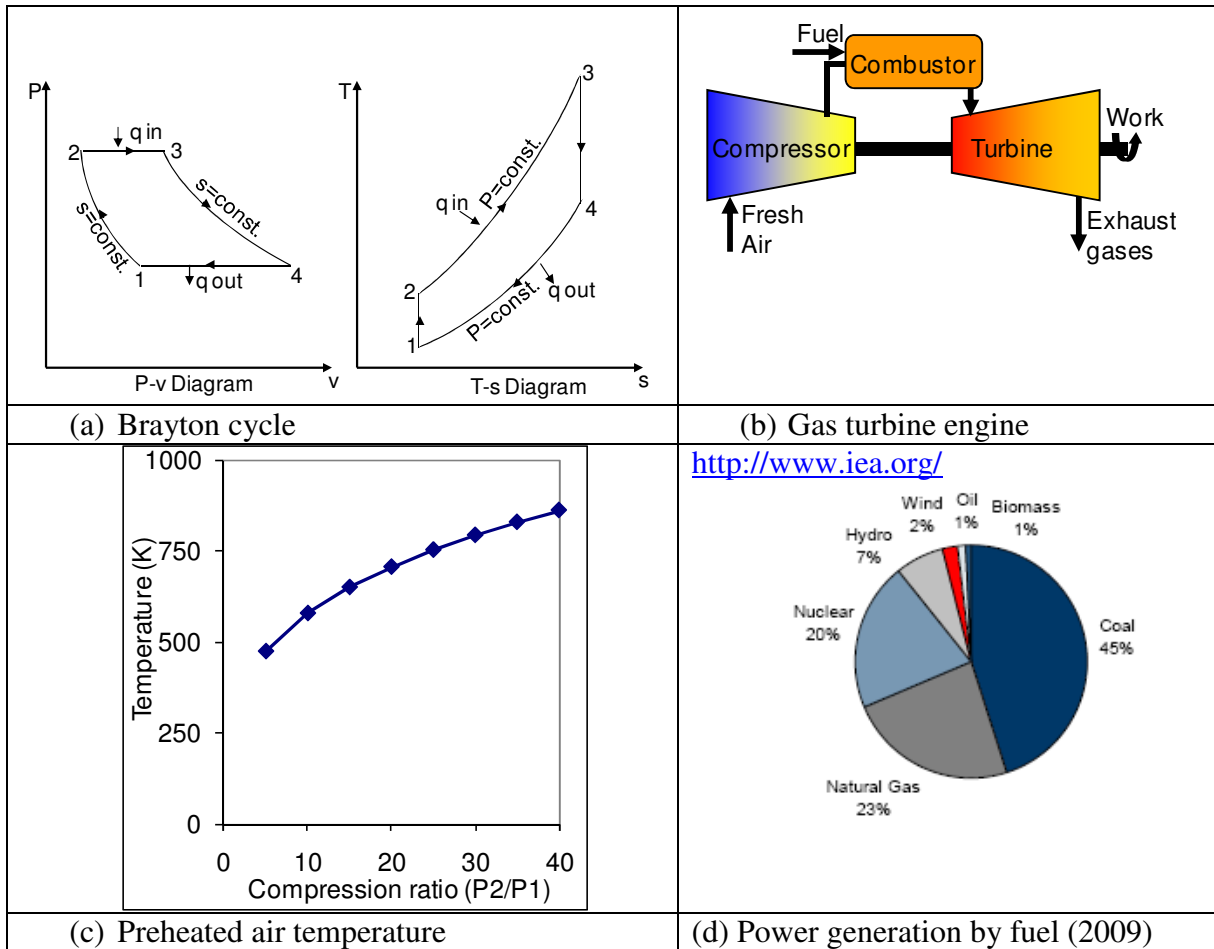


Figure 1.1 (a-c) Gas turbine operation and (d) power generation by fuel.

Figure 1.2(a) shows a GE-7FA gas turbine engine used for power generation. A schematic of land based gas turbine combustor is shown in Figure 1.2(b). The air from compressor is split in two parts as combustion air and cooling/dilution air. The cooling/dilution air is used to cool the combustor liner as well to reduce the temperature of combustion product gases to match the requirement of gas turbine blades as well as to tailor the temperature profile to minimize thermal stress on the blades. Typical land based gas turbine combustor operates at pressure of about 15atm and the combustor length is about 60inch. Figure 1.2(c) shows GE-90 gas turbine engine used in aircraft and a schematic of gas turbine combustor is shown in Figure 1.2(d). It can be observed that the combustion pressure varies from about 40atm at

take-off to about 10atm at cruise. The combustor is significantly smaller (about 10inch) as compared to the land based gas turbine combustor (about 60inch). Typical values for land based as well as aircraft GT combustor are listed in Table 1.1.

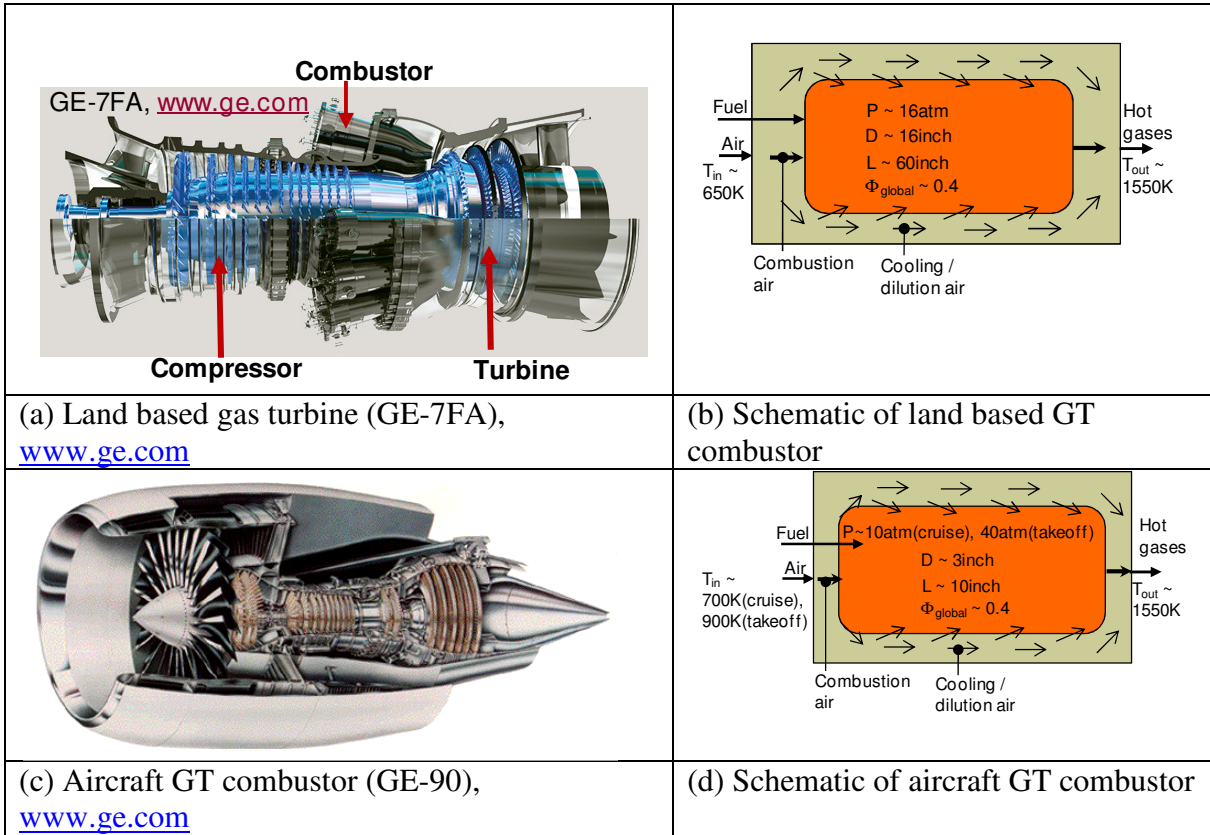


Figure 1.2 Gas turbine combustor.

Table 1.1 Typical parameters for land based and aeropropulsion gas turbine combustor

	Land based gas turbine combustor	Aircraft gas turbine combustor
Length	60inch	10inch
Residence time	20ms	2-3ms
Thermal intensity	15MW/m ³ -atm	150MW/m ³ -atm
Fuel	Natural gas	Kerosene based liquid fuel
Pressure	15atm	10atm(cruise),40atm(takeoff)
Flame stabilizer	Swirler	Swirler
Fuel introduction	Lean premixed	Liquid fuel atomization

The focus of this dissertation is on development of advanced combustion technology called colorless distributed combustion (CDC) for land based gas turbine application. CDC combustor employs direct injection of both air and fuel in the combustor without any need for a flame stabilizer such as swirlers which are used in conventional gas turbine combustors. The benefits of CDC technology are ultra-low pollutant emission, improved pattern factor, low noise emission, stable combustion and low pressure drop across the combustor. Thermal intensity of interest is about $15\text{MW}/\text{m}^3\text{-atm}$ operating on natural gas and with possible extension to high thermal intensity aircraft application using liquid fuel. The next section describes basic gas turbine design considerations.

1.2 Gas Turbine Combustor Design Considerations

The basic considerations for designing a gas turbine combustor are shown in Figure 1.3 [Lefebvre, A. H., 1999] and each consideration will be discussed briefly in this section.

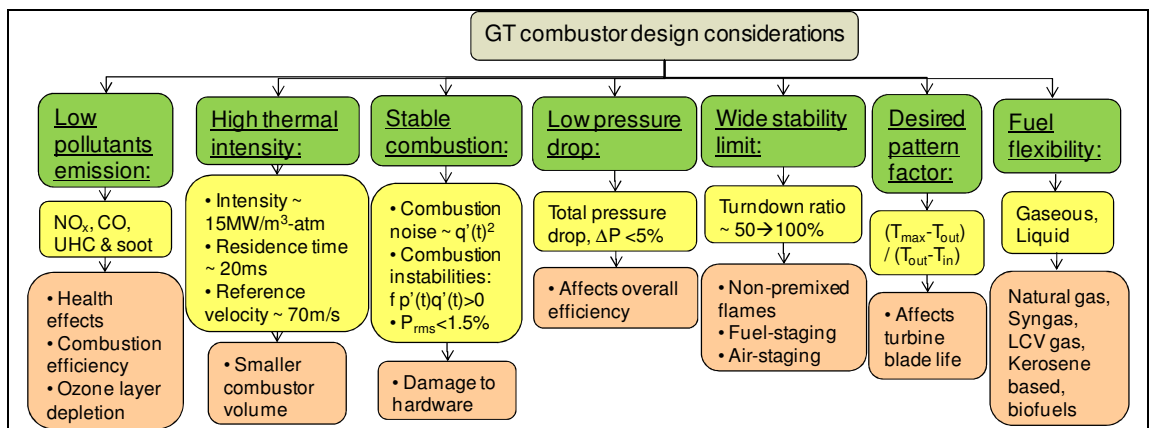


Figure 1.3 Gas turbine design considerations [Lefebvre, A. H., 1999].

1.2.1 Low Pollutant Emission

Lower pollutant emission has governed the design and development of land based gas turbine combustors to a large extent. Unburned hydrocarbon emissions directly relate to combustion efficiency and almost 100% combustion efficiency (ultra low UHC emissions) is desired from the gas turbine combustors as it directly relates to the fuel costs. Figure 1.4 shows typical trade-off for NO_x and CO/UHC for a gas turbine combustor. Higher CO emissions are observed at both low and high equivalence ratios and NO_x emissions are high at higher equivalence ratios up to stoichiometry and decreases in fuel rich condition. Hence there is a small operational window where both NO_x and CO emissions are in acceptable range. Soot, which is mostly carbon particles, is formed in fuel rich condition and is hard to eliminate once it is formed. The regulations from EPA restricts the NO_x emissions for a land based gas turbine combustor burning natural gas to be less than 15ppm for units > 250MW, less than 25ppm for units in range of 15-250MW and less than 42ppm for units <15MW [Environmental Protection Agency Federal Register, 2006].

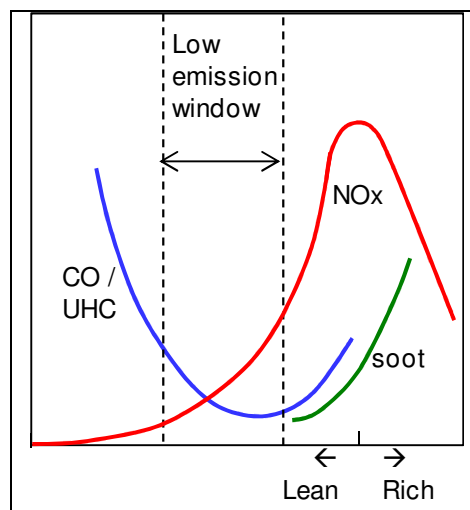


Figure 1.4 Pollutant trade-off.

1.2.2 High Thermal Intensity

The generally accepted definition of thermal intensity in literature is amount of heat energy released per unit time in a unit volume of combustor scaled by the operating pressure [Vincent, E. T., 1950]. Land based gas turbine combustors operate at thermal intensity range of 5-50MW/m³-atm [Vincent, E. T., 1950]. The state of the art GE DLN 2.6 combustor which is widely used in popular gas turbine engines such as GE-7FA (see Figure 1.2(a)) operates at thermal intensity of about 15MW/m³-atm [Vandervort, C. L., 2001]. Higher thermal intensity would result in smaller combustor volume for same thermal load; hence higher thermal intensity is desired to reduce space as well as the weight of the gas turbine engine and hence reduce the hardware costs. Higher thermal intensity is even more desirable for aerospace application as weight as well as space is a premium. Generally, aircraft gas turbine combustor operates at thermal intensity of about 150MW/m³-atm.

1.2.3 Stable Combustion

State of the art gas turbine combustors operate in ultra-lean premixed mode to avoid hot spot regions and minimize the NO_x emissions. Near lean operational limit the combustor is susceptible to combustion instabilities. Combustion instabilities are large amplitude pressure oscillations due to coupling between oscillatory heat release process (unsteady combustion) and a natural acoustic mode of the combustor. Combustion instabilities are undesirable because it induces stress due to fatigue on the combustor components, induces thermal stress to the components as well as may result in flame flashback or blow off. Combustion instability in gas turbine combustor is one of the active topics for combustion research mostly for ultra-lean premixed

combustors [Lieuwen, T. C. and Yang, V., 2005]. Different techniques of active and passive control of combustion instabilities have been pursued to minimize and control unstable behavior of the combustor. However, it is desirable to design a combustor which results in very small pressure oscillations. Industrially accepted value for pressure fluctuations (root mean square) is 1.5%rms.

1.2.4 Low Pressure Loss

Overall pressure loss is defined by the ratio of total pressure drop across the combustor to the inlet total pressure and is given by equation 1.1 below. Pressure loss in the combustor is directly related to the total efficiency of the gas turbine cycle hence minimum pressure loss is desirable. Generally, overall pressure loss across a gas turbine combustor range from 4-8% [Lefebvre, A. H., 1999]. It may be noted that this pressure loss is calculated in cold flow condition.

$$\text{Overall pressure loss} = \frac{P_{in}^{total} - P_{out}^{total}}{P_{in}^{total}} \quad (\text{equation 1.1})$$

Estimate of pressure drop due to combustion for a constant area duct is given by equation 1.2 below.

$$\text{Combustion pressure drop} = \Delta P_{combustion}^{total} = P_{in}^{dynamic} \times \left(\frac{T_{out}}{T_{in}} \right) \quad (\text{equation 1.2})$$

For practical combustors combustion pressure drop is about 0.5-1% of the inlet total pressure [Lefebvre, A. H., 1999].

1.2.5 Wide Stability Limit

Wider stability limits are desirable for gas turbine combustor part load operation. The state of the art combustors operate at 50-100% load without influencing the emission profiles [Vandervort, C. L., 2001]. For aircraft engines the flexibility is even

more desirable as the power requirements vary significantly (factor of 2-3) during taxi, take-off and cruise.

1.2.6 Desired Pattern Factor

Temperature distribution at the combustor outlet is important to maximize the turbine blade life and minimize thermal stresses in the blades [Lefebvre, A. H., 1999]. Pattern factor quantifies the unevenness in temperature distribution at the combustor exit and is given by the following equation 1.3.

$$Pattern\ factor = \frac{T_{max}^{out} - T_{avg}^{out}}{T_{avg}^{out} - T_{avg}^{in}} \quad (\text{equation 1.3})$$

It may be noted that a tailored temperature profile may more desirable such that the thermal stresses are minimum at the hub as higher thermal stresses can be tolerated at the blade tips.

In the next section one of the most important design criteria of minimizing the pollutant formation is discussed. Firstly, different pollutant formation mechanisms are described followed by discussion on the abatement strategies used in the industry.

1.2.6 Fuel flexibility

It is desirable to have flexibility to burn different kinds of fuels based on the availability. Generally natural gas is used for land based gas turbines. However, syngas produced from gasification plants (IGCC) plants, and low calorific value fuels can also be utilized in the gas turbine combustors. Aircraft engines generally use kerosene based liquid fuels such as Jet-A or JP-8. Flexibility to burn alternative fuels such as biofuels will also be required in future with continuous depletion of petroleum resources.

1.3 Pollutant Formation

Different mechanisms of pollutant (NO_x , CO/UHC and soot) formation is shown in Figure 1.5.

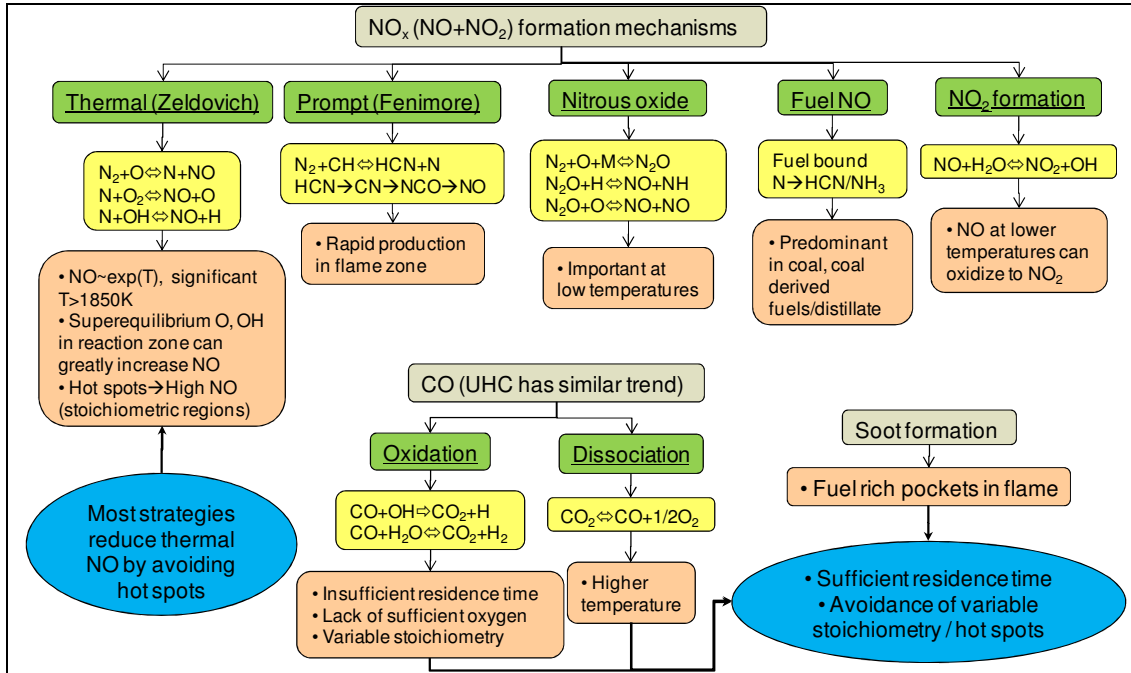


Figure 1.5 Pollutant formation [Lefebvre, A. H., 1999].

1.3.1 NO_x Formation

NO_x is one of the most important pollutant and it has influenced the development of gas turbine combustor significantly [Correa, S. M., 1992] due to its harmful effects such as contribution to photochemical smog formation, acid rain and ozone layer depletion. Stricter emission regulations have pushed the gas turbine combustor development towards ultra low NO_x emissions. NO_x is mostly mixture of nitric oxide (NO) and nitrogen dioxide (NO_2). NO at lower temperature can oxidize to NO_2 , however, NO forms major portion (about 90%) of NO_x mixture and hence the formation mechanisms of NO are discussed here. NO_2 is formed in the post flame zone due to further oxidation of formed NO. NO could be formed by oxidation of

atmospheric nitrogen with oxygen at high temperatures (thermal mechanisms) or via other chemical kinetic pathways involving fuel chemistry. Different NO formation mechanisms are described below.

1. Thermal (Zeldovich mechanism)

Thermal NO is formed due to oxidation of atmospheric nitrogen. N_2 , O_2 and O are considered to be in equilibrium and N atoms are assumed to be at steady state (Turns, S. R., 2000]. Figure 1.6 shows the NO formation rates at different operating temperatures and oxygen concentrations (see Figure 1.6(a)) as well as NO emission at various residence times (see Figure 1.6(b)). The NO formation rate rises exponentially at temperatures above 1850K hence avoidance of gas pockets (hot spots) above temperature of 1850K can significantly reduce NO emissions. NO increases linearly with residence time, however the NO levels are much below the equilibrium value for a typical gas turbine combustor due to slower rate of NO formation and insufficient time to achieve equilibrium (see Appendix E). Thermal NO is generally considered to be formed in post flame zone and it is the major contributor of total NO formed in a combustion system. Thermal NO formation rate is given below in equation 1.4.

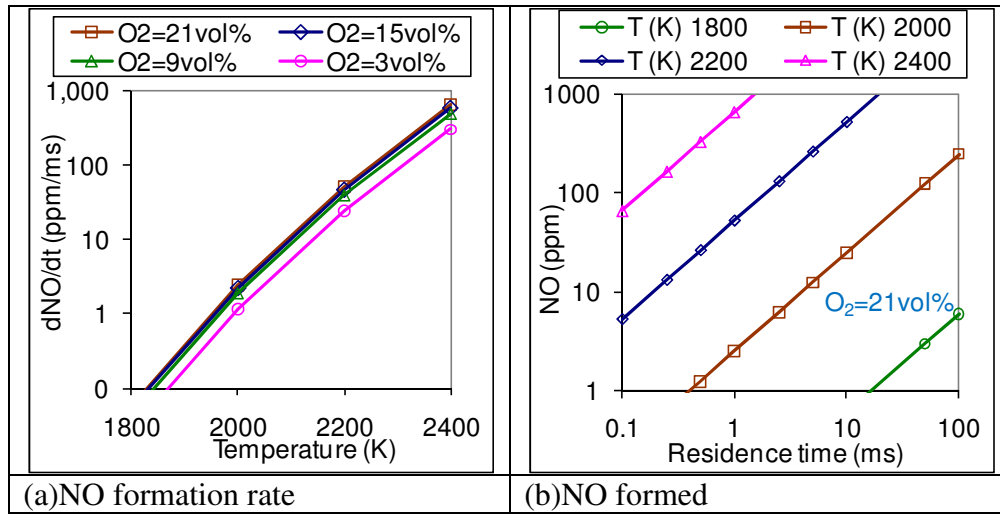
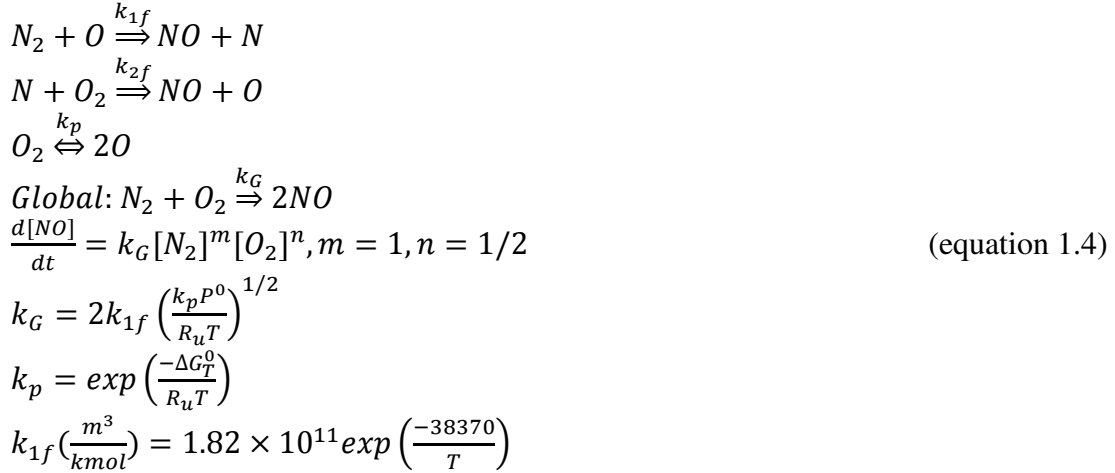


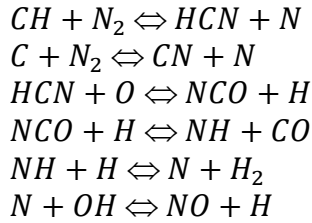
Figure 1.6 NO formation via thermal Zeldovich mechanism.

In flame zone, equilibrium assumption is not valid, super equilibrium (O, OH atoms) concentration of radicals can be several order of magnitude greater than equilibrium concentration. This can greatly increase the NO formation rates [Turns, S. R., 2000].

2. Prompt (Fenimore Mechanism)

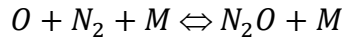
Prompt NO is intimately linked to combustion chemistry of hydrocarbons and NO is rapidly produced in the flame zone. Prompt NO is formed very early in the flame region especially in fuel rich condition [Fenimore, C. P., 1971]. Nitrogen is converted

to HCN by reacting with CH radical and follows the prompt route $\text{HCN} \rightarrow \text{CN} \rightarrow \text{NCO} \rightarrow \text{NO}$ to form prompt NO [Lefebvre, A. H., 1999].



3. Nitrous oxide (N_2O intermediate Mechanism)

N_2O intermediate mechanism is important in fuel lean ($\Phi < 0.8$) combustion and at low temperature conditions. Initially N_2O is formed with reaction of O radical with nitrogen [Miller, J. A. and Bowman, C. T., 1989, Lefebvre, A. H., 1999].



This N_2O gets oxidized to NO by the reactions shown below.



4. Fuel NO

In this mechanism NO is formed mostly due to oxidation of fuel bound nitrogen and this mechanism is dominant in coal and coal derived fuels and well as liquid distillate fuel. However contribution of fuel NO is negligible for natural gas combustion for gas turbine application.

The contribution to total NO from different formation mechanisms for lean-premixed combustion of methane is given in Table 1.2 below. The contributions are obtained analytically [Lefebvre, A. H., 1999]. From the table it may be noted the at

higher temperatures thermal mechanism is major contributor to total NO formed however at lower temperatures prompt and nitrous oxide mechanisms are dominant.

Table 1.2 Contribution to total NO from different mechanisms [Lefebvre, A. H., 1999].

Temperature	Equivalence ratio	Thermal	Prompt	Nitrous oxide	Fuel
1900K	0.8	60%	30%	10%	0%
1500K	0.6	5%	65%	30%	0%

1.3.2 CO (UHC) Formation

Carbon monoxide is formed in fuel-rich pockets in the combustion zone where there is lack of availability of oxygen for complete conversion to CO₂. Carbon monoxide will also be formed where the equivalence ratio is closer to stoichiometric due to dissociation of CO₂ at higher temperatures. Good fuel/air mixing, avoidance of fuel rich pockets and hot stoichiometric regions will result in reduction of carbon monoxide levels. Carbon monoxide levels are also higher at lean condition where temperatures are low resulting in lower burning rate and hence lower conversion of CO to CO₂ [Lefebvre, A. H., 1999]. At lean condition, residence time plays an important role in complete conversion of carbon monoxide to carbon dioxide. Gas turbine combustors operate at lean condition hence the role of residence time on CO conversion is important to consider while designing the combustor. It is found that the UHC emissions and CO emissions are related and the factors influencing CO also influence UHC [Lefebvre, A. H., 1999].

1.3.3 Soot Formation

Soot is formed in fuel-rich zones due to insufficient mixing between fuel and air [Lefebvre, A. H., 1999]. Mostly to prevent soot formation avoidance of formation of fuel-rich pockets is considered to be an effective way.

NO_x is one of the most important pollutant and it has driven the design of gas turbine combustors to a large extent. The next section discusses NO_x abatement strategies used in industry including gas turbines, furnaces as well as boilers.

1.4 NO_x Abatement Strategies

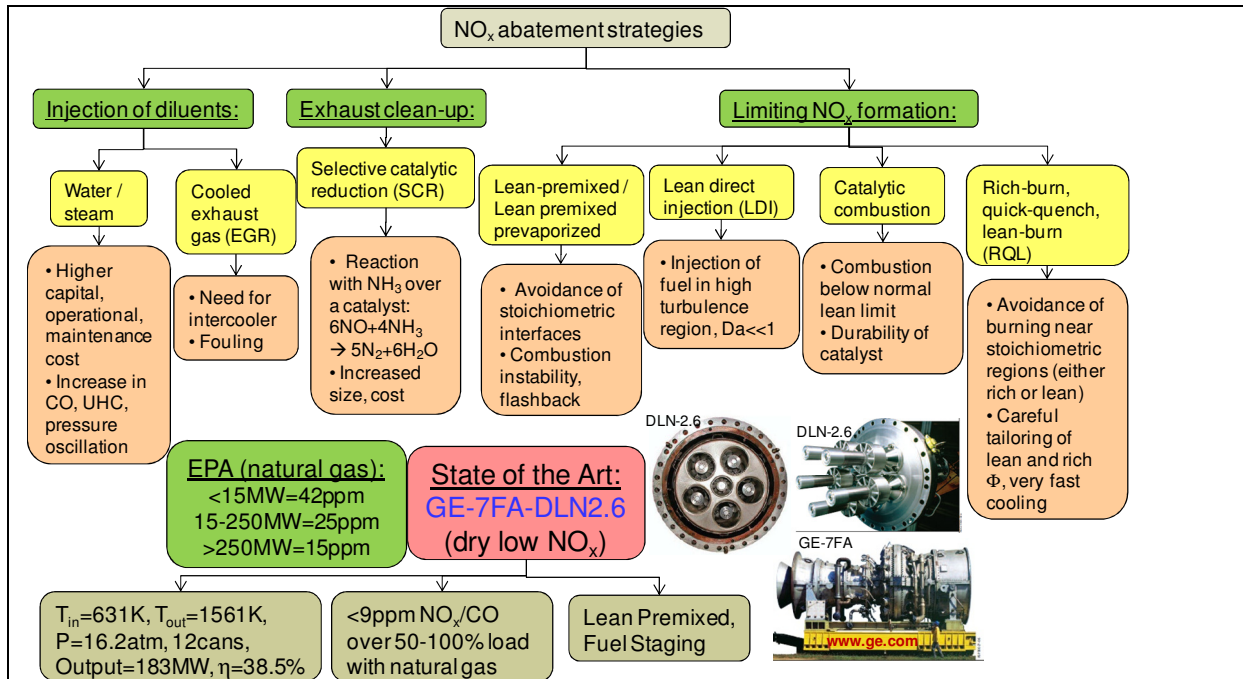


Figure 1.7 NO_x abatement strategies [Lefebvre, A. H., 1999].

Most of the NO_x abatement strategies include suppression of NO_x formation via thermal mechanism by avoiding hot spot regions in the combustor. Other strategies used are elimination of NO_x after it is formed as well as prevention of NO_x formation. The NO_x abatement strategies are described in Figure 1.7.

1.4.1 Injection of Diluents

1. Water/Steam Injection:

Water or steam injection is implemented to reduce the reaction zone temperature and hence to reduce the NO formation rate in the reaction zone. A schematic of water/steam injection is shown in Figure 1.8. However, there are many drawbacks of this technology, such as higher capital cost, higher fuel consumption, cost associated with water treatment and potential for corrosion and maintenance. Due to lower temperatures CO and UHC emissions are higher with use of this technique [Lefebvre, A. H., 1999].

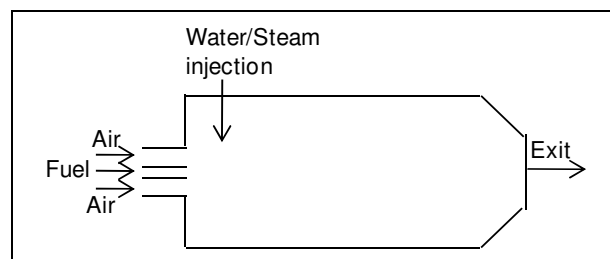


Figure 1.8 Water/Steam injection [Lefebvre, A. H., 1999].

2. Exhaust Gas Recirculation (EGR):

EGR also works on the same underlying principle of water/steam injection to reduce the flame temperature by recirculating cooled combustion products. A schematic of exhaust gas recirculation is shown in Figure 1.9. Major limitation for this technology comes from need for an heat exchanger between exhaust and inlet [Lefebvre, A. H., 1999]. Little combustor development is required however this technology can only be used with very clean fuel to avoid fouling.

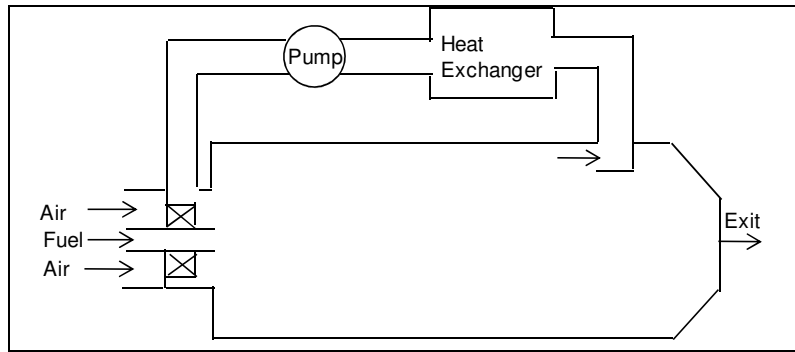
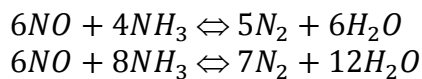


Figure 1.9 Exhaust gas recirculation [Lefebvre, A. H., 1999].

1.4.2 Exhaust Clean-up

In this technique the NO_x in gas turbine exhaust is converted to molecular nitrogen by injecting ammonia in presence of a catalyst [Lefebvre, A. H., 1999].



Major problem with this technique is requirement of control loop system to feed desired amount of ammonia as well as increase in weight and size of the equipment.

1.4.3 Limiting NO_x Formation

1. Lean premixed/lean premixed prevaporized:

Ultra-low-emission combustors rely on near perfect mixing of fuel and air before combustion to avoid any hot spot regions [Lefebvre, A. H., 1999, Rankin, D. D., 2007]. The combustor is operated in low emission window at temperatures less than 1850K. A schematic of lean premixed/lean premixed prevaporized combustor is shown in Figure 1.10. This technology is now widely used in land based gas turbine combustor and it has demonstrated single digit NO_x/CO emission levels [Vandervort, C. L., 2001]. However, a lean premixed combustor suffers from the problem of combustion instability (see Figure 1.10) and blowout when operating near the lean

limit. Other problem is the possibility of flashback in low velocity regions, such as boundary layers and problem of auto ignition that can be very dangerous in practical systems. It is also difficult to achieve sufficient turn down for part load operation. Good fuel/air mixing is required to achieve lower emissions as shown the schematic of Figure 1.10.

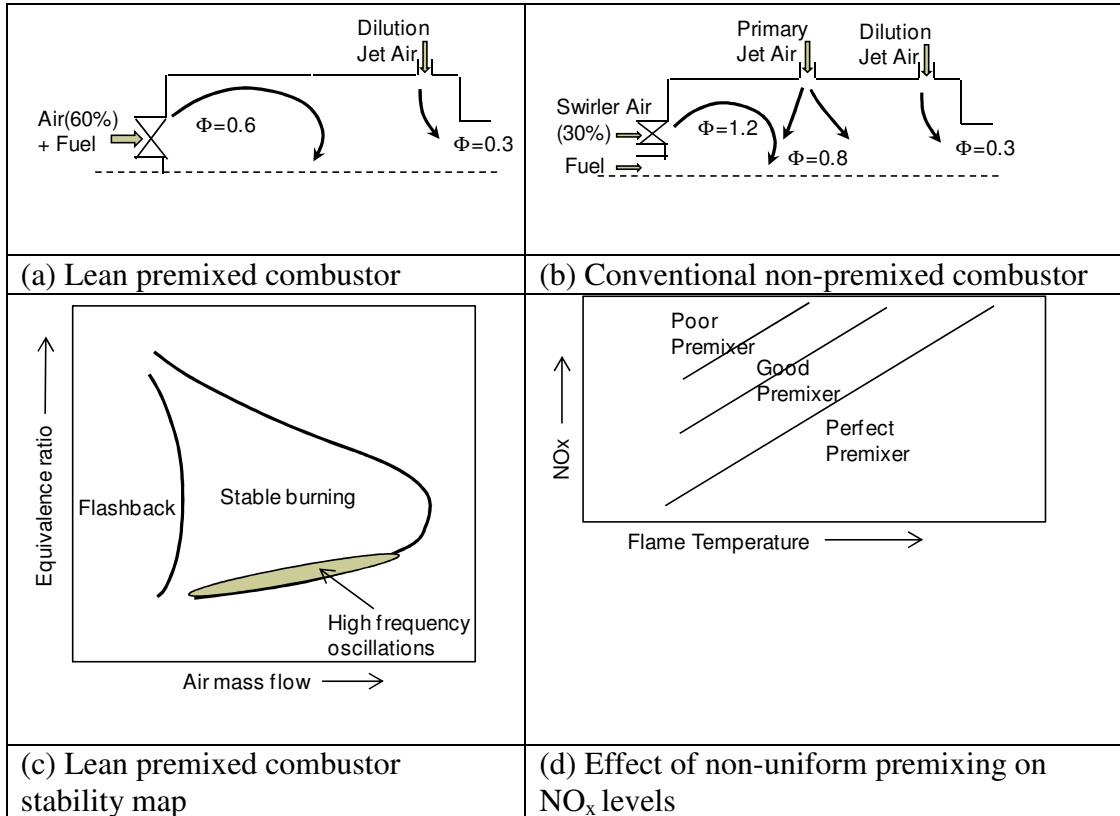


Figure 1.10 Lean premixed/lean premixed prevaporized [Lefebvre, A. H., 1999].

2. Lean direct injection

Lean direct injection combustor operates in non-premixed combustion mode at overall lean equivalence ratio and ensuring fast mixing between fuel and air such that they essentially burn in lean premixed mode and produce NO_x emissions similar to lean premixed combustion mode [Correa, S. M., 1992]. Multipoint fuel injection systems have been investigated to achieve low NO_x emissions and each fuel injection

system has a swirler to ensure fast turbulent mixing and gas recirculation for flame stabilization. The challenge is to achieve sufficiently fast turbulent mixing at large length scales and elevated pressure conditions.

3. Catalytic combustion

A schematic and principle of catalytic combustor is shown in Figure 1.11. Catalytic combustor can operate at lower temperature because activation energy barrier is lower as compared to the homogeneous gas phase reactor as shown in Figure 1.11 [Lefebvre, A. H., 1999, Rankin, D. D., 2007]. This results in considerably lower NO_x emissions due to avoidance of hot regions. A catalytic combustor is generally composed of a low temperature reactor which operates at temperature lower than about 1270K and a high temperature reactor which operates at temperature above 1270K. The low temperature reactor is supplied with premixed air/fuel mixture and it has a catalyst bed over which heterogeneous reactions takes places at equivalence ratio that is lower than the normal lean flammability limit of the fuel. The problem associated with catalytic reactor is to sustain high activity of catalyst for long period of time and to achieve large operational range. The second reactor is thermal reactor which raises the temperature of gases to turbine inlet temperature and reduces CO and UHC.

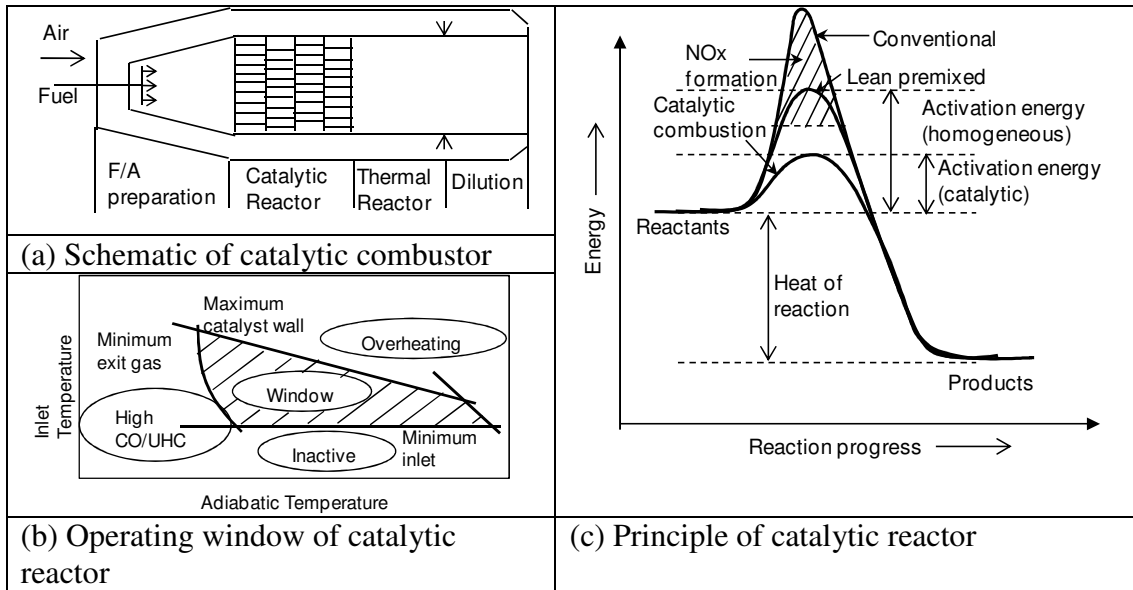


Figure 1.11 Catalytic combustion.

4. Rich-burn, quick-quench, lean-burn (RQL):

In this technique combustion is initiated in a fuel-rich primary zone (equivalence ratio between 1.2-1.6) where NO_x formation rates are lower due to lack of oxygen and lower temperature. This zone also results in high CO and UHC production. After this rapid mixing and quenching occurs by additional combustion air to prevent combustion from happening near stoichiometric regions where NO_x formation rates are very high. This is followed by lean burning regime where NO_x formation rates are lower due to lower associated flame temperature. The operational equivalence ratio in this region is about 0.5-0.7, temperatures are maintained low so as to reduce thermal NO_x but high enough to convert CO and UHC emissions. The concept is depicted in Figure 1.12 [Turns, S. R., 2000]. Critical factors that need to be considered while designing RQL combustor are careful tailoring of rich and lean equivalence ratios and very fast cooling rates so that combustion regime shifts rapidly from rich to lean without going through the high NO_x route as shown in Figure 1.12. The drawback of this technology is increased hardware and complexity of the system.

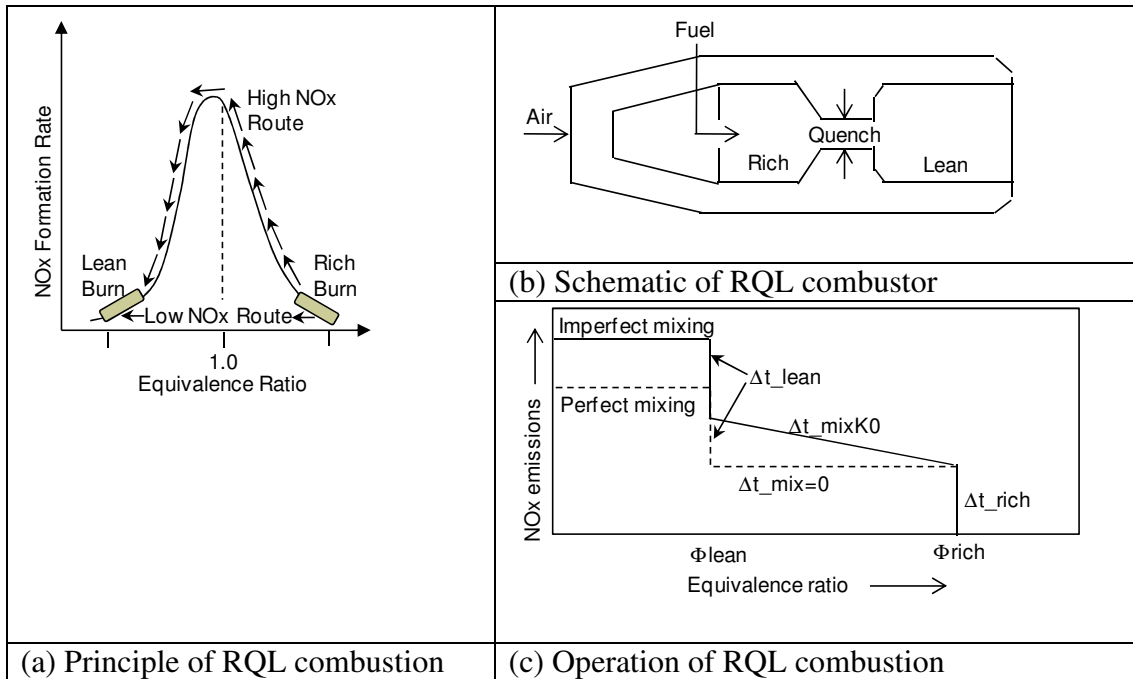


Figure 1.12 Rich burn-quick quench-lean burn (RQL) concept.

Another technique used for furnaces or burners include reduction of the formed NO to N_2 by using a reburning fuel. Further downstream of combustion zone, oxygen needs to be introduced for complete conversion of the fuel. This technique is mostly used for coal fired power plants and waste incineration plants where fuel NO is significant. In another technique pure oxygen can be used as oxidizer to avoid direct oxidation of nitrogen in air with the oxygen however this technique is expensive due to requirement of pure oxygen as an oxidizer and leak proof combustion system.

In the next section high temperature air combustion (HiTAC) technology which has been successfully demonstrated for furnace application is introduced. HITAC has demonstrated significant reduction in NO_x emissions with added advantage of significant fuel savings. Colorless Distributed Combustion (CDC) which is the focus of present dissertation derives key features from the HiTAC technology.

1.5 High Temperature Air Combustion (HiTAC)

Colorless distributed combustion (CDC), which is the focus of this dissertation, is based on the concept of high temperature air combustion (HiTAC) and in this section the features of HiTAC technology are discussed. HiTAC technology suppresses thermal NO_x formation in the reaction zone by avoidance of hot spot regions. This technology is mostly focused on application for furnaces which operate at relatively lower thermal intensity ($<1\text{MW}/\text{m}^3\text{-atm}$) as compared to gas turbine combustors ($5\text{-}50\text{MW}/\text{m}^3\text{-atm}$) [Vincent, E. T., 1950]. The concept of HiTAC has been successfully demonstrated to achieve low NO_x and CO emissions using range of gaseous, liquid as well as solid fuels [Gupta, A. K., *et al.*, 2003]. For this technology the auto-ignition temperature of gaseous fuel with air has been prescribed as the minimum limit of combustion air temperature. This temperature is generally above 1300K. It may be noted that above the auto ignition temperature a flame stabilizer is not necessary and the injected fuel spontaneously ignites and depending on the mixing conditions it can lead to distributed reaction zone instead of concentrated flame fronts that will be formed in conventional diffusion flames. The high temperature air combustion work has been known by different names such as Flameless Oxidation (FLOX) [Wunning, J. A., and Wunning, J. G., 1997] and MILD combustion [Cavaliere, A. and de Joannon, M., 2004].

The basic concept of HiTAC and its comparison with conventional furnace combustion is shown in Figure 1.13. In conventional furnace flame, fuel and air are injected close to each other so that direct mixing between fuel and air takes place and a concentrated flame is stabilized in the region where stoichiometric mixture of fuel

and air is present (F^*A). This results in high flame temperature region ($>1850K$) which results in high NO_x levels (thermal NO levels) as known from the Zeldovich mechanism [Miller, J. A. and Bowman, C. T., 1989, Correa, S., M., 1992] (also see Figure 1.6). The flame is stabilized by the entrainment of product gases (B) which provides the high temperature ignition energy source.

However, in HiTAC, preheated air (H) and fuel (F) injection locations are discrete, and both fuel and air streams first entrains the product gases (B), thus avoiding direct mixing between the fuel and air streams. Mixing between air and entrained product gases forms the hot and low oxygen concentration (diluted) mixture (BH). Weak reaction between fuel and entrained product gases (F^*B) can also take place due to entrainment of product gases in fuel stream. This is then followed by main reaction zone between fuel-product gas mixture and the hot and diluted oxidizer (F^*B)*(BH). To avoid a concentrated flame front it is important that the fuel is uniformly distributed and then spontaneously ignited to provide distributed reaction zone. Due to distributed reactions the high temperature stoichiometric regions are minimized in resulting in lower NO_x (thermal NO) emissions.

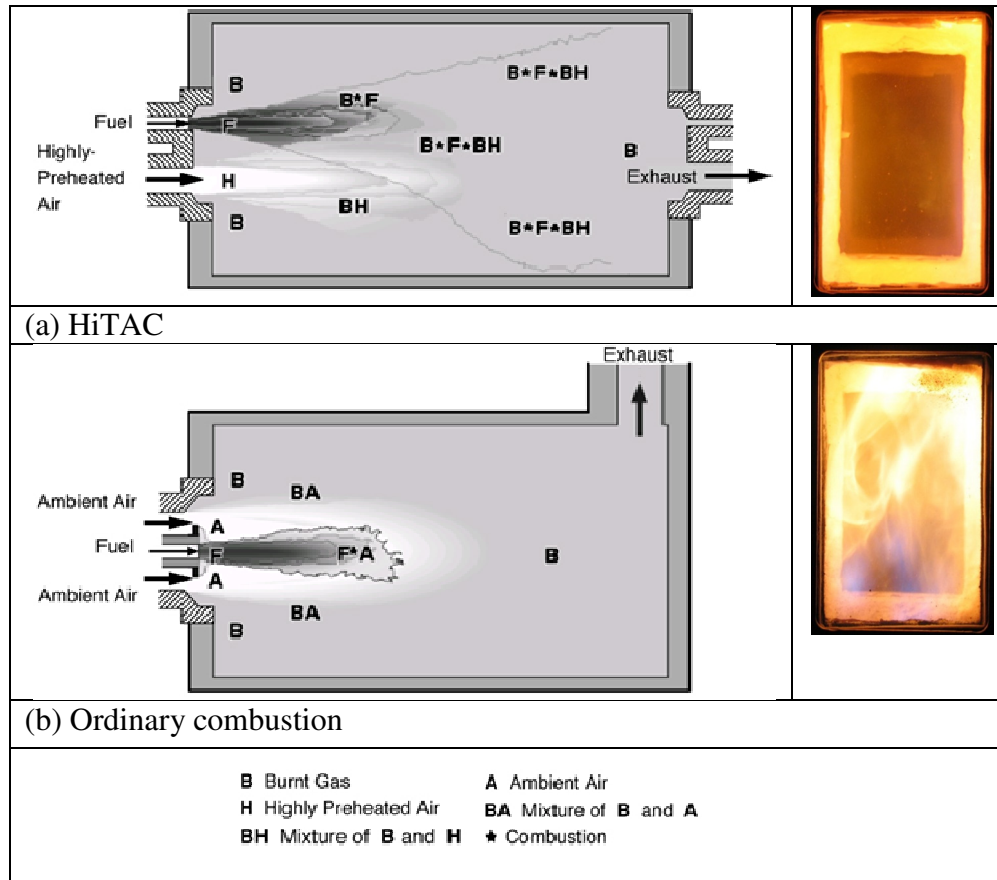


Figure 1.13 Conceptual difference between (a) high temperature air combustion (HiTAC) and (b) ordinary combustion [Gupta, A. K., *et al.*, 2003].

Preheating of air stream was employed using regeneration to achieve high temperature air (H) which further results in fuel energy savings. However, it has been recognized that preheating of air is not necessarily required to achieve distributed reactions [Kumar, S., 2007]. Another feature of HiTAC flames is stable combustion without any requirement of flame stabilizer such as swirler or bluffbody, hence it may result in low pressure drop across the combustor. It may be noted that for HiTAC flames, direct injection of high velocity fuel and air jets are employed and hence various configurations of fuel air injection can be used to achieve most desirable combustion conditions.

Figure 1.14(a) shows the global flame features of propane-air flames in cross flow for the effect of inlet air temperature and oxygen concentration [Gupta, A. K., *et al.*, 2003]. The figure suggests that with increase in air preheat temperature the visible light intensity from the flame increases; however as the oxygen concentration is decreased the flame volume increases and the visible intensity decreases significantly and under controlled conditions the flame can even become colorless [Gupta, A. K., *et al.*, 2003]. Figure 1.14(b) shows that as the oxygen concentration is decreased the flames cannot be sustained at lower temperatures (shown as forced ignition limit) and the temperature needs to be raised above the auto ignition temperature to sustain combustion. From Figure 1.14 it can be noted that HiTAC flames operate at high temperature and low oxygen concentration region.

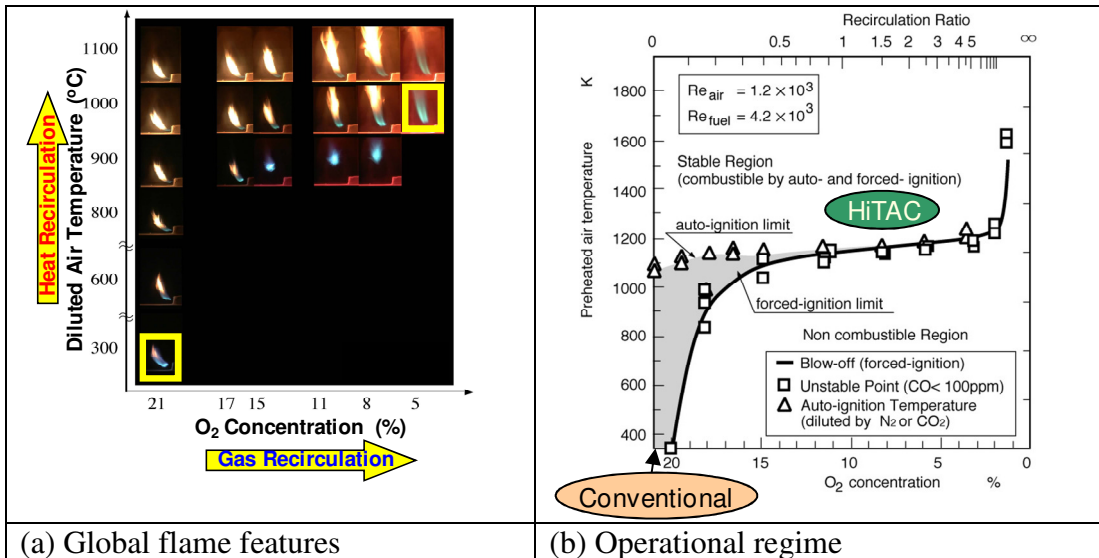


Figure 1.14 Effect of air temperature and oxygen concentration on (a) global flame behavior (b) operational regime of propane-air flames [Gupta, A. K., *et al.*, 2003].

Figure 1.15 shows numerical results of turbulent diffusion flames of methane and air with and without dilution with nitrogen [Gupta, A. K., *et al.*, 2003]. The figure suggests that with dilution the temperature rise as well as peak temperatures are much

smaller as compared to ordinary flame; the reaction zone is also much thicker as compared to the thin reaction flame front encountered in ordinary combustion. The figure suggests that with preheated as well as diluted reactants the reaction zone is much more distributed as compared to the ordinary flame front because of low local reaction rates from diluted reactants.

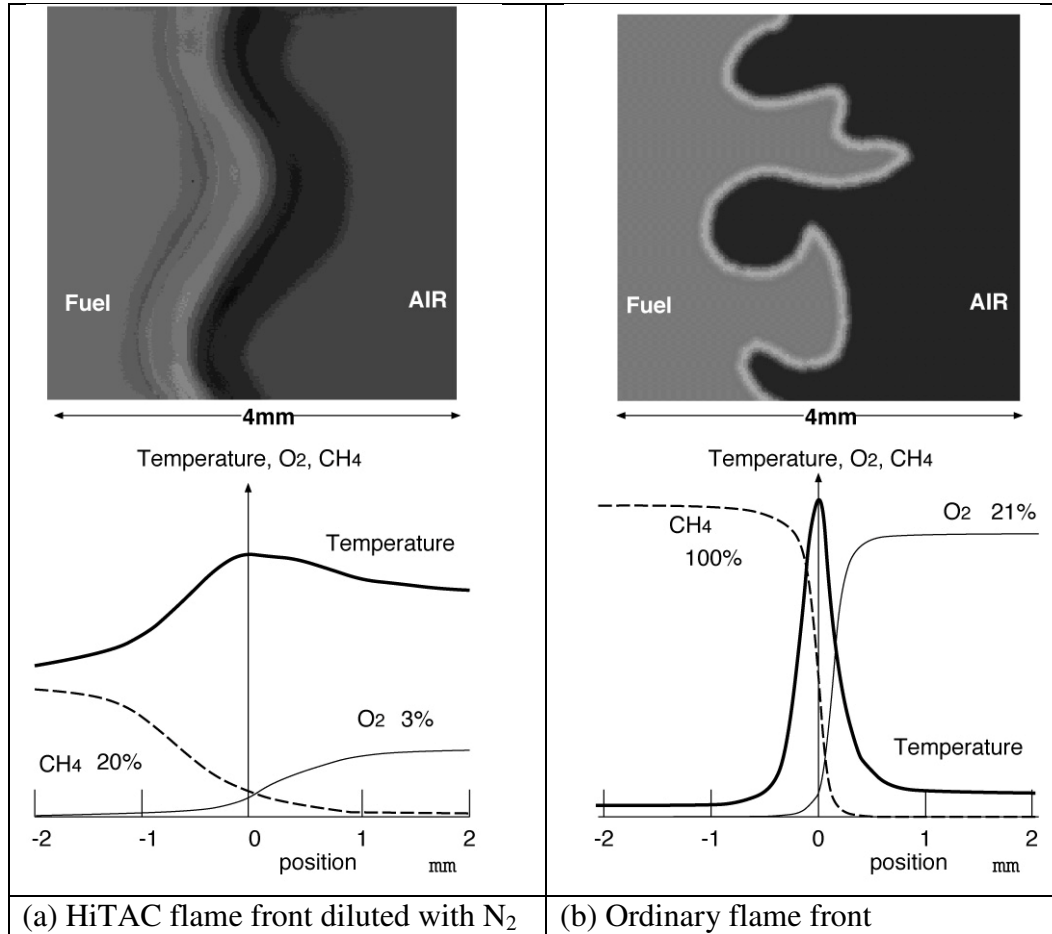


Figure 1.15 Flame structure for ordinary combustion and high temperature air combustion (HiTAC) for furnaces [Gupta, A. K., *et al.*, 2003].

Figure 1.16 shows conceptual temperature history of streamlines passing through the flames for ordinary combustion and HiTAC [Gupta, A. K., 2003]. It may be observed that for ordinary combustion the inlet temperature is at ambient condition but the peak temperature is near adiabatic flame temperature at stoichiometry. This

results in high NO_x formation from ordinary combustion, however in HiTAC a regenerator is used to preheat the combustion air above auto ignition temperature of the fuel and even though the exit temperature is similar to that for ordinary combustion the peak temperatures are much lower than that realized in ordinary combustion (see Figure 1.14). This is expected to avoid the regions with high NO_x formation rates and hence minimize NO_x emissions.

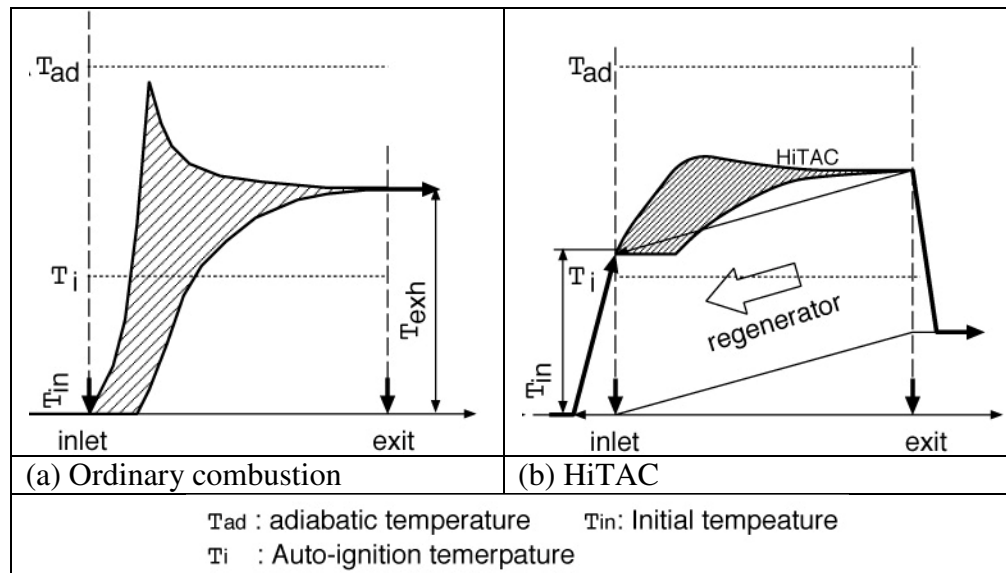


Figure 1.16 Conceptual temperature profiles for (a) ordinary combustion and (b) high temperature air combustion (HiTAC) [Gupta, A. K, *et al.*, 2003].

From above discussion it can be noted that key features of HiTAC flames are discrete and direct injection of air and fuel and operation at elevated temperature and low oxygen concentration condition and these features will be incorporated while designing a CDC combustor. HiTAC technology has been successfully demonstrated and implemented for furnaces and its application can be extended to higher thermal intensity gas turbine combustors. It has been recognized that high temperature air is not essential to achieve low emissions and henceforth, we call the technology as

colorless distributed combustion (CDC) focused on application to gas turbine combustors.

1.6 Objective

The objective of the present work is development of CDC technology for application to higher thermal intensity gas turbine combustors which operate at thermal intensity range of 5-50MW/m³-atm [Vincent, E. T., 1950] as compared to furnaces which operate at thermal intensity of less than 1MW/m³-atm (HiTAC). High thermal intensity results in smaller confinement volume for the same thermal load and hence results in higher velocities, lower residence time and difficulty in containing and stabilizing flame in the combustor. Smaller confinement volume is also expected to affect the gas recirculation and air jet profiles. The objective of the present work is sequential development of high thermal intensity CDC combustor from 5MW/m³-atm up to 198MW/m³-atm with careful control of different critical parameters. The major investigations reported in this dissertation are listed below.

1. Numerical investigation of gas recirculation and fuel/air mixing characteristics for different flow configurations and use the information to improve design of CDC combustor.
2. Numerical examination the residence time distribution characteristics inside the CDC combustor to achieve optimum performance.
3. Investigation of various air and fuel injection configurations for enhanced CDC combustor performance.
4. Investigation of effect of fuel and air injection diameter on performance of CDC combustor.

5. Investigation of effect of thermal intensity and operation at high thermal intensity up to $198\text{MW/m}^3\text{-atm}$ for CDC combustor in both non-premixed and premixed combustion modes.
6. Examination of effect of hydrogen addition to methane fuel at high thermal intensity of $85\text{MW/m}^3\text{-atm}$ for CDC combustor.
7. Examination of effect of dilution methane fuel with inert gases and air in non-premixed mode at ultra-high thermal intensity of $170\text{MW/m}^3\text{-atm}$ for CDC combustor.
8. Operation of liquid fuel (ethanol) in both direct injection and premixed prevaporized combustion mode at ultra high thermal intensity of $170\text{MW/m}^3\text{-atm}$ for CDC combustor.

Chapter 2 CDC Design Considerations

CDC derives key features from HiTAC technology as described in previous chapter. Important factors that need to be considered while designing a CDC combustor are listed in Figure 2.1. They include gas-recirculation, fuel/oxidizer mixing, thermal intensity and flow configurations. Simple computations and calculations are performed and the results are presented in this chapter to understand the effect of each parameter on combustor performance.

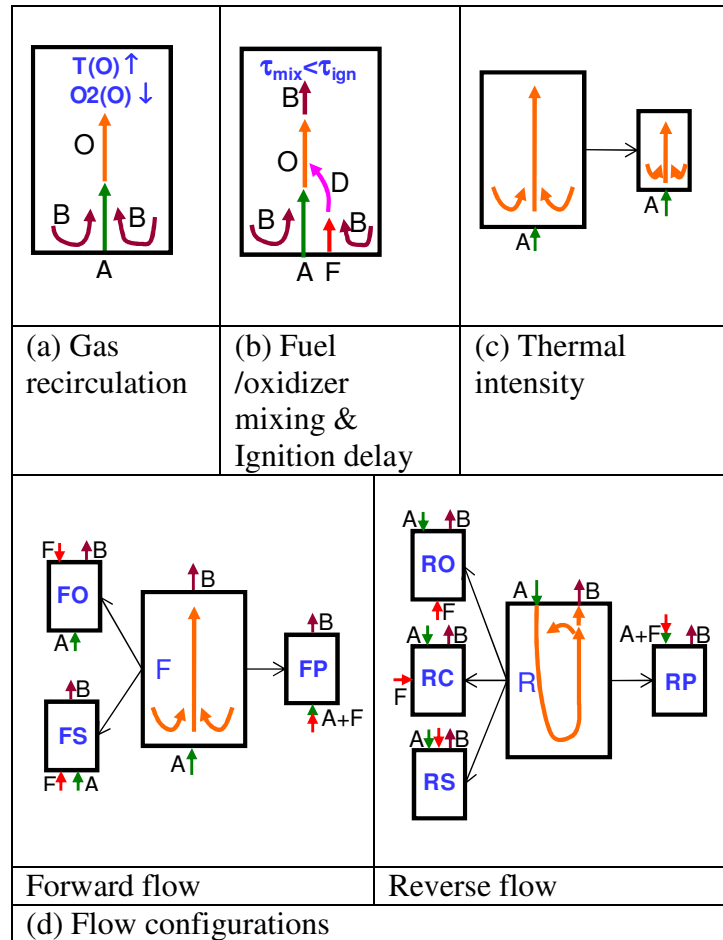


Figure 2.1 Important factors for designing a CDC combustor.

2.1 Gas Recirculation

Partial entrainment of hot product gases into the injected air jet is required to raise the temperature and reduce the oxygen concentration of the oxidizer (mixture of injected air and hot product gases). To understand the variation of recirculation ratio (defined as the ratio of mass of entrained product gases to the mass of injected air) with the injected air jet characteristics, correlation available in the literature [Ricou, F. P. and Spalding, D. B., 1961, Hussein, H. J., *et al.*, 1994] has been used. The correlation is for a non-reacting variable density free air jet, injected in a quiescent medium and is given below in equation 2.1.

$$\text{Recirculation ratio} = \frac{\dot{m}_{rec}}{\dot{m}_{jet}} = C_e \frac{X}{D^*} - 1 \quad (\text{equation 2.1})$$

\dot{m}_{rec} = recirculated mass flux

\dot{m}_{jet} = initial jet mass flux

$$C_e = 0.32$$

X = distance along the jet centerline

$$D^* = D \left(\frac{\rho_{jet}}{\rho_{rec}} \right)^{1/2}$$

D = jet diameter

ρ_{jet} = injected jet density

ρ_{rec} = recirculated gas density

It may be noted that the entrainment rate in a reacting jet is lower than a non-reacting jet [Han, D. and Mungal, M. G., 2001]. For free reacting jet the constant, $C_e=0.13$ as compared to 0.32 for non-reacting jet (see equation 2.1). Yang, W. and Blasiak, W., 2005, suggested that for lower oxygen concentration oxidizer the

constant C_e increases and it lies closer to non-reacting value of 0.32, where the oxygen concentration is less than 5%. However, considering the product gas entrainment achieved prior to ignition, correlation for a variable density, non-reacting jet can be used. Moreover, the variation of recirculation ratio with jet diameter as well as the temperature of the injected air can be beneficial to understand the effect of these parameters that will be useful to design a combustor. In a gas turbine the temperature of combustion air will increase with increase in pressure ratio due to near isentropic heating in the compressor. The variation of recirculation ratio with injected air temperature is shown in Figure 2.2(a). The recirculated gas temperature is assumed to be 1700K and air jet diameter is $D=3/16$ inch. It can be observed that recirculation ratio increases, at a given distance from air injection location, for higher air injection temperature (recirculation ratio $\sim T_{\text{air}}^{1/2}$). From Figure 2.2(a) it can be observed that for variation of injected air temperature from 300 to 700K the recirculation ratio increases from 2.23 to 3.93 at a distance of 4.5inch from air injection location. The effect of air injection diameter on recirculation ratio is shown in Figure 2.2(b). The air injection temperature is 300 K and the recirculated gas temperature is assumed to be 1700K. It can be observed that the recirculation ratio varies significantly with air injection diameter (recirculation ratio $\sim 1/D$). The recirculation ratio at a distance of 4.5inch from the air injection port the recirculation ratio decreases significantly from 2.23 to 0.38 with increase in air injection diameter from D to $7D/3$.

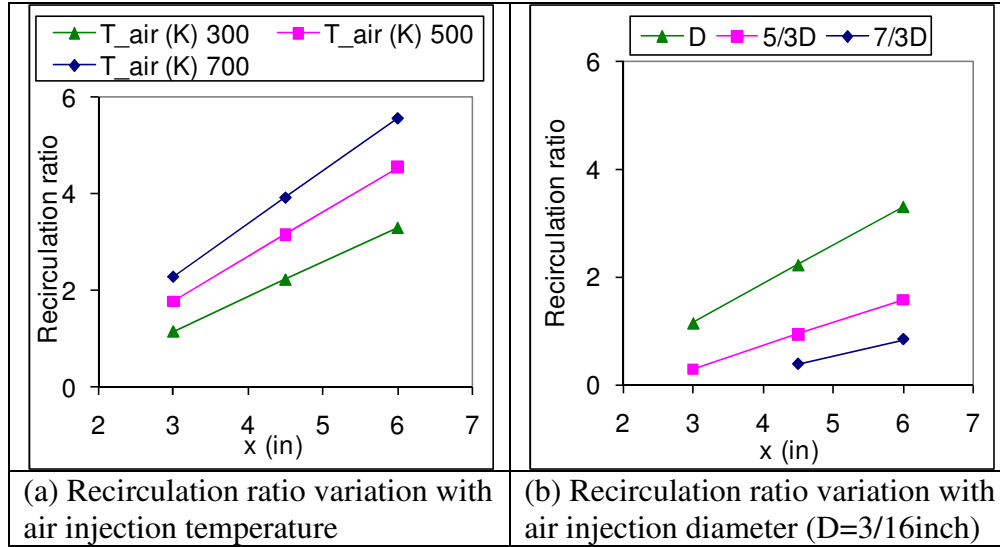


Figure 2.2 Variation of recirculation ratio with (a) air injection temperature and (b) air injection diameter for a free jet ($D=3/16$ inch).

From the figure it can be noted that the recirculation ratio is independent of the air injection velocity and only depends on the jet diameter and density of injected and recirculated gases. To achieve higher product gas recirculation smaller air injection diameter is desired, however smaller air injection diameter will result in higher air injection velocity and hence increased pressure drop. This problem could be alleviated by increasing the number of air jets with smaller diameter to increase gas recirculation while maintaining the same velocity and pressure drop. The injected air temperature as well as the product gas density will mostly be fixed based on the compressor pressure ratio as well as the overall operating equivalence ratio.

2.2 Ignition Delay

At higher recirculation ratios the oxidizer (mixture of recirculated product gases and injected air) temperature will increase and the oxygen concentration will decrease. With increase in the temperature of the oxidizer the ignition delay time of fuel will decrease so as to achieve conditions of spontaneous ignition. To obtain the

values of oxidizer temperature and oxygen concentration with recirculation ratio, chemical kinetic simulations have been performed for an adiabatic well stirred reactor (residence time = 100ms). Methane is used as the fuel and both fuel and air are introduced at inlet temperature of 300K and equivalence ratio of 0.8 using the GRI 3.0 reaction mechanism [Smith, G. P., *et al.*]. Product gas from the reactor is mixed with air in the second reactor to form the oxidizer as shown in Figure 2.3. The ratio of mass flow rates in first reactor (mrec2) and the mass flow rate of air (mair2) in the second reactor will govern the recirculation ratio.

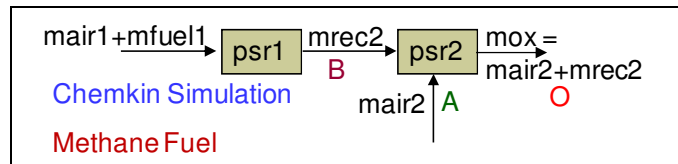


Figure 2.3 Set up for Chemkin simulations to obtain oxidizer temperature and O₂ concentration.

The results of oxidizer temperature and oxygen concentration are presented in Figure 2.4(a). It can be observed that for recirculation ratio in the range of 2-3, the temperature of oxidizer is about 1530-1655K and oxygen concentration of 9.4-8vol.%. For spontaneous ignition of fuel and oxidizer mixture the ignition delay time should be well below the residence time in the combustor. The correlation for ignition delay time for methane fuel is given below in equation 2.2 [Li, S. C. and Williams, F. A., 2002].

$$\text{Ignition delay} = t_{ig} = \frac{2.9 \times 10^{-13} [O_2]^{-1}}{T^{-0.31} \exp\left(-\frac{12000}{T}\right)}, T \leq 1300K \quad (\text{equation 2.2})$$

$$\text{Ignition delay} = t_{ig} = 6.25 \times 10^{-16} [O_2]^{-1} \exp\left(\frac{23000}{T}\right), T \geq 1400K$$

units = seconds, $\frac{\text{moles}}{\text{cm}^3}$, K

The ignition delay time decreases exponentially with increase in temperature and increases linearly with increase in oxygen concentration. Chemical kinetic calculations have been performed to calculate the ignition delay for a closed homogeneous reactor using GRI 3.0 mechanism [Smith, G. P., *et al.*]. The ignition delay time is defined here as the time where peak OH radical concentration is present. The ignition delay times obtained from chemical kinetic simulations are presented here in Figure 2.4(b) along with the results obtained from those using equation 2.2. It can be observed from Figure 2.4(b) that the ignition delay time is about 1ms for recirculation ratio of 3. Figure 2.4(c) shows ignition delay time variation with oxygen concentration and temperature of oxidizer. For chemical kinetic simulations nitrogen is used as the diluent. From the figure it can be understood that ignition delay time is significantly affected by the temperature as compared to oxygen concentration and to achieve ignition delay time less than 1ms the temperature required is above 1600K. For diluted oxygen concentration case with 3%O₂, the diluted air temperature is close to 1800K to achieve ignition delay time of less than 1ms. This temperature is closer to the temperature where significant amount of NO formation is present. While designing a CDC combustor it should be noted that to achieve distributed reactions ignition delay time should be greater than the mixing time of fuel in oxidizer however, to achieve complete combustion the ignition delay time should be much less than the residence time in the reactor.

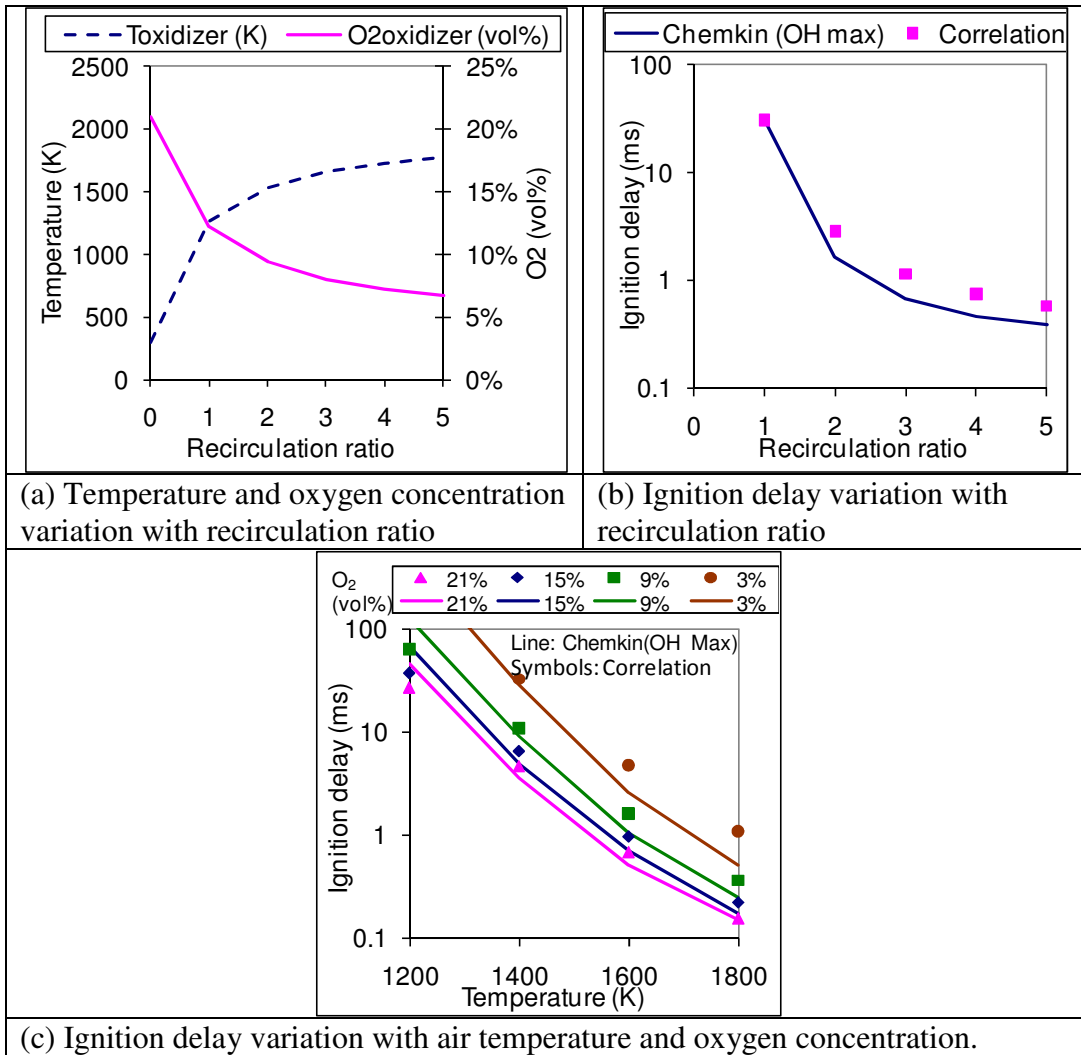


Figure 2.4 (a) Temperature and oxygen concentration variation (b) ignition delay variation with recirculation ratio and (c) ignition delay variation with temperature and oxygen concentration.

2.3 Fuel/Oxidizer Mixing (Turbulent Mixing Time)

Turbulent mixing time based on the life time of large eddies is calculated based on the correlation given below in equation 2.3 [Turns, S. R., 2000, Forney, L. J., Nafia, N., 1998]. From the correlation it can be noted that the turbulent mixing time varies directly as diameter of the jet and inversely as the air injection velocity. Hence, the turbulent mixing time varies as D^3 for the same mass flowrate, where D is the diameter of jet. Hence reduction in air injection diameter can result in significant

reduction in the mixing time and can lead to enhanced mixing of fuel in the oxidizer mixture.

$$\text{Mixing time} = \tau_{mix} = \frac{l_0}{v'_{rms}} = \frac{D}{U} \quad (\text{equation 2.3})$$

D = jet diameter

U = air injection velocity

$$l_0 = \text{integral length scale} = \frac{D}{10}$$

$$v'_{rms} = \frac{U}{10} (\text{assuming turbulence intensity} = 10\%)$$

The variation of the turbulent mixing time with change in jet diameter and the jet velocity is shown in Figure 2.5(a). From the figure it may be noted that for jet velocity of about 100m/s the turbulent mixing time of the order of 0.1ms could be achieved. Increase in jet diameter results in significant increase in turbulent mixing time, for example for jet velocity of 100m/s the turbulent mixing time increases from 0.05ms to 0.11ms for increase in jet diameter from D to $7D/3$, where $D=3/16$ inch. However, it may be noted that with increase in jet diameter the jet velocity will decrease significantly for same mass flow rate. Hence, the variation of mixing time with respect to jet diameter for same mass flow rate is presented in Figure 2.5(b). The jet velocity is assumed to be 128m/s for jet diameter of D , where $D=3/16$ inch. It may be noted that the jet injection velocity of 128m/s has been used in the CDC combustor investigated in this dissertation. For this flow rate the jet velocity is about 46m/s for jet diameter of $5D/3$ and 28m/s for jet diameter of $7D/3$. From the figure we can observe that the turbulent mixing time increases one order of magnitude from 0.04 ms for jet diameter of D to 0.47ms for jet diameter of $7D/3$. Higher mixing time can result in insufficient mixing and hence, can lead to higher pollutant emission. However, smaller jet diameter will result in higher pressure drop across the

combustor. It may be noted that these values of jet diameter has been used in the present investigation of CDC combustor.

Variation of pressure loss with air injection velocity and temperature is presented in Figure 2.5(c). Pressure loss is calculated from equation 1.1 in cold flow condition. From the figure it can be noted that the pressure loss increases significantly with increase in air injection velocity as well as temperature. Hence there is a compromise between smaller turbulent mixing time (see Figure 2.5(a)) and lower pressure loss (see Figure 2.5(c)) with increase in air injection velocity. Figure 2.5(d) shows pressure loss for three different temperatures and it can be noted that pressure loss increases with increase in temperature due to increase in air injection velocity.

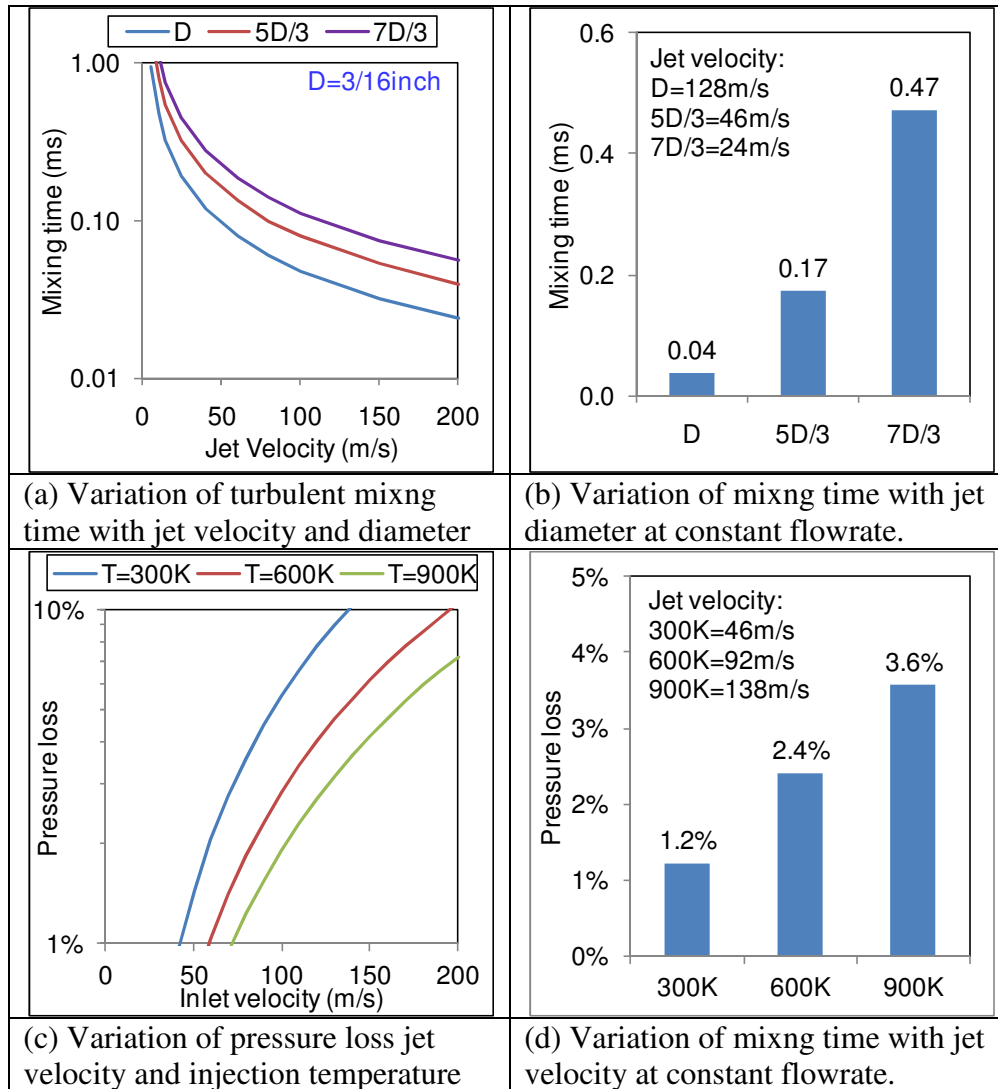


Figure 2.5 Variation of mixing time and pressure loss with jet velocity.

2.4 Fuel/Oxidizer Mixing (Jet Decay in Cross-Flow)

Fuel oxidizer mixing is generally governed by “jet in cross flow” mode where the fuel jet experiences cross flowing oxidizer stream to form a reactive mixture. Fast fuel/oxidizer mixing is desired such that a uniform reactive mixture is formed prior to ignition to result in distributed reactions. To understand the behavior of fuel jet decay in cross flow, correlation available in literature [Han, D., *et al.*, 2000] is used. The correlation is given below in equation 2.4 and different parameters used in this correlation are shown in Figure 2.6(a).

$$\frac{y}{rd} = A \left(\frac{x}{rd} \right)^B \quad (\text{equation 2.4})$$

$$r = \left(\frac{\rho_i \times v_i^2}{\rho_c \times v_c^2} \right)^{\frac{1}{2}}$$

$$A = 2.05, B = 0.28$$

The fuel jet decay obtained from the CFD simulation is compared from that obtained from the correlation (equation 2.4). Realizable k-e model with standard wall functions is used to model turbulence in the CFD simulations and 5% inlet turbulent intensity is used for both air and fuel inlet. The geometry and mesh for CFD simulation is shown in Figure 2.6(b), sufficiently large domain along the length (80d) and height (40d) is chosen so as to avoid influence of confinement on the fuel jet profile. The fuel jet diameter is $d=D/3$ where $D=3/16$ inch, this value of the fuel injection diameter has been used later in the present work. The result of fuel jet decay scaled by the fuel injection diameter, d , is presented in Figure 2.6(c). From Figure 2.6(c) it can be noted that for higher velocity of the cross flowing jet (smaller “ r ”) lower penetration and faster decay of fuel jet is obtained which may result in better mixing of fuel with oxidizer. The fuel injection velocity has been kept constant at 97m/s for the investigation. It may be noted that this fuel injection velocity has been used in the present work. From comparison of CFD results with the available correlation in literature it could be noted that CFD over predicts the fuel jet decay and faster decay is obtained in the CFD simulation. For these simulations commercial software FLUENT was used. It may be noted that CFD simulations have been used in this dissertation as a tool to understand the flowfield features which can be useful while designing CDC combustor.

To understand the effect of fuel injection diameter on fuel jet decay at constant fuel flow rate, results of fuel jet penetration with variation in fuel injection diameter is plotted in Figure 2.6(d) using the correlation given in equation 2.4. From the correlation, variation of jet centerline with respect to fuel injection diameter for a constant fuel flow rate is given by $y \sim 1/d^{0.72}$. It can be inferred that increase in fuel injection diameter results in decrease in fuel jet penetration for constant fuel flow rate. The cross flowing velocity is kept constant at 18m/s and the fuel injection velocity varies from 97m/s for fuel injection diameter of “d” to 11m/s for fuel injection diameter of “3d”. It may be noted that increase in fuel injection diameter significantly decreases the penetration of fuel jet. From equation 2.3 it may be noted that increase in fuel injection diameter also results in increase in turbulent mixing time and slower mixing in fuel jet.

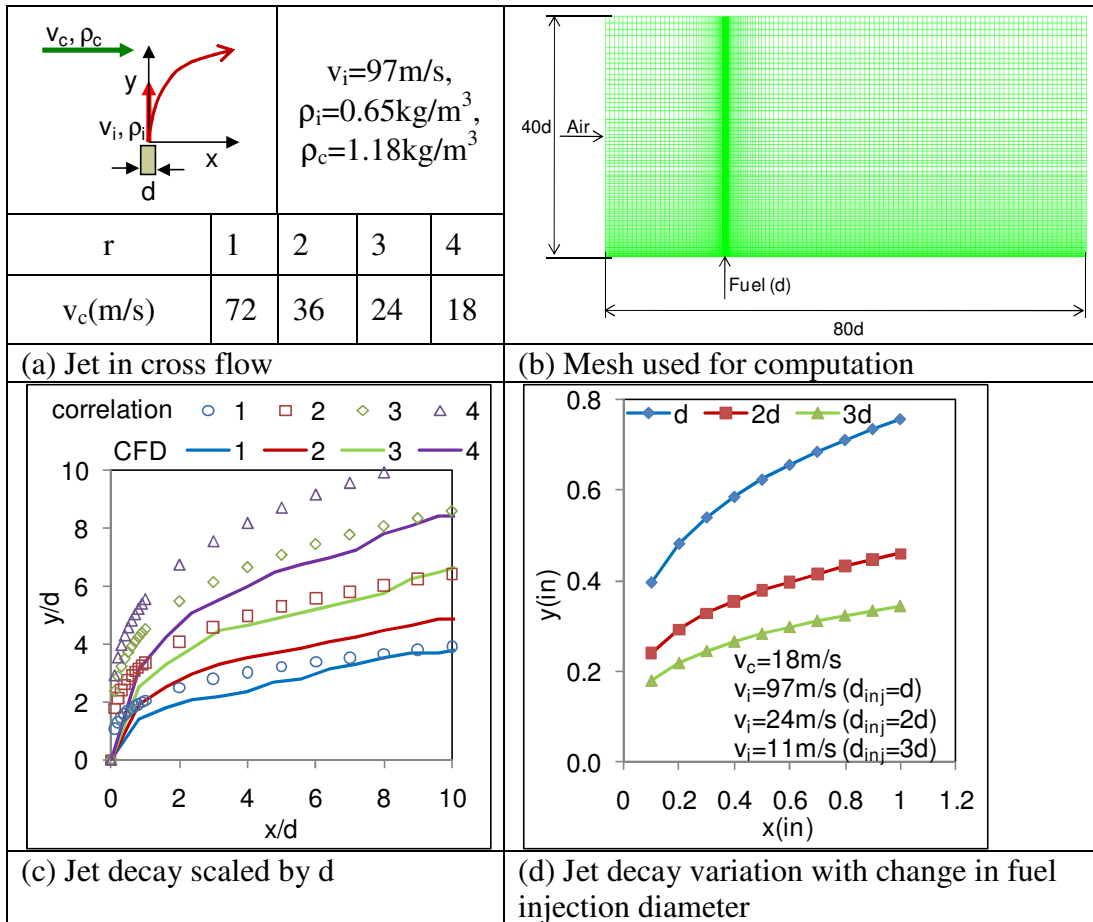


Figure 2.6 Jet decay in cross-flow ($d=D/3$, $D=3/16\text{inch}$, fuel=methane).

2.5 Thermal Intensity and Flow Configuration

The generally accepted definition of thermal intensity in literature is the amount of heat energy released per unit time in a unit volume of combustor scaled by the operating pressure [Vincent, E. T., 1950]. The unit of thermal intensity is $\text{MW/m}^3\text{-atm}$. Hence, at higher operating pressure for a given flow velocity the amount of heat energy released per unit volume would be higher for the same thermal intensity. Therefore by definition, thermal intensity is a representative of the residence time of gases in the combustor. Furnaces operate at lower thermal intensity, generally $<1\text{MW/m}^3\text{-atm}$, however, gas turbine combustors operate at much higher thermal intensities in the range of $5\text{-}50\text{MW/m}^3\text{-atm}$ [Vincent, E. T., 1950]. The thermal

intensity of popular land based gas turbine combustor is about 15MW/m³-atm [Vandervort, C. L., 2001]. Higher thermal intensity is desired to reduce the hardware weight as well as to reduce the capital cost of the system. The variation of residence time with thermal intensity is shown in Figure 2.7(a). The calculation is performed for air density at reactor temperature of 1996K (adiabatic flame temperature at $\phi=0.8$) using equation 2.5 [Turns, S. R., 2000] given below. The residence time varies inversely with increase in thermal intensity in the combustor as shown in Figure 2.7(a). Thermal intensity of about 50MW/m³-atm results in residence time of less than 10ms.

$$\text{Residence time} = t_{res} = \frac{\rho V}{\dot{m}} \quad (\text{equation 2.5})$$

ρ = average gas density in combustor

V = combustor volume

\dot{m} = total mass flow rate through combustor

Higher thermal intensity will result in lower residence time of gases inside the combustor and this result in many challenges to design a combustor. The challenges include difficulty to stabilize the flame, higher flow velocities as well as difficulty in achieving complete conversion of fuel. Conversion of carbon monoxide is a slow process and lower residence time will result in higher levels of CO at the combustor exit. To understand the effect of residence time on NO and CO emissions, chemical kinetic simulations were performed assuming perfectly stirred reactor using GRI-3.0 mechanism [Smith, G. P. *et al.*] and the results are shown in Figure 2.7(b). The equivalence ratio used for the computations is 0.8. The NO formed by thermal Zeldovich mechanism is calculated from equation 1.4 and shown in Figure 2.7(b).

The temperature and oxygen concentration used for calculation is from equilibrium calculations equivalence ratio of 0.8 for methane fuel and the diluent is nitrogen. From the figure it can be noted that CO emissions increases sharply at lower residence time (<10ms), the NO emissions vary mostly linearly with increase in residence time. This is because of a specific NO formation rate at given condition (1.29ppm/ms at 1996K and 4.39vol% O₂, see Figure 1.6) hence lowering residence time can result in lower NO emissions which can be beneficial while designing advanced low NO_x combustors. Higher residence time will result in more time for conversion from CO to CO₂ and hence result in low CO emissions. The CO conversion rate with residence time is shown in Figure 2.7(c) and from the figure it can be inferred that the CO conversion rate is much higher at low residence time, this means that if gases are allowed to have more time before exiting the combustor it will result in lower CO emissions even though the average residence time is the same. The calculation for average residence time of 25ms with different percentage of gases having low residence time is shown in Figure 2.7(d). From the figure it can be noted that if we have higher percentage of gases having low residence time CO emissions will increase even though the average residence time is same of all the cases. For example, if we have all the gases having residence time of 25ms the CO emission from perfectly stirred reactor will be 971ppm. However, if 71vol% of gases has residence time of 5ms and 29vol% of gases has residence time of 75ms (giving 25ms of average residence time) CO emission will be 1788ppm. Hence, favorable residence time distribution where we have minimal fraction of gases having low residence time we can have higher conversion of CO and consequently lower CO emissions.

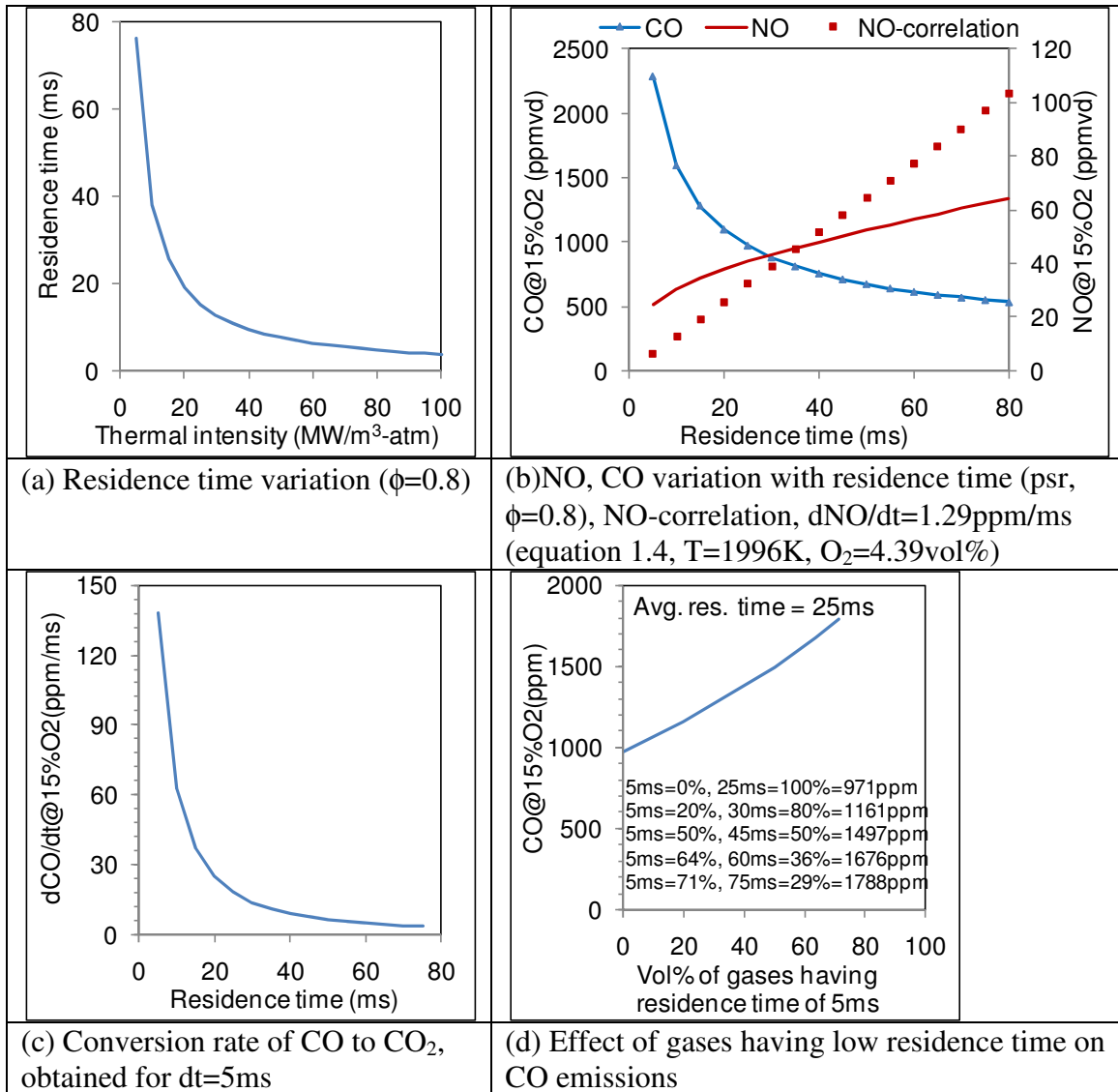


Figure 2.7 (a) Effect of thermal intensity on residence time (b) effect of residence time on NO and CO levels (perfectly stirred reactor, $\phi=0.8$) (c) CO conversion rate variation with residence time (d) effect of gases having low residence time on CO emissions.

For same thermal load, higher thermal intensity would result in smaller confinement volume. With reduction in volume, the confinement effects are expected to dominate the flowfield as well as the jet profiles. To understand the effect of confinement on jet profile and gas recirculation inside the combustor, CFD simulations were performed on an axisymmetric jet as shown in Figure 2.8.

Different air and fuel injection configurations could be realized for a CDC combustor. For sake of classification, flow configurations can be termed as forward flow “F” if the air injection location is from the same end of exit or reverse flow “R” if the air injection location is on the opposite end of exit (see Figure 2.1(d)). Fuel can be injected from the same end of air injection “S”, opposite end of air injection “O”, in cross flow “C” or in premixed with air “P”. The combination of air and fuel injection location can be used to identify a particular flow configuration. For example flow configuration “RS” suggests that air injection location is on opposite end relative to exit and fuel injection location is on same end relative to air injection (opposite end to exit). This nomenclature is used in this dissertation to identify different flow configurations. To examine the effect of flow configuration two types of geometries with only air injection were considered for CFD simulation. In the first geometry air exits from the opposite end of air injection and this geometry is representative of forward flow configuration (denoted as “F” see Figure 2.8(a)). In the other geometry air exits the confinement volume from the same side of air injection and this geometry is representative of reverse flow configuration (denoted as “R” see Figure 2.8(b)). The mesh used for the simulations is shown in Figure 2.8(c) and appropriate refinement is performed near the region of high shear. Realizable k-e model with standard wall functions was used to model turbulence with inlet turbulence intensity of 5%. Realizable k-e model has been shown to provide more accurate prediction of profile and spreading of non-reacting round jets [Shih, T., *et al.*, 1995]. Convergence was obtained when the residuals for all the variables were less than 1E-04. Air at normal temperature and pressure is used as the fluid. The centerline jet velocity

profile obtained from the CFD simulations was compared with the correlation for free jet given in equation 2.6 [Hussein, H. J. *et al.*, 1994] below. For these simulations commercial software FLUENT was used.

$$\frac{V_x}{V_i} = 5.9 \left(\frac{X}{D} - 27 \right)^{-1} \quad (\text{equation 2.6})$$

V_x = jet centerline velocity

V_i = initial jet velocity

X = distance along the jet centerline

D = jet diameter

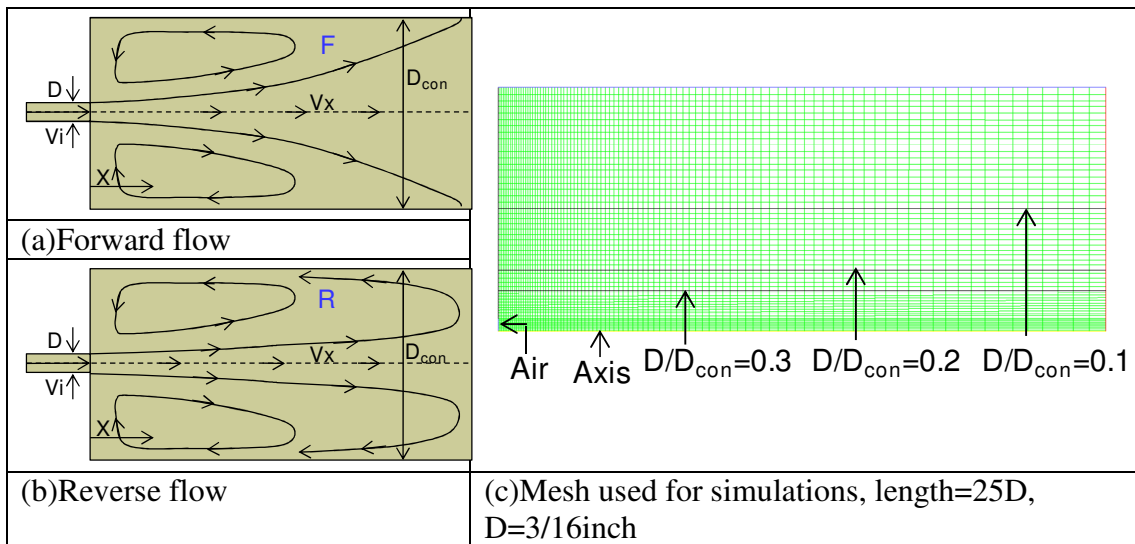


Figure 2.8 Geometry and mesh for forward and reverse flow configurations.

Results of the CFD simulations are presented in Figure 2.9 for both jet decay and gas recirculation inside the combustor. From Figure 2.9(a) it can be observed that for smaller confinement volume the jet decays faster as compared to the free jet. Moreover for the reverse flow configuration “R” the jet decay is more rapid as compared to the forward flow configuration “F”. This may be because of higher shear due to the flow in opposite direction for the reverse flow mode. CFD simulations predict higher decay of free jet as compared to the correlation given in equation 2.6.

The results for gas recirculation are presented in Figure 2.9(b). It may be noted that for smaller confinement volume, maximum gas recirculation is limited by the confinement size. The gas recirculation increases along the length, reaches a peak value and then decreases. This also suggests that higher thermal intensity may pose problems of stabilization of reactions as well as problem with high temperature mixture preparation that is critical to achieve reactions in CDC mode. Reverse flow configuration results in lower gas recirculation as compared to the forward flow configuration. It may be noted that for reverse flow configuration while calculating the mass flow rate of the recirculated gases the mass flow rate of injected air is subtracted from the total flow rate having the negative velocity as the mass flow rate of injected air has to reverse before exiting the combustor. The gas recirculation for free jet is slightly over predicted by the CFD simulations as compared to the correlation given in equation 2.1.

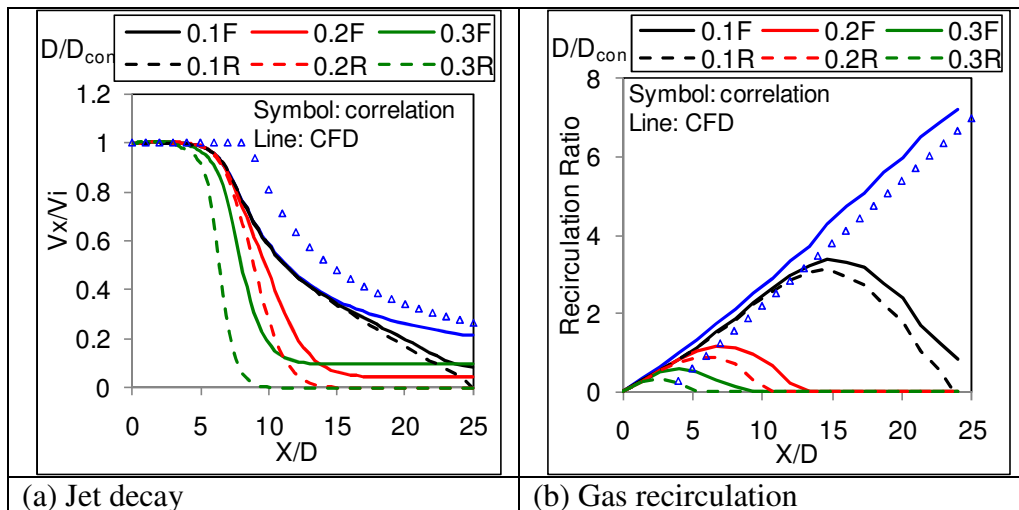


Figure 2.9 Jet decay and gas recirculation in confinement.

Carbon monoxide oxidation is a slow process; hence residence time has a significant effect on the CO emissions as observed from Figure 2.7(b). Residence

time distribution was obtained for configurations “F” and “R” by using a tracer having same properties as that of air at confinement ratio $D/D_{con}=0.2$ (see Figure 2.8(c)). After obtaining a steady state solution of the flowfield, the tracer concentration at the air inlet is set to 1 at time = 0, and only tracer conservation equation is solved in a transient mode with time step size of 0.1ms for both the configurations. The tracer is tracked from the air injection location to simulate the presence of reaction zone near the air injection location. The tracer concentration at the outlet is monitored with respect to time. The residence time is obtained from equation 2.7.

$$Residence\ time = t_{res} = \frac{1}{C_{mix}} \int_0^{C_{mix}} t dC \quad (\text{equation 2.7})$$

$$C_{mix} = 0.0445(\text{methane fuel, perfect mixing, } \Phi = 0.8)$$

$$C_{mix} = 1(\text{for only air})$$

$$C = \text{tracer mass fraction at exit}$$

$$t = \text{time}$$

The residence time profile obtained from numerical simulations is compared for the case of a perfectly stirred reactor. The exit tracer concentration profile with respect to time, for a perfectly stirred reactor corresponding to a step input of tracer at the inlet is given below in equation 2.8.

$$\frac{C}{C_{mix}} = 1 - \exp\left(-\frac{t}{t_{res}}\right) \quad (\text{equation 2.8})$$

C = tracer mass fraction at exit

$C_{mix} = 0.0445$ (methane fuel, perfect mixing, $\Phi = 0.8$)

$C_{mix} = 1$ (for only air)

t = time

t_{res} = residence time

Where, the residence time (t_{res}) for a perfectly stirred reactor is obtained from equation 2.5.

Residence time frequency distribution for a perfectly stirred reactor is given by equation 2.9. For these simulations commercial software FLUENT was used.

$$\frac{d(C/C_{mix})}{dt} = \frac{1}{t_{res}} \exp\left(-\frac{t}{t_{res}}\right) \quad (\text{equation 2.9})$$

C = tracer mass fraction at exit

$C_{mix} = 0.0445$ (methane fuel, perfect mixing, $\Phi = 0.8$)

$C_{mix} = 1$ (for only air)

t = time

t_{res} = residence time

The results for tracer mass fraction contours, tracer exit mass fraction profile and residence time frequency distribution is shown in Figure 2.10. The residence time calculated from equation 2.5 is 23.8ms for a perfectly stirred reactor having the same volume and flowrate. The residence time obtained from equation 2.7 for forward flow mode “F” is 23.8ms and that for reverse flow mode “R” is 15.2ms. It may be noted that the residence time for the forward flow configuration is very close to that for the perfectly stirred reactor; however, for the reverse flow configuration residence time is

less as compared to a perfectly stirred reactor. This may be due to insufficient penetration of injected air jet, which results in large “dead” region near the closed end in the reverse flow configuration. This dead zone can be observed from the tracer mass fraction contour as shown in Figure 2.10(b) where very low concentration of tracer (mass fraction~0) is present near the opposite end of air injection. This suggests lower effective volume for the reverse flow configuration. The distribution of residence time is also important as the gases which escapes much earlier can result in significant levels of CO emissions at the exit even though the average residence time is same in the combustor. From frequency distribution plot given in Figure 2.10(d) we can observe that for reverse flow configuration more tracer has lower residence time of <10ms as compared to the forward flow configuration. This may be due to closer vicinity of gas exit near the air injection location which results in early inception of tracer from the exit (see Figure 2.10(c)). Hence for the investigated geometry, reverse flow configuration suggests lower residence time of gases as compared to forward flow geometry and this may result in adverse pollutant emission profile of carbon monoxide. It may be noted that these conclusions could not be generalized for reverse and forward flow configurations and for other geometries we could obtain different results depending on the flowfield inside the combustor. For certain cases reverse flow configuration could result in full penetration inside the confinement volume and due to reverse flow geometry the time required for the gases to escape is higher as compared to the forward flow geometry resulting in favorable combustion characteristics.

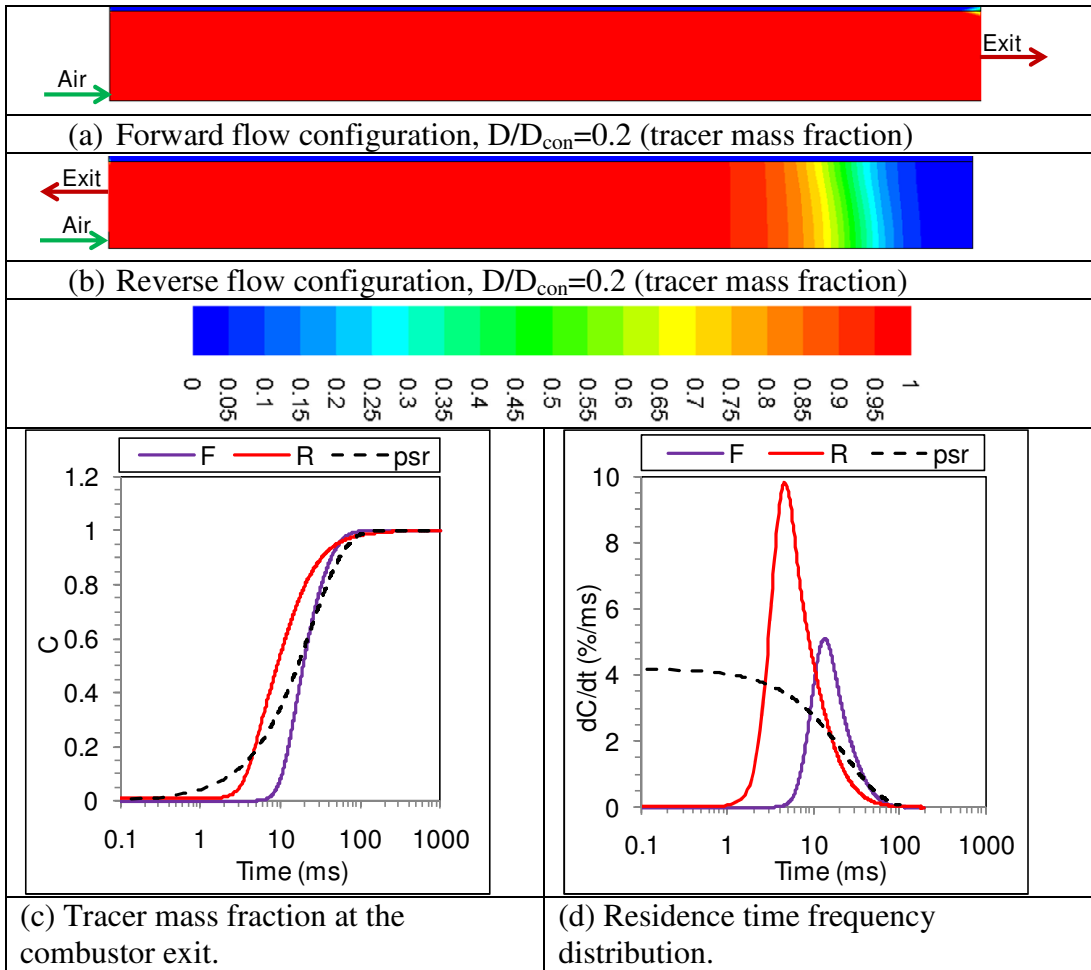


Figure 2.10 (a) Tracer mass fraction at the combustor exit and (b) residence time frequency distribution for configurations F and R (psr=perfectly stirred reactor).

Chapter 3 : Literature Review

This chapter reviews the work on investigation of low emission combustor which employs discrete and direct injection of fuel and air in a confined chamber at high velocity so as to avoid flame stabilization. This work is known by different names in the literature such as High Temperature Air Combustion (HiTAC) [Gupta, A. K., *et al.*, 2003], Flameless Oxidation (FLOX) [Wunning, J. A. and Wunning, J. G., 1997, Colorado, A. F., *et al.*, 2010, Luckerath, R., *et al.*, 2008, Verrissimo, A. S., *et al.*, 2011, Xing, X., *et al.*, 2007, Lammel, O., *et al.*, 2010], Moderate and Intense Low Oxygen Dilution (MILD) combustion [Cavaliere, A. and de Joannon, M., 2004, Ozdemir, I. B. and Peters, N., 2001, Szego, G. G., *et al.*, 2009, Weber, R., *et al.*, 2005, Mi, J., *et al.*, 2009], High Intensity Low Emission (HILE) burner [Kumar, S., 2002, 2005, 2007] Fuel/Oxidant Direct Injection (FODI) furnace [He, Y., 2008, Sobiesiak, A., *et al.*, 1998] and Stagnation Point Reverse Flow (SPRF) combustor [Bobba, M. K., 2007, Gopalakrishnan, P., 2008].

In a review paper by Cavaliere, A. and de Joannon, M., 2004, MILD combustion was defined by combustion process where inlet temperature of reactants is above auto ignition temperature and temperature rise in combustion process is lower than the auto ignition temperature of reactant mixture. They differentiated MILD combustion from HiTAC combustion by suggesting that in HiTAC the temperature rise in combustion process is greater than the auto ignition temperature of reactants even though the temperature of reactants is higher than the auto ignition temperature of reactant mixture.

It may be noted that in stagnation point reverse flow combustor the fuel was injected coaxially with air and not discretely, however this investigation is also included in the consideration as conventional flame stabilization is avoided by high velocity of air injection. Other interesting combustor concept where fuel is injected in a recirculation region called Trapped Vortex Combustor (TVC) [Hsu, K. Y., *et al.*, 1998, Melo, M. J., *et al.*, 2009, Straub, D. L., *et al.*, 2005, Edmonds, R. G., *et al.*, 2008] is also included in consideration and it involves direct injection of fuel in the combustion chamber. Other combustors included here are Princeton Asymmetric Whirl Combustor (PAWC) [Yetter, R. A., *et al.*, 2000] where fuel is directly injected in very strong swirling fluid and Jet Stirred Reactor (JSR) [Shuman, T. R., 2000] where premixed air and fuel is injected in a very small scale combustor.

For sake of comparison a state of the art dry low NO_x (DLN 2.6) combustor is also included [Vandervort, C. L., 2001] which is used in GE-7FA land based gas turbine combustor. It may be noted that the DLN technology uses lean premixed combustor to minimize NO_x emission. Fuel staging is used to operate the combustor at part load conditions. The combustor results in single digit NO_x and CO emissions for 50-100% load condition at elevated pressure of about 16atm at firing temperature (combustor exit temperature) of 1561K.

Figure 3.1 show the thermal intensity variation for low emission combustors investigated by different authors. The combustors are arranged in increasing order of thermal intensity. Generally combustors having thermal intensity less than $1\text{MW}/\text{m}^3\text{-atm}$ are intended for furnace application and thermal intensity greater than $10\text{MW}/\text{m}^3\text{-atm}$ are intended for gas turbine combustor application. Thermal intensity

between 1-10MW/m³-atm [Kumar, S., *et al.*, 2002, 2005, Verrisimo, A. S., *et al.*, 2011] are intended for high thermal intensity furnace application. The corresponding flow configuration is also included in the figure.

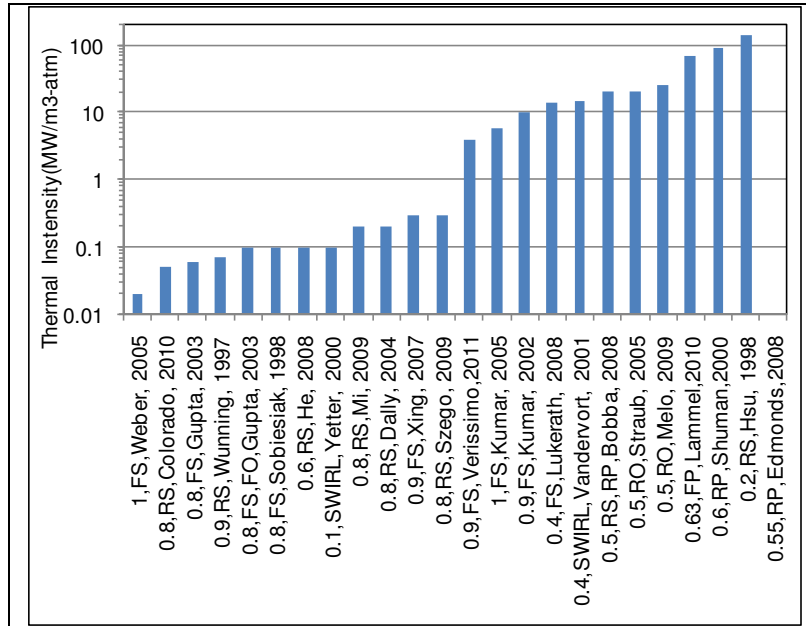


Figure 3.1 Thermal intensity of combustors reported in literature.

Figure 3.2 shows NO_x and CO emission levels for these combustors. For all the combustors the pollutant emission level are normalized at 15% of O₂ concentration so that the performance of these combustors could be compared. The pollutant level at most desirable operating point and the corresponding equivalence ratio is also included in the figure. Among the combustors investigated for gas turbine application, the stagnation point reverse flow combustor [Bobba, M., K., 2008] and flameless oxidation combustor [Luckerath, R., *et al.*, 2008] produced ultra low emissions of about 1ppm NO_x and less than 10ppm CO. It may be noted that these combustors operated in coaxial injection of fuel in air stream and not in discrete injection of fuel and air.

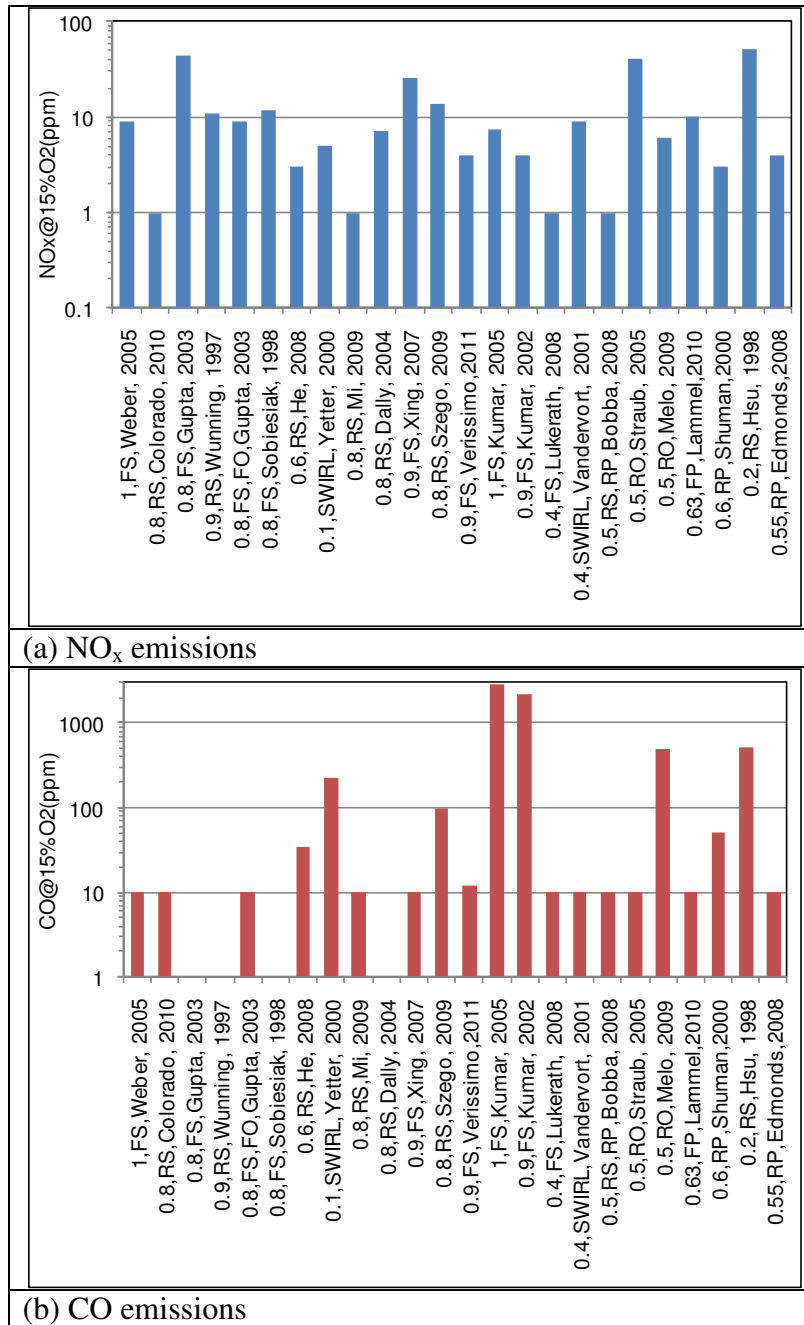


Figure 3.2 NO_x/CO emissions from combustors reported in literature.

Figure 3.3 shows the length scale of these combustors and it may be noted that the combustors having length scale of above 20 inches are generally intended for furnace application and smaller size combustors are intended for gas turbine combustion application. Combustor operating at low thermal intensity of 0.02MW/m³-atm has

length scale of 246 inch [Weber, R., *et al.*, 2005] and combustor operating at high thermal intensity of $144\text{MW/m}^3\text{-atm}$ has length scale of only 1.6 inch [Hsu, K. Y., *et al.*, 1998].

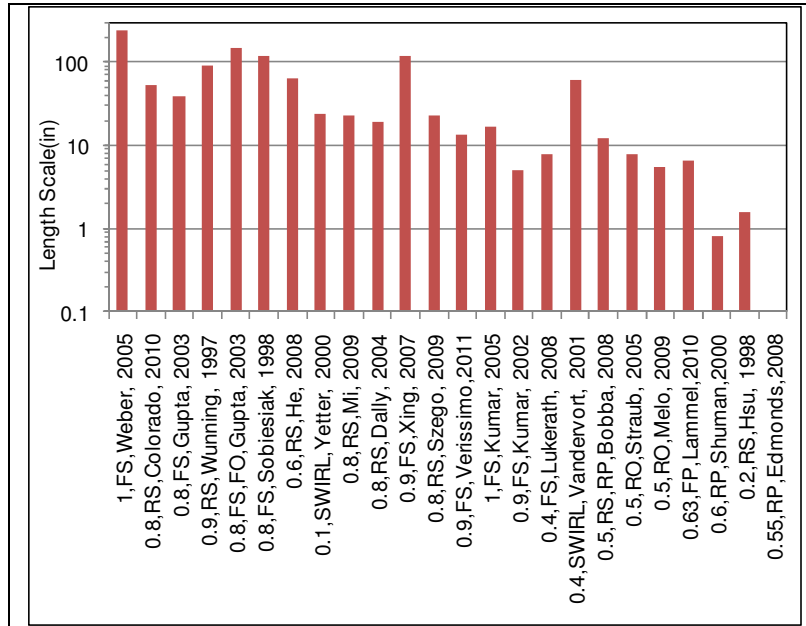


Figure 3.3 Length scale of combustors reported in literature.

Figure 3.4 shows the heat load of these combustors. It may be noted that the experimental furnaces generally employ higher heat load as compared to experimental gas turbine combustors because of large length scale of operation. The state of the art gas turbine combustor [Vandervort, C. L., 2001] operates at very high heat load of 46000kW because it is a practical gas turbine combustor operating at much higher pressure of about 16atm .

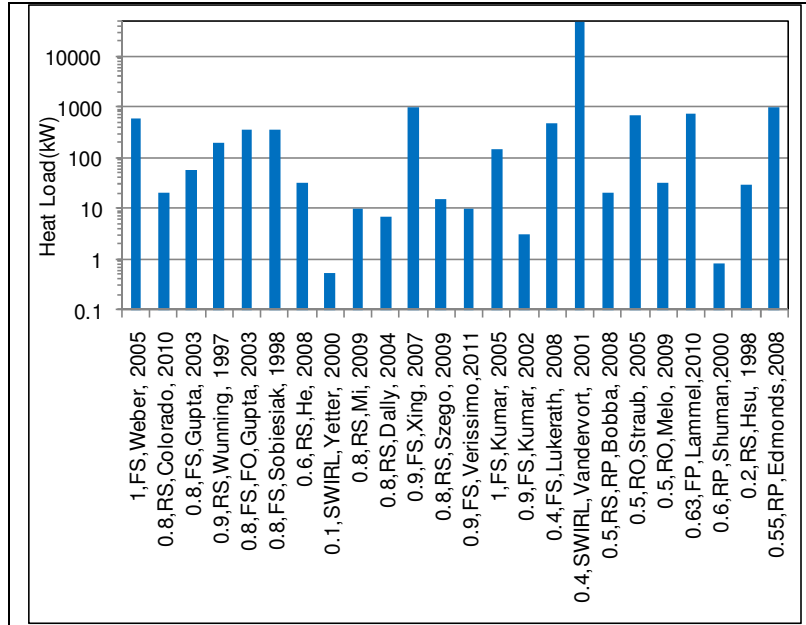


Figure 3.4 Heat load for combustors reported in literature.

Figure 3.5 shows air and fuel injection velocity and turbulent mixing time scales (D/U) for these combustors. From the figure it may be noted that air and fuel injection velocity is about 100m/s for these low emission combustors. Such high velocities are required to avoid stabilization of conventional diffusion flames and enhance turbulent mixing. Consideration of mixing time scale is essential as faster mixing is desirable to achieve lower emission levels. From the figure it may be noted that that turbulent mixing time scale is mostly less than 0.1ms for these combustors. [Kumar, S., *et al.*, 2005] suggested that turbulent mixing time scale of less than 0.086ms is required to achieve satisfactory performance.

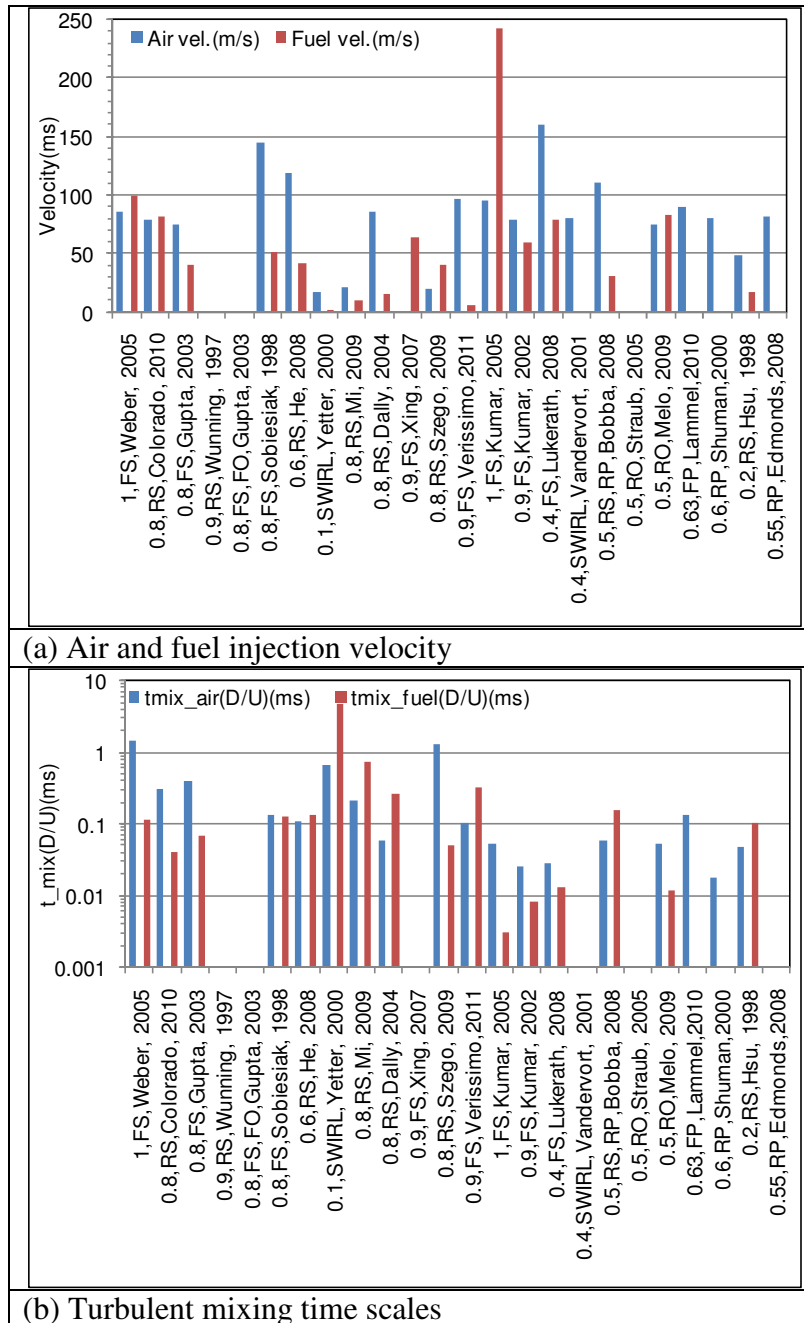


Figure 3.5 (a) Air and fuel injection velocity and (b) turbulent mixing time (D/U) for combustors reported in literature.

Figure 3.6 shows the air injection temperature and operating pressure for these combustors. Generally high temperature air (above auto ignition temperature of fuel, above 1000K) is used for furnace application. For gas turbine application high

temperature air (about 600K) is used to simulate the temperature rise in the compressor. Operating pressure for furnace application is 1atm. However gas turbine combustors operate at higher pressures. The state of the art combustor operates at about 16atm [Vandervort, C. L., 2001] pressure. High pressure investigation at 20atm for low emission flameless oxidation combustor was performed by Luckerath, R., *et al.*, 2008, and this was the first investigation of flameless combustion at high pressure. High pressure investigations for trapped vortex combustor have been performed previously [Straub, D. L., *et al.*, 2005, Edmonds, R. G., *et al.*, 2008].

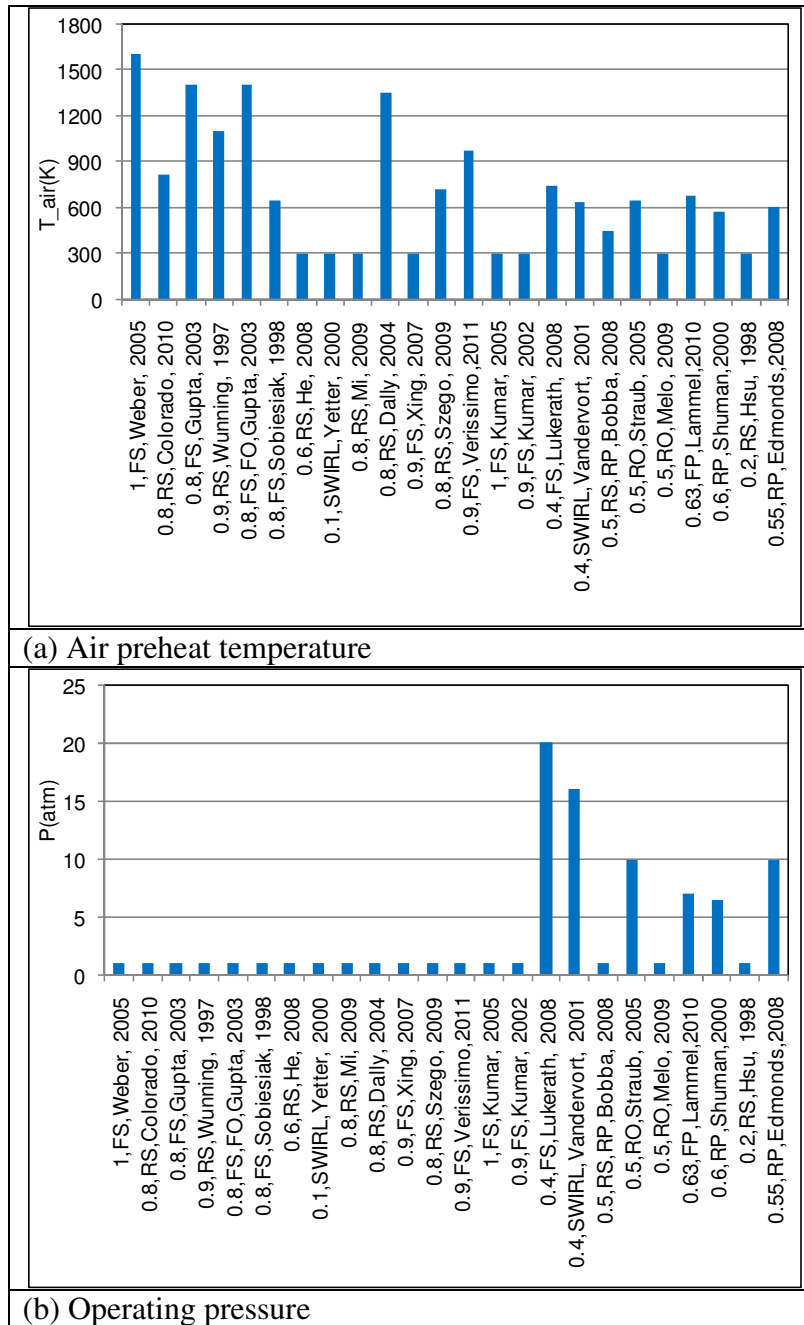


Figure 3.6 (a) Air preheat temperature and (b) operating pressure for combustors reported in literature.

3.1 Furnace Application

The development of low emission combustors for furnace application has been performed for thermal intensity less than $1\text{MW}/\text{m}^3\text{-atm}$. Large combustion volume is

available in furnaces to achieve stable and complete combustion as the main purpose of furnaces is to heat a product. It can be observed that the length scale for these combustors is higher than 20 inches as observed from Figure 3.3. The air injection temperature is also much higher than the ambient temperature as initially it was thought that the temperature of air is required to be above the auto ignition temperature of fuel to achieve low emissions [Gupta, A. K., *et al.*, 2003]. From Figure 3.2 it can be observed that the CO emissions for these combustors are generally about 10 ppm however large variation in NO emissions has been reported. It can also be noted that the air and fuel injection velocities are about 100 m/s for these combustors so that a conventional diffusion flame cannot be stabilized and lower emissions could be achieved. All the combustors intended for furnace application operate at atmospheric pressure condition. Various forward and reverse flow geometries with different fuel injection schemes have been investigated for furnace operation as seen from Figure 3.1. Features of each of these combustors are briefly described below.

Weber, R., *et al.*, 2005, investigated MILD combustion at thermal intensity of $0.02 \text{ MW/m}^3\text{-atm}$ for range of gaseous, liquid and solid fuels including natural gas, heavy and light fuel oil and coal. The furnace had a very large length scale of about 246 inches and large air and fuel injection diameters resulted in much higher turbulent mixing time scales (1.46 ms for air). Preheated air was supplied using a pre combustion chamber and very high preheat temperature of about 1600 K was used. Oxygen was added at the combustor inlet to have 21% O_2 at the main combustor inlet. The furnace operated in forward flow configuration with fuel injected from

same side of air injection. NO_x at the inlet of combustion chamber was about 110ppm and at the exit was about 140ppm resulting in about 9ppm of net NO emission at 15% O_2 level. No detectable level of CO was found at the combustor exit. Uniform heat flux was observed in the furnace suggesting homogeneous combustion process. Mancini, M., *et al.*, 2007, performed chemical kinetic modeling of the strong air and weak fuel jet to understand the chemical changes in these jets before entrainment of fuel jet in the air jet followed by main reaction zone. The IFRF furnace investigated by Weber, R., *et al.*, 2005, was the subject of examination. From modeling it was concluded that very little combustion happened in the fuel jet with only about 6% fuel consumption occurring before the main reaction. This suggests that the entrainment of product gases in fuel jet only results in weak reactions.

Colorado, A. F., *et al.*, 2010, investigated combustion of lower heating value fuel such as biogas (60% CH_4 and 40% CO_2) as well as natural gas (97% CH_4) in a self recuperative reverse flow FLOX furnace at thermal intensity of $0.05\text{MW/m}^3\text{-atm}$. The furnace was about 53inch in length. For both the fuels very uniform temperature profile was observed with flameless mode with temperature standard deviation of 10K as compared to temperature standard deviation of 114K for conventional mode suggesting very uniform temperature field inside the combustor. The reverse flow geometry resulted in very low NO_x (1ppm) and CO (<10ppm) emissions. The air preheat temperature was 810K which is lower than the auto ignition temperature of natural gas suggesting that very high temperature is not necessary to achieve low emissions. It was observed that fuel dilution (with carbon dioxide in this case) had minimal effect on NO_x and CO emissions. In flameless mode the heat transfer

efficiency was observed to be much higher as compared to the conventional mode (70% as compared to 40%) and this increase in efficiency was attributed to the recuperative system used for the flameless mode. In recuperative burner the heat is transferred continuously between the hot flue gases and combustion air by a heat exchanger. Recuperative system used in this work was a honeycomb made of cordierite which is used to extract heat from hot exhaust gases and transfer it to the combustion air. It may be noted that even though the mixing time scale for air injection was on higher side (0.309ms) very low NO_x and CO emissions were obtained from this burner.

Gupta, A. K., *et al.*, 2003, investigated a 58kW regenerative HiTAC burner with elliptical air nozzles and circular fuel nozzles. Fuel nozzles were positioned around the air injector to operate in a forward flow configuration using natural gas as the fuel. The furnace was about 39inch in length. It may be noted that in a regenerator heat is absorbed by a heat storing media such as ceramic monoliths by passing flue gas through it and then heat is recovered from the heat storage media by passing the combustion air through it and this cycle repeats alternately. Four burners were used with two burners operating simultaneously and switching with other two burners on the other side every 30s. The NO_x emissions decreased from 210ppm to 44ppm when the combustion mode changed from ordinary combustion to distributed mode. This transition happened when the furnace temperature exceeded 1123K. In ordinary combustion usual flame was observed however in distributed mode flame in the furnace was very difficult to observe near the burner but in the area between fuel nozzles slightly blue color light was observed suggesting decomposition and ignition

of fuel. Different cases were investigated and it was observed that NO_x emissions were affected more by air jet velocity as compared to fuel jet velocity. The difference between maximum and minimum temperature was only 69K in distributed mode suggesting a uniform temperature field in the furnace.

In 1997, Wunning, J. A. and Wunning J. G., 1997 introduced the name flameless oxidation (FLOX) as a technique to suppress thermal NO_x by avoiding hot spot regions in the furnace. Under the conditions of internal gas recirculation, combustion was observed without any visible or audible flame and hence it was named as flameless oxidation (FLOX). It was suggested that air preheat is not a strict requirement to achieve flameless oxidation; however in this study high air preheat temperatures were used (about 1100K). It was also mentioned that flameless mode can be achieved not only by discrete injection of fuel and air but also by common injection as well as in premixed mode. The flameless mode resulted in about 16dB noise reduction as compared to the flame mode. Both regenerative as well as recuperative burners were successfully demonstrated. A reverse flow regenerative (FLOX REGEMAT[®] 350, also see Lupant, D., *et al.*, 2007) burner that had a cycle time of 20s where three honeycomb regenerators alternately cools the flue gases and heats the combustion air was tested. NO_x emission of about 11ppm was reported with air preheat temperature of about 1100K and thermal intensity of $0.07\text{MW}/\text{m}^3\text{-atm}$ at length scale of 92inch. The FLOX burner has been patented (Wunning, J., 1996, #5570679)

Gupta, A. K., *et al.*, 2003 investigated a 350kW furnace operating in forward flow configuration with fuel injected from same side (“FS”) as well as opposite side

(“FO”) of air injection to study the effect of fuel-air nozzle configuration. The thermal intensity for this furnace was $0.1\text{MW/m}^3\text{-atm}$ and length scale was 150inch. The combustion air was preheated to 1400K using regenerator with switching cycle of 30s. The “FO” flow configuration was expected to have enhanced dilution of fuel and air stream. The difference between maximum and minimum temperature was 80K for “FS” configuration however it decreased to 20K for “FO” configuration suggesting more uniform thermal field for configuration “FO”. The difference was about 120K for the conventional combustion mode. The furnace also achieved waste heat recovery in regenerator up to 77% and this directly relates to significant energy saving. Performance with respect to NO_x and CO emissions was similar for both “FS” and “FO” configurations with NO_x emission of about 9ppm as compared to 128ppm in conventional mode. CO emissions were about 10ppm in both the HiTAC configurations and conventional combustion configuration. Visually low luminosity flames were observed in major part of the combustion volume simulating well stirred reactor features without actually having high agitating momentum.

Sobiesiak, A., *et al.*, 1998 investigated a Fuel/Oxidant Direct Injection (FODI) burner which operated in forward flow mode. Plurality of air and fuel injection ports were used and air and fuel were injected at an angle so as to delay the fuel air mixing and enhance the recirculation and mixing of product gases before ignition. The burner was designed based on the calculation from solution of strong-jet/weak-jet (SJWJ) system investigated by Grandmaison, E. W., *et al.*, 1998. These calculations provided results for entrainment rates as well as the point of confluence of fuel jet with the air jet for different injection schemes. The fuel jet was considered the weak jet and air jet

was considered as the strong jet based on the momentum ratio between two jets. The NO_x emission for this burner was 12ppm at thermal intensity of $0.1\text{MW}/\text{m}^3\text{-atm}$ and furnace length scale of 118inch. The air preheat temperature was 650K which is much lower than the auto ignition temperature of the fuel. The turbulent mixing time scale was also high with value of about 0.131ms for the air jet. The FODI burner has been patented (Besik, F. K., 1998, #5772421).

He, Y., 2008, investigated a Strong-Jet/Weak-Jet furnace having a single air and fuel injection port. The higher momentum flux air jet was termed as Strong-Jet and the fuel jet was termed as Weak-Jet. The strategy to directly inject air and fuel inside the chamber was termed as FODI (fuel/oxidant direct injection). The combustor had reverse flow geometry and resulted in very low NO_x (3ppm) and CO(34ppm) emissions at thermal intensity of $0.1\text{MW}/\text{m}^3\text{-atm}$. The length scale of the combustor was 63inch. Effect of fuel/air momentum flux, fuel/air nozzle separation and fuel injection angle was investigated in detail. Lower injection angle was observed to result in lower NO_x emission and higher fuel injection velocity was observed to result in higher dilution of fuel jet before combustion and hence resulted in lower NO_x emissions.

An interesting whirl combustor (PAWC) was investigated by Yetter, R. A., *et al.*, 2000 where normal temperature air was injected tangentially and the product gases exits axially from the combustor. The swirl number for this combustor was very high (about 17) suggesting very strong tangential momentum as compared to axial momentum. Typical swirl number for conventional swirl stabilized combustor is about 0.5-0.7. The combustor operated at thermal intensity of $0.1\text{MW}/\text{m}^3\text{-atm}$ and

length scale of the combustor was 24inch. Two types of fuel injection schemes were investigated, in the first scheme fuel was injected axially along the combustor centerline (symmetric) and in the second case fuel was injected near the air injection location in strong cross-flow (asymmetric). The fuel injection near the air jet in strong cross-flow resulted in favorable emission characteristics. For this combustor unusual stability limit below equivalence ratio of 0.1 was observed due to high temperature central region that supplies high temperature gases as well as radicals. Very low NO_x emission of about 5ppm and CO emission of about 225ppm were reported for the asymmetric case. It may be noted that for this geometry the turbulent mixing time for air jet was high with a value of about 0.659ms, even then the NO_x emission level was very low. For this combustor the NO_x emission level increased to about 25ppm and CO emission level decreased to less than 10ppm at equivalence ratio of 0.4. This combustor design has been patented (Glassman, I., 1994, #5307621).

Mi, J., *et al.*, 2009, investigated a small scale (23inch) furnace for the effect of air and fuel injection momentum as well as air/fuel premixing in a recuperative furnace. The thermal intensity was 0.2MW/m³-atm with air preheat temperature of 723K and normal temperature of fuel injection. The fuel nozzle was injected coaxially and not discretely in this furnace. The fuel nozzle was in the shape of a bluff body which is used to stabilize conventional combustion by protruding the nozzle inside furnace. When the furnace temperature was above 1073K the nozzle is retracted to transition the reaction regime to MILD combustion. Effect of premixing was investigated by further retracting the fuel nozzle inside the air supply tube. The retraction increased the mixedness of fuel and air; however it also led to decrease in the jet momentum.

The NO_x emission increased by retraction of fuel jet probably due to the more dominant effect of lowering of jet momentum while retracting the fuel nozzle. Hence the case when fuel nozzle is flush mounted with the combustion chamber gave the best results. It was also concluded that there is critical momentum required for air jet to sustain MILD combustion. Above the critical momentum both mixedness and jet momentum had minimal effect. Fully premixed mode also resulted in very low NO_x emissions (about 1ppm).

Dally, B. B., *et al.*, 2004, investigated a MILD combustion furnace at thermal intensity of $0.2\text{MW/m}^3\text{-atm}$ in reverse flow configuration. The furnace had length scale of 19inch. Firstly, the furnace is heated up to 1073K using premixed mixture of methane and air and then fuel is introduced to make transition to MILD combustion. They observed that dilution of fuel with CO_2 or N_2 reduced the NO_x emissions significantly and resulted in invisible flame. Diluting methane up to fuel mass fraction of 0.15 resulted in NO_x emission of less than 1ppm even in non-premixed mode. Greater reduction in NO_x emission was observed with CO_2 dilution. Higher NO_x emissions were observed with 100% propane (25ppm) and 100% ethylene (42ppm) as compared to methane fuel. They concluded that dilution with inert gases delays the ignition of fuel and allows fuel to mix with more recirculated gases before reaction and hence suppresses the NO_x formation. They suggested that premixing the fuel stream with exhaust gases can result in lower NO_x emissions. Plessing, T., *et al.*, 2004, compared highly turbulent premixed flame structure with mild combustion reaction zone in the furnace geometry used by Dally, B. B., *et al.*, 2004. They observed only small temperature rise in mild combustion as compared to sharp

temperature rise in turbulent premixed flame. OH intensity in mild combustion was observed to be much lower and homogeneously distributed as compared to turbulent premixed flames where flame wrinkling was observed. It was noted that the dilution with exhaust gases increases the chemical time scales as compared to turbulent time scales.

Xing, X., *et al.*, 2007, investigated flameless combustion by injecting normal temperature air in the furnace. The operating thermal intensity was about $0.3\text{MW}/\text{m}^3\text{-atm}$ and length scale was 118inch. The furnace operated in forward flow mode with coaxial injection of fuel and air instead of discrete injection. Initially, a diffusion flame was stabilized at lower flowrates. The flameless mode was achieved by increasing the flowrate (hence velocity) of natural gas where the flame zone was observed to become invisible. However, this furnace resulted in high NO_x levels (26ppm) but low CO levels (<3ppm). This also suggests that even with coaxial injection higher level of NO_x could be produced.

Szego, G. G., *et al.*, 2009, investigated stability characteristics of a MILD combustion burner which operates in reverse flow configuration where the exit ports are located between the air and fuel injection ports. The air preheat temperature was of 723K, thermal intensity was about $0.3\text{MW}/\text{m}^3\text{-atm}$ and length scale was about 23inch. For the baseline case NO_x emission was about 14ppm. Effect of air preheat temperature was investigated and it was observed that NO_x emissions decrease from 14ppm at air preheat temperature of 723K to about 12ppm for air preheat temperature of 300K. Amount of heat extracted had significant effect of NO_x emissions as the emission level decreased to 7ppm from 14ppm by increasing heat extraction from

25% to 42%. Peculiar trend was observed with increase in equivalence ratio where increase in equivalence ratio from 0.8 to 0.9 resulted in decrease in NO_x emission to 8ppm from 14ppm. Fuel dilution with CO₂ or N₂ (up to 76% by mass) resulted in significant reduction in NO_x emission (up to 48%). It was postulated that the fuel jet momentum controls the stability of the system and lower fuel jet momentum results in lower penetration and hence lowers entrainment of the burned gases and hence a minimum fuel jet momentum (fuel/air momentum ratio=0.006) is required to achieve combustion in MILD regime.

Verisimmo, A. S., *et al.*, 2011, investigated a forward flow flameless combustor at thermal intensity of 3.8MW/m³-atm which represents high thermal intensity furnace application. The length scale of this combustor was small with length scale of 13.4inch. Very low NO_x of about 4ppm and low CO of about 12ppm were observed for this combustor at equivalence ratio of 0.9. The air preheat temperature was 973K and turbulent mixing time scale for air injection was 0.104ms. An interesting trend was observed for this combustor, when air flow rate was increased at constant fuel flow rate to change the equivalence ratio the reaction zone was observed to move towards the air injection location. This was postulated to be because of faster entrainment and mixing of fuel jet in the higher momentum air jet resulting in shifting of reaction zone towards the air injection location.

Kumar, S., *et al.*, 2002 investigated high intensity low emission combustor focused on high thermal intensity furnace application. The thermal intensity was 10MW/m³-atm as opposed to <1MW/m³-atm demonstrated in previous studies at that time. This combustor had a frustum of a cone inside the combustion chamber to aid in

recirculation of the gases. The combustor achieved 10-15dB reduction in noise level. In this work it was reported that high air preheat temperature is not a pre-requisite to achieve low emissions and in this work fuel and air were used at ambient temperature condition as opposed to use of recuperator/regenerator system used in previous studies. MILD combustion was defined in this work as having normalized spatial temperature variation of less than 15%. Experimentally very weak and barely visible flame was observed in MILD combustion mode. Eventhough low NO_x emissions of about 4ppm was obtained, high levels of CO emissions (2300ppm) were registered even after using staged air (10%excess) to oxidize CO.

Kumar, S., *et al.*, 2005, examined the scaling criteria for MILD combustion burners and different strategies were discussed to scale the burner from 3kW to 150kW. Different approaches such as keeping the inlet velocity constant (CV), keeping the residence time constant (CRT) were considered. Keeping the velocity constant led to increase in mixing time (D/U , as D is increased) as well as decrease in the thermal intensity and keeping the residence time constant (constant thermal intensity) resulted in significantly higher velocities leading to unacceptable pressure drop. A different approach was successfully demonstrated where the burner major dimensions were scaled based on the CRT approach to keep the thermal intensity constant, however number of air and fuel injection ports were increased to result in similar mixing time scale (D/U). The air and fuel injection velocities were similar to maintain the pressure drop across the combustor to approximately same level. Air and fuel injection diameter were also kept similar by increasing the number of air and fuel injection ports. It was suggested in this work that the mixing time scale (D/U) should

be less than 0.086ms for the burner to effectively operate in MILD combustion regime. The burner was operated with both LPG (45MJ/kg-K) and producer gas (4.5 MJ/kg-K). It was observed that the scaled burner resulted in 8dB noise reduction as compared to conventional flame, and very uniform temperature and species field. For the scaled burner the CO emission level was quite high (2900ppm) however low NO level was achieved (8ppm). With producer gas the NO level was very low of about 1ppm and CO level was about 630ppm.

3.2 Gas Turbine Application

Recently novel distributed combustion technology has been investigated for application to gas turbine combustor development. It may be noted that the state of the art gas turbine combustor (DLN-2.6) for land based power generation system operates at thermal intensity of about $15\text{MW}/\text{m}^3\text{-atm}$ and the length scale of this combustor was 60inch. This combustor produced less than 9ppm of NO_x as well as CO emissions for 50-100% load condition [Vandervort, C. L., 2001]. The inlet temperature is about 631K and outlet temperature is 1561K with operating pressure of 16atm.

Luckerath, R., *et al.*, 2008, investigated flameless combustion in forward flow configuration for application to gas turbine combustors. At the time of investigation this was the first study at elevated pressure for flameless combustion and the combustor was operated at pressure of 20atm. The fuel was introduced in the combustor by injecting the fuel coaxially with respect to high velocity air jet. The fuel nozzle was retracted so as to achieve some degree of partial premixing. This feature might also be responsible to achieve very low NO_x emissions of about 1ppm and CO

emissions of less than 10ppm at equivalence ratio of 0.4 from the combustor even at elevated pressure. The thermal intensity of the combustor was $14\text{MW/m}^3\text{-atm}$ and length scale was about 8inch. Very large nozzle velocity of about 160m/s was employed so that the turbulent mixing time for the air jet was very low with value of about 0.028ms. It was observed that nozzle velocity had significant effect on the mixing process and low emission window was significantly extended by increasing the nozzle velocity and more distributed reaction zone was observed. Effect of hydrogen addition on flameless combustion condition was investigated and it was found that addition of hydrogen increases the NO_x emission but extends the lean operational limit so that the combustor can be operated leaner to give lower NO_x emissions. It was observed that decreasing the equivalence ratio makes the reaction zone more homogeneous. This combustor design has been patented (Wunning, J. G., and Wunning, J. A., 2006, #7062917). Schutz, H., *et al.*, 2008, analyzed pollutant formation for the flox combustor investigated by Luckeath, R., *et al.*, 2008 using chemical kinetic simulation by GRI 3.0 mechanism. They found that the thermal Zeldovich mechanism contributed about 41% of total NO_x formed and prompt Fenimore mechanism and intermediate N_2O mechanism contributed 27% and 32% respectively. They suggested that in flameless regime all three mechanisms contribute significantly to total NO_x formed.

Gopalakrishnan, P., 2008 and Bobba, M. K., 2007, investigated reverse flow geometry to achieve very low NO_x (1ppm) and CO (<10ppm) emissions in both premixed and non-premixed conditions. This combustor operated at thermal intensity of $20\text{MW/m}^3\text{-atm}$ at equivalence ratio of 0.5 and combustor length scale was about

12inch. In this geometry the fuel was injected coaxially with air and this surrounding air acted as a shield from the hot product gases that prevented fuel from igniting prior to proper mixing with air and hence the combustor gives performance close to premixed combustion even in the non-premixed mode of operation. Liquid Jet-A fuel was also tested and it also resulted in very low emission levels (less than 10ppm for both NO and CO). Liquid Jet-A was injected directly and coaxially inside the combustor without any atomizer. The combustor was observed to be stable very close to the lean flammability limit of methane and this was postulated to be the reason for such low emissions. It was observed that the combustion is stabilized near the stagnation region opposite to the air injection location having low velocities and high turbulence levels. It was observed that the flame was in thin reaction zone regime. It was noted that the product gas entrainment does not have significant effect on the combustor performance and the lower emission levels are due to the ability of combustor to operate stably at lean condition. This combustor design has been patented (Zinn, B. T., *et al.*, 2007, #7168949).

Another interesting design is a trapped vortex combustor technology where fuel is injected in a vortex that is trapped between two plates or in a cavity in the path of combustion air flow to enhance flame stability. These combustors demonstrated exceptional lean operational limits of overall equivalence ratio less than 0.2 due to much richer burning reaction zone in a small cavity associated with the trapped vortex which serves as a continuous ignition source for combustion. The mixture in the trapped vortex is generally rich so that the hot gases produced are highly reactive for ignition of mixture in the main combustion chamber.

Straub, D. L., *et al.*, 2005, investigated rich-burn, quick-mix, lean-burn (RQL) trapped vortex combustor at operating pressure of 10atm. The length scale of this combustor was 8inch. RQL concept has been used in conventional gas turbine combustor designs by axially staging air and having two different combustion zones in rich and lean regime to minimize NO_x emission by avoiding near stoichiometric combustion however in TVC concept the air is radially staged. In trapped vortex combustor concept a cavity having high temperature circulating gases is used to stabilize combustion and the cavity region is the fuel rich region. The cavity flow was not observed to be affected by the main air flow rate. Cavity equivalence ratio of about 1.5 resulted in favorable emission profiles. Increasing the residence time in the cavity resulted in lower NO_x emissions. Very low CO emissions of less than 10ppm were obtained however high NO_x emissions were registered (about 40ppm).

A novel combustor model for application to gas turbine combustor was investigated by Melo, M. J., *et al.*, 2009, by establishing large recirculation zone in the combustion chamber. The length scale of this combustor was 5.5inch. Fuel was injected in the recirculation zone which consists of hot and diluted mixture of combustion air and product gases which is above the auto ignition temperature of fuel. The combustor resulted in low NO_x levels (6ppm) however much higher CO emission levels (500ppm) at equivalence ratio of 0.5.

Lammel, O., *et al.*, 2010, investigated FLOX combustion at high power density of about 68MW/m³-atm and achieved low NO_x and CO levels (<10ppm) at equivalence ratio of 0.63. Air and fuel were injected in forward flow premixed mode at elevated pressure of 7atm. It may be noted that this combustor was advancement to the

combustor investigated by Luckerath, R., *et al.*, 2008, which operated at low thermal intensity of $14\text{MW/m}^3\text{-atm}$. In this combustor the air injection diameter was increased to 12mm from 4.5mm to allow more air flow as well as to reduce the pressure drop across the combustor. The length was reduced to 6.7inch from 8inch that was used by Luckerath, R., *et al.*, 2008. An advanced mixer was designed to premix air and fuel to a desirable degree before injecting the mixture in the combustor as opposed to partially premixing air and fuel as investigated by Luckerath, R., *et al.*, 2008. The combustor was also tested with propane and hydrogen-natural gas mixture fuel. It was observed that with addition of hydrogen the NO_x levels increased at a given equivalence ratio, however it decreased with operation of combustor at leaner mixtures and less than 10ppm NO_x was achieved for 50% hydrogen content fuel. In this investigation it was suggested that the power density with respect to the dome area is also important and it was mentioned that for gas turbine application power density in excess of $10\text{MW/m}^2\text{-atm}$ is required for satisfactory performance.

Jet stirred reactor having reverse flow geometry and operating in premixed mode was investigated by Shuman, T. R., 2000. The reactor was very small (0.8inch in length) and the investigation was focused on the effect of residence time, pressure and inlet temperature on combustion characteristics of lean premixed combustion. Very low residence time of about 0.5ms was also investigated. This combustor operated at thermal intensity of $90\text{MW/m}^3\text{-atm}$. It was observed that NO_x was lowest at intermediate residence time suggesting no clear trends could be concluded with respect to residence time for NO_x emissions. At lower residence time it was observed that the free radicals, such as O, OH and CH fill the combustion volume causing high

formation rates of NO_x . It was observed that increasing inlet temperature and operating pressure tend to reduce NO_x emissions. It was concluded that the reactions occurs in chemical rate limiting regime due to fast turbulent mixing. This combustor was mostly intended for fundamental flame studies for conventional gas turbine application instead of actual implementation and development of distributed combustion technology. The turbulent mixing time for air jet was very small for this reactor (about 0.018ms) to provide intense mixing condition. A conceptual Time-Optimized Flame Cavity (TOFC) which is a jet-stirred reactor inside primary combustion zone was also discussed that could be implemented in a gas turbine combustor. The basic idea is to have optimal residence time to minimize NO_x emissions and it was postulated that the combustor could yield NO_x as low as 3ppm.

Very high intensity trapped vortex combustor has been developed at air force research laboratory (AFRL). Hsu, K. Y., *et al.*, 1998, investigated a conceptual trapped vortex combustor where the vortex is trapped between a forebody disc and an afterbody disc and the blockage ratio was about 76%. The thermal intensity of this combustor was $144\text{MW/m}^3\text{-atm}$ with very small length scale of 1.6inch. Air was injected in the cavity so as to reinforce the vortex in the cavity. The afterbody diameter of about 0.73 times the forebody diameter and cavity length of about 0.59 times the forebody diameter was found to give favorable results of low pressure drop as well as stable flame. For the reacting flow condition very low pressure drop of about 1.5% was observed. Very low lean blowout equivalence ratio of 0.05 was obtained suggesting highly effective stabilizing influence of the trapped vortex. However, very high NO_x emission of about 52ppm and high CO emission of about

520ppm were reported at overall equivalence ratio of 0.2. For this combustor the turbulent mixing time was about 0.048ms.

Advanced vortex combustor based on the concept of trapped vortex combustor was investigated by Edmonds, R. G., *et al.*, 2008 at the National Energy Technology Laboratory. Ultra low NO_x, CO and UHC emissions (4, 4, 0ppm) were obtained at equivalence ratio of 0.55 with very low pressure drop of 1.75% as the combustor did not require any swirl vanes to stabilize the flame. The combustor was tested at elevated pressure of 10atm. Very low pressure fluctuations of less than 0.15%rms were achieved which was an order of magnitude lower than industrial accepted level of 1.5%rms. This combustor design has been patented (Kendrick, D., *et al.*, 2006, #7003961).

A summary of other relevant details of combustor performance operating in various configurations reported in literature is given in Table F.1 of Appendix F. The combustors are arranged in increasing order of thermal intensity. The table includes details such as flow configuration, heat load, type of fuel used, operating pressure, air and fuel velocity, turbulent mixing times and injection temperature apart from NO_x and CO emissions for these combustors.

3.3 Flame Investigations

This section summarizes flame investigations from various authors under high temperature low oxygen concentration conditions.

Gupta, A. K., 2004, investigated the characteristics of gaseous flames using high temperature air. The fuel injection is cross flow as shown in Figure 3.7 from a 1mm diameter hole and air preheat temperature above 1300K was used. The

momentum ratio (“r”, see equation 2.4) was kept constant in this study. Air was preheated using honeycomb regenerator and diluted with inert gas to simulate low oxygen concentration condition (up to 2%). It was observed that flames with high air preheat temperature were more stable and homogeneous both temporally and spatially. Temperature fluctuations (root mean square) decreased significantly from 197K to 4K with increase in air preheat temperature from 308K to 1473K and reduction in oxygen concentration from 21% to 4%. It was noted that HiTAC flames resulted in more uniform heat flux due to thermal field uniformity and hence resulted in more efficient heating in furnaces. Flame volume was observed to increase with decrease in oxygen concentration. Colorless flame was observed for oxygen concentration below 2% with methane fuel and this was termed as colorless combustion. The visible emission from flame was observed to be shifted towards green due to dominance of C_2 radical under HiTAC condition. It was noted that the flame stability was infinite under HiTAC condition due to temperature of oxidizer being higher than the auto ignition temperature of fuel.

Gupta, A. K., *et al.*, 1999, investigated the flame structure and emission characteristics for the effect of air preheat temperature and oxygen concentration in cross flow mode shown in Figure 3.7. It was observed that increase in air preheat temperature and decrease in oxygen concentration and it was attributed low Damkohler number as compared to normal temperature air combustion. It was suggested that at high temperature and low oxygen concentration condition the mixing time higher however the increase in chemical time is much more leading to decrease in Damkohler number. With decrease in oxygen concentration the flame

color was observed to change from yellow to blue to bluish green to green color and at very low oxygen concentration of less than 2% no color was observed and this was termed as colorless combustion. At lower oxygen concentration (<5%) green color flame was observed due to domination of C2 radical emission. With increase in air temperature the light intensity was observed to increase. Ignition delay time was calculated from flame standoff distance and it was observed that with increase in air temperature the ignition delay time decreases significantly.

Mortberg, M., *et al.*, 2007, investigated flow field features of HiTAC flames using particle image velocimetry technique for jet in cross flow configuration shown in Figure 3.7. It was observed that the fuel jet penetration was higher in high temperature air and turbulence level was lower. Mortberg, M., 2005, observed significantly enlarged reaction zone (via OH* chemiluminescence imaging) at high temperature and low oxygen concentration oxidizer condition and attribute it to low oxygen concentration which reduces the reaction rates and hence larger volume is required for combustion. In this work ignition delay time was estimated from the standoff distance of reaction zone from fuel jet injection and it was observed that the ignition delay time decreases with increase in air preheat temperature. Ignition delay time was observed to be significantly greater for lower calorific value fuel. Mortberg, M., *et al.*, 2006, investigated flowfield and combustion features of methane and a low calorific value fuel (12% CH₄ in N₂). The fuel jet velocity was about 25m/s and the cross flow velocity was 0.9m/s. For low calorific value fuel case almost colorless flames were observed. They observed higher turbulence and vorticity for low calorific value fuel case as compared to methane. Lower calorific value fuel revealed smaller

penetration in cross flow, higher ignition delay time and uniform distribution of radicals as compared to methane fuel.

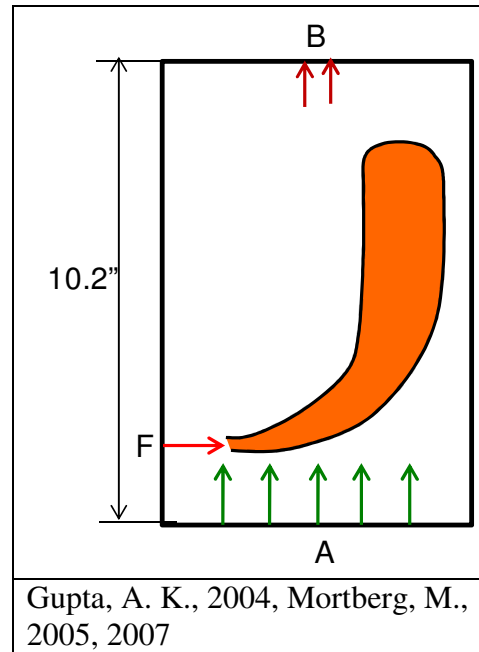


Figure 3.7 Jet in cross flow of high temperature and diluted air.

Lille, S., *et al.*, 2005, investigated jet in co-flow configuration as shown in Figure 3.8. Hot flue gases from another burner were used instead of high temperature air from regenerator that was used in jet in cross-flow investigation shown in Figure 3.7. The air preheat temperature was about 1150K and O_2 concentration varied from 6-21%. Fuel/air velocity was kept constant in this investigation and fuel (propane) was injected from a 0.5mm diameter hole. The flue gas velocity was about 1m/s and fuel injection velocity was 26m/s. It was observed that with decrease in oxygen concentration in co-flowing gases the flame luminosity decreases and its size increases, similar to the observations made for jet in cross-flow experiments. At oxygen concentration lower than 10% no flame was visible.

Yang, W. and Blasiak, W., 2004, investigated the effect of oxygen concentration and temperature of co-flowing air (see Figure 3.8) on the flame size and they

observed that flame length significantly increased with decrease in oxygen concentration. They suggested that at low oxygen concentration condition the combustion phenomenon is very similar to well stirred reactor condition with volumetric combustion instead of a flame front. Increase in temperature of co-flowing gases was observed to increase the flame length slightly and the reason was attributed to lower mixing due to smaller density of oxidizer and higher temperature.

Dally, B. B., *et al.*, 2002, investigated jet in hot co-flow in geometry similar to that shown in Figure 3.8. The fuel jet diameter was 4.25mm and co-flow diameter was 82mm. The temperature of co-flowing gas was 1300K with oxygen concentration of 3%, 6% and 9%. 50% H_2 +50% CH_4 was used as the fuel. It was observed that with low oxygen concentration the visible emissions were low and the reason was attributed to suppression of radicals at low oxygen concentration. The peak temperature was significantly lower for low oxygen concentration condition. The OH radical concentration and CO levels was almost 3times less at 3% O_2 as compared to 9% O_2 with very wide reaction zone of 6mm. Much smaller NO levels were observed for low O_2 level.

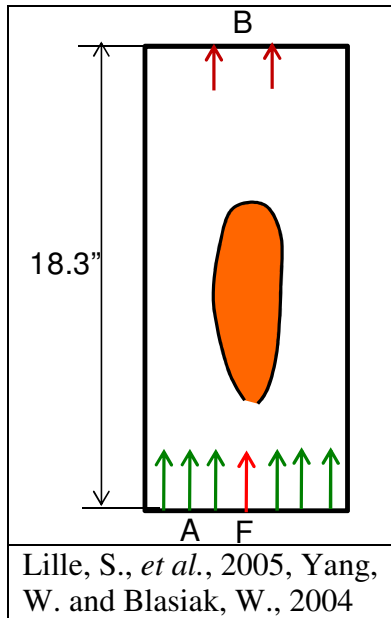


Figure 3.8 Jet in co-flow of flue gases.

Choi, G. M., and Katsuki, M., 2000, investigated the effect of fuel injection location, simulating different fuel mixing conditions. Air was heated up to temperature of 1423K from an alternating-flow regenerative preheater. Fuel was injected from four locations as shown in Figure 3.9 and significant variation in NO was observed for different cases. Minimum NO was observed for fuel location “F4” due to uniform mixing of fuel and suggested distributed combustion. NO emission was found to be independent of temperature and equivalence ratio for this case. Very high NO was observed for fuel injection location “F2” due to fuel injection in recirculating flow and accumulation of fuel in the central region with lower mixing.

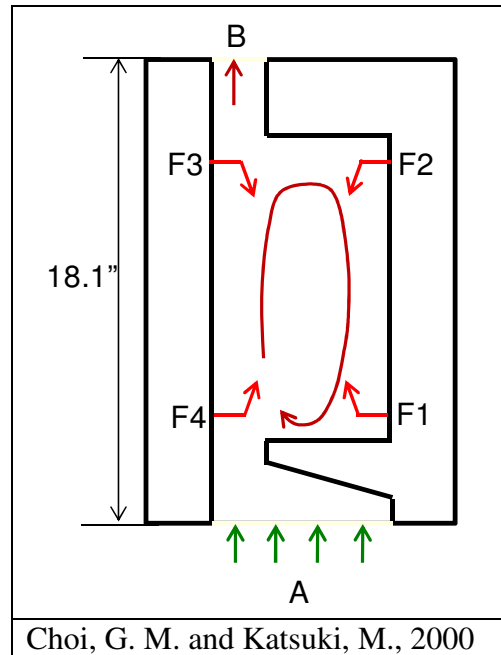


Figure 3.9 Effect of fuel mixing.

Cavigiolo, A., *et al.*, 2003, investigated mild combustion in a laboratory scale burner as shown in Figure 3.10. Air and fuel were partially premixed before entering the combustion chamber. The air/fuel mixture entrains large amount of burned gases to result in dilution of reactants. Air was mixed with nitrogen to simulate gas recirculation and preheated up to 1600K. It was suggested that recirculation ratio of about 4 and air preheat temperature of about 1100K is required for transition to mild combustion regime for methane fuel. It was observed that NO emission decreased from 65ppm to less than 5ppm when the combustion regime transitioned from conventional mode to mild combustion mode. The residence time for these experiments was greater than 1000ms suggesting very low thermal intensity.

Effuggi, A., *et al.*, 2008, investigated natural gas and biogas (simulating low calorific value fuels) in the burner shown in Figure 3.10. Natural gas had composition of 90vol.% methane and 10vol.% ethane by and biogas had composition of 50vol%

methane and 50vol% nitrogen. It was observed that the recirculation ratio of about 3.5 with natural gas and 2.7 for biogas was required for transition to mild combustion as opposed to recirculation ratio of 4 required for methane fuel (Cavigiolo, A., *et al.*, 2003). The reason attributed to lower recirculation ratio requirement with natural gas due to presence of more reactive ethane fuel and internal dilution of fuel for biogas. The temperature required to transition to mild combustion did not change with fuel composition. This investigation suggested suitability of mild combustion for lower heating value fuel.

Derudi, M., *et al.*, 2007, investigated mixture of hydrogen and methane in a laboratory burner shown in Figure 3.10. It was observed that about 50% higher jet velocity is required with hydrogen enriched (30 vol% H₂) combustion to avoid flame stabilization and operation in MILD combustion regime. This was attributed to much higher flame velocity of hydrogen as compared to methane. The minimum recirculation ratio and temperature required for transition to mild combustion also decreases with addition of hydrogen to methane.

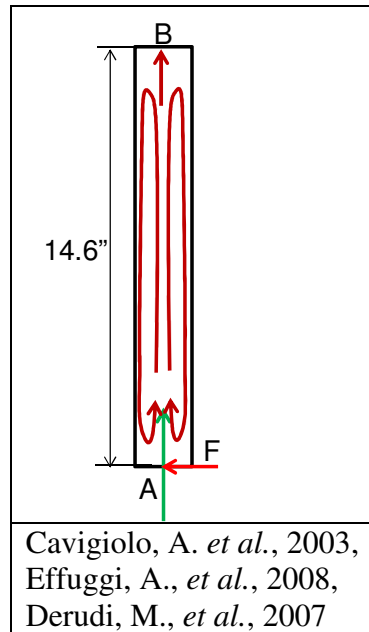


Figure 3.10 Mild combustion furnace.

3.4 Dissertation Outline

As observed from Figure 3.1 very few studies have been reported at thermal intensity higher than $25\text{MW/m}^3\text{-atm}$. FLOX combustor [Lammel, O., 2010] operates at thermal intensity of $68\text{MW/m}^3\text{-atm}$ however the fuel and air is well premixed before introduction in the combustor. Jet stirred reactor [Shuman, T. R., 200] operates at thermal intensity of $90\text{MW/m}^3\text{-atm}$ but it also operates in premixed flow mode. This combustor had a very small length scale (0.8inch in length) and was used for fundamental flame investigation instead of application of technology to practical combustors. Trapped vortex combustor [Hsu, K. Y., *et al.*, 1998] operates at very high thermal intensity of $144\text{MW/m}^3\text{-atm}$ in non-premixed mode, however, it resulted in very high NO_x (52ppm) and CO(520ppm) emission levels (see Figure 3.2). It can also be noted that the combustors reported in literature operate in various fuel and air injection configurations such as forward flow (F) reverse flow (R) with fuel injection

from same side (S), opposite side (O) or in premixed (P) mode with respect to air injection (see Figure 3.1). The objective of this dissertation is investigation of the features of different flow configurations as well as development of high thermal intensity combustor with careful consideration of different parameters for CDC combustor.

The dissertation elaborates sequential development of high thermal intensity CDC combustor up to thermal intensity of $198\text{MW}/\text{m}^3\text{-atm}$. The focus here is on land based gas turbine application. Various flowfield configurations in both reverse and forward flow modes as well as different combinations of fuel injection schemes has been investigated at range of thermal intensities in the dissertation. The summary of the investigated flow-field configurations in this dissertation is presented in Figure 3.11.

In Chapter 4, investigation of low thermal intensity combustor operating at intensity of $5\text{MW}/\text{m}^3\text{-atm}$ is presented with comparison of different flow field configurations. The investigated flow-field configurations in this chapter is shown in Figure 3.11(a) and (b). Both premixed and non-premixed flow modes were investigated. The combustor operates at thermal load of 25kW and has four air and fuel injection ports. This chapter also includes the investigation of effect of air and fuel injection diameter on the flowfield and emission characteristics of the CDC combustor for a forward flow configuration. Results for exit gas emission level, global flame pictures, and flowfield and residence time characteristics were included. The flowfield was obtained using CFD simulations. Methane was used as the fuel and normal temperature and pressure air was used as oxidizer.

In Chapter 5, examination of medium thermal intensity combustor up to $40\text{MW}/\text{m}^3\text{-atm}$ is presented and the geometries investigated are shown in Figure 3.11(c) and (d). Three different confinement sizes operating at 20, 30 and $40\text{MW}/\text{m}^3\text{-atm}$ were investigated for a forward flow configuration where fuel is injected from the same side of the air injection (see Figure 3.11(c)). These combustors operate at heat load of 25kW with four air and four fuel injection ports. A simpler and smaller combustor having full optical access and single air and fuel injection jet was investigated at thermal intensity of $28\text{MW}/\text{m}^3\text{-atm}$ (see Figure 3.11(d)). The combustor operates at heat load of 6.25kW and both forward and reverse flow configurations in premixed and non-premixed modes were investigated. The results include the exit gas emissions, global flame pictures, OH^* distribution to locate the reaction zone and flowfield and residence time characteristics. Flowfield was obtained using CFD simulations. Methane was used as the fuel and normal temperature and pressure air was used as oxidizer. The flow configurations and air and fuel injection diameters of the smaller combustor investigated in the chapter are similar to that investigated for the larger combustor investigated in Chapter 4.

In Chapter 6, investigation of high thermal intensity up to $85\text{MW}/\text{m}^3\text{-atm}$ for CDC combustor is presented. The heat load of combustor is 6.25kW. Only reverse flow configuration was investigated in detail as it showed promise to achieve desirable combustion characteristics. The effect of fuel injection location was investigated. Figure 3.11(e) and (f) shows the geometry that has been investigated in this chapter. Global flames pictures, OH^* distribution along with the exit gas emissions results as well as the flowfield characteristics are included. The flowfield was obtained using

CFD simulations. Effect of hydrogen addition to methane fuel was also investigated at thermal intensity of $85\text{MW/m}^3\text{-atm}$ in reverse-cross flow configuration. Normal temperature and pressure air was used as oxidizer.

In Chapter 7 the combustion characteristics of the down selected geometry operating at thermal intensity variation from $53\text{-}85\text{MW/m}^3\text{-atm}$ are presented (see Figure 3.11(g)). The down selected geometry operates at thermal load range of $3.91\text{-}6.25\text{kW}$ and uses larger air injection diameter ($d_{\text{air}}=5D/3$ as compared to D used previously (Chapter 5 and 6) , where $D=3/16\text{inch}$) to minimize the pressure drop across the combustor. In this investigation air flow rate was kept constant and fuel flow rate was varied to simulate different power settings of the gas turbine combustors. Higher air injection temperature of 600K was investigated to simulate the temperature rise in compressor due to near isentropic heating. Dynamic pressure fluctuations were measured to obtain the stability of combustor operation. Heat loss from the combustor was also estimated by measuring the exit gas temperature. Other results include the exit gas emission level, OH^* distribution, global pictures as well as flowfield inside the combustor. The flow field was obtained using particle image velocimetry in non-reacting flow condition with only air flow. Further reduction in volume resulted in ultra-high thermal intensity combustor operating at thermal intensity of $156\text{-}198\text{MW/m}^3\text{-atm}$. For this combustor both gaseous as well as liquid fuel were tested and the results for pollutant emissions are presented. The effect of fuel dilution effect on the performance of high intensity combustor is also included.

Chapter 8 includes summary and Chapter 9 includes conclusions from present work and recommendations for future work.

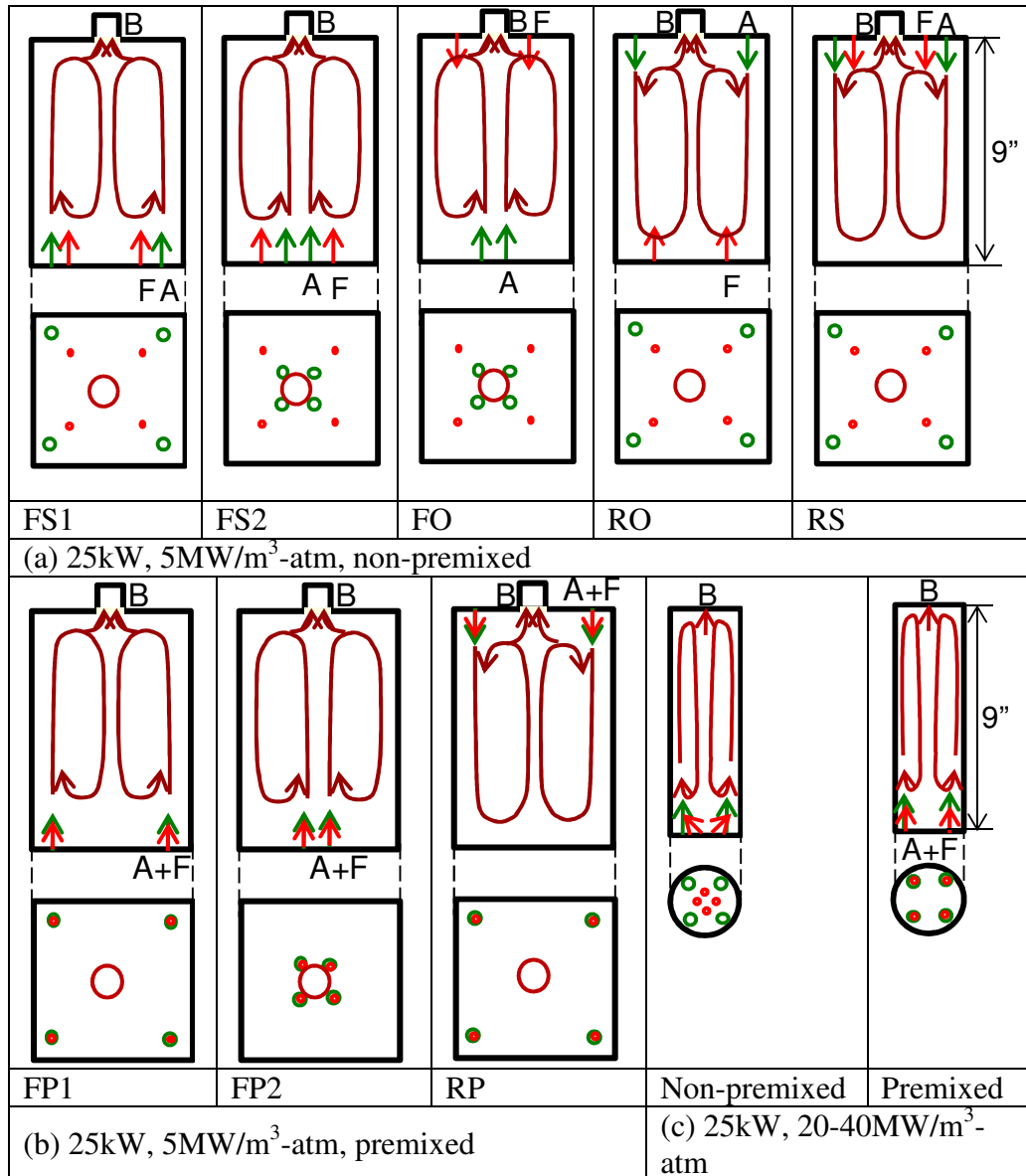


Figure 3.11 Combustor designs investigated in the present work

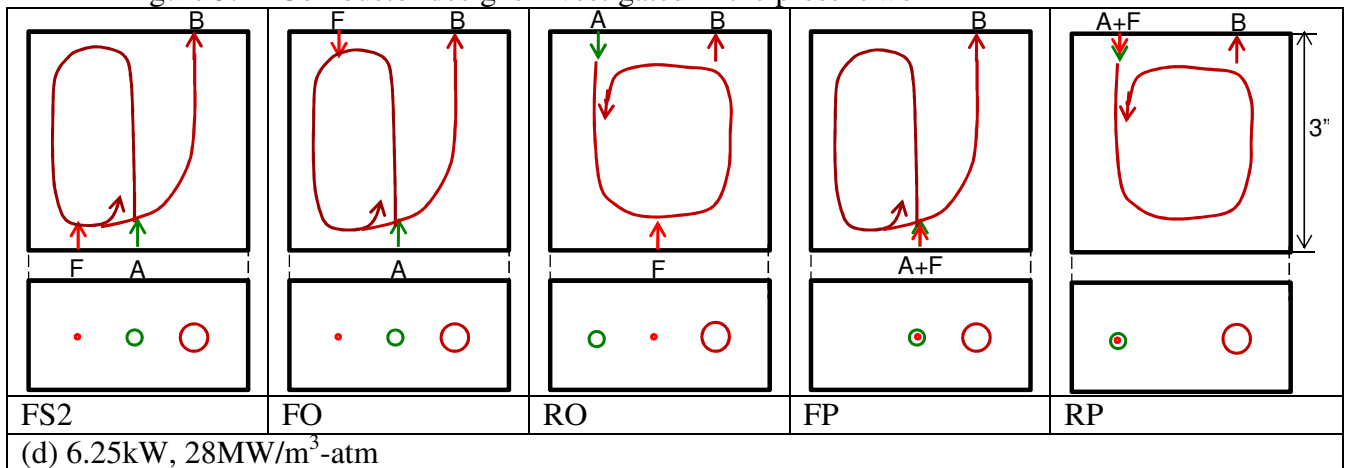


Figure 3.11 Combustor designs investigated in the present work (contd ...).

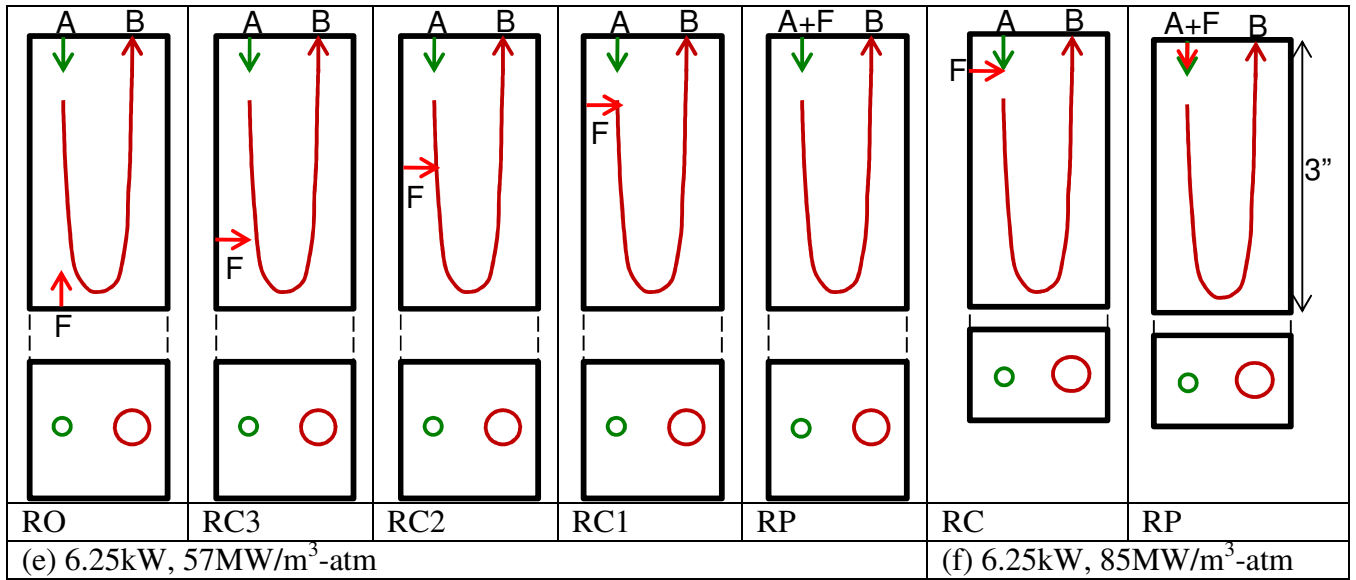


Figure 3.11 Combustor designs investigated in the present work (contd ...).

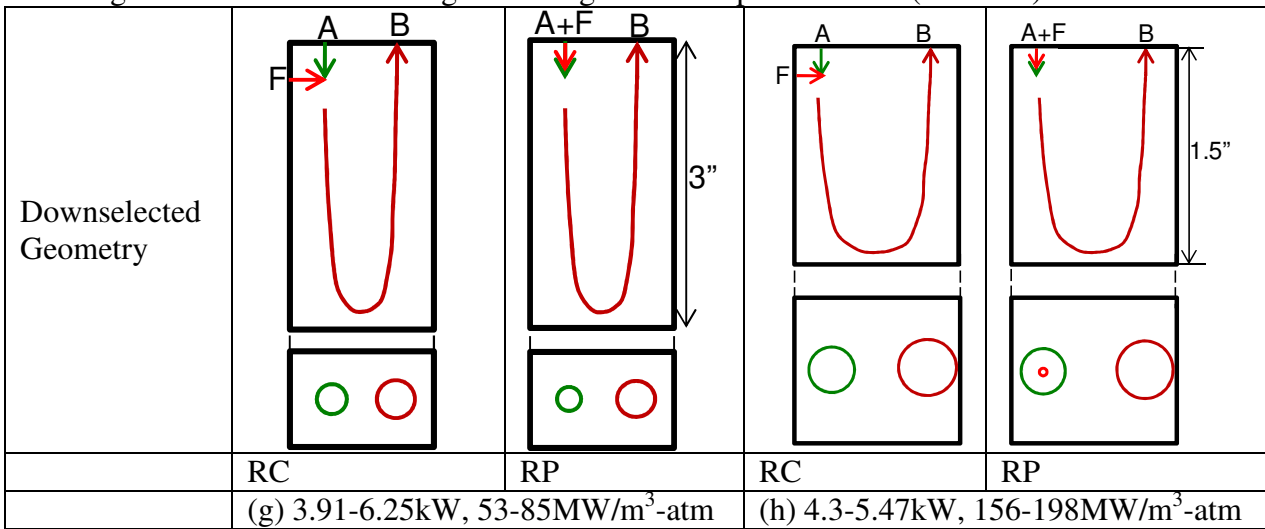


Figure 3.11 Combustor designs investigated in the present work (contd ...).

Chapter 4 Low Thermal Intensity ($5\text{MW}/\text{m}^3\text{-atm}$)

A low thermal intensity CDC combustor operating at $5\text{MW}/\text{m}^3\text{-atm}$ was designed by using numerical simulations. CFD was used to investigate the flowfield and gas recirculation characteristics inside the combustor and select appropriate parameters for combustor. The details of CFD simulations are not presented here and it could be found elsewhere [see ref C.1, Appendix A]. This chapter examines a total of nine flowfield configurations including eight different sample configurations to achieve CDC conditions with minimal pollutant formation and a baseline diffusion flame configuration. The eight CDC configurations include five forward flow and three reverse flow configurations operating in five non-premixed combustion modes and three premixed combustion modes. The diffusion flame mode was used for initial heating as well as start-up of the combustor which can be later transitioned to CDC mode of operation. The forward and reverse flow configurations include variations where the fuel injection is from the same side of air injection or opposite side of air injection. Initially, for all eight configurations same fuel and air injection diameters are used to examine the effect of flow field configuration on combustion characteristics. The effect of fuel and air injection diameter was investigated for one of the forward flow configurations which resulted in most desirable combustion characteristics. The results from the diffusion flame mode and the eight different configurations were compared for flowfield, fuel/air mixing and residence time characteristics using numerical simulations and with experiments using global pictures and exit emissions.

4.1 Experimental Setup (5MW/m³-atm)

The CDC test facility had optical quartz windows from three sides and the fourth side had ports for physical diagnostic probes and for ignition of the mixer in the enclosed combustion chamber, see Figure 4.1(a). The combustor was operated at a heat load of 25kW (with thermal intensity of 5MW/m³-atm) using methane as fuel. Both methane and air were injected at ambient temperature of 300K and the combustor operated at atmospheric pressure. The fuel injection velocity was 97m/s and the air injection velocity was 128m/s at equivalence ratio of 0.8.

The combustor was allowed to run for about 20minutes in each configuration before taking the experimental data. Gas analyzer was used to obtain the NO and CO emission level, see Appendix G for further details. The emission readings were observed to stabilize within 3minutes for change in experimental condition (here change in equivalence ratio for the same configuration). The experiments were repeated three times for each configuration and the uncertainty was estimated to be about ± 1 ppm for NO and $\pm 20\%$ for CO emissions. Digital camera with constant f-stop setting of 3.2 and shutter speed of 1/13s was used to acquire global flame images for all the configurations.

Figure 4.1 shows schematic diagrams of different configurations for the low thermal intensity CDC combustor. The experimental combustor has a square cross-section with aspect ratio (length/width) of 1.5 and the length of the combustor is 9inch. Fuel and air injection holes are on the diagonals of both top (see Figure 4.1(k)) and bottom side (see Figure 4.1(l)) of the chamber in the sets of four. The combustion product gas exits from the top side, see Figure 4.1(k). It can be noted that the relative

positioning, with respect to combustor centreline, of air and fuel injection ports on both top and bottom side is same. Different combinations of fuel and air injection can be used to examine the effect of flowfield configuration. In the present study a total of nine different configurations have been investigated including a diffusion mode and both non-premixed and premixed modes that show potential for operation in CDC condition.

In the first configuration, air is injected below the fuel injection location as shown in Figure 4.1(b). Due to jet expansion along the length of the pipe the air flow is more uniform at the inlet of the combustor. This is the baseline case of diffusion flame configuration (herein referred as “D”) and the flame is stabilized due to a weak recirculation region present in the combustor. The position of fuel injection for the configuration “D” is shown in Figure 4.1(l) and the positioning of the air injection ports at the pipe inlet is shown in Figure 4.1(m). This configuration is also used for start-up and initial heating of the combustor which later can be transitioned to other configurations. It may be noted that other eight configurations cannot be started directly and requires initial heating of the combustor to initiate combustion in these configurations.

Second configuration is a forward flow configuration wherein both air and fuel are injected from the bottom side of the combustor. In this configuration fuel is injected from the same side of air injection and is referred here as “FS1”, see Figure 4.1(c). In configuration “FS1” both air and fuel streams will entrain the product gases followed by the entrainment of fuel jet into the strong air jet and spontaneous ignition is expected to occur downstream after sufficient entrainment of burned gases. Fuel

stream is placed between the injected air and the recirculated gases to aid in better mixing with product gases and entrainment of fuel stream in the air jet. The direction of recirculated product gases is from the top side to the bottom side along the centreline of the combustor.

Third configuration is also a forward flow configuration wherein both air and fuel are injected from the bottom side of the combustor. The fuel is injected from the same side of air injection and is referred here as “FS2”, see Figure 4.1(d). In configuration “FS2” both air and fuel streams will entrain the product gases followed by the entrainment of fuel jet into the strong air jet and spontaneous ignition is expected to occur downstream after sufficient entrainment of burned gases. The difference between configuration “FS1” and “FS2” is in the positioning of air jet. In configuration “FS2” air jet is placed between the fuel jet and the combustor centreline whereas in configuration “FS1” air jet is placed between fuel jet and the corner of the combustor. The direction of recirculated product gases is from the top side to the bottom side along the corner of the combustor in configuration “FS2”.

In the fourth configuration air is injected from the bottom side and fuel is injected from the top side as shown in Figure 4.1(e). This configuration is also a forward flow configuration with fuel injection from the opposite side of air injection and here referred as configuration “FO”. The air injection ports are same as that as that of the air injection port for configuration “FS2”. This configuration enables a large separation between the air and fuel injection jets. The injected air first entrains the product gases and forms a high temperature and diluted oxidizer as it reaches the top

side where fuel is injected. Better mixing between air and product gases before meeting the fuel jet is expected in this configuration.

In the fifth configuration both air and fuel are premixed and injected from the bottom side and here it is referred as “FP1”. The fuel/air mixture injection port is same as that of the air injection port for configuration “FS1”, see Figure 4.1(f).

In sixth configuration also air and fuel is thoroughly mixed prior to injection from the bottom side of the combustor as shown in Figure 4.1(g). This configuration is labelled as “FP2”. The positioning of the fuel/air mixture injection port is same as the position of air injection port for configuration “FS2”. Premixed flow mode theoretically provides minimal hot spot regions and hence serves as baseline case for comparison with non-premixed mode for NO and CO emissions. As the reactions in non-premixed mode reaches closer to the distributed regime the NO emissions are expected to reduce towards the NO emission level for premixed flow mode.

Seventh configuration has both air and fuel injection port from the top side and combustor operates in reverse flow mode as shown in Figure 4.1(h). This configuration is labelled as “RS”. Both air and fuel jets are expected to entrain the product gases and further downstream the fuel jet will get entrained into the strong air jet. After sufficient entrainment of hot gases the mixture is expected to ignite spontaneously. The fuel jet is positioned in between air jet and the recirculating gas stream to aid in entrainment of fuel jet into the strong air jet.

In eighth configuration the fuel jet is positioned on the bottom side and air jet is positioned on the top side of the combustor as shown in Figure 4.1(i). This configuration enables large separation between air and fuel jet. The injected air first

entrains the product gases and forms a high temperature and diluted oxidizer as it reaches the bottom side where fuel is injected. Better mixing between air and product gases before meeting the fuel stream is expected in this configuration. This configuration is labelled here as “RO” suggesting that the configuration operates in reverse flow mode with fuel injected from the opposite side of the air injection.

Ninth configuration is reverse flow premixed configuration where both air and fuel are thoroughly mixing prior to injection in the combustor from top side of the combustor; see Figure 4.1(j). The air/fuel mixture injection port is located in the same position as that of the air injection port for configuration “RS” and “RO”. This premixed flow configuration is labelled here as “RP”.

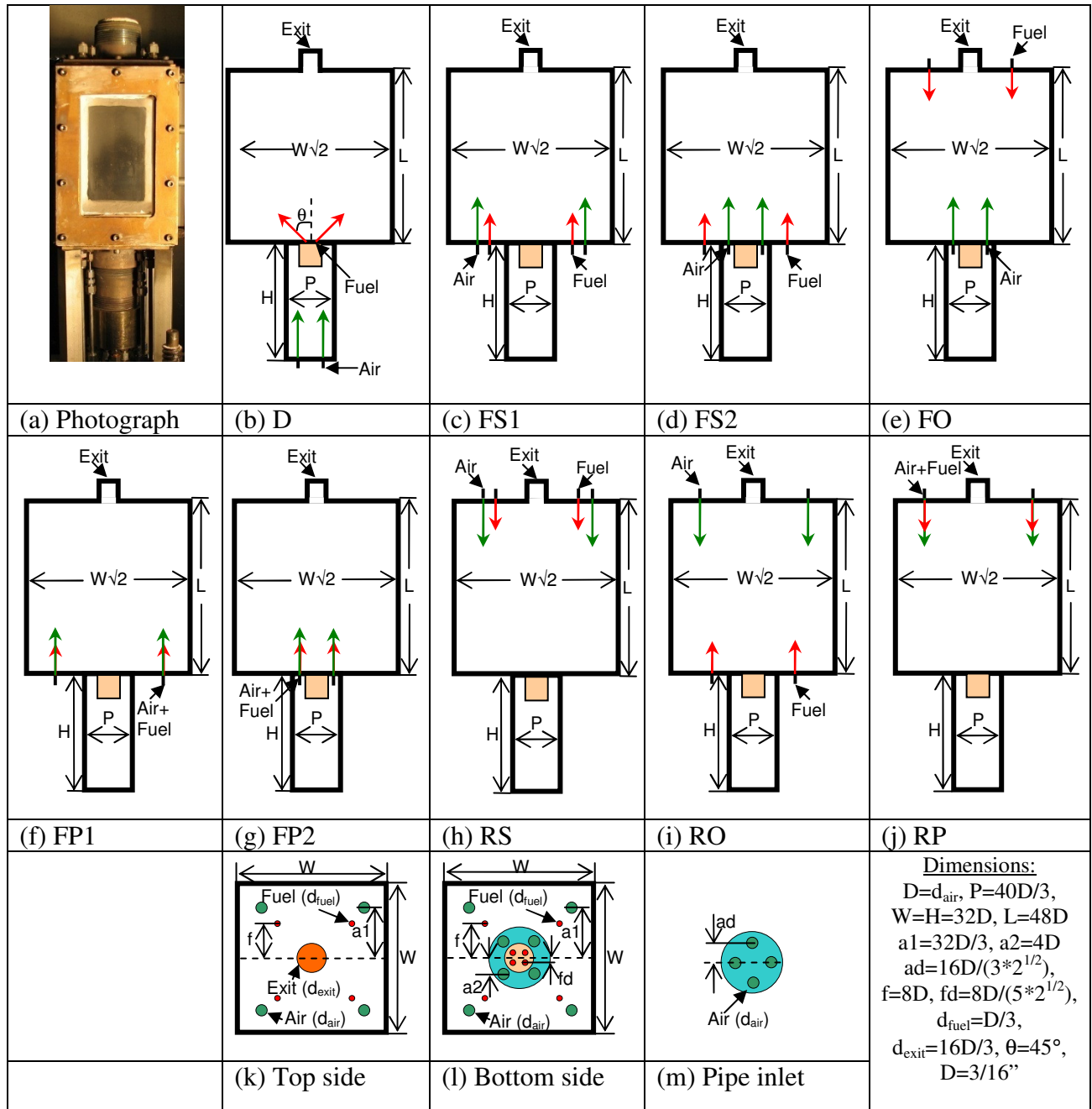


Figure 4.1 (a) Photograph and (b-m) schematics of different flow configurations for low thermal intensity ($5\text{MW}/\text{m}^3\text{-atm}$) CDC combustor.

4.2 Numerical Setup ($5\text{MW}/\text{m}^3\text{-atm}$)

The flowfield characteristics under non-reacting condition are examined for the nine configurations using numerical simulations. The mass flow rates of air and fuel (methane) corresponds to heat load of 25kW and equivalence ratio of 0.8. The

corresponding fuel injection velocity is 97m/s and air injection velocity is 128m/s. The temperature for both air and fuel jet is 300K and operating pressure is 1atm. Momentum ratio for the two jets (air/fuel) is 28 hence air jet is the dominant jet for the present case. For premixed combustion mode only air is considered as the fluid medium and corresponding air injection velocity is 128m/s. The compressibility effect is considered while obtaining the flow field solution as the Mach number of air injection is about 0.37 which is above the suggested limit of 0.3. The flowfield and species distribution is solved using a steady state, implicit, finite volume based solver. SIMPLE algorithm is used for pressure velocity coupling. Full hexahedral grid is used to minimize the grid size and appropriate refinement of grid is performed in the regions with higher gradients. Geometrical symmetry is used to reduce the computational time and only one-eighth of the geometry with grid size of about 0.5million cells was modeled. The grid used in present simulations is shown in Figure 4.2. Realizable k-e model with standard wall functions is used to model turbulence. Realizable k-e model has been shown to provide more accurate prediction of profile and spreading of non-reacting round jets [Shih, T., *et al.*, 1995]. Convergence is obtained when the residuals for all the variables are less than 1E-04. The centerline jet velocity profile obtained from the numerical solution was compared with the correlation for free jet given in equation 2.6 [Hussein, H. J., *et al.*, 1994].

The recirculation (rec.) ratio inside the combustor obtained from numerical simulation was compared with the correlation given in equation 2.1 [Ricou, F. P. and Spalding, D. B., 1961].

Carbon monoxide oxidation is a slow process; hence residence time has a significant effect on the CO emissions (see Figure 2.7(b)). Lower residence time is also expected to result in higher emission levels of unburned hydrocarbon (UHC) and lower combustion efficiency. Residence time distribution was obtained for the CDC combustor by using a tracer having same properties as that of air. After obtaining a steady state solution of flowfield, the tracer concentration at the air inlet was set to 1 at time = 0, and only tracer conservation equation was solved in a transient mode with time step size of 5ms. The tracer was tracked from the air injection location to simulate the presence of reaction zone near the air injection location for premixed mode of combustion. The tracer concentration at the outlet was monitored with respect to time. The residence time was obtained by equation 2.7.

The residence time profile obtained from numerical simulations is compared for the case of a perfectly stirred reactor. The exit tracer concentration profile with respect to time, for a perfectly stirred reactor corresponding to a step input of tracer at the inlet is given in equation 2.8. The residence time (t_{res}) for a perfectly stirred reactor is obtained by equation 2.5. Residence time frequency distribution for a perfectly stirred reactor is given by equation 2.9.

For all simulations commercial software FLUENT was used.

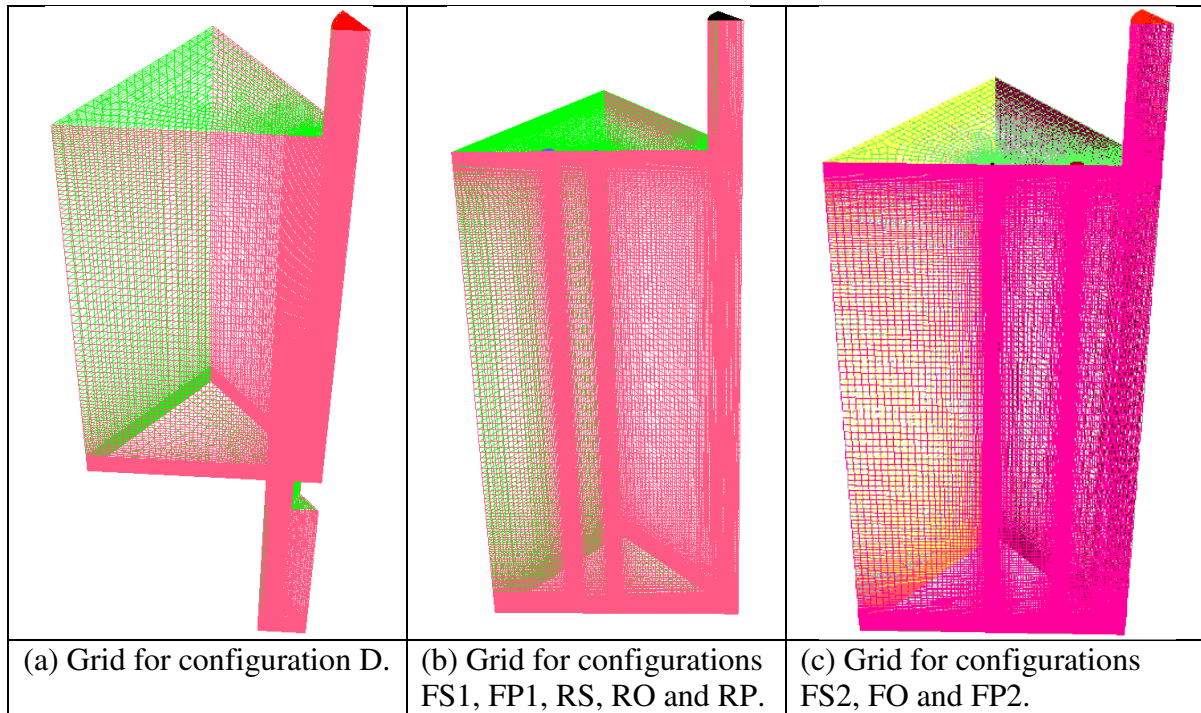


Figure 4.2 Grid used for numerical simulation for different flowfield configuration.

4.3 Results and Discussion

4.3.1 Flowfield Characteristics

Figure 4.3 shows velocity contour plots for the nine configurations investigated here. In the diffusion flame mode (see, Figure 4.3(a)) rapid air jet decay is observed due to confinement from the pipe. Uniform air flow is observed near the fuel injection location where fuel is injected at 45° angle. The flame is stabilized due to the fuel injector which acts as a bluff body. The recirculated hot product gases also aid in stabilization of the flame which recirculate inside the combustor.

Velocity contour plots for the forward flow modes are shown in Figure 4.3(b). Air jet decays along the length of the combustor and mostly complete decay is observed as the air jet reaches the top of combustor. Due to high momentum of air jet, the fuel jet entrains into the air jet for both configurations “FS1” and “FS2”. In configuration

“FS2” due to closeness of air jets to each other the air jets bend towards each other, which makes the product gases even more likely to escape earlier from the combustor. In opposed flow configuration “FO” the fuel jet is sheared due to the mixture of hot product gases and the air jet. In all the forward flow modes the fuel jet decay is fast suggesting better mixing. The velocity contour plots for the forward flow configuration in premixed flow mode (“FP1” and “FP2”) is shown in Figure 4.3(c), from the contour plots it can be observed that the absence of fuel jet does not affect the air jet profile significantly.

Figure 4.3(d) shows velocity contour plots for the reverse flow configurations “RS”, “RO” and “RP”. For configuration “RS” the fuel jet gets entrained into the air jet due to the presence of recirculated gases. For configuration “RO” the fuel jet decay is faster due to shearing because of recirculated gases.

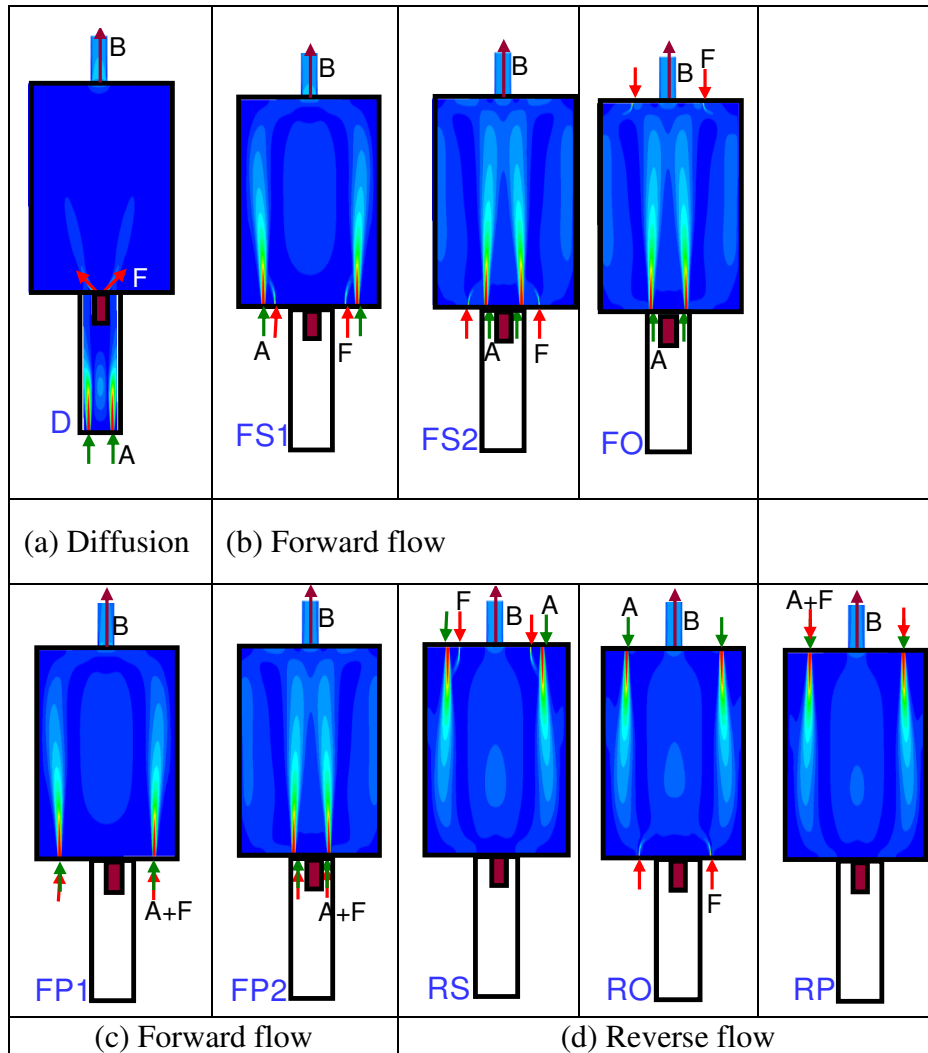


Figure 4.3 Velocity contour plots for different flowfield configurations.

4.3.2 Residence Time Characteristics and Pressure Loss

Residence time calculation for three premixed flow modes (“FP1”, “FP2” and “RP”) is shown in Figure 4.4. Figure 4.4(a) shows exit mass fraction profile of the tracer and Figure 4.4(b) shows the residence time frequency distribution. The average residence time for the three cases is 589ms for “FP1”, 588ms for “FP2”, 590ms for “RP” and 585ms for perfectly stirred reactor (psr). This suggests that the average residence time is very close to that calculated for a perfectly stirred reactor irrespective of the flow configuration. However as observed from the frequency

distribution plot, configuration “FP1” has the highest fraction of tracer particles having lowest residence time, whereas configuration “RP” has lowest fraction of tracer particles having low residence time. This means that fraction of gases having lower residence time can have significantly higher CO levels which can lead to overall high emission of CO in the exit gases (see Figure 2.7(b)). This could also be observed from early inception of tracer at the exit for configuration “FP2” as compared to configuration “RP”. Hence the residence time calculation suggests that the reverse flow configuration can result in lowest CO emissions.

Overall pressure loss for the cold flow condition was obtained for configurations “FP1”, “FP2” and “RP” from the CFD simulations based on equation 1.1. The pressure loss is shown in Figure 4.4(c). From the figure it may be noted that the pressure loss is about 8.5% and is independent on the flowfield configurations. The pressure loss calculated from simple calculations based on the inlet and outlet velocities is about 8.7% which is very close to the values obtained from the CFD simulations.

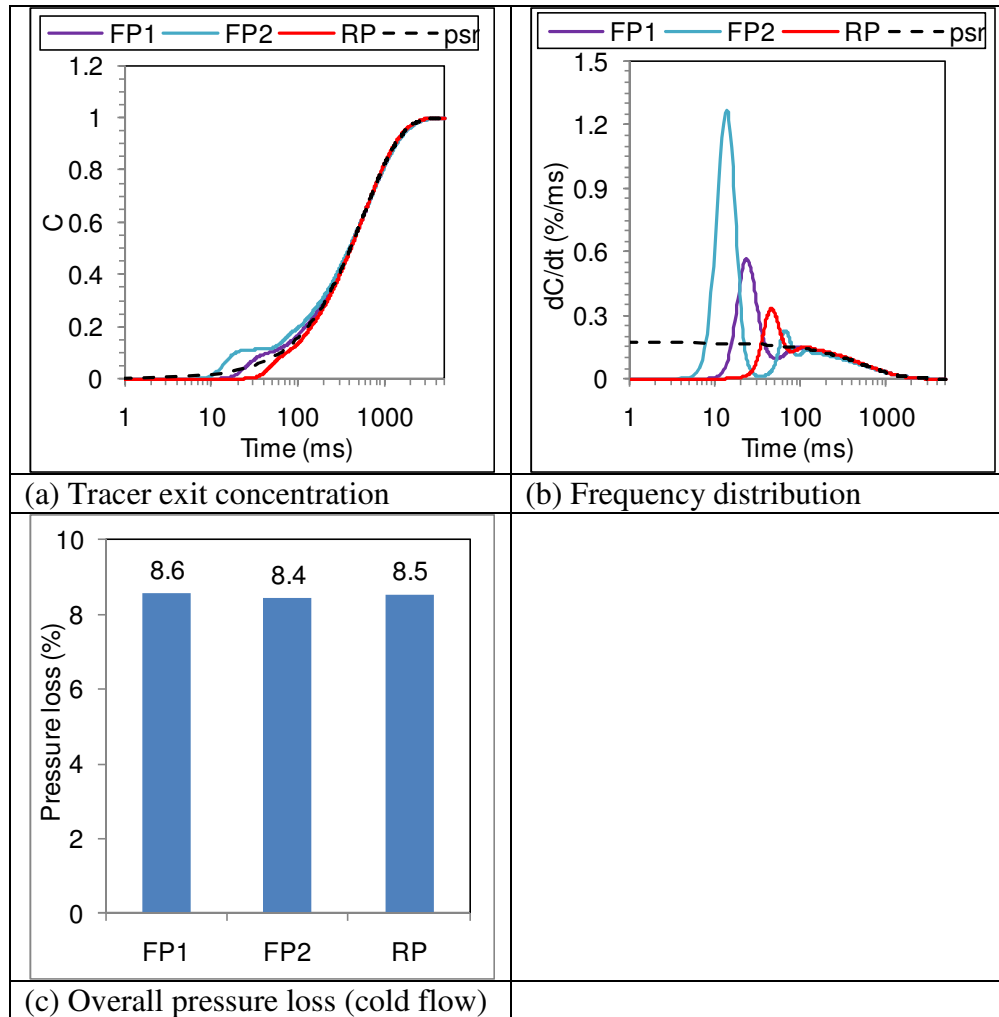


Figure 4.4 (a,b) Residence time characteristics and (c) pressure loss (cold flow) of different flowfield configurations.

4.3.3 Global Pictures

Global pictures of combustion zone operating in the nine configurations at equivalence ratio of 0.8 are shown in Figure 4.5. The combustor has optical access from three sides (quartz window size of $21.3D \times 34.7D$ for the combustor side of $32D \times 48D$). A black painted metal sheet is placed in the background to provide greater contrast, minimize the effect of light reflecting from the background, and enhance the flame visibility.

For configuration “D”, which is closer to a traditional diffusion flame mode, flame fronts can be observed and reaction zone is seen to be not distributed uniformly in the combustor. Both bluish (near fuel injection) and yellowish regions of the flame could be observed, see Figure 4.5(a). As the fuel is injected at an angle of 45° towards the four corners of the combustor, reaction zone is mostly confined towards the corners of the combustor and low light intensity region is present in the central region. As the fuel injection velocity is large (97m/s) the flame is not attached to the fuel injection ports and is stabilized due to the weak recirculation region present in the combustor.

For “FS1” configuration (see, Figure 4.5(b)) the reaction zone is observed to be uniformly distributed in the combustor. In this configuration, since both air and fuel are injected from bottom side of the combustor the reaction proceeds mostly along the length of the combustor towards the top side, which results in relatively high temperature product gases present near the top side of the combustor (also as seen from the higher glow from the combustor wall on the top side of the combustor).

For “FS2” configuration (see, Figure 4.5(c)) very low visible emissions could be observed and no distinct flame fronts could be identified suggesting more uniformly distributed reaction zone in the combustor. In this configuration, since both air and fuel are injected from the bottom side of the combustor the reaction proceeds mostly along the length of the combustor towards the top side, which results in relatively high temperature product gases present near the top side of the combustor (also as seen from the higher glow from the combustor wall on the top side of the combustor).

For “FO” configuration (see, Figure 4.5(d)) very low visible emissions could be observed and no distinct flame fronts could be identified suggesting more uniformly

distributed reaction zone in the combustor similar to that observed for configuration “FS2”. In this configuration, since air is injected from bottom side and fuel is injected from top side of the combustor the reaction zone is present near the top side, which results in relatively high temperature product gases present near top side of the combustor (also as seen from higher glow from the combustor wall on the top side of the combustor).

Both configurations “FP1” and “FP2” result in almost colorless reaction zone as observed from Figure 4.5(e) and (f). It may be noted that these configurations operate in premixed flow mode. Similar to configurations “FS1” and “FS2” the premixed flow modes also result in higher glow of combustor walls near the top side of the combustor.

Global pictures for configuration “RS” are presented in Figure 4.5(g). The lower portion of the combustor is observed to have very low light emissions. This may be due to absence of reaction zone in the lower portion of the combustor. At this condition the reaction zone is observed to be shifted towards one side of the combustor (right side), this may be reason for higher glow of the combustor wall on the right side of the combustor. This configuration was also observed to be unstable with distinct fluctuations of the reaction zone observed visually. In this configuration, though the reaction zone was not found to cover the complete combustion volume, distinct flame fronts were not observed as seen in the case of configuration “D”.

In “RO” configuration (see Figure 4.5(h)) very low visible emission is observed and the reaction zone is observed to be more uniformly distributed. Low emissions suggest that this flame can be called as colorless to name this as colorless distributed

combustion (CDC). It can also be observed that the glow of combustor wall is higher at the top side as compared to the bottom side; this is because near the top side of the combustor mostly product gases are present. With air injection from the top side the air stream entrains the product gases and relatively low temperature gas mixture (air and product gas) is present near the bottom side of the combustor. From bottom side fuel is injected which reacts with the oxidizer to form relatively high temperature product gases which turns towards the central region of combustor (away from the walls) and moves towards top side of the combustor.

Global pictures of premixed flow mode for reverse flow configuration “RP” is shown in Figure 4.5(i). The light intensity emitting from the combustor is higher as compared to forward flow premixed configurations “FP1” and “FP2”. Higher glow of combustor walls is observed near the bottom side of the combustor, this may be due to the reaction proceeding from top side towards bottom side of the combustor resulting in higher temperature gases present near the bottom side of the combustor.

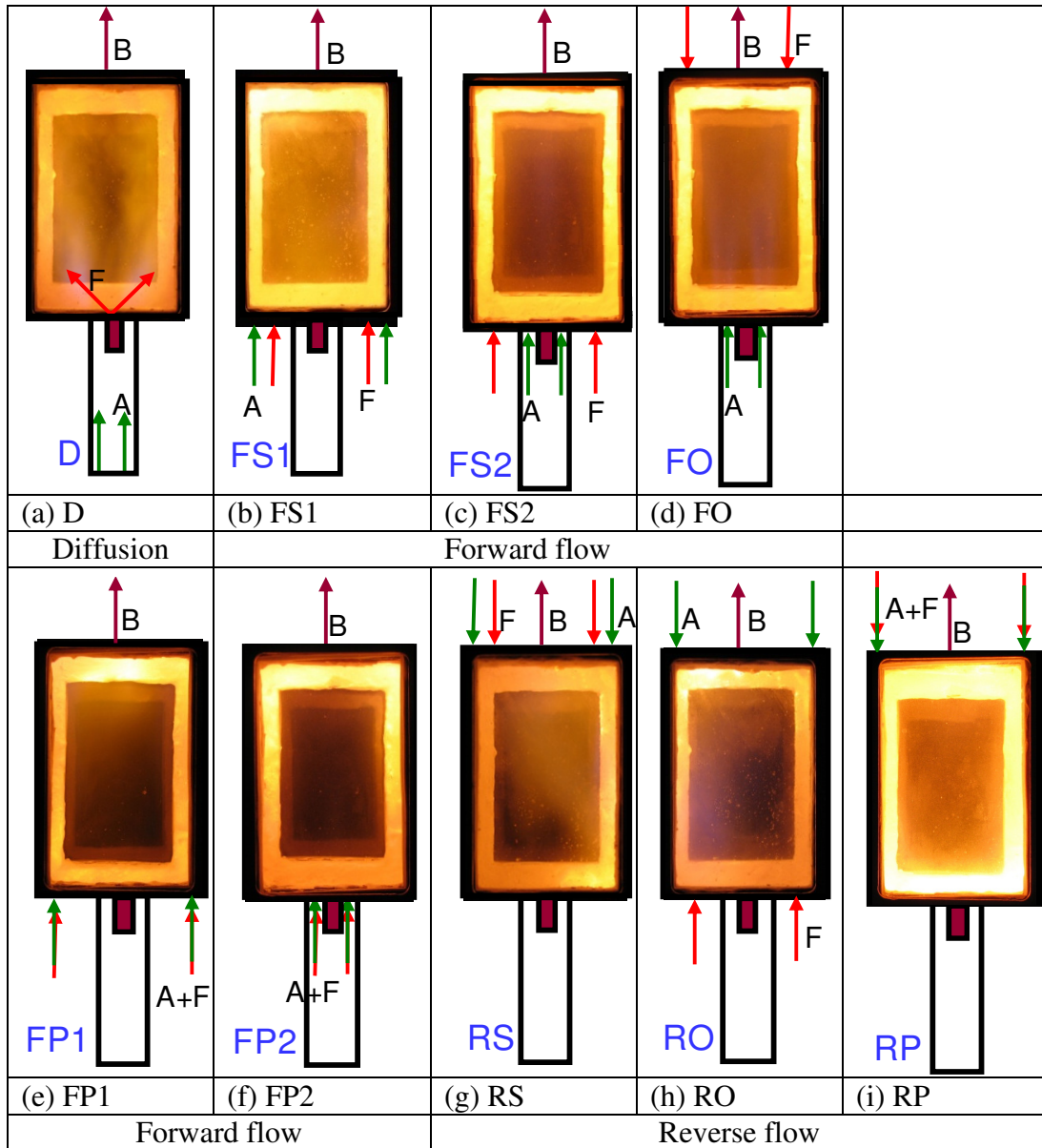


Figure 4.5 Global pictures for different flowfield configurations.

4.3.4 NO and CO Emissions

NO emission levels corrected to 15%O₂ in exit gases for the nine configurations at equivalence ratio of 0.8 are shown in Figure 4.6(a). NO is produced through two major reaction mechanisms for hydrocarbon flames, namely thermal (Zeldovich) and prompt (Fenimore) mechanism [Miller, J. A. and Bowman, C. T., 1989, Correa, S. M., 1992]. In thermal mechanism, NO is formed in high temperature zone and is the

major contributor to NO formed in the diffusion flames (see Figure 1.6). Prompt NO is formed in the reaction zone by rapid reaction of hydrocarbon radicals (CH) with molecular nitrogen [Miller, J. A. and Bowman, C. T., 1989]. At higher temperature zones ($T > 1850\text{K}$) thermal mechanism is the major contributor to the total NO formation; however, prompt mechanism can be important where the contribution from thermal NO is very small (for example in fuel rich flames, or in low temperature regions). The distributed reactions mostly suppress the formation of NO through thermal mechanism due to avoidance of high temperature regions.

In all the nine configurations very low NO levels are observed (mostly less than 10ppm). It may be noted that the configuration “D” is a lifted diffusion flame mode, instead of a traditional attached diffusion flame mode, because the velocity of fuel and air injection are very high ($\sim 100\text{ m/s}$) [Turns, S. R., 2000]. Hence fuel dilution with the product gases takes place before the ignition due to weak recirculation of product gases present, which reduces the high temperature reaction zones. Lower NO levels about 1ppm are observed especially for premixed configurations “FP1”, “FP2” and “RP”. This may be due to minimal hot spot regions present for the premixed flow mode as compared to the non-premixed flow modes due to uniform mixing of fuel and air prior to ignition. In non-premixed flow modes, configuration “FS2” resulted in very low NO level of about 3ppm followed by configuration “FO” and “FS1” producing about 6ppm and 7ppm of NO emissions respectively. Configurations “RO” and “RS” produced much higher NO emissions ($\sim 10\text{ppm}$).

Figure 4.6(b) shows the CO concentration levels corrected to 15%O₂ in the exit gases. It can be observed that the lifted diffusion flame (configuration “D”) produced

significantly higher CO levels (1074ppm) as compared to other configurations. This can be attributed to non-uniform mixing in configuration “D” (from regions of variable stoichiometry near the flame front) and more uniform reaction zone in other configurations. Configuration “FP2” also produced higher CO levels (663ppm), this may be due to lower residence time associated with configuration “FP2”. Reverse flow premixed mode configuration “RP” produced very low CO emission (5ppm), possibly due to more desirable residence time distribution in reverse flow configuration as compared to forward flow configuration as observed from Figure 4.4. The premixed flow configuration “FP1” resulted in low levels of CO emissions of about 35ppm. This is in accordance to the residence time available for these configurations as shown in Figure 4.4. In non-premixed mode, configuration “RO” and “FS1” produced lower CO emissions of about 35ppm. Configurations “FO”, “FS2” and “RS” produced intermediate levels of CO emissions (about 250ppm). Configuration “RS” was observed to be more unstable visually as compared to other configurations which may lead to non-uniform mixing and variable stoichiometry and this can also be the reason for higher CO emission in this configuration. Configuration “FO” and “FS2” produced higher CO emissions as compared to configuration “FS1” possibly due to smaller residence time (see Figure 4.4). Configuration “FO” and “FS2” have air injection location same as configuration “FP2” and configuration “FS1” has same air injection location as configuration “FP1”.

Hence, from NO and CO emission profile it could be noticed that reverse flow configuration produce lower level of CO emission possibly due to higher associated

residence time and configuration “RP” produced ultra low NO (1ppm) and CO(5ppm) emissions. In non-premixed mode configuration “FS1” produced low NO (7ppm) and CO(33ppm). This non-premixed configuration is investigated in further detail in the following sections. The effect of both air and fuel injection diameter is investigated for this configuration.

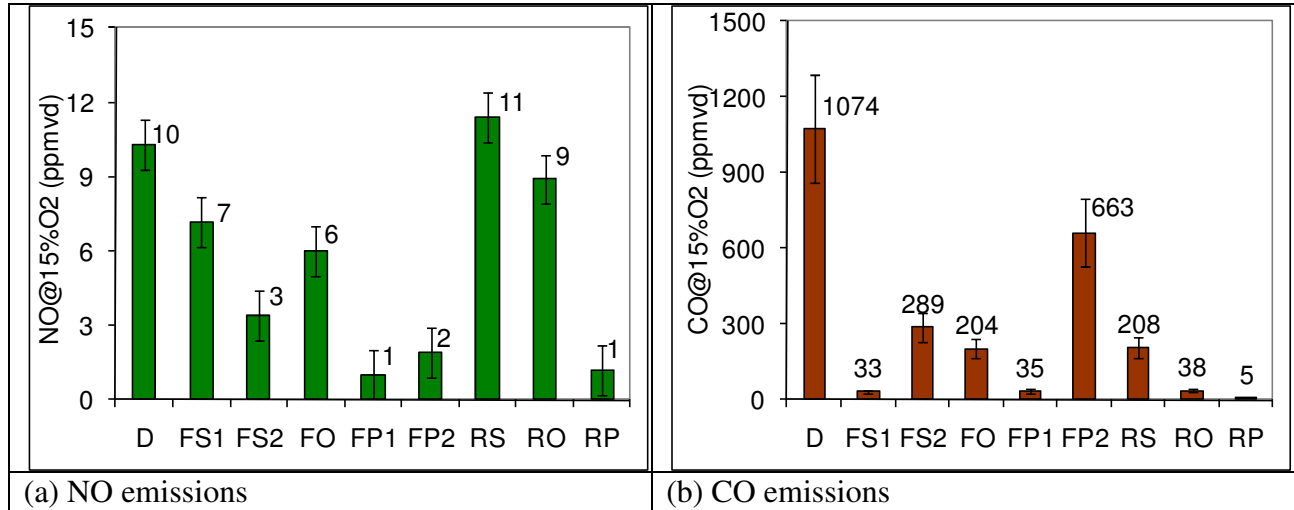


Figure 4.6 NO and CO emissions for different flowfield configurations.

4.4 Effect of Air and Fuel Injection Diameter (configuration “FS1”)

In the present study three air injection port sizes and three fuel injection port sizes have been investigated for configuration “FS1” (see Figure 4.1(c)). The positioning and distance between the air and fuel injection ports is the same for all cases. The experimental condition for the five cases under investigation is presented in Table 4.1. The case with smallest air ($d_{air}=D$) and fuel ($d_{fuel}=D/3$) injection port is considered as the baseline case and is used to examine the effect of air and fuel injection diameter by changing one parameter at an instance. It may be noted that air jet is the dominant jet as the momentum ratio variation of air/fuel jet over the range of conditions investigated here is 5-254. It may be noted that the turbulent mixing time (D/U) for air jet varies from 0.038ms to 0.463ms and for fuel jet it varies from

0.016ms to 0.433ms. The criteria as described by Kumar, S., 2005, to achieve distributed combustion was having turbulent mixing time of less than 0.086ms. Hence for the present case the effect of slower mixing will be examined on combustion characteristics.

Table 4.1 Different cases investigated for the effect of air and fuel injection diameter.

D=3/16''	d _{air}	d _{fuel}	Air inj. vel. (m/s)	Fuel inj. vel. (m/s)	Momentum ratio (air/fuel) ($\Phi=0.8$)	$\tau_{air}(ms)$ (D/U)	$\tau_{fuel}(ms)$ (D/U)
			$\Phi=0.8$				
Baseline case							
Case 1	D	D/3	128	97	28	0.038	0.016
Effect of fuel injection diameter							
Case 2	D	2D/3	128	24	112	0.038	0.132
Case 3	D	D	128	11	254	0.038	0.433
Effect of air injection diameter							
Case 4	5D/3	D/3	46	97	11	0.173	0.016
Case 5	7D/3	D/3	24	97	5	0.463	0.016

4.4.1 Numerical Results

Figure 4.7(a) shows the velocity contour plots along the diagonal plane (containing air and fuel injection ports) for the effect fuel injection diameter. It can be observed that for smaller fuel injection diameter (higher momentum of fuel jet) the fuel jet decay is delayed. The point of confluence of air and fuel jet shifts to downstream location with increase in momentum of fuel jet. The change in fuel injection diameter has minimal effect on the air jet characteristics as observed from Figure 4.7(a). Figure 4.7(b) shows velocity contour along the diagonal plane (containing the air and fuel injection ports) for effect of air injection diameter. It can be observed that for larger air injection diameter the point of confluence between air and fuel injection port shifts to the downstream location. This may be due to relatively weaker cross flow for the

case of larger air injection diameter which delays the decay of fuel jet [Grandmaison, E. W., *et al.*, 1998, Yimer, I., *et al.*, 2001, Han, D., *et al.*, 2000].

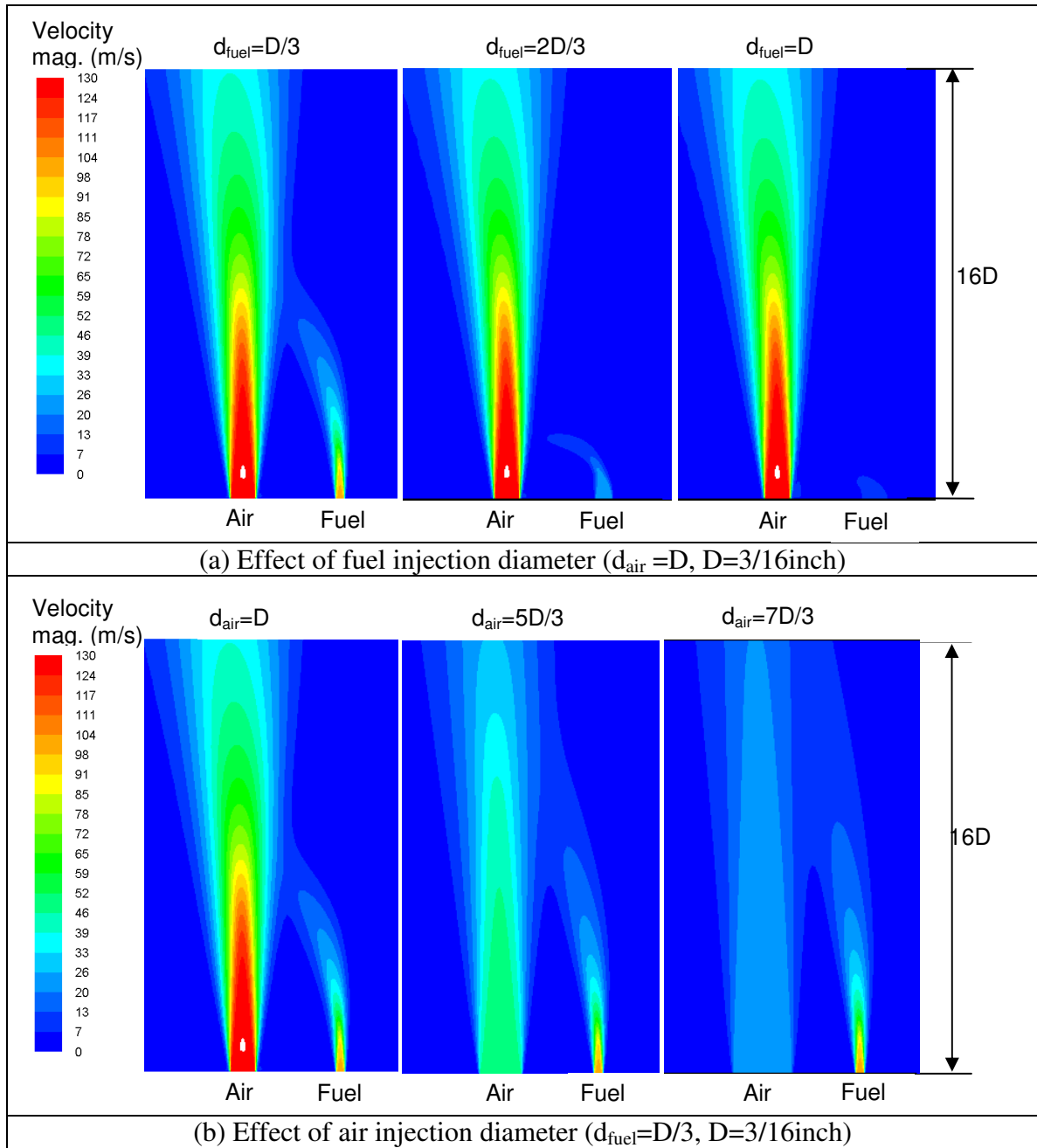


Figure 4.7 Velocity contours plots of configuration “FS1” for effect of air and fuel injection diameter.

The centerline velocity decay plot of air jet for different fuel injection diameters also reveals almost similar profiles of the air jet (see Figure 4.8(a)). It can also be

observed that the centerline velocity decay of air jet is faster as compared to a free jet (equation 2.6). The centerline velocity decay for the three air injection port diameters is shown in Figure 4.8(b). It can be observed that the centerline velocity decay is similar but faster as compared to the decay for a free jet (equation 2.6).

Pressure loss in cold flow condition is calculated based on equation 1.1 from the results of CFD simulations. The results are calculated for air inlet and the combustor exit and are presented in Figure 4.8(c,d). From the figure it can be observed that varying the fuel injection diameter had minimal effect on the overall pressure loss and this is expected as the fuel is low momentum jet which has minimal impact on the flowfield inside the combustor. However increasing the air injection diameter significantly decreases the overall pressure loss and only 0.4% pressure loss is encountered for air injection diameter of 7/16. Hence smaller air injection diameter will result in higher pressure loss but better turbulent mixing and these factors need to be considered while designing a combustor. It may be noted that the pressure loss obtained based on the inlet and exit velocities from equation 1.1 is 8.7%, 1.2% and 0.3% for air injection diameter of 3/16", 5/16" and 7/16" respectively. This suggests that the values obtained from CFD simulations is very close to the values based on simple calculations.

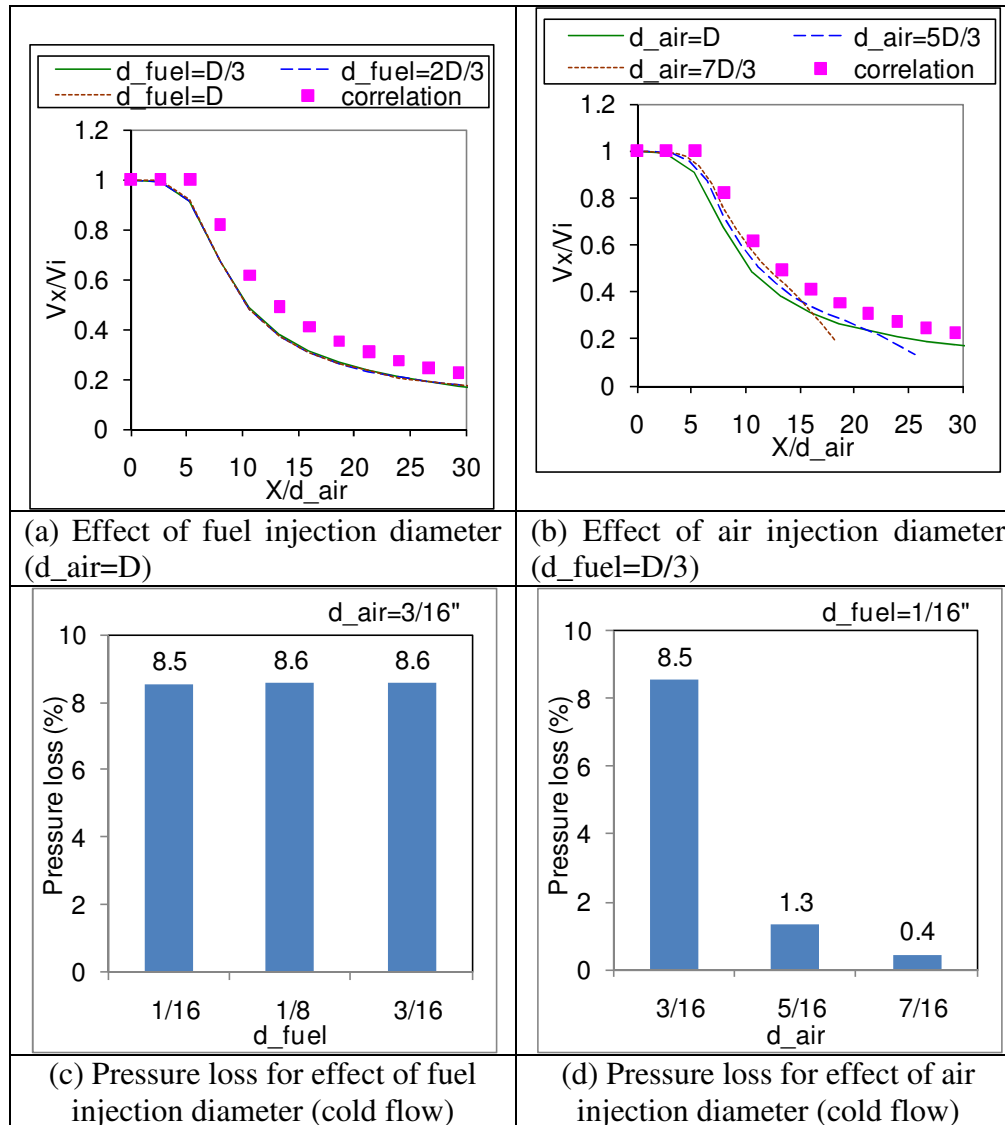


Figure 4.8 (a,b) Centerline velocity decay of air jet (X is distance along the air jet, $D=3/16$ inch) and (c,d) pressure loss for effect of air and fuel injection diameter.

The centerline methane mass fraction profile for the air jet is presented in Figure 4.9(a). It can be observed that early mixing between fuel and air jet is obtained for the case with lower fuel jet momentum (larger fuel injection diameter) (as also observed from the velocity contours of Figure 4.7(a)). However, the (air jet centerline) methane mass fraction profiles are similar for fuel injection diameter of $2D/3$ and D . The methane mass fraction profile along the centerline of air jet is presented in Figure 4.9(b). It can be observed that the centerline methane mass fraction profiles are

almost similar with increase in air injection diameter. Even though the fuel/air mixing is delayed with increase in air injection diameter (see, Figure 4.7(b)) the methane mass fraction profiles scaled with the air injection diameter reveals similar profiles.

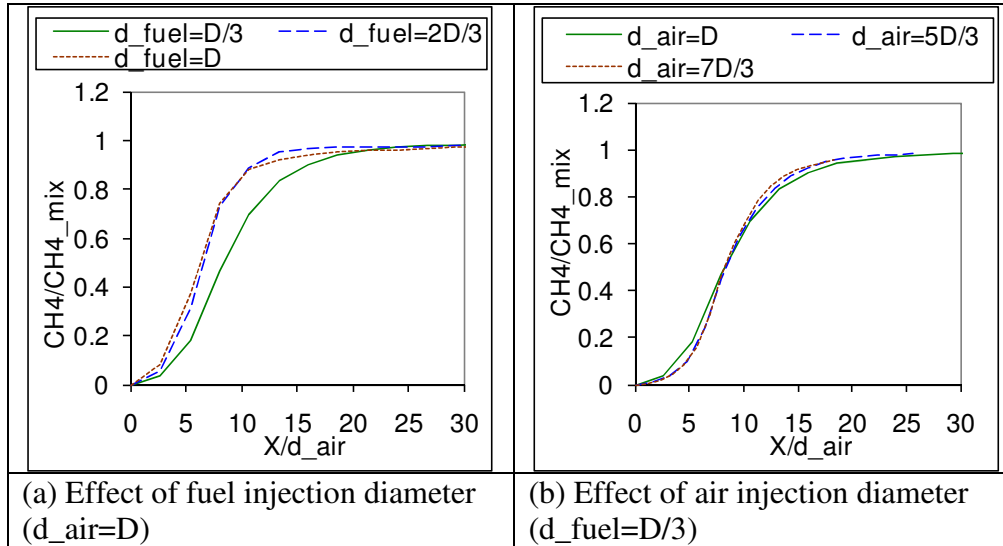


Figure 4.9 Centerline methane mass fraction variation for air jet (X is distance along the air jet, $CH4_{mix}=0.045$ for perfect mixing, $D=3/16$ inch) for effect of air and fuel injection diameter.

The centerline velocity decay and methane mass fraction profile along the fuel jet is presented in Figure 4.10(a), (b) and (c) for the effect of fuel injection diameter. It can be observed that for higher momentum of fuel jet the velocity and mass fraction profiles are closer to the corresponding velocity decay profile for free jets (equation 2.6). However, as the momentum of fuel jet is decreased (with increase in diameter) the jet decays rapidly as compared to the corresponding free jets. This implies that the cross flow (due to entrainment due to air jet) has significant effect on the decay of fuel jet at larger diameter. At larger diameter of fuel jet the methane mass fraction decay is more than the velocity decay. This may be due to higher velocity of the cross flow due to air jet.

The decay of velocity and methane mass fraction for the fuel jet is presented in Figure 4.10(a), (d) and (e) for the effect of air injection diameter. It can be observed that the velocity and methane mass fraction decay profiles are similar; however, the decay is higher as compared to the free jet (equation 3.6). As the air injection diameter is increased the velocity decay profile for the fuel jet moves closer the free jet decay profile. This may be due to relatively weaker cross flow present for the case with larger air injection diameter.

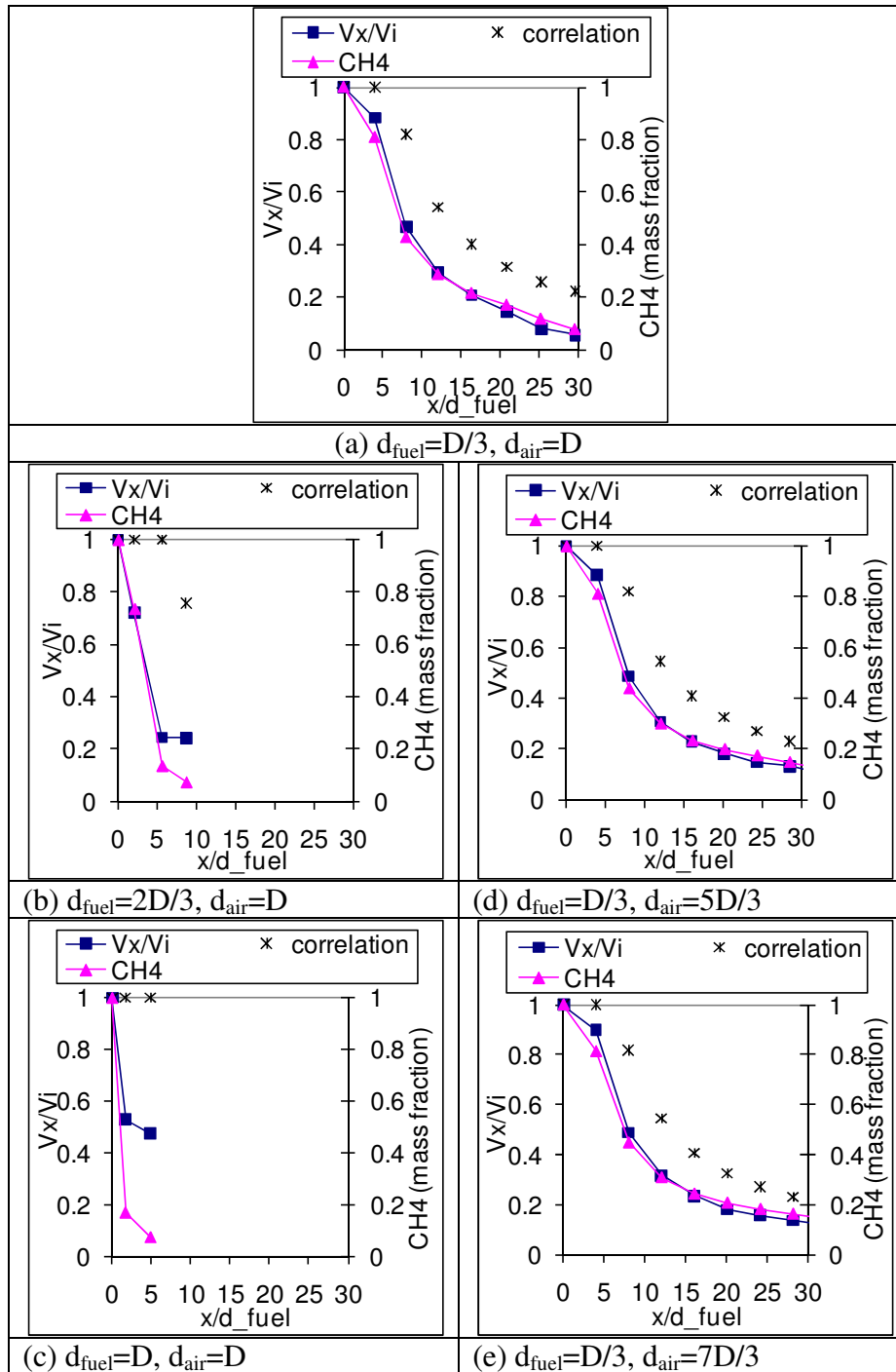


Figure 4.10 Centerline velocity and methane concentration decay for the fuel jet (x is distance along the fuel jet, $D=3/16$ inch) for effect of air and fuel injection diameter.

Figure 4.11(a) shows the recirculation ratio variation along the length of combustor for the effect of fuel injection diameter. It can be observed that the recirculation ratio profiles are very similar; this is due to the fact that the flowfield

inside the combustor is mostly governed by the air jet as the air jet is the dominant jet for the cases investigated here (see Table 4.1). The recirculation ratio increases along the length of combustor and reaches a maximum and then decreases. The initial recirculation ratio is higher than that of a free jet (equation 2.1); however, the maximum recirculation ratio is very close to that of a free jet at the same distance from injection.

Figure 4.11(b) shows the recirculation ratio variation along the length of the combustor for the effect of air injection diameter. It can be observed that the recirculation ratio is significantly lower for larger air injection diameter. It may be noted that maximum recirculation ratio for a specific air injection diameter is very close to the recirculation ratio for a free jet (equation 2.1) at the same distance, (see Figure 4.11(b)). It may be noted that higher recirculation ratio is desirable as it results in lower ignition delay time and favors spontaneous ignition of fuel to provide distributed reactions (equation 2.2). Moreover, the turbulent mixing for the smaller air injection diameter is better as compared to larger air injection diameter (equation 2.3, see Table 4.1). Hence, it is expected that the case with smaller air injection diameter will result in more distributed reactions and lesser hot spot regions.

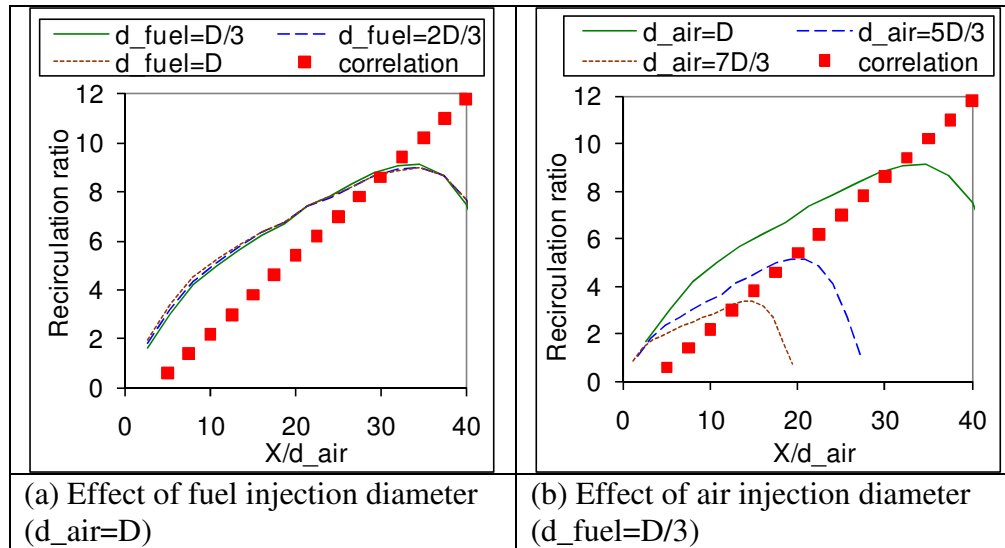


Figure 4.11 Recirculation ratio variation for air jet (X is distance along the air jet, $D=3/16$ inch) for effect of air and fuel injection diameter.

4.4.2 Experimental Results

Figure 4.12 shows the emissions of nitric oxide (NO) and carbon monoxide (CO) with change in fuel and air injection diameter. Changing fuel injection diameter has minimal effect on NO emission (see Figure 4.12(a)); however, small increase in CO emissions was observed with increase in fuel injection diameter (see Figure 4.12(b)). It may be noted that for larger fuel injection diameter the fuel jet mixes earlier with the air jet (see Figure 4.7(a) and 4.9(a)). The ignition of fuel/air mixture will take place after sufficient amount of product gases are entrained and the mixture temperature rises above the auto-ignition temperature. Hence, for the present case it is possible that the fuel/air mixing is sufficiently faster before the ignition of fuel occurs. With increase in air injection diameter the turbulent mixing time is significantly reduced (equation 2.3, see Table 4.1) which may lead to variable stoichiometry and more hot-spot regions to result in higher NO [Miller, J. A. and Bowman, C. T., 1989] and CO levels. Hence for the present case both NO and CO emission levels are significantly higher with increase in air injection diameter. For all

cases CO level increases significantly with increase in equivalence ratio. This is due to lack of availability of oxygen as well as dissociation of CO_2 at high temperatures at higher equivalence ratio [Turns, S. R., 2000]. The NO levels for non-premixed operation (case 1-5, Table 4.1) are almost constant with increase in equivalence ratio. It may be noted that in non-premixed combustion reaction takes place at an overall equivalence ratio which is higher (close to stoichiometry) than the inlet equivalence ratio. Hence if the reaction zone is stabilized at similar equivalence ratio the NO level will be almost similar with increase in inlet equivalence ratio (see Figure 4.12(a),(c)).

From the investigation of the effect of fuel and air injection diameter it can be noted that the smallest air (D) and fuel (D/3) injection diameter resulted in lowest level of NO and CO emissions and present favourable conditions to achieve CDC flames. Hence, for further investigation of higher heat release intensity combustor air injection diameter of D and fuel injection diameter of D/3 shows potential to reduce the pollutant emissions.

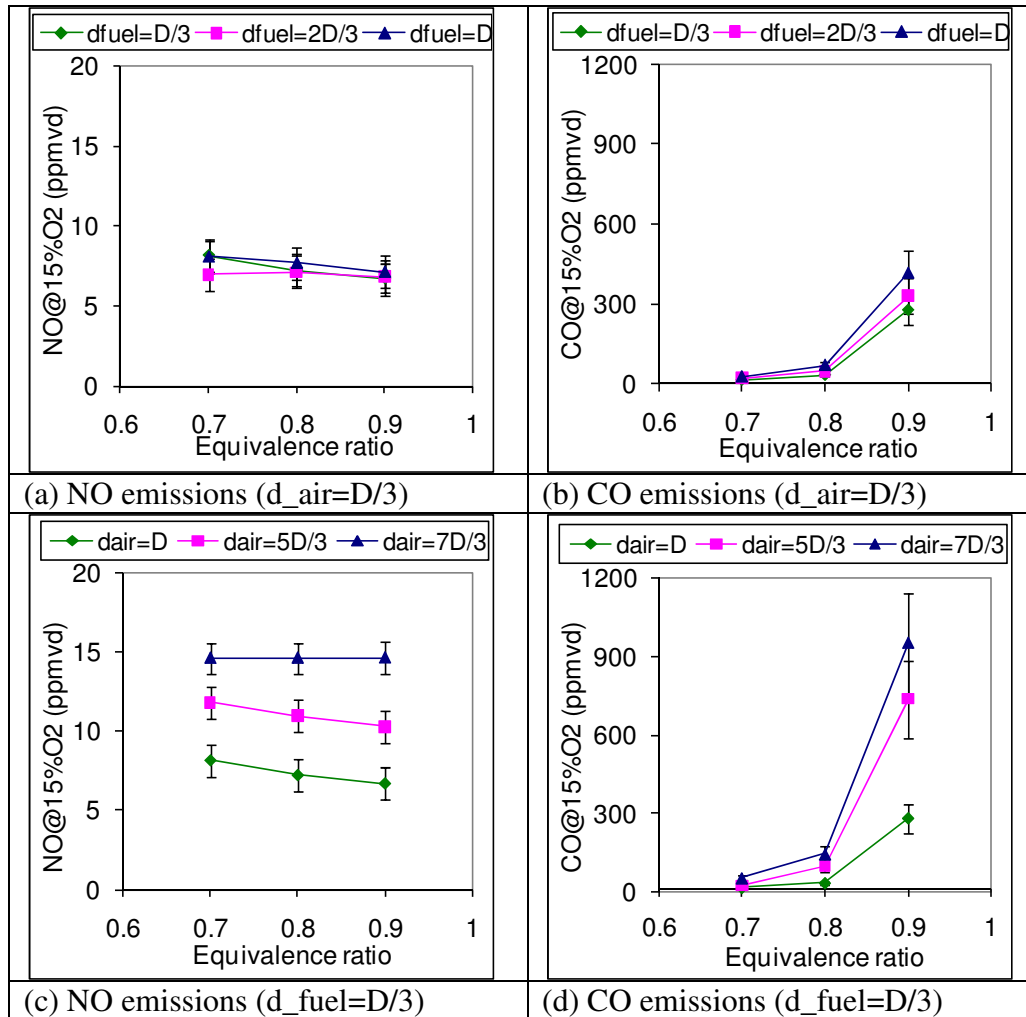


Figure 4.12 NO and CO emissions for effect of fuel and air injection diameter.

4.4 Conclusions

Eight different flowfield configurations have been examined here with specific focus on flowfield and fuel/air mixing using numerical simulations and experimental studies. The flow field configurations were observed to have minimal effect on the dominant air jet and pressure loss across the chamber; however it had significant effect on the fuel jet characteristics as well as the fuel/air mixing. Premixed flow modes (“RP”, “FP1” and “FP2”) resulted in ultra low NO emission level of only about 1ppm at $\Phi=0.8$. The CO emission level for the reverse flow configuration in premixed mode (“RP”) was only 5ppm at $\Phi=0.8$, this may be due to more favourable

residence time characteristics in reverse flow configuration. Amongst the non-premixed flow configurations, configuration “FS1” resulted in low NO (7ppm, $\Phi=0.8$) and CO (33ppm, $\Phi=0.8$) emissions and this configuration may be advantageous for practical use in the combustors.

Configuration “FS1” which was observed to provide favorable results was further investigated for the effect of fuel and air injection diameter both numerically and experimentally. In numerical investigation it was observed that the larger fuel injection diameter results in faster mixing between air and the fuel jet. However, almost similar NO and slightly higher CO levels were observed with increase in fuel injection diameter. With increase in air injection diameter the mixing between the air and fuel jet reveals similar profile but significantly lower gas recirculation was observed. The pressure loss across the chamber was significantly reduced with increase in air injection diameter. For smaller air injection diameter faster turbulence mixing is expected to result in favorable emission characteristics and both NO and CO emissions were observed to decrease with decrease in air injection diameter. Operation at higher thermal intensity for configuration “FS1” will be investigated in the next chapter.

Chapter 5 Medium Thermal Intensity (20-40MW/m³-atm)

Investigation at higher thermal intensity was performed by reducing the combustor volume for forward flow configuration “FS1”. Air and fuel injection scheme similar to configuration “FS1” that was presented in Chapter 4 was used for three different combustor volumes resulting in thermal intensity of 20, 30 and 40MW/m³-atm. In next part of the investigation a simpler and smaller combustor was designed and tested consisting of single air and fuel injection ports operating at thermal intensity of 28MW/m³-atm. The smaller combustor was investigated for both forward and reverse flow configurations with different fuel injection locations in both non-premixed and premixed flow modes. Numerical investigation was performed to obtain the flow field and residence time characteristics and experimental investigation was performed to obtain the exhaust emissions, reaction zone location by OH* chemiluminescence imaging as well as global imaging.

5.1 Experimental and Numerical Setup (20, 30 and 40MW/m³-atm)

Figure 5.1 shows a schematic of forward flow configuration of CDC combustor used for investigation with smaller confinement sizes resulting in higher thermal intensities in range of 20–40MW/m³-atm. It may be noted this configuration is similar to configuration “FS1” investigated at lower thermal intensity of 5MW/m³-atm in Chapter 4 (see Figure 4.1(c)). In both cases air jets are adjacent to the combustor wall and fuel is injected between the air jet and centerline of the combustor. The gases are expected to recirculate downwards along the combustor centerline thus aiding in entrainment of the fuel jet and to move along the length of the combustor adjacent to the combustor wall for both low and high intensity combustor. The difference

between low and high thermal intensity combustor is in the fuel injection angle and location; in low intensity combustor (see Figure 4.1(c)) the fuel is injected normal to the bottom side and fuel injection location is in the plane of air injection and combustor centerline. However, for high intensity combustor the fuel is injected at an angle of 45° with respect to combustor centerline towards the combustor walls and the fuel injection location is in the vertical plane in between the two air injection ports. This means that direct mixing between the air and fuel jet is avoided to promote reactions that favors CDC mode [Gupta, A. K., *et al.*, 2003].

The combustor comprises of quartz tube with fuel and air injection ports at the base of the tube. Three different sizes of quartz tubes are examined to determine the effect of confinement and resulting thermal intensities of 20, 30 and $40\text{MW/m}^3\text{-atm}$. Initially combustor is started in diffusion flame mode and later transitioned to the CDC mode. In diffusion flame mode air is injected upstream of the fuel injection location as shown in Figure 5.1(a). In the non-premixed CDC mode air is supplied with four jets adjacent to the fuel injection ports. The location of fuel and air injection ports is at the base of quartz tube (see Figure 5.1(b)). In premixed CDC mode (see Figure 5.1(c)) air and fuel are mixed at an upstream location and injected at the base of the quartz tube. In both non-premixed and premixed modes the flame is stabilized due to the presence of favorable recirculation of product gases inside the quartz tube. The mass flowrates of air and fuel (methane) correspond to heat load of 25kW (for the range of thermal intensities investigated here). The inlet temperature for both air and fuel jet is 300K and operating pressure is 1 atm.

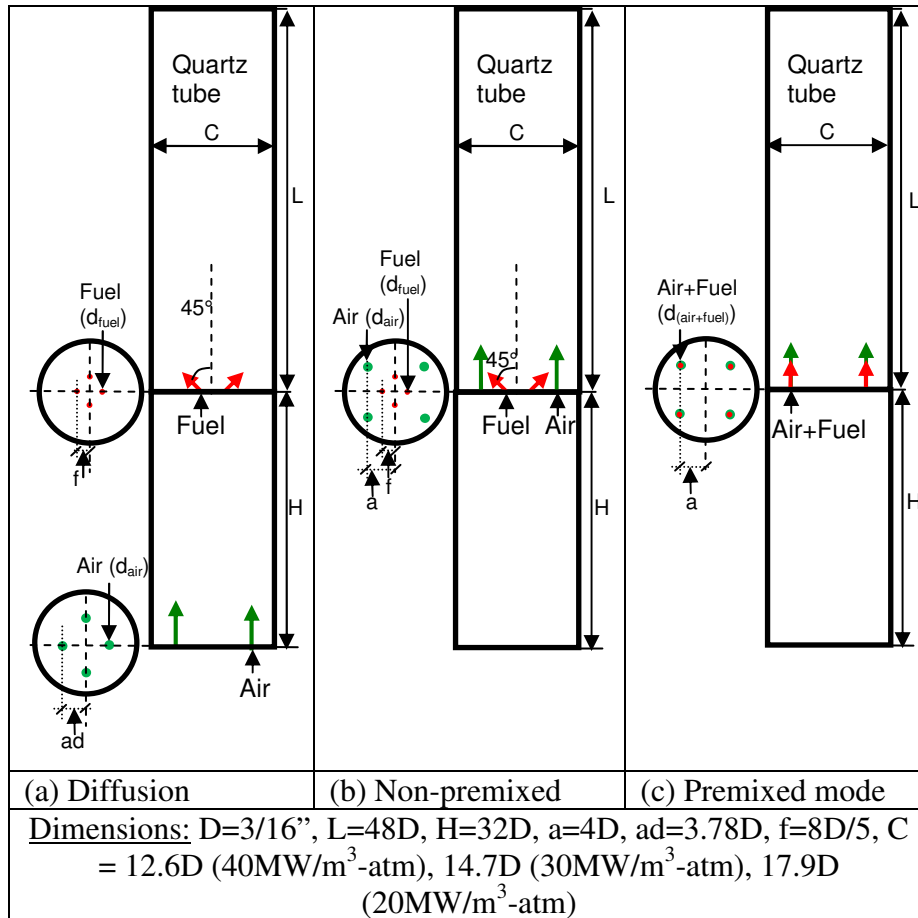


Figure 5.1 Schematic diagrams of medium thermal intensity ($20, 30$ & $40\text{MW/m}^3\text{-atm}$) CDC combustor.

The combustor was allowed to run for about 10 minutes in each configuration before taking the experimental data. Gas analyzer was used to obtain the NO and CO emission level, see Appendix G for further details. The emission readings were observed to stabilize within 3 minutes for all changes in experimental condition (for example, change in equivalence ratio for the same configuration). The experiments were repeated three times for each configuration and the uncertainty was estimated to be about ± 0.5 ppm for NO and $\pm 10\%$ for CO emissions. Digital camera was used to record the global flame images with f-stop setting of 2.7 and at a shutter speed of $1/8\text{s}$ for all the configurations.

The flowfield, jet profile, fuel/air mixing and gas recirculation under non-reacting condition is examined for the non-premixed cases using numerical simulations. The flow rates correspond to heat load of 25kW and equivalence ratio of 0.8. This equivalence ratio represents high power settings of gas turbine combustor operation. The flowfield and species distribution is solved using a steady state, implicit, finite volume based method. SIMPLE algorithm is used for pressure velocity coupling. Compressibility effects are included in the investigation as the air injection velocity was about 128m/s corresponding to Mach number of about 0.37. Fuel injection velocity was about 97m/s Full hexahedral grid is used to minimize the grid size and appropriate refinement of grid is performed in the regions with higher gradients. Geometrical symmetry is used to reduce the computational time and only one-eighth of the geometry was modeled. Realizable k-e model with standard wall functions is used to model turbulence. Convergence is obtained when the residuals for all the variables are less than 1E-04. The centerline jet velocity profile obtained from the numerical solution is compared with the correlation given in equation 2.6 for free jet. The recirculation ratio inside the combustor obtained from numerical simulation was compared with the correlation given in equation 2.1 for entrainment in a free jet.

For all simulations commercial software FLUENT is used.

5.2 Results and Discussion

Figure 5.2 shows grid used for numerical simulation and the velocity contour and pathline plots in the plane containing air injection port for the effect of confinement size. For smallest confinement size (thermal intensity of 40MW/m³-atm) the air injection port is closer to the combustor walls (see Figure 5.2(b)) and jet is observed

to be present along the combustor wall. For thermal intensity of $30\text{MW/m}^3\text{-atm}$ the air jet is observed to deflect towards the combustor walls and the jet decay is earlier (see Figure 5.2(c)) as compared to the case with thermal intensity of $40\text{MW/m}^3\text{-atm}$. For larger confinement sizes (lower thermal intensity of $20\text{MW/m}^3\text{-atm}$) the location of jet is away from the combustor wall and the jet is observed to decay faster (see Figure 5.2(d)) as compared to the other two confinement sizes that provided higher thermal intensity.

To gain insight on the flowfield and recirculation of gases inside the combustor mass-less particles, injected from the air injection port, are tracked (pathlines). Mass-less particles follow the gaseous medium exactly as there is no drag and inertia forces associated with the particles. The pathline plots for the three heat release intensity are presented in Figure 5.2(e-g). For this figure, 14 pathlines are presented for the sake of illustration. It can be observed that for smallest confinement size ($40\text{MW/m}^3\text{-atm}$) a long recirculation region is present along the centreline of the combustor. For the largest confinement size ($20\text{MW/m}^3\text{-atm}$) the recirculation region is smaller as compared to the other two confinement sizes. For the largest confinement size the recirculation of gases are from both sides of the jet (along the centreline and near the wall, see Figure 5.2(g)).

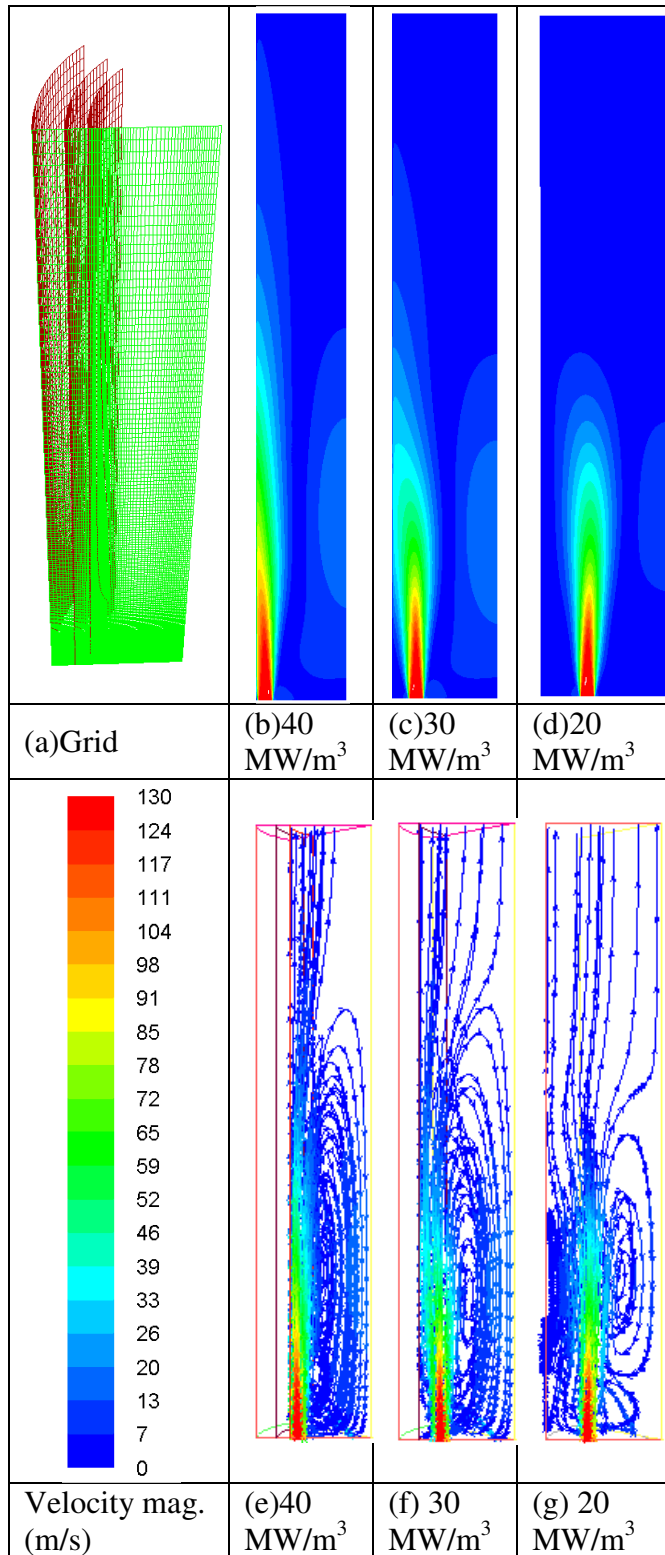


Figure 5.2 (a) Grid (b-d) Velocity contour plots and (e-g) pathline (14 pathlines) plots for three thermal intensity cases.

Figure 5.3(a) shows the centerline velocity decay of air jet and Figure 5.3(b) shows the recirculation ratio variation for the three confinement sizes. The velocity decay for smaller confinement size (higher thermal intensity) is delayed as compared to the case with larger confinement size (see Figure 5.3(a)). This is similar to that observed from the velocity contour plots (see Figure 5.2(b)). It can be observed that the velocity decay is larger as compared to that of a free jet. The relatively smaller velocity decay for smaller confinement size may be due to the vicinity of the combustor wall to the air jet. It may be noted that this is contrary to that observed in Figure 2.9(a) where smaller confinement volume (higher thermal intensity) resulted in faster decay of air jet. This further suggests that careful investigation is required while designing CDC combustor.

Recirculation of product gases and mixing with the combustion air is desired for increasing the temperature (and reducing oxygen concentration) of the oxidizer and promote spontaneous ignition of the fuel [Gupta, A. K., *et al.*, 2003]. It can be observed from Figure 5.3(b) that the recirculation ratio is significantly affected by the confinement size. For smaller confinement size the recirculation ratio is smaller as compared to larger confinement size. This is similar to the observation made from figure 2.9(b) where the recirculation ratio reduced significantly with higher thermal intensity. Maximum recirculation ratio for largest confinement size ($20\text{MW/m}^3\text{-atm}$) is about 2.7 as compared to recirculation ratio of 1.6 for smallest confinement size ($40\text{MW/m}^3\text{atm}$). Smaller recirculation ratio will lead to lower increase in the temperature of oxidizer (see Figure 2.4(a)) and may adversely affect the stabilization of the reaction zone. The recirculation ratio will also change the local oxygen

concentration that will impact the local temperature and the subsequent NO_x production.

Overall pressure loss is calculated from CFD simulation results based on equation 1.1 and is presented in Figure 5.3(c). From the figure it can be noted that the overall pressure loss is independent of thermal intensity (confinement volume). The pressure loss calculated based on the inlet and exit velocity is 8.7% and this value is very close to the value obtained from the CFD simulations.

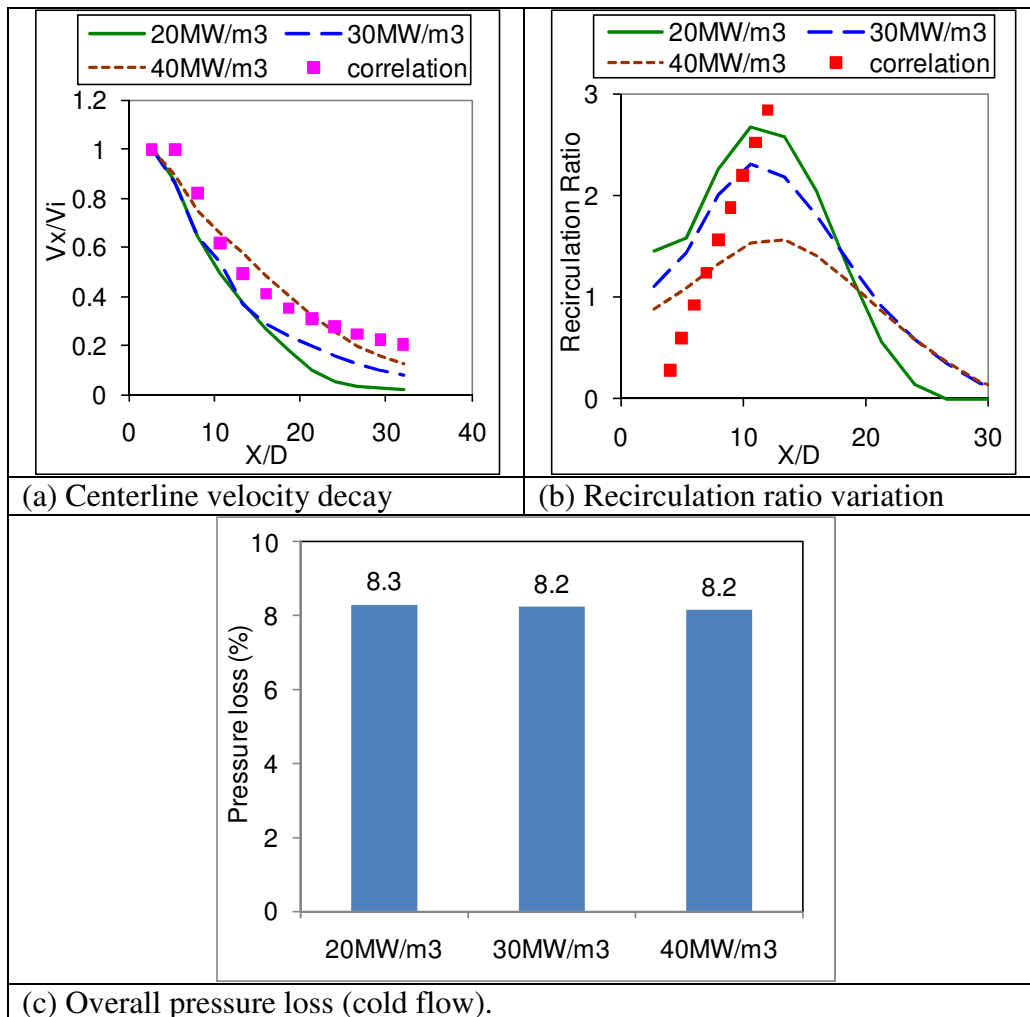


Figure 5.3 (a) Centerline velocity decay, (b) Recirculation ratio variation and (c) overall pressure loss for the three thermal intensity cases.

Figure 5.4(a-c) shows the global flame photographs for diffusion flame for the three confinement sizes at overall equivalence ratio of 0.7. Diffusion flame was used for the combustor startup which was later used to transition to other combustion modes. It may be noted from the Figure that the diffusion flames are not confined inside the combustion volume and very long flames could be observed for all the three confinement sizes. This suggests that the combustor does not operate at high thermal intensity as the reaction zone is not limited to the combustion volume.

Figure 5.4(d-f) shows non-premixed CDC flames at equivalence ratio of 0.7. For all three confinement sizes it can be observed that the flames are contained inside the quartz tube and all the heat is released inside the confinement resulting in thermal intensity in range of 20–40MW/m³-atm. For all three confinement sizes two distinct reaction zones are observed which are oblong in shape along the length of the combustor. This may be due to the reaction zone stabilizing along the air jet periphery instead of stabilizing near the fuel injection location. This reveals that further improvements must be made with distributed reactant preparation. The mixture of recirculated product gas, air and fuel, prompt ignition after achievable entrainment of product gases. Only two reaction zones are visible due to overlap of air jets along the line of sight. The results also show that the reaction zone is longer for smaller confinement size (40MW/m³-atm) as compared to larger confinement size (20MW/m³-atm). This may be due to longer recirculation region as well as delayed decay of the air jet for higher thermal intensity case as shown in Figure 5.2 and 5.3.

Figure 5.4(g-i) shows the flame photographs of premixed CDC flames. For all the three thermal intensities the flames are confined inside the quartz tube. As compared

to the non-premixed CDC flames, the flames in premixed modes are lifted and are stabilized some distance downstream. In this case also the flames at higher thermal intensity ($40\text{MW/m}^3\text{-atm}$) are longer as compared to the flames for low thermal intensity ($20\text{MW/m}^3\text{-atm}$). In premixed flame mode the flames are stabilized due to recirculated product gases as well as reduction of velocity of the gas mixture due to expansion of air jet. The reduction of velocity helps to reduce the entrainment of gases into the reactant gas mixture.

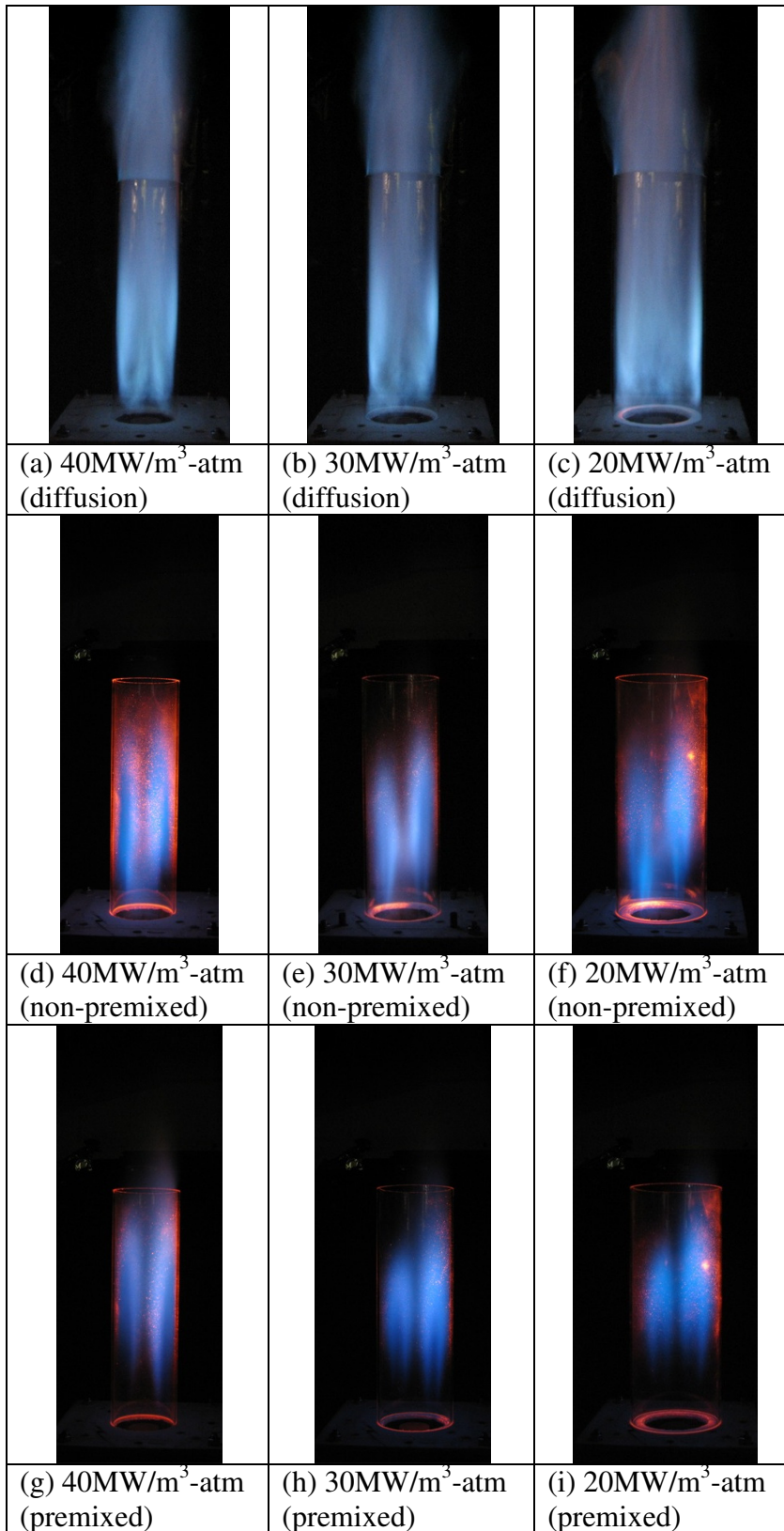


Figure 5.4 Global pictures for (a-c) Diffusion, (d-f) non-premixed CDC and (g-i) premixed CDC for the three thermal intensity cases.

Figure 5.5 shows the emission of NO and CO from non-premixed CDC flames as affected by the variation of equivalence ratio from 0.5–0.7. Avoidance of high temperature zone results in reduction of NO formation due to thermal mechanism in CDC flames. Figure 5.5(a) shows that NO increase with increase in equivalence ratio and very low level of NO (5ppm) is observed at equivalence ratio of 0.5. Higher NO levels are observed with increase in equivalence ratio because of higher associated flame temperatures at higher equivalence ratio. However, there is minimal effect of thermal intensity on the NO emission level as observed from Figure 5.5(a). This is contrary to that observed in Figure 2.7(b) where NO_x emission was observed to decrease at higher thermal intensity operation. This may be because of minimal contribution of NO formation from thermal mechanism due to suppression of hot spot regions. For thermal mechanism the NO emission will increase with increase in residence time (see Figure 1.6). Figure 5.5(b) shows the CO emission level with change in equivalence ratio from 0.5–0.7 at three heat release intensities. Minimum CO levels are observed for equivalence ratio of 0.6 and highest CO levels are observed at equivalence ratio of 0.5. This may be because at lower equivalence ratio the flame temperatures are lower resulting in lower conversion of CO to CO_2 [Lefebvre, A. H., 1998]. At higher equivalence ratio of 0.7 the CO levels are higher. This may be due to dissociation of CO_2 at high temperatures as well as lower availability of oxygen at higher equivalence ratios [Lefebvre, A. H., 1998]. The confinement size has significant effect on CO levels as observed from Figure 5.5(b). For larger confinement size (lower thermal intensity) CO levels are lower. The conversion of CO is slower as compared to other species and hence residence time

has significant effect on the CO levels (see Figure 2.7). Higher thermal intensity (lower combustor volume) results in lower associated residence time hence this might be the reason for lower conversion of CO to CO₂, resulting in higher CO levels for higher heat release intensity case as observed from Figure 5.5(b).

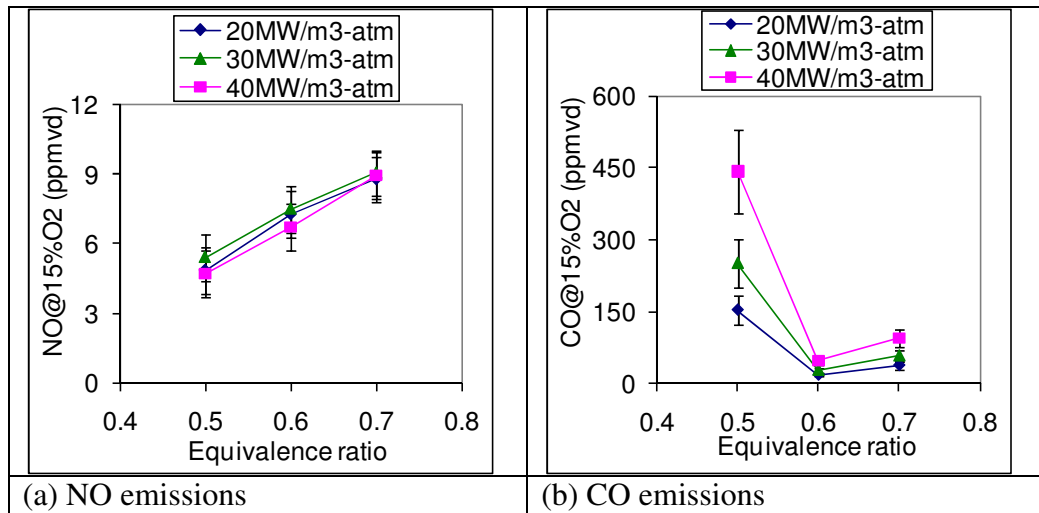


Figure 5.5 (a) NO and (b) CO emissions for the three thermal intensity cases.

5.3 Experimental and Numerical Set Up (28MW/m³-atm)

A simple combustor having single air and fuel injection diameter as shown in Figure 5.6(a,b) was designed. The combustor has three ports on both top and bottom side. The top right port is for exit of hot product gases from the combustor (see Figure 5.6(c)). Air and fuel injection ports could be chosen from other available ports to result in desired flowfield configuration. Bottom left port is for pilot flame. Pilot flame is used for initial heating of the combustor and to start other flow configurations. Photograph of the pilot flame is shown in Figure 5.6(d). Air and fuel flow rates are slowly increased until reactions are stabilized in the combustor, after which the pilot flame is withdrawn, and ceramic plug is inserted in that port to avoid any aerodynamic distortions.

The combustor has optical access from both front and back side. On the right side quartz window is present for introduction of laser sheet, which could be used for detailed investigation of flowfield as well as the reaction zone.

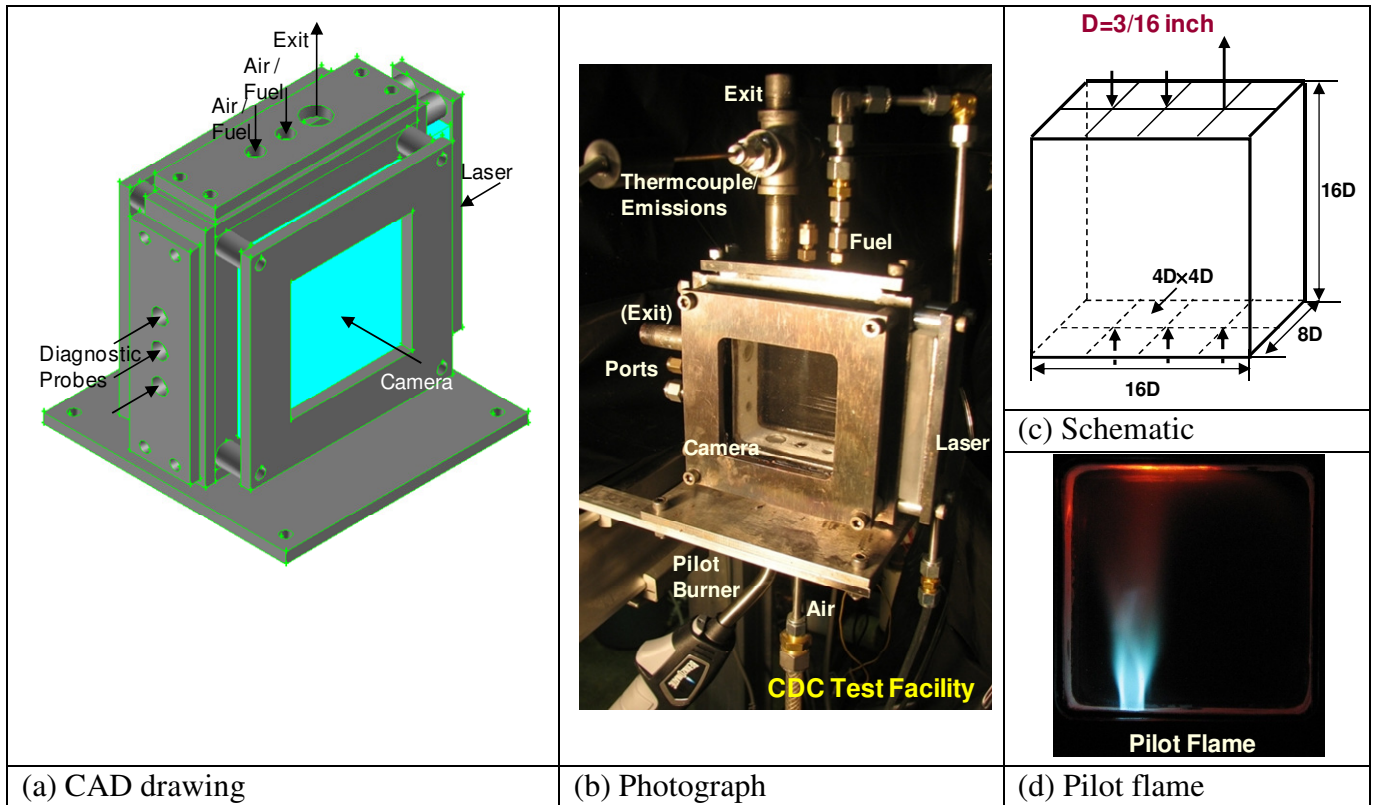


Figure 5.6 Medium thermal intensity ($28\text{MW/m}^3\text{-atm}$) CDC combustor (a) CAD drawing (b) photograph (c) schematic diagram (d) pilot flame used for initial heating.

Figure 5.7 shows different flowfield configurations which were investigated in the present work. It may be noted that the configurations are similar to that investigated at lower thermal intensity ($5\text{MW/m}^3\text{-atm}$) as described in detail in Chapter 4 (see Figure 4.1).

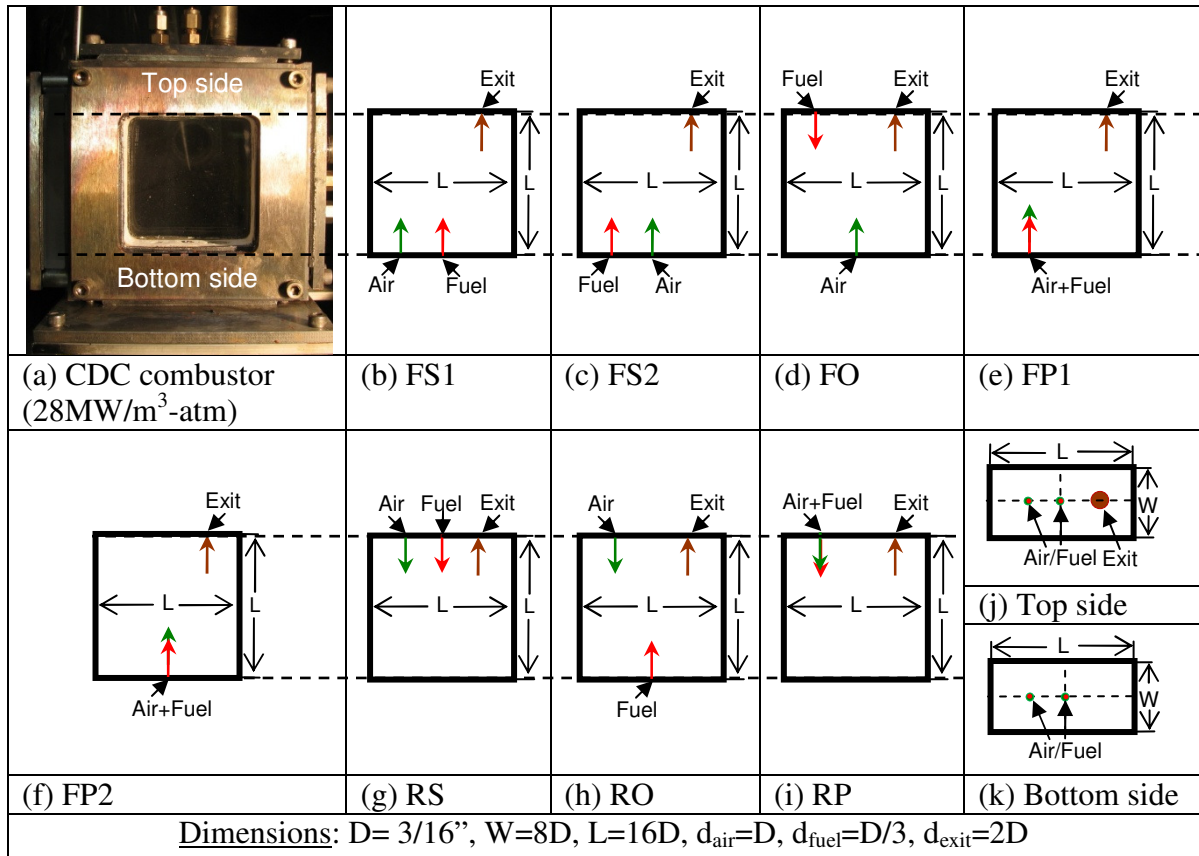


Figure 5.7 (a) photograph and (b-i) schematic diagrams of different flow configurations examined for medium thermal intensity ($28\text{MW}/\text{m}^3\text{-atm}$) CDC combustor.

The combustor was operated at a heat load of 6.25kW at high thermal intensity ($28\text{MW}/\text{m}^3\text{-atm}$) using methane as the fuel. Both methane and air were injected at ambient temperature of 300K and the operating pressure was 1atm . The inlet fuel injection velocity was about 97m/s and the air injection velocity varied from 128m/s to 205m/s and this combination provided variation of equivalence ratio from 0.8 to 0.5 , respectively.

The combustor was allowed to run for about 20minutes in each configuration before taking experimental data. Gas analyzer was used to obtain the NO and CO emission level, see Appendix G for further details. The emission readings were observed to stabilize within 3minutes for any change in experimental condition (here

change in equivalence ratio for the same configuration). The experiments were repeated three times for each configuration and the uncertainty was estimated to be about ± 0.5 ppm for NO and $\pm 10\%$ for CO emissions. Digital camera with constant f-stop setting of 3.5 and shutter speed of 1/8s was used. The chemiluminescence intensity from OH* radicals in the flame was obtained using a ICCD camera coupled with a narrow band interference filter (OH* at 307nm) with camera f-stop setting of f-11, exposure time of 2s and gain of 280 for the forward flow configurations and camera f-stop setting of f-8, exposure time of 0.5s and gain of 100 for reverse flow configurations.

Figure 5.8 shows the grid used for the numerical investigation for different configurations. The grid is appropriately refined near the region of high shear. Full hexahedral grids were used to minimize the cell count as well as numerical diffusion. Geometrical symmetry was used to reduce the computational time and only one-half of the geometry with grid size of about 0.35 million cells was used. The mass flow rate of air corresponds to a heat load of 6.25kW at equivalence ratio of 0.8 using methane as the fuel. The corresponding air injection velocity is approximately 128m/s in both the cases. Compressibility effects are included in the numerical simulation as the air injection Mach number is about 0.37. These injection velocities are characteristic of those utilized in gas turbine combustors. The temperature of air jet was 300K and the operating pressure was 1atm. The flowfield was solved using a steady state, implicit, finite volume based method. SIMPLE algorithm was used for pressure velocity coupling. Realizable k-e model with standard wall functions was used to model turbulence. Inlet turbulence intensity of 5% was used for both air and

fuel jets and length scale was 0.07 times the hydraulic diameter. Convergence was obtained when the residuals for all the variables were less than 1E-04.

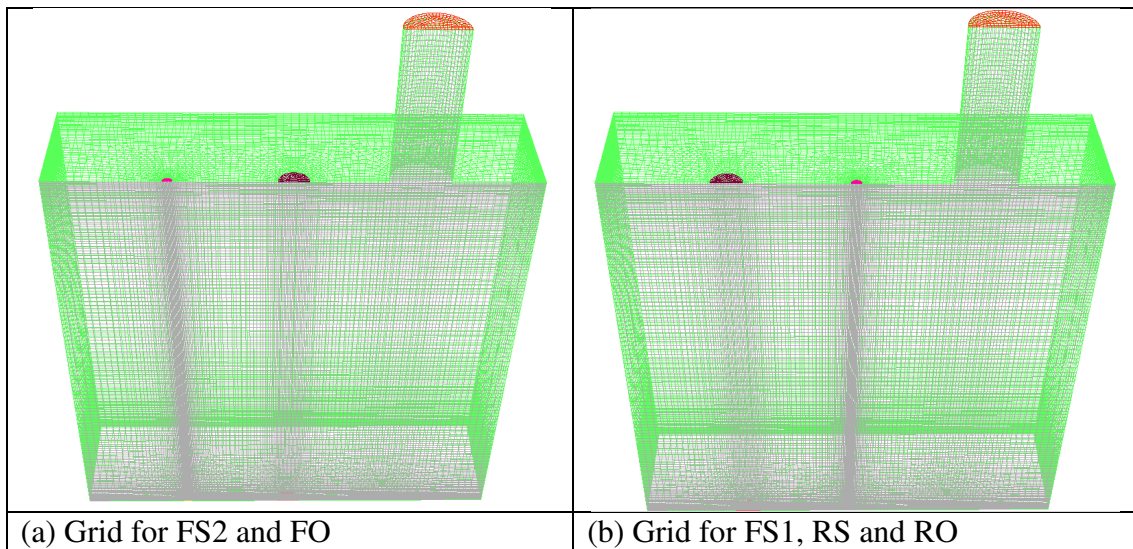


Figure 5.8 Grid used for different configurations.

5.4 Results and Discussion

5.4.1 Flowfield Characteristics

Figure 5.9 shows the velocity contour plots for the non-premixed configurations. As observed from the contour plots, air jet decays along the length of the combustor; however, the combustor length (16D) appears to be insufficient for complete decay of the air jet. One interesting feature that can be noted from the contour plots for configurations “FS2” and “FO” is the bending of air jet away from the exit location (see Figure 5.9(b) and (c)). This suggests that a significant portion of the injected air flow turns away from the exit and recirculate inside the combustor from the left side of air jet. The velocity contour plot for configuration “FS1” is shown in Figure 5.9(a). It can be observed that the air jet does not bend as observed for configurations “FS2” and “FO”, suggesting that the gases recirculate from both sides of the air jet. For configuration “FS1” the fuel jet decay is delayed suggesting weaker cross flow for

this configuration as observed from the velocity contour plots (see Figure 5.9(a)). The cross flow from the recirculating gases near the fuel injection for configurations “FS1” and “FO” is expected to be strong hence the fuel jet decay is faster suggesting faster fuel/oxidizer mixing for these configurations. For configurations “RS” and “RO” the air jet splits in two parts and recirculate from both left and right side of the air jet. The contour plots also suggests that the cross flow from recirculating gases near the fuel injection is very weak for configuration “RS”, and hence the fuel jet decay is delayed for this configuration as observed from the velocity contour plots (see Figure 5.9(e)). The cross flow from the recirculating gases near the fuel injection for configurations “RO” is expected to be strong (see Figure 5.9(d)) hence the fuel jet decay is faster suggesting faster fuel/oxidizer mixing for these configurations, which is desirable to achieve reactions closer to distributed regime.

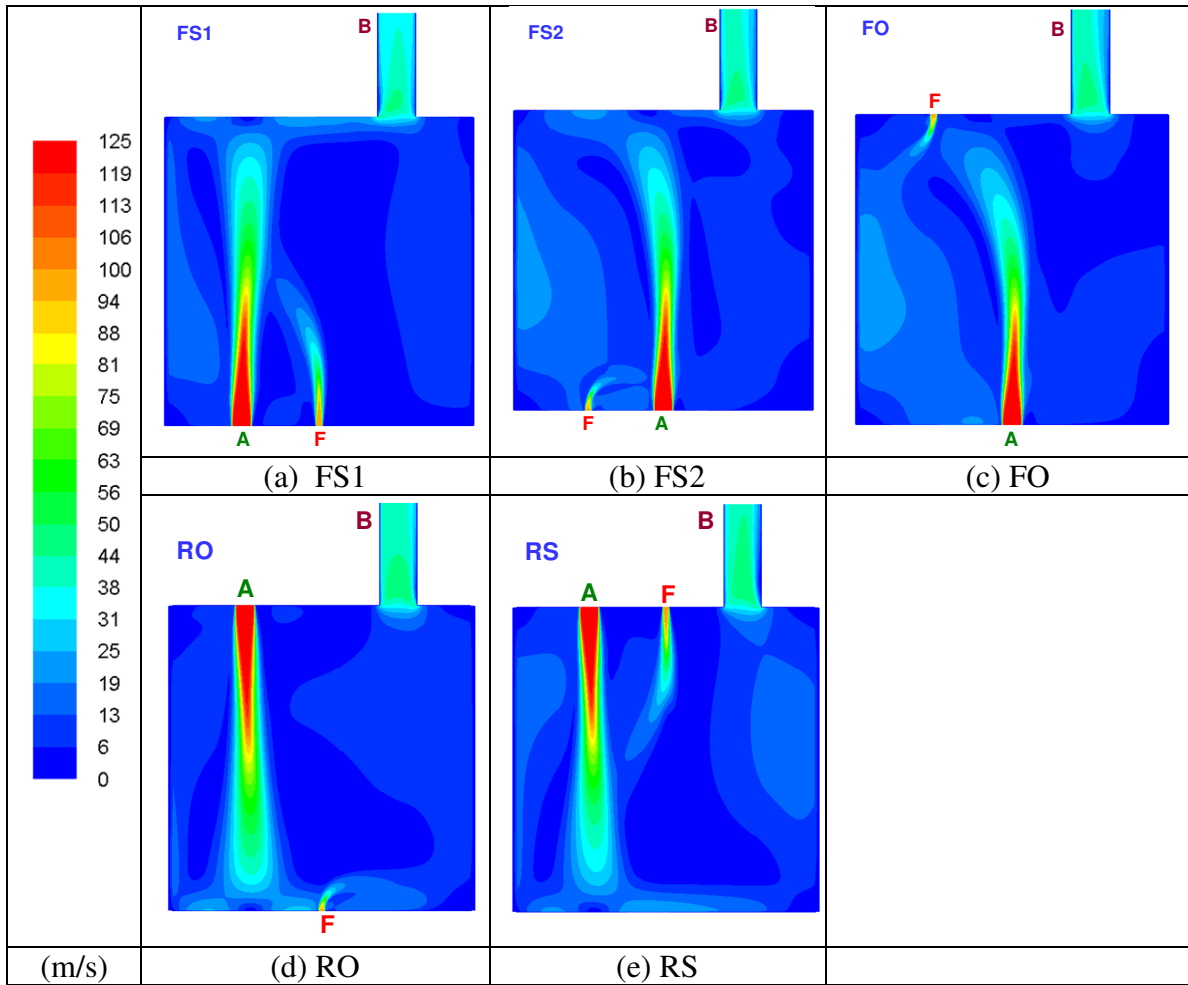


Figure 5.9 Velocity magnitude contour plots for different configurations.

Figure 5.10(a) shows centerline velocity decay for air jet and its comparison with free jet decay (equation 2.6) for the three forward flow configurations. It can be observed that the decay of air jet is much faster as compared to the free jet suggesting that the confinement has significant effect on the air jet. Configuration “FS1” suggests delayed decay of air jet as compared to the other two non-premixed configurations. Figure 5.10(b) shows the decay of fuel jet and its comparison with free jet (equation 2.6) for the three forward flow configurations. It can be observed that the fuel jet decay is significantly faster for configurations “FS2” and “FO” as

compared to configuration “FS1”. This reveals slower mixing for configurations “FS1” and this may result in lower stability for this configuration.

Variation of recirculation ratio of gases inside the combustor along the length of the combustor as well as a comparison with the entrainment ratio in a free jet (equation 2.1) is presented in Figure 5.10(c). The recirculation ratio is defined as the ratio of mass flow rate of the recirculated gases (with negative velocity, considering the positive direction is from bottom side to the top side) of gases to the mass flow rate of the injected air at a given distance from air injection. The figure reveals that the variation of recirculation ratio along the length of combustor is significantly different for confined chamber as compared to entrainment ratio for the free jet case. The amount of recirculation near the air injection is much higher for all three configurations as compared to free jet. This may be due to the presence of recirculating gases inside the combustor that turns towards the bottom side of the combustor after coming from combustor side walls. It may be noted that although the recirculation ratio is higher as compared to the entrainment in free jet, the recirculation ratio increases initially and then decreases along the length of the combustor, suggesting that the maximum recirculation is limited by the confinement size. It can also be observed that the recirculation ratio for configuration “FS1” is significantly lower than the recirculation ratio for configurations “FS2” and “FO”.

The portion of recirculated gases from the fuel side of the combustor is shown in Figure 5.10(d). The fuel side is the side of air jet where fuel is injected, hence for the present investigation fuel side for configurations “FS2” and “FO” is the left side of air injection and for configuration “FS1” is the right side of air injection. From Figure

5.10(d) it can be noted that the gases recirculate almost entirely from the fuel side for configurations “FS2” and “FO”; however, only about 40% of gases recirculate from the fuel side for configurations “FS1”. Recirculation ratio calculations reveal that configuration “FS1” may result in unstable combustion. This was also observed from experiments and combustion could not be sustained for configuration “FS1”. The premixed mode where air was injected from the side port as in “FS1” also could not sustain the flame experimentally (configuration “FP1”). Therefore from now onwards only results corresponding to configurations “FS2”, “FO” and “FP2” are presented for the forward flow configurations.

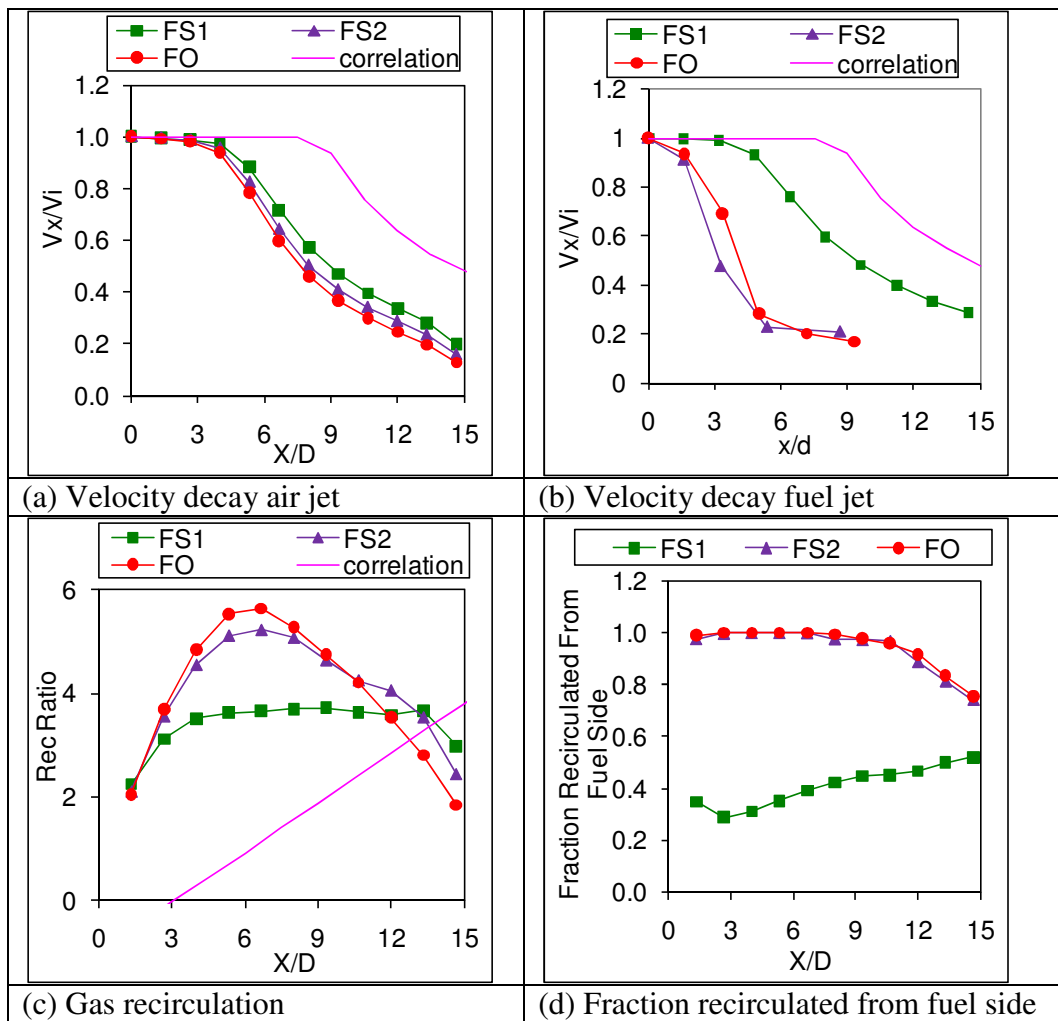


Figure 5.10 Velocity decay and gas recirculation for forward flow configuration.

The mass fraction of tracer at the combustor exit for a step input of tracer at the fuel inlet, and comparison with exit tracer profile of perfectly stirred reactor case (equation 2.8) for the two non-premixed cases is shown in Figure 5.11(a). The tracer has same properties as that of fuel (methane). For configurations “FS2” and “FO” the tracer is injected from the bottom-left and top-left port respectively, hence these cases simulates the presence of reaction zone near the bottom-left and top-left portion of the combustor. It may be noted that for no recirculation case (plug flow reactor) the tracer profile will show a step rise at the time corresponding to residence time for the combustor. The average residence time for the two cases as obtained from equation 2.7 is 92ms and 94ms for configurations “FS2” and “FO”, respectively. It may be noted that these values are very close to that calculated for perfectly stirred reactor from equation 2.5 (90ms). Therefore for these configurations the average residence time is mostly dependent on the combustor volume irrespective of the flow configurations investigated here. This also suggests that the average residence time is not affected significantly for different location of tracer injection for the present case. Even though the average residence time may be the same, the residence time frequency distribution is important to consider, as significant amount of CO may be emitted if some fraction of tracer has significantly lower residence time. Residence time frequency distribution plot for the two non-reacting cases and comparison with residence time frequency distribution for a perfectly stirred reactor (equation 2.7) is shown in Figure 5.11(b). The Figure suggests that configuration “FS2” has higher fraction of tracer having lower residence time (<10ms). This can also be observed from early inception of tracer at exit for configuration “FS2” as compared to “FO”

(see Figure 5.11(a)). Hence the computations suggest that configurations “FS2” may produce higher level of CO as compared to configuration “FO” if the reaction zone is closer to the fuel injection location.

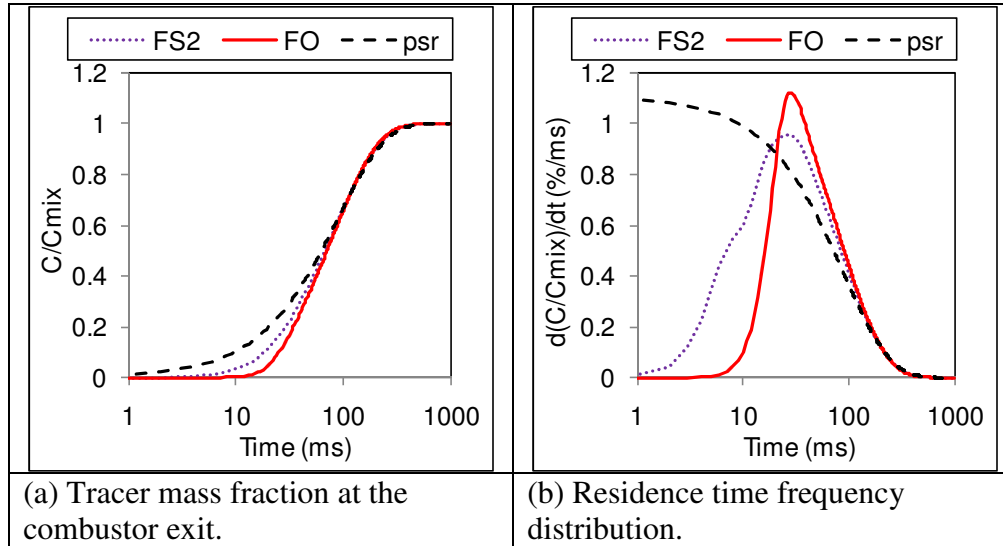


Figure 5.11 (a) Tracer mass fraction at the exit and (b) residence time frequency distribution for configurations “FS2” and “FO” (psr=perfectly stirred reactor).

Figure 5.12(a) shows centerline velocity decay for air jet and its comparison with free jet decay (equation 2.6) for the reverse flow configurations “RS” and “RO”. It can be observed that the decay of air jet is much faster as compared to the free jet decay suggesting that the confinement has significant effect on the air jet. Figure 5.12(b) shows the decay of fuel jet and its comparison with free jet (equation 2.6) for the reverse flow configurations “RS” and “RO”. It can be observed that the fuel jet decay is significantly faster for configurations “RO” as compared to configuration “RS”. This reveals slower mixing for configurations “RS” and this may result in lower stability for this configuration.

Variation of recirculation ratio of gases inside the combustor along the length of the combustor as well as comparison with entrainment ratio for free jet (equation 2.1)

is presented in Figure 5.12(c). The recirculation ratio is defined as the ratio of mass flow rate of the recirculated gases (with negative velocity, considering the positive direction is from top side to the bottom side) of gases to the mass flow rate of the injected air at a given distance from air injection for these reverse flow configurations. It may be noted that for calculating the mass flow rate of the recirculated gases the mass flow rate of injected air is subtracted from the total flow rate having the negative velocity as the mass flow rate of injected air has to reverse before exiting the combustor. Figure 5.12(a) reveals that the variation of recirculation ratio along the length of combustor is significantly different for confined chamber as compared to entrainment ratio for a free jet case. The amount of recirculation near the air injection is much higher for all three configurations as compared to the free jet. This may be due to the presence of recirculating gases inside the combustor that turns towards the air jet from top side of the combustor. It may be noted that although the recirculation ratio is higher as compared to the entrainment in free jet, the recirculation ratio increases initially and then decreases along the length of the combustor, suggesting that the maximum recirculation is limited by the confinement size. It can also be observed that the recirculation ratio for configuration “RS” is significantly higher than the recirculation ratio for configuration “RO”, and this may be due to the effect of fuel injection jet which also will entrain the gases inside the combustor. The portion of recirculated gases from the fuel side of the combustor is shown in Figure 5.12(b). The fuel side is the side of air jet where fuel is injected, hence for the present investigation fuel side for configurations “RS” and “RO” is the

right side of air injection. From the Figure 5.12(b) it can be noted that the gases recirculate from both sides of the air jet for both configurations “RS” and “RO”.

Experimentally, configuration “RS” was not able to stabilize combustion hence onwards no results are presented for “RS” configuration and only results corresponding to configurations “RO” and “RP” are presented.

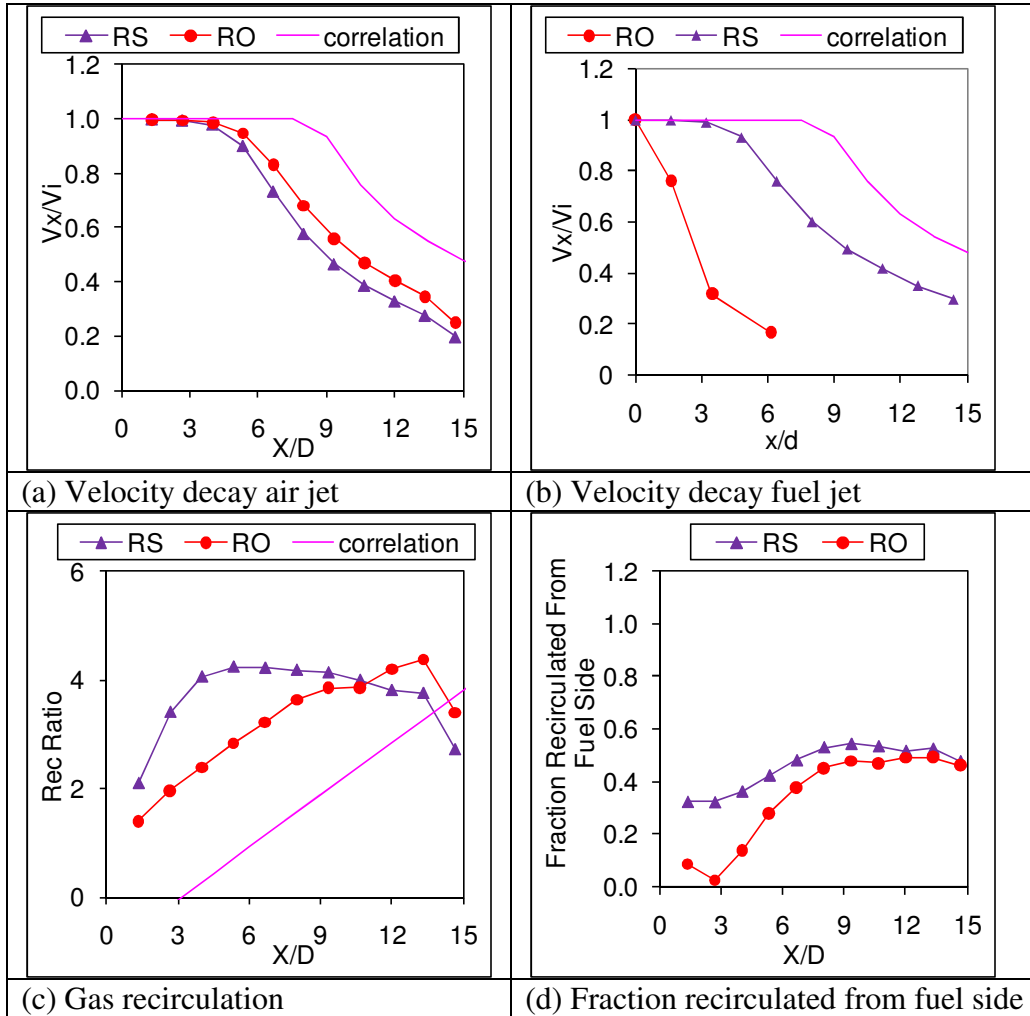


Figure 5.12 (a-b) Velocity decay and (c-d) gas recirculation for reverse flow configurations.

5.4.2 Global Pictures

Global photographs for different configurations for the CDC combustor are shown in Figure 5.13. The combustor has full optical access with quartz window size of

16D×16D for the combustor side of 16D×16D where D is the diameter of air jet. The photographs are taken with black background for enhancing visibility of the reaction zone.

For configuration “FS2” (Figure 5.13(a-d)) bluish region is observed around the air jet and along the top-left combustor walls in an inverted “U” shape. However, as the equivalence ratio is decreased the visible intensity was observed to decrease contrary to that observed for the “FO” case. At equivalence ratio of 0.5 oblong shaped bluish regions is observed starting from the top-left and extending towards the bottom-right portion of the combustor for configuration “FS2”. Minimal yellowish emissions are observed for “FS2” configuration. For configuration “FO” (see Figure 5.13(e-h)) bluish region is present in the vicinity of injected air jet suggesting the presence of reaction zone near the air injection location. At equivalence ratio of 0.7 and 0.8 the bluish region starts near air jet, extends towards the top side of the combustor and is observed to be present along the top-left side of the combustor (along the combustor walls) in an inverted “U” shape (see Figure 5.13(e-h)) similar to that observed for the “FS2” configuration. At lower equivalence ratios (0.5 and 0.6) higher yellowish emissions were observed from the combustor contrary to lower yellowish emission observed for configuration “FS2”. This yellowish emission could be due to presence of soot for this configuration. Global photographs for the “FP2” configuration are presented in Figure 5.13(i-l). In this configuration lower visible emissions as compared to configurations “FS2” and “FO” are observed. Similar to non-premixed configurations, bluish region is observed in the vicinity of air jet, suggesting the presence of reaction zone around air jet. For equivalence ratio of 0.7

and 0.8 inverted “U” shaped bluish region is also observed similar to that observed for “FS2” configuration. At equivalence ratio of 0.7 yellowish regions are almost absent for the premixed mode. The flame blowout occurred below equivalence ratio of 0.7 hence the corresponding results for equivalence ratio of 0.6 and 0.5 are not presented.

Global flame photographs for reverse flow configuration “RO” is shown in Figure 5.13(m-p). From the figure it may be noted that the bluish region, possibly suggesting the presence of reaction zone, is present along the air jet and near the bottom portion of the combustor. The reaction zone splits in two parts near the bottom portion of the combustor suggesting recirculation from both sides of the air jet. For the premixed mode “RP” (see Figure 5.13(q-t)) very low visible emissions could be observed, and the reaction zone location is found to be around the air jet as well as near the bottom portion of the combustor. At equivalence ratio of 0.6 (Figure 5.13(s)) very low visible emissions are observed which is mostly bluish in appearance and the reaction zone appears to be on both left and right side of the air jet.

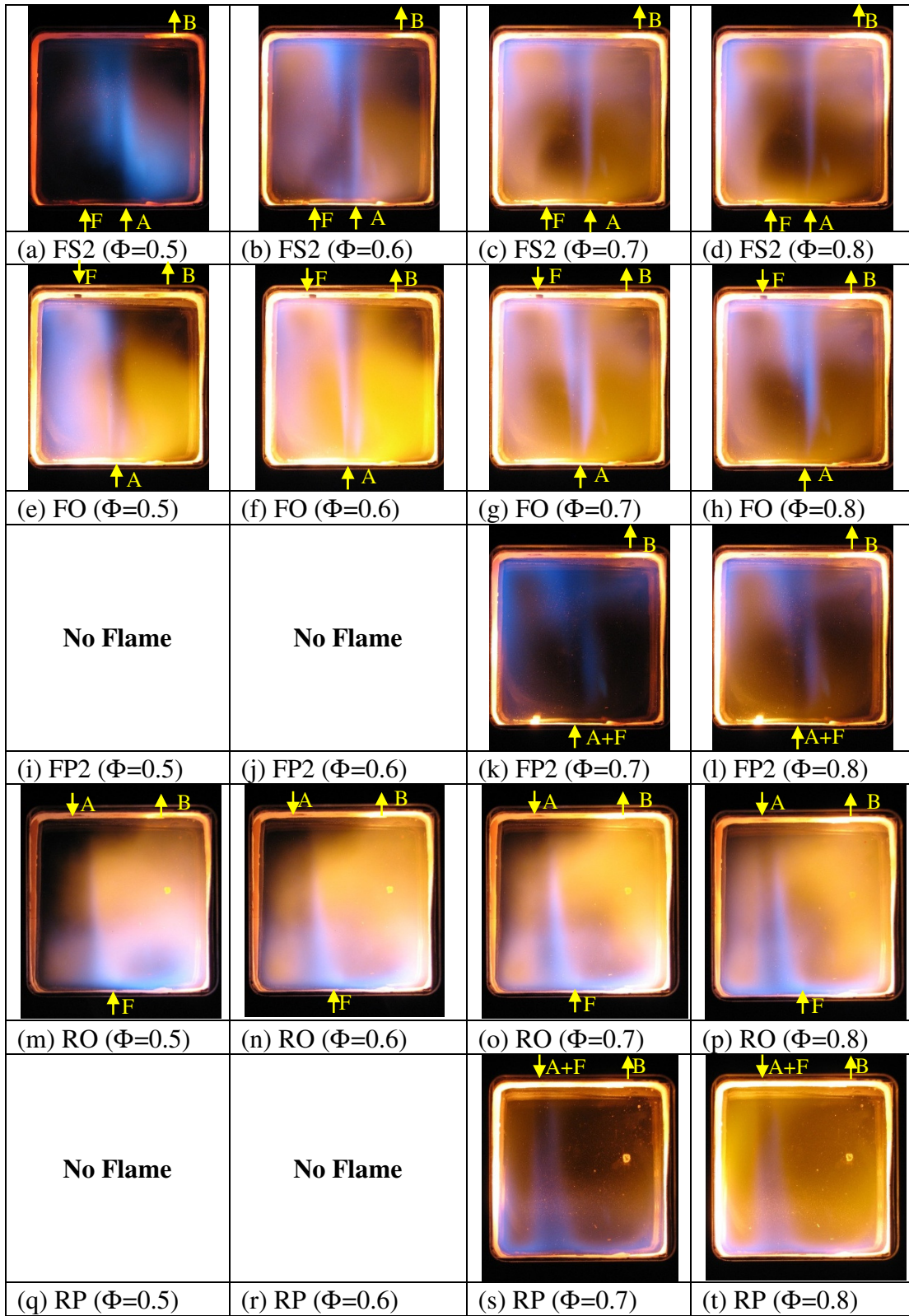


Figure 5.13 Global pictures for different configurations (A=Air, F=Fuel, B=Burned gases).

5.4.3 OH* Distribution

Chemiluminescence emissions of OH* radical depicts the location reaction zone in a combustor. OH* distribution for the CDC combustor is shown in Figure 5.14. The OH* distribution for configuration “FS2” is shown in Figure 5.14(a-d) and at equivalence ratio of 0.5 the reaction zone is present near the air injection jet in an oblong shape similar to that observed from the global image (see Figure 5.13(a)). As the equivalence ratio is increased the reaction zone moves towards the top side of the combustor, away from the air injection location (see Figure 5.14(a-d)) and at equivalence ratio of 0.8 the reaction zone is present near the top-left side adjacent to the combustor walls. As the equivalence ratio is increased the air injection velocity decreases, this will result in delayed entrainment of the fuel jet due to relatively weaker cross flow at higher equivalence ratios. This suggests that the mixing between fuel and air jet is delayed and hence the reaction zone shifts away from the air jet at higher equivalence ratios. Similar phenomenon was observed by [Verissimo, A. S., 2011] where they observed that the reaction zone moved away from the air injection location with increase in equivalence ratio for a forward flow configuration. The reaction zone for equivalence ratio range from 0.6-0.8 is mostly in an inverted “U” shape similar to that observed from the global images (see Figure 5.13(a-d)).

For configuration “FO” at equivalence ratio of 0.5 the reaction zone is observed to be distributed and confined in the left portion of the combustor as shown in Figure 5.14(e). This was also observed from the global flame image (see Figure 5.13(e)). As the equivalence ratio is increased the reaction zone is observed to move towards the top portion of the combustor and the towards the air jet injection location in an

inverted “U” shaped reaction zone region (similar to that observed from the global images, Figure 5.13(f-h)). This may be due to lower air injection velocity with increase in equivalence ratio which pushes the reaction zone towards the air injection location. This trend is opposite of that observed for configuration “FS2” where the reaction zone moved away from the air injection location with increase in equivalence ratio.

OH^* distribution for premixed flow configuration (“FP2”) is shown in Figure 5.14(i-l). For the premixed configuration the reaction zone is mostly present near the top-left portion of the combustor similar to that observed for the forward flow configurations “FS2” and “FO”. This can also be observed from the global flame images, see Figure 5.13(i-l). In premixed mode, injected air and fuel mixture entrains product gases and as the mixture moves along the combustor length the temperature increases resulting in ignition of the mixture and hence this results in stabilization of reaction zone near top portion of the combustor.

OH^* distribution for the reverse flow configuration “RO” is shown in Figure 5.14(m-p). It may be noted that the intensity level for forward flow and reverse flow configurations could not be compared as the camera settings were different for these two configurations (see Section 5.3). The reaction zone is observed to be present near the bottom portion of combustor (see Figure 5.14(m-p)) as also observed from the global images from Figure 5.13(m-p). As the equivalence ratio is decreased the reaction zone moves away from the air injection location, this may be due to higher air injection velocity which pushes the reaction zone away from the air injection location. For the premixed mode of combustion “RP” (see Figure 5.14(s-t)) the

reaction zone is present on both left and right side of the air jet near the bottom portion of the combustor. This is also observed from the global flame pictures shown in Figure 5.13(s-t).

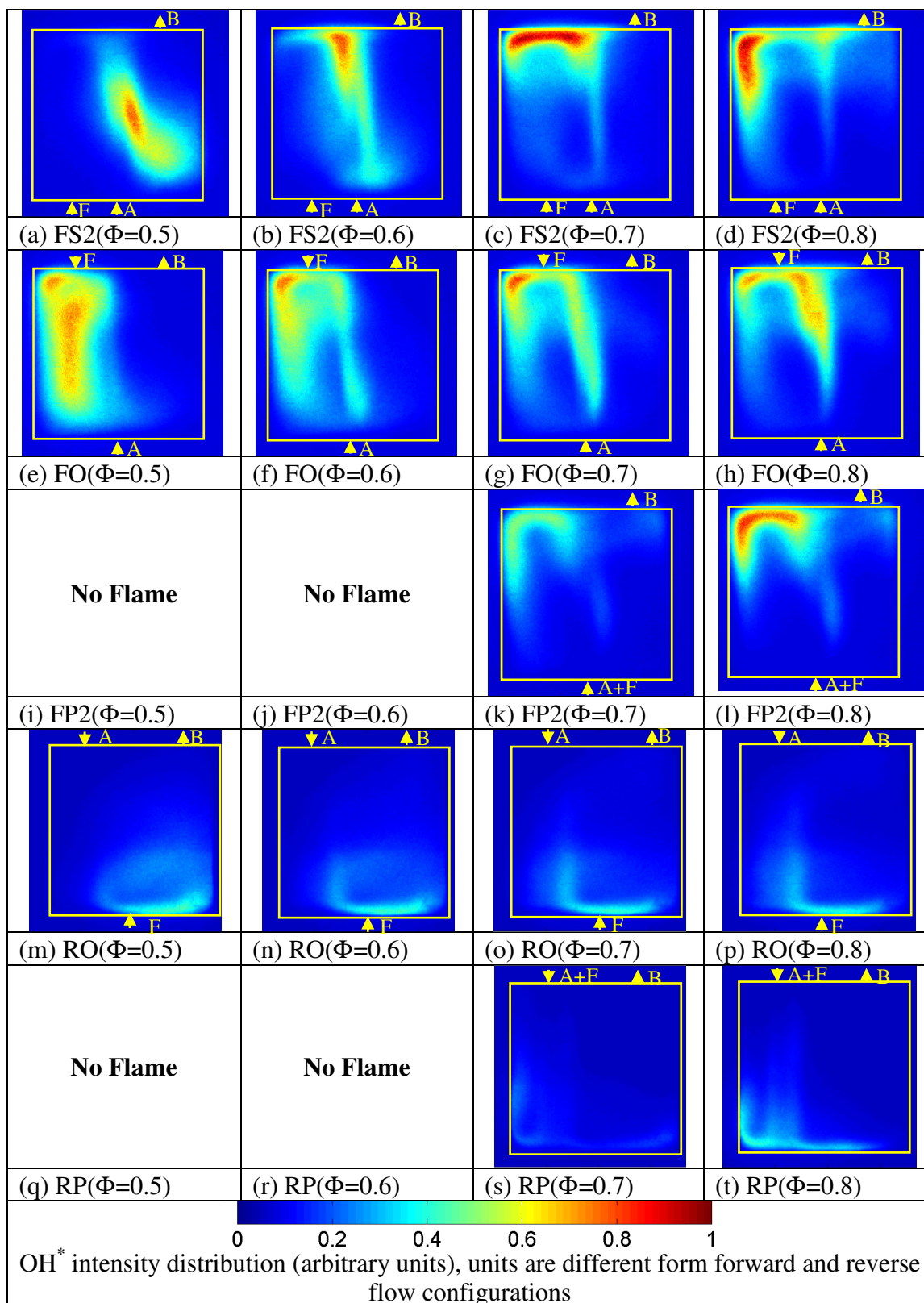


Figure 5.14 OH* distribution for different configurations.

5.4.4 NO and CO Emissions

NO emission levels corrected to 15% O₂ in exit gases for the CDC combustor is shown in Figure 5.15(a). In all the three forward flow configurations “FS2”, “FO” and “FP2” very low NO levels (single digit NO levels) are observed. Lowest NO levels are observed for the premixed mode (“FP2”) where the NO level was found to be only about 1ppm. Theoretically premixed combustion mode will have minimal hot spot region resulting in lowest NO level and hence this is considered baseline case for lowest NO emissions. For non-premixed configurations “FS2” and “FO”, NO emission levels are higher as compared to the premixed combustion mode “FP2”. This suggests that further improvement in mixture preparation is required to further reduce the emissions. Configuration “FO” produced about 10ppm and configuration “FS2” produced about 5ppm of NO at equivalence ratio of 0.5.

Lowest NO levels are observed for the reverse flow premixed mode “RP” with NO level of only about 1ppm. Theoretically, premixed combustion mode will have minimal hot spot region resulting the lowest NO level. For the non-premixed configurations “RO” the NO emission levels are much higher as compared to the premixed combustion mode (10-15ppm). Configuration “RO” produced highest NO level and the trend of decreasing NO with increase in equivalence ratio further suggests that for this configuration the reaction zone is not closer to distributed regime, because for a perfectly stirred reactor NO level is expected to increase with increase in equivalence ratio. This suggests further investigation of other configurations is required to achieve reactions closer to distributed regime resulting in lower NO level.

CO emission level corrected to 15% O₂ in exit gases for the CDC combustor is shown in Figure 5.15(b). It can be observed that configuration “FO” produced lowest CO levels among the forward flow configurations, and configuration “FS2” and “FP2” produced much higher CO levels. This can be attributed to higher residence time of the burned gases in configuration “FO” as observed from Figure 5.11. The conversion of CO to CO₂ is slower as compared to other species and hence residence time has significant effect on the CO levels (see Figure 2.7). As observed from Figure 5.14(e-h) in configuration “FO” the reaction zone is stabilized in the top-left portion of the combustor towards the combustor walls, hence the product gases turn towards the bottom side of the combustor and proceed towards the exit from the centre region of the combustor. This allows for higher residence time for the burned gases and hence higher conversion of CO into CO₂. This has been simulated by injecting tracer from the fuel injection location on top side for configuration “FO”. For configuration “FS2” the reaction zone is stabilized (see Figure 5.14(a-d)) near the air injection location and this is simulated by injecting the tracer from fuel injection from the bottom side of the combustor for configuration “FS2” (see Figure 5.11). Higher CO emissions for configuration “FS2” also suggest lower combustion efficiency and this may lead to lower associated temperatures in the combustor resulting in lower NO emissions. Lower NO emissions have been observed for configuration “FS2” as compared to configuration “FO”, see Figure 5.15(a). At higher equivalence ratio of 0.7 and 0.8 the CO levels are higher. This may be due to dissociation of CO₂ at high temperatures as well as lower availability of oxygen at higher equivalence ratios. For premixed mode “FP2” highest CO levels are observed for the range of equivalence

ratios investigated here. This may be due to the presence of reaction zone closer to the combustor exit in forward flow mode (see Figure 5.14(k-l)), resulting in significantly lower residence time available for the conversion of CO to CO₂.

The CO emission level corrected to 15% O₂ in the exit gases for the CDC combustor in reverse flow configuration is shown in Figure 5.15(b). It can be observed that premixed configuration, “RP” produced lowest CO levels, and non-premixed configurations “RO” produced much higher CO levels. Both the reverse flow configurations produce lower CO levels as compared to the forward flow configurations. This can be attributed to variable stoichiometric combustion for the non-premixed mode “RO” as compared to the premixed mode “RP”. This further supports the case for careful preparation of the reactants prior to the mixture ignition. Lower CO emission level for premixed reverse flow mode “RP” as compared to the premixed forward flow mode “FP2” is possibly due to higher associated residence time in the reverse flow configuration as compared to forward flow configuration.

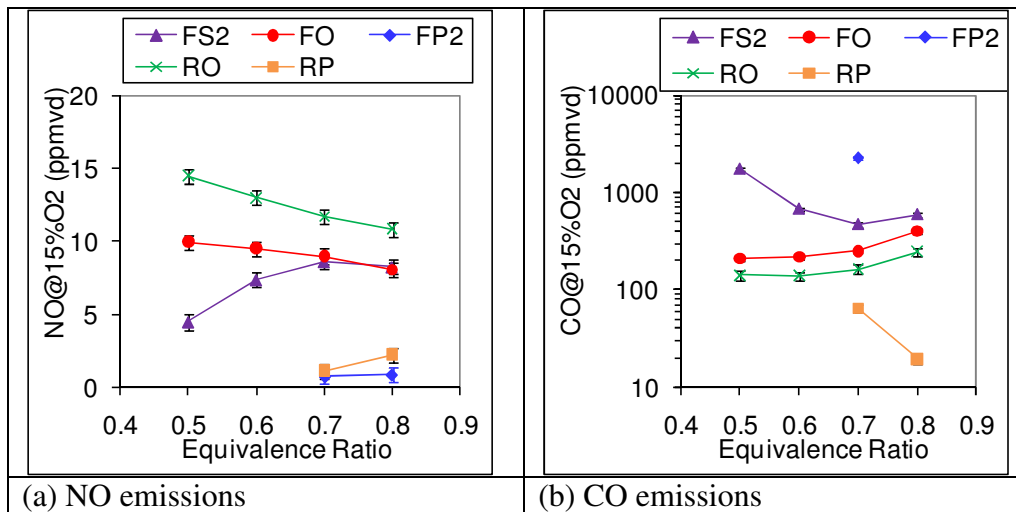


Figure 5.15 (a) NO emissions and (b) CO emissions for different configurations.

5.4.5 Lean Operational Limit

Wider stability limits (lower lean operational limit) is desirable to achieve higher turndown ratio for part-load gas turbine operation. Lean operational limit for the five configurations is shown in Figure 5.16. To obtain lean operational limit air flow rate was slowly increased at constant heat load until blowoff occurred. Configuration “RO”, which operates in non-premixed mode, has lowest lean operational limit ($\Phi=0.32$) as compared to other configurations. The premixed modes “FP2” and “RP” has the highest lean operational limit of $\Phi=0.65$ and 0.6 respectively. Configuration “FO” has lower lean operational limit as compared to configuration “FS2”, this may be due to higher residence time available in configuration “FO” resulting in higher combustion efficiency.

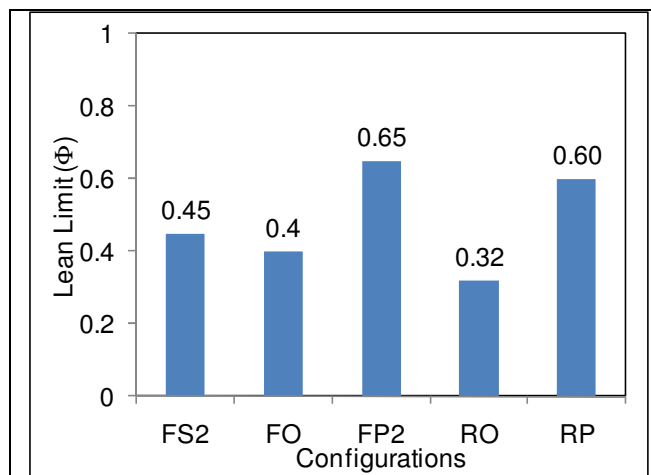


Figure 5.16 Lean operational limit for different configurations.

5.5 Conclusions

CDC combustor is examined at medium thermal intensity of 20, 30 and $40\text{MW/m}^3\text{-atm}$ for three confinement sizes for configuration “FS1” as well as for a simpler combustor having single air and fuel injection ports operating at thermal intensity of $28\text{MW/m}^3\text{-atm}$. The effect of confinement was investigated both

numerically and experimentally for non-premixed and premixed flames. Numerical investigation revealed that smaller confinement size results in delayed decay of centerline velocity of the air jet as well as lower recirculation ratio of product gases inside the combustor. Pressure loss across the combustor was found to be independent of the confinement volume size. A larger recirculation region is observed for smaller confinement size and this may be the reason for longer reaction zone observed experimentally. Global reaction zone images revealed that for both non-premixed and premixed CDC modes the reaction zone was observed to be contained inside the quartz tube for all three confinement sizes resulting in thermal intensities of 20, 30 and 40MW/m³-atm. For higher thermal intensity case the reaction zone was observed to be longer. The effect of confinement had minimal effect on NO emission level; however, the CO emission level increased significantly at higher thermal intensity. This may be due to lower residence time associated with higher heat release intensity case. At equivalence ratio of 0.6 only 8ppm of NO and low CO emission (about 20–50ppm) have been obtained in non-premixed mode.

Five different flowfield configurations, including two premixed mode and three non-premixed modes, have been examined using numerical simulations and experimental studies at thermal intensity of 28MW/m³-atm. Numerical simulations suggest that significant recirculation of gases was present and maximum recirculation was limited due to the confinement. Experimental studies show low NO emissions (9ppm for “FS2”, 9ppm for “FO” and 1ppm for “FP2”) for non-premixed and premixed modes for forward flow configurations at $\Phi=0.7$. High CO emissions were observed for premixed flow configuration “FP2” (2300ppm, $\Phi=0.7$) as well as “FS2”

configuration (465ppm, $\Phi=0.7$). However, the opposed flow configuration produced lower level of CO emissions (250ppm for “FO”, $\Phi=0.7$) possibly due to relatively higher residence time of the product gases inside the combustor for this configuration. Under the investigated conditions, the opposed flow non-premixed configuration “FO” shows better promise to achieve lower NO as well as CO emissions and favourable combustion characteristics that are closer to the colorless distributed combustion (CDC) regime amongst the forward flow configurations investigated. For reverse flow configuration very low NO (2ppm) and CO (64ppm) emissions were obtained for premixed mode. Reverse opposed flow configurations in non-premixed mode resulted in higher NO emissions of about 12ppm at $\Phi=0.7$ but lower CO emissions of 163ppm at $\Phi=0.7$. Better mixture preparation is expected to further reduce NO and CO emissions levels. In the next chapter different fuel, air injection schemes are further investigated to achieve lower pollutant emissions and higher thermal intensity.

Chapter 6 : High Thermal Intensity (57-85MW/m³-atm)

Reverse flow geometries were investigated at even higher thermal intensities up to 85MW/m³-atm. It may be noted that the state of the art gas turbine combustors operates at thermal intensity of about 15MW/m³-atm [Vandervort, C. L., 2001]. However even higher thermal intensities are desirable to minimize the hardware weight as well as cost. Different fuel injection locations have been investigated in the present chapter including fuel injection location in cross-flow for a combustor operating at thermal intensity of 57MW/m³-atm. Addition of hydrogen to methane fuel has also been investigated at thermal intensity of 85MW/m³-atm and the reaction zone characteristics have been reported in this chapter.

6.1 Experimental Set Up (57MW/m³-atm)

Figure 6.1 show photograph and schematics of the CDC combustor examined here. The combustor operates at thermal intensity of 57MW/m³-atm. The combustor has both length to depth ratio and length to width ratio of 2. Air was injected from the top side from the top as shown in Figure 6.1(g). Exit is located on the top side (see Figure 6.1(g)). Fuel injection port was on the bottom side (see Figure 6.1(b) and (h)) and on the left side (see Figure 6.1(c-e) and (i)). Only one set of air and fuel injection ports were used at a time. The exit diameter, air and fuel injection diameter and the corresponding injection velocities were same for all configurations.

In the present study five different configurations have been investigated at thermal intensity of 57MW/m³-atm. In the first configuration air was injected from the top side and the fuel from the bottom side of the combustor, and this configuration is

referred here as “RO” (reverse flow, with fuel and air on opposite side), see Figure 6.1(b). This configuration enables a large separation between the air and fuel injection jets. The injected air is expected to first entrain the product gases and form a high temperature and diluted oxidizer as it reaches the bottom side where fuel is injected. Hot and diluted oxidizer stream is expected to turn towards the injected fuel jet and recirculate inside the combustor. Better mixing between air and product gases before meeting the fuel stream is expected in this configuration. The low velocity region near bottom side of the combustor is also expected to aid in stabilization of reactants in the reaction zone.

In configurations two to four (See Figure 6.1(c-e)), air is injected from the top side and fuel is injected in the cross-flow to the air jet, and the configurations are referred here as “RC1”, “RC2” and “RC3”, where “RC3” has fuel injection port near the bottom side and “RC1” has fuel injection port near the top side of the combustor. Injection of fuel in the cross flow is expected to enhance mixing of fuel with the oxidizer, and further downstream (near bottom side) the fuel and oxidizer mixture is expected to react in distributed combustion regime.

In the fifth configuration both air and fuel are premixed and injected from top side of the combustor (herein referred as “RP”), see Figure 6.1(f). The entrained product gases inside the combustor are expected to aid in spontaneous ignition of the premixed mixture of air and fuel. Theoretically the premixed mode will provide minimum thermal NO_x and this mode is considered as baseline case in comparison to the non-premixed cases. It may be noted that configurations discussed here cannot be started directly. The combustion may be started in the conventional diffusion mode

and then transitioned to CDC mode of combustion. Alternatively, a pilot flame (not shown here) may be used for initial heat up, which can then be transitioned to appropriate CDC flow modes.

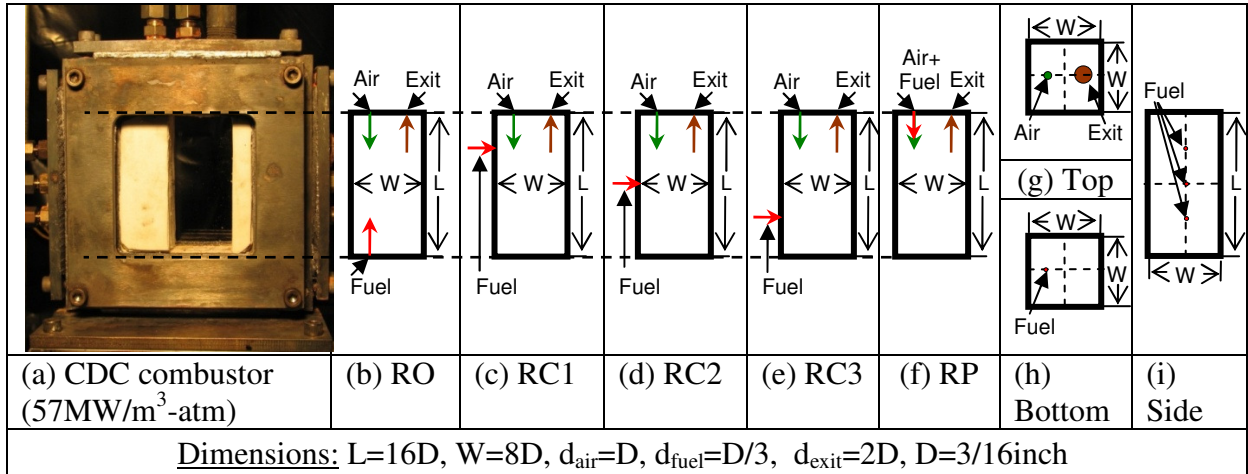


Figure 6.1 (a) photograph and (b-i) schematic diagrams of different configurations for high thermal intensity (57MW/m³-atm) CDC combustor.

The combustor was operated at heat load of 6.25kW at high thermal intensity of 57MW/m³-atm using methane as fuel. Both methane and air were injected at ambient temperature of 300K and the operating pressure was 1atm. The inlet fuel injection velocity was about 97m/s and the air injection velocity varied from 128m/s to 205m/s and this combination provided change in equivalence ratio variation from 0.8 to 0.5, respectively.

The combustor was allowed to run for about 20minutes in each configuration before taking the experimental data. Gas analyzer was used to obtain the NO and CO emission level, see Appendix G for further details. Emission readings were observed to stabilize within 3minutes for any change in experimental condition (here change in equivalence ratio for the same configuration). The experiments were repeated three times for each configuration and the uncertainty was estimated to be about ± 0.5 ppm for NO and $\pm 10\%$ for CO emissions. The chemiluminescence intensity from OH^{*}

radicals in the flame was obtained using an ICCD camera coupled with a narrow band interference filter (307nm for OH^{*}) with camera f-stop setting of f-8, exposure time of 0.5s and gain of 100 for all the conditions.

6.2 Results and Discussion

6.2.1 OH^{*} Distribution

The OH^{*} distribution for reverse-cross flow configurations “RC1”, “RC2”, “RC3”, “RO” and “RP” is shown in Figure 6.2. Configuration “RC1” has fuel injection closer to the air injection jet, near the top left portion of the combustor. Hence the reaction zone is observed to be near the top-left portion of the combustor as observed from Figure 6.2(a-d). This suggests that the burned gases will have higher residence time available for further conversion of CO as the gases will move down and then reverse to exit from the combustor from top side. As the fuel injection location is moved down (configuration “RC2”, see Figure 6.2(e-h)), the reaction zone is also observed to shift downwards and towards bottom right of the combustor suggesting lower residence time for the burned gases. For configuration “RC3” the fuel is injected near the bottom left end of the combustor. For this configuration the reaction zone is present mostly near bottom right side of the combustor as seen in Figure 6.2(i-l). Hence, configuration “RC3” is expected to have lower residence time for hot gases as compared to other cross-flow configurations “RC1” and “RC2”.

The OH^{*} distribution for configuration “RO” is shown in Figure 6.2(m-p). At equivalence ratio of 0.5 the reaction zone is present near the bottom right region (see Figure 6.2(m)). As the equivalence ratio is increased the reaction zone moves towards the left side and upwards along the air jet. It may be noted that in configuration “RO”

fuel is injected further away from the air injection location as compared to configuration “RC3” (from the bottom side) and hence the corresponding reaction zone is observed near the right side of the combustor (see Figure 6.2(m-p)). Hence this configuration is expected to have lower residence time for burned gases as compared to the cross-flow configurations.

OH^* distribution for premixed flow configurations “RP” is shown in Figure 6.2(q-t). For the premixed configuration the reaction zone is mostly present near the bottom portion of the combustor and along the air jet. For the premixed configuration “RP” the reaction zone is mostly confined near the left bottom side of combustor as compared to non-premixed case “RO” where the reaction zone was stabilized near bottom right portion of the combustor. This suggests higher residence time is available for burned gases for conversion of CO to CO_2 . In the premixed mode the injected air and fuel mixture entrains the product gases and as the mixture moves along the combustor length the temperature increases resulting in ignition of the mixture and hence presence of reaction zone near the bottom portion of the combustor.

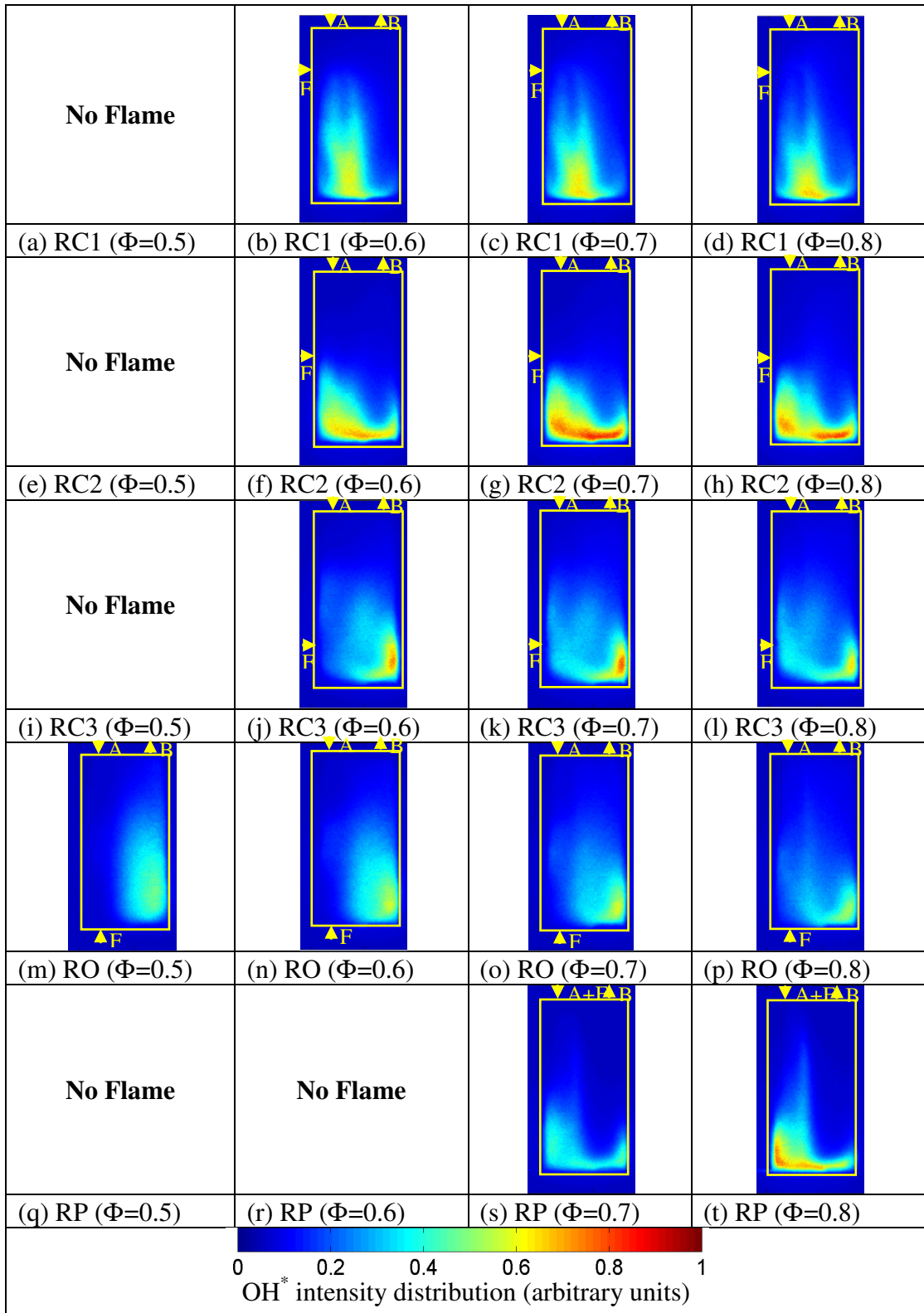


Figure 6.2 OH* distribution for different configurations.

6.2.2 NO and CO Emissions

NO emission levels corrected to 15% O₂ in exit gases for four configurations (“RC1”, “RC2”, “RC3”, “RO” and “RP”) for the CDC combustor are shown in Figure 6.3(a). Lowest NO levels are observed for the premixed mode “RP” with NO level of only about 1-2ppm. Theoretically premixed combustion mode will have minimal hot spot region resulting the lowest NO level. For the non-premixed configuration “RO” the NO emission levels are much higher as compared to the premixed combustion mode (10-15ppm). From Figure 6.3(a) it can be observed that as the fuel is injected in cross-flow, closer to the air jet, NO emissions are lower. Configuration “RC1” produced lowest NO emissions among all the non-premixed cases investigated here. The emission level in non-premixed mode “RC1” is about 3ppm at $\Phi=0.7$. For this configuration NO level increases with increase in equivalence ratio thus suggesting reactions closer to distributed regime. Configuration “RC3” produced higher NO levels as compared to configuration “RC1”; this suggests that faster mixing of fuel jet, due to strong cross-flowing air jet, is important to achieve ultra low emission level.

The CO emission level corrected to 15% O₂ in the exit gases for the CDC combustor is shown in Figure 6.3(b). It can be observed that premixed configuration, “RP” produced lowest CO levels, and non-premixed configurations “RO” produced much higher CO levels. This can be attributed to variable stoichiometric combustion for the non-premixed cases as well as lower residence time of the burned gases for configuration “RO” as compared to the premixed mode “RP” (see discussion corresponding to Figure 6.2). This further supports the case for careful preparation of

reactants prior to the mixture ignition. Minimum CO emissions were obtained for configuration “RC1” for which CO emission level was about 57ppm at $\Phi=0.7$. The CO levels increased as the fuel injection location was moved away from the air injection port. This may be due to better mixing of fuel jet as well as higher residence time available for the burned gases for configuration “RC1” as compared to “RC2” and “RC3” (see the discussion for Figure 6.2). The CO emission level for “RC1” was even lower than that for the corresponding premixed flow mode “RP”. Hence, faster mixing due to injection of fuel into a cross flow of high velocity air jet and higher residence time results in good combustion characteristics and favourable emission profiles.

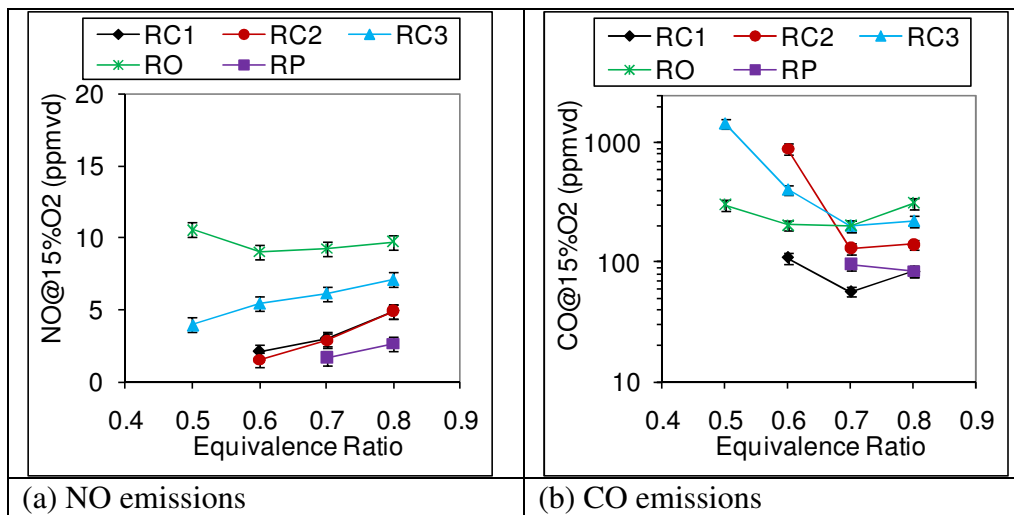


Figure 6.3 (a) NO emissions (b) CO emissions for different configurations.

6.2.3 Lean Operational Limit

Wider stability limits (lower lean operational limit) is desirable to achieve higher turndown ratio for part-load gas turbine operation. Lean operational limit for five configurations is shown in Figure 6.4. To obtain lean operational limit air flow rate was slowly increased at constant heat load until blowoff occurred. Configuration RO,

which operates in non-premixed mode, has lowest lean operational limit as compared to other configurations ($\Phi=0.4$). As fuel is injected in cross flow to enhance mixing of fuel and oxidizer, the lean operational limit also increases. Configuration “RC3”, “RC2” and “RC1” has lean operational limits of $\Phi=0.44$, 0.5 and 0.54, respectively. The premixed mode “RP” has the highest lean operational limit of $\Phi=0.6$. From the lean operational limit plot it can be noted that configurations having better mixing and lower hot-spot regions behave closer to the premixed mode. Furthermore, change in fuel injection location (for example from “RC1” to RO”) could be used to extend the lean operational limit (from $\Phi=0.54$ to 0.4) and hence this can be useful to achieve higher turndown.

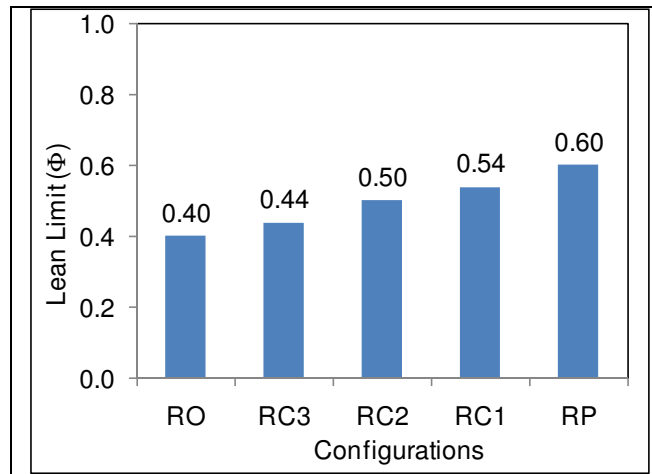


Figure 6.4 Lean operational limit for different configurations.

6.3 Experimental and Numerical Set Up (85MW/m³-atm)

Figure 6.5 shows a photograph and schematics of the high thermal intensity (85MW/m³-atm) CDC combustor examined here. The combustor has rectangular cross section with width to depth ratio of 1.5 and length to depth ratio of 3. The combustor is similar to the combustor shown in Figure 6.1 but with smaller

combustor depth ($16D/3$ as compared to $8D$). Air is injected from the top as shown in Figure 6.5(b) and 6.5(d) and gas exit is also located on the top (see Figure 6.5(b) and (d)). This mode of combustor operation configuration is referred to as reverse flow mode. Fuel injection port is positioned on the side (see Figure 6.5(b) and (c)); hence for the present investigation fuel is injected in cross-flow with respect to air injection. The cross flow injection location is shifted further up towards the air injection location (distance from top side= $2D$) as compared to the combustor shown in Figure 6.1. For configuration “RC1” the fuel injection location is at distance of $4D$ from the top side. Only one set of air and fuel injection ports are used. For the premixed mode of operation air and fuel is mixed at an upstream location and injected through the air injection port. For this geometry, the effect of hydrogen addition to methane fuel is investigated for the combustion characteristics.

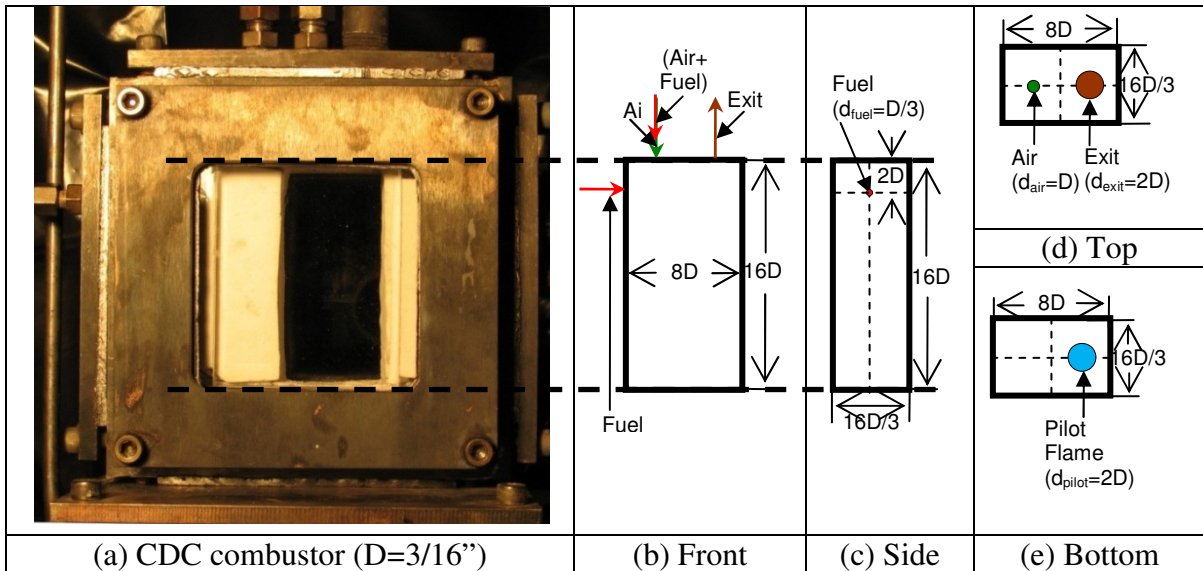


Figure 6.5 (a) photograph and (b-e) schematic diagrams for high thermal intensity ($85\text{MW/m}^3\text{-atm}$) CDC combustor.

6.3.1 Experimental Set Up

In the present study two different amount of hydrogen addition (4wt% and 8wt%) to methane fuel cases along with pure methane fuel cases (0wt%) have been investigated at constant thermal intensity of $85\text{MW/m}^3\text{-atm}$ in both premixed and non-premixed modes. The details of different cases investigated are given in Table 6.1. The combustor was operated at a constant heat load of 6.25kW at high thermal intensity ($85\text{MW/m}^3\text{-atm}$) using methane and hydrogen mixture as the fuel. Both fuel and air were injected at ambient temperature (300K) and the operating pressure was 1atm. The inlet fuel injection velocity varied from 97-136m/s for hydrogen addition from 0-8wt%. The air injection velocity varied from 128-124m/s (0-8wt% H_2) to 205-198m/s (0-8wt% H_2) and this combination provided change in equivalence ratio variation from 0.8 to 0.5, respectively. The variation for air injection velocity at a particular equivalence ratio is because of different amounts of air required for different methane/hydrogen fuel mixture at same equivalence ratio and heat load. The details of experimental conditions for different cases are shown in Table 6.1.

Table 6.1 Different cases investigated for the effect of hydrogen addition.

Cases	H ₂ (wt%)	H ₂ (vol%)	H ₂ (heat load%)	V _{fuel} (m/s)	V _{air} (m/s) ($\Phi=0.8$)	T _{adiabatic} (K) ($\Phi=0.8$)	Ignition delay (ms) (T _{reactor} =1500K)	Flame speed (cm/s) ($\Phi=0.8$) (T _u =300K)
1.	0	0	0	97	128	1996	1.08	29
2.	4	25	9	118	126	2011	0.33	34
3.	8	41	17	136	124	2024	0.15	39
4.	0	0	0	-	139	1996	1.08	29
5.	4	25	9	-	139	2011	0.33	34
6.	8	41	17	-	139	2024	0.15	39

The combustor was allowed to run for about 20minutes in each configuration before taking the experimental data. Gas analyzer was used to obtain NO and CO emission level, see Appendix G for further details. The emission readings were observed to stabilize within 3 minutes for any change in experimental condition (here change in equivalence ratio for the same configuration). The experiments were repeated three times for each configuration and the uncertainty was estimated to be about ± 0.5 ppm for NO and $\pm 10\%$ for CO emission. Digital camera with constant f-stop setting of f-3.5 and shutter speed of 1/40s was used for global flame imaging. The chemiluminescence intensity from OH^* radicals in the flame was obtained using an ICCD camera coupled with a narrow band interference filter (OH^* at 307 nm) with camera f-stop setting of f-8, exposure time of 0.5s and gain of 100 for all the conditions.

6.3.2 Numerical Set Up

The flowfield pattern, jet profile, gas recirculation and residence time under non-reacting condition is examined for the reverse flow geometry shown in Figure 6.5. As air is the dominant jet in the present examination (momentum ratio, air/fuel jet~28), the air jet is expected to govern the flowfield behavior inside the combustor. Hence only the air flow is computed in the present investigation to understand the flowfield pattern inside the combustor. The mass flow rate of air corresponds to heat load of 6.25kW at equivalence ratio of 0.8 using methane as the fuel. The corresponding air injection velocity is about 128m/s. These injection velocities are characteristic of those utilized in gas turbine combustors. The temperature of inlet air jet was 300K and the operating pressure was 1atm. The flowfield was solved using a steady state,

implicit, finite volume based method and SIMPLE algorithm was used for pressure velocity coupling. Full hexahedral grid was used to minimize the grid size and appropriate refinement of grid was performed in the regions with higher gradients. The grid used for CFD simulations is shown in Figure 6.6(a). Geometrical symmetry was used to reduce the computational time and only one-half of the geometry with grid size of about 0.32 million cells was used. Realizable k-e model with standard wall functions was used to model turbulence. Inlet turbulence intensity of 5% was used for both air and fuel jets and length scale was 0.07 times the hydraulic diameter. Convergence was obtained when the residuals for all the variables were less than $1E-04$. The centerline jet velocity profile obtained from the numerical solution was compared with the correlation for free jet given in equation 2.6. The recirculation (rec.) ratio inside the combustor obtained from numerical simulation was compared with the correlation given in equation 2.1.

Carbon monoxide oxidation is a slow process; hence residence time has a significant effect on the CO emissions. Lower residence time is also expected to result in higher emission levels of unburned hydrocarbon (UHC) and lower combustion efficiency. Residence time distribution was obtained for the CDC combustor by using a tracer having same properties as that of air. After obtaining a steady state solution of flowfield, the tracer concentration at the air inlet was set to 1 at time = 0, and only tracer conservation equation was solved in a transient mode with time step size of 0.5ms. The tracer was tracked from the air injection location to simulate the presence of reaction zone near the air injection location. The tracer

concentration at the outlet was monitored with respect to time. The residence time was obtained by equation 2.7.

The residence time profile obtained from numerical simulations is compared for the case of a perfectly stirred reactor. The exit tracer concentration profile with respect to time, for a perfectly stirred reactor corresponding to a step input of tracer at the inlet is given in equation 2.8. The residence time (t_{res}) for a perfectly stirred reactor is obtained by equation 2.5. Residence time frequency distribution for a perfectly stirred reactor is given by equation 2.7.

For all simulations commercial software FLUENT was used.

6.4 Results and Discussion

6.4.1 Flowfield Characteristics

Figure 6.6 shows the velocity contour and pathline plots for the reverse flow CDC combustor. As observed from the contour and pathline plots, air jet decays along the length of the combustor; however, the combustor length ($16D$) appears to be insufficient for complete decay of air jet. The air jet penetrates till the bottom of combustor and after hitting the bottom surface it reverses the direction to escape from the combustor exit located on top side. From the pathline plots (see Figure 6.6(c)) it can be observed that the gases also partially recirculate inside the combustor. These hot recirculated gases are expected to lower the oxygen concentration of the injected air upon its mixing with the incoming air and increase the temperature of the air to help assist in spontaneous ignition of fuel and thus result in distributed combustion.

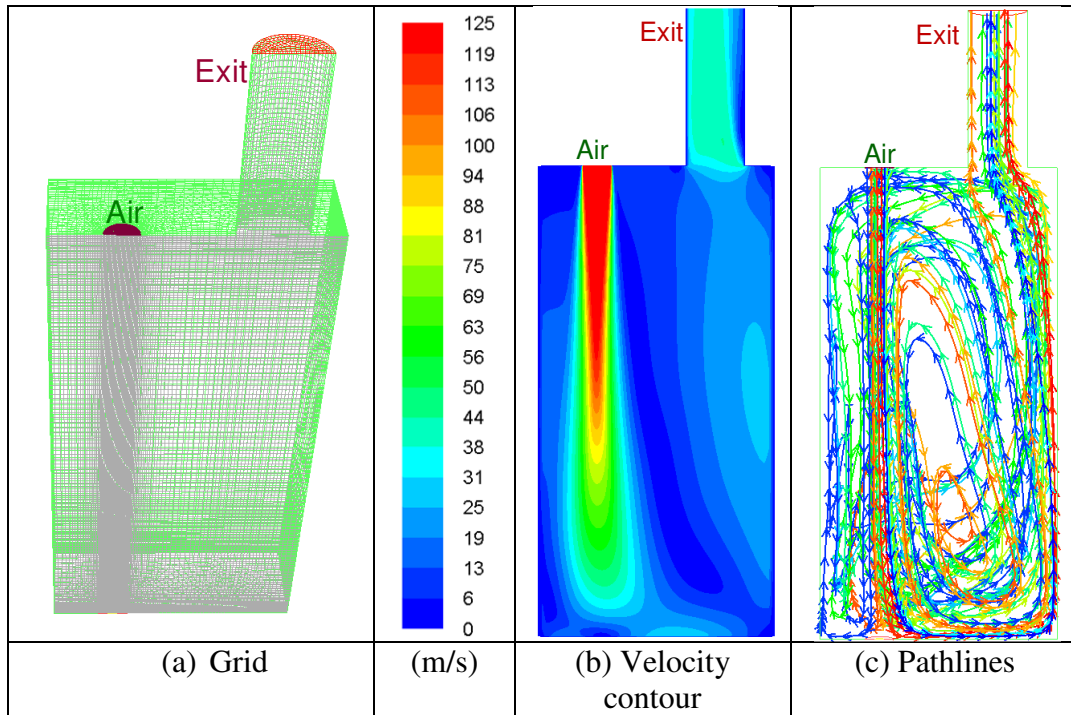


Figure 6.6 (a) Grid used for CFD simulation and (b) velocity magnitude contour plot (c) pathline plot (15 pathlines tracked from air injection).

Figure 6.7(a) shows centerline velocity decay for air jet and its comparison with free jet decay (equation 2.6) for the CDC combustor. It can be observed that the decay of air jet is much faster as compared to the free jet. Variation of recirculation ratio of gases inside the combustor along the length of the combustor as well as a comparison with the entrainment ratio in a free jet (equation 2.1) is presented in Figure 6.7(b). The recirculation ratio is defined as the ratio of mass flow rate of the recirculated gases (with negative velocity, considering the positive direction is from top side to the bottom side) of gases to the mass flow rate of the injected air at a given distance from air injection. It may be noted that for calculating the mass flow rate of the recirculated gases the mass flow rate of injected air is subtracted from the total flow rate having the negative velocity as the mass flow rate of injected air has to reverse before exiting the combustor. Figure 6.7(b) reveals that the variation of

recirculation ratio along the length of combustor is significantly different for confined chamber as compared to entrainment ratio for a free jet case. The amount of recirculation near the air injection is much higher for the CDC combustor as compared to a free jet. This may be due to the presence of recirculating gases inside the combustor that turns towards the air jet near the top side of the combustor after reversing its direction (see Figure 6.6(c)). It may be noted that although the recirculation ratio is higher as compared to the entrainment in free jet, the recirculation ratio increases initially and then decreases along the length of the combustor, suggesting that the maximum recirculation is limited by the confinement size.

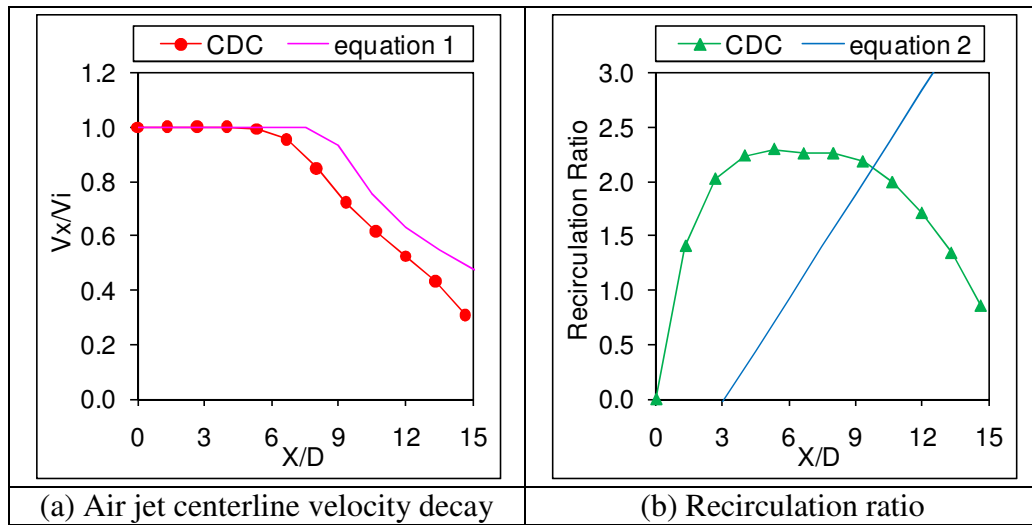


Figure 6.7 (a) Air jet centerline velocity decay and (b) Variation of recirculation ratio along the length (X) of the combustor, $D=d_{air}$.

The mass fraction of tracer at the combustor exit for a step input of tracer (mass fraction = 1) at the air inlet, and comparison with exit tracer mass fraction profile of a perfectly stirred reactor case (equation 2.9) is shown in Figure 6.8(a). For the present case the tracer is injected from the air injection port. Hence this case simulates the presence of reaction zone near the top-left portion (near air injection port) of the

combustor. It may be noted that for no recirculation case (plug flow reactor) the tracer profile will show a step rise at the time corresponding to residence time for the combustor. The average residence time for the CDC combustor as obtained from equation 2.7 was 33ms. It may be noted that these values are very close to that calculated for perfectly stirred reactor from equation 2.5 (31ms). This suggests that the average residence time is not affected significantly for tracer injection from the top side for the present case. Even though the average residence time may be same, the frequency distribution of residence time is important to consider, as significant amount of CO may be emitted if some fraction of tracer has significantly lower residence time. Residence time frequency distribution plot for the CDC combustor and its comparison with residence time frequency distribution for a perfectly stirred reactor (equation 2.9) is shown in Figure 6.8(b). The figure suggests that perfectly stirred reactor (psr) has higher fraction of tracer having lower residence time (<10ms). This can also be observed from early inception of tracer at exit for psr as compared to CDC combustor case (see Figure 6.8(a)). Hence the computations suggest that reverse flow CDC combustor can achieve lower emission of CO as compared to perfectly stirred reactor if the reaction zone is closer to the air injection port.

It is recognized that the flowfield will be different in reacting conditions (lower residence time, lower gas recirculation, delayed decay of jets); however, comparative study of non-reacting condition provides important insights about the flow field pattern, jet profile, gas recirculation and residence time.

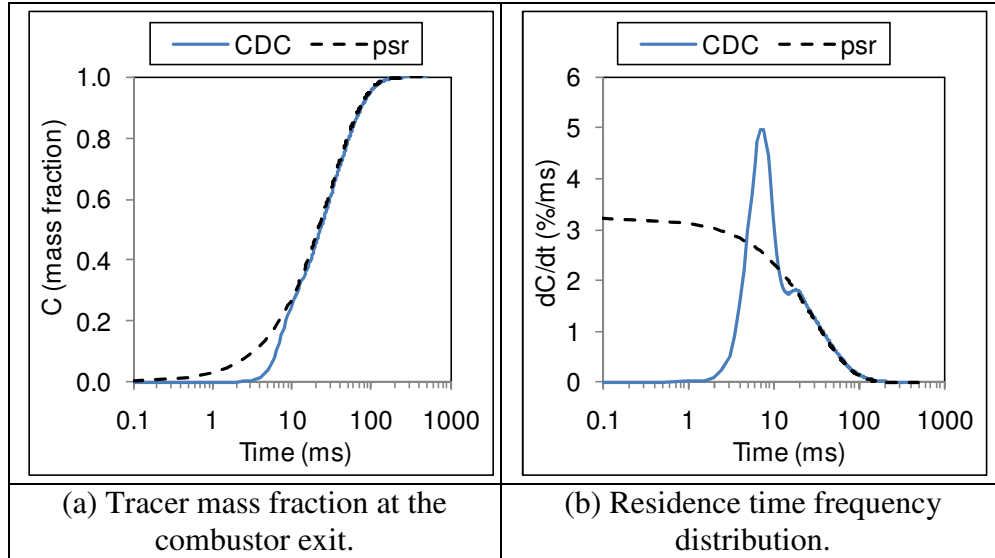


Figure 6.8 (a) Tracer mass fraction at the exit and (b) residence time frequency distribution for CDC combustor and comparison with perfectly stirred reactor (psr).

6.4.2 Global Pictures

Global photographs for the CDC combustor are shown in Figure 6.9. The combustor has full optical access in the test section having quartz windows of size $8D \times 16D$ for the combustor size of $8D \times 16D$, where D is the air injection diameter, $D=3/16$ inch. Only photographs for methane fuel case (case 1 and 4, see Table 6.1) are shown in both non-premixed and premixed mode. For both non-premixed and premixed mode of operation almost no colour of the flame (hence called colorless combustion) is observed and most of the visible light emissions is emanating from the glow of combustor walls. For premixed combustion mode higher glow from the combustor walls near the bottom is present, suggesting the presence of high temperature gases possibly due to the presence of reaction zone in that region. For all the cases combustor wall glow decreases with decrease in equivalence ratio due to lower associated adiabatic flame temperatures. For non-premixed case flame could not be sustained at equivalence ratio of 0.5 and for premixed case flame could not be

sustained at equivalence ratio of 0.5 and 0.6 hence the corresponding combustion zone photographs are not presented. However for realistic gas turbine conditions with high air preheat temperatures at inlet to the combustor (from the compressor) we anticipate the onset of stable flame at much lower equivalence ratios. Under these conditions the stability limits of the flame will be much improved.

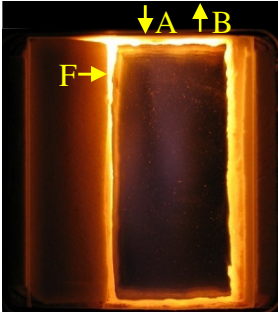
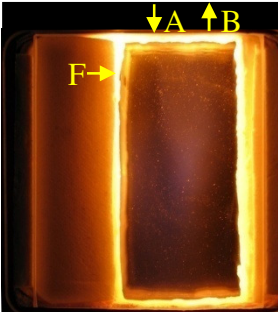
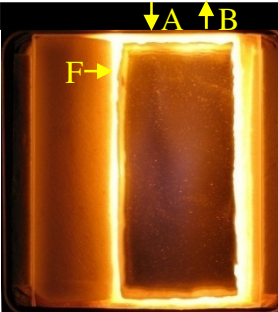
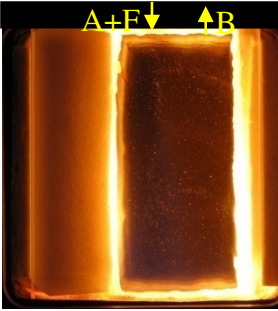
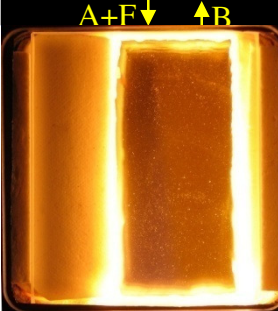
No Flame			
(a) Non-premixed ($\Phi=0.5$)	(b) Non-premixed ($\Phi=0.6$)	(c) Non-premixed ($\Phi=0.7$)	(d) Non-premixed ($\Phi=0.8$)
No Flame	No Flame		
(e) Premixed ($\Phi=0.5$)	(f) Premixed ($\Phi=0.6$)	(g) Premixed ($\Phi=0.7$)	(h) Premixed ($\Phi=0.8$)

Figure 6.9 Global pictures for pure methane fuel for (a-d) non-premixed (e-h) premixed mode (A=Air, B=Burned gases, F=Fuel).

6.4.3 OH^* Distribution

The OH^* distribution for the CDC combustor for non-premixed mode (cases 1-3, see Table 6.1) is shown in Figure 6.10. For pure methane (case 1, see Table 6.1) the reaction zone is observed to be present towards the left side of combustor, which then spreads along the length of the combustor (see Figure 6.10(a-d)). With hydrogen addition of 4 and 8wt% (cases 2 and 3 respectively, see Table 6.1) reaction zone is

observed to shift towards the fuel injection location. This is attributed to smaller ignition delay time and higher flame speed for hydrogen enriched methane fuel [Cheng, R. K. and Oppenheim, A. K., 1984] as compared to pure methane fuel. Reduction in ignition delay time may result in earlier ignition of the fuel/oxidizer mixture and result in shifting of reaction zone towards the fuel injection location. The intensity of OH^* radicals is observed to increase (see Figure 6.10(e-h) and 6.7(i-l)) and this may be because of higher OH^* radical concentration in the flame due to addition of hydrogen [Derek, D. R., 2007]. Shifting of reaction zone towards the fuel injection location is expected to increase the residence time of burned gases inside the combustor which aid in conversion of CO to CO_2 . Furthermore, higher concentration of OH radicals is expected to increase the conversion of CO to CO_2 [Derek, D. R., 2007]. Hence, addition of hydrogen to methane fuel can aid in reduction of CO emissions. For all the cases increase in equivalence ratio resulted in higher OH^* radical emission as observed from Figure 6.10.

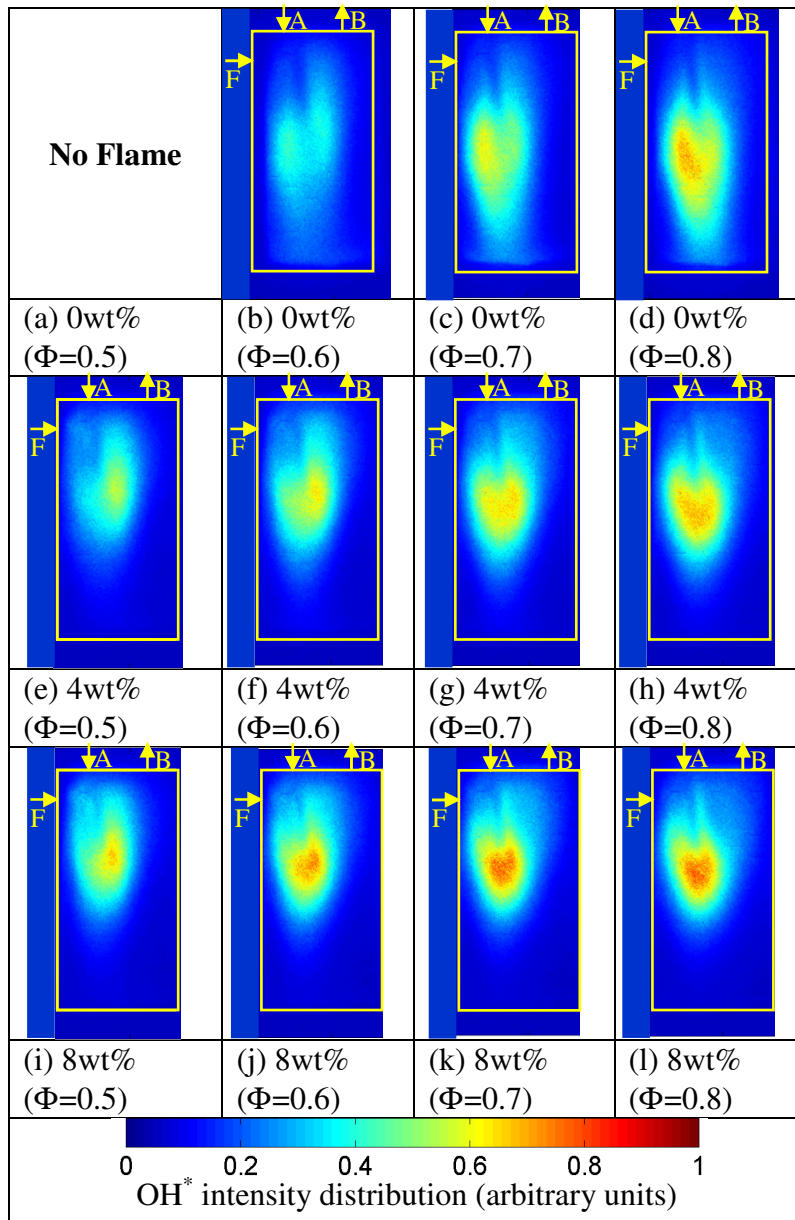


Figure 6.10 OH* distribution of non-premixed mode for (a-d) 0wt% H_2 , (e-h) 4wt% H_2 , and (i-l) 8wt% H_2 (A=Air, B=Burned gases, F=Fuel).

The OH* distribution for CDC combustor for premixed mode (cases 4-6, see Table 6.1) is shown in Figure 6.11. Similar to the non-premixed mode, addition of hydrogen resulted in higher OH* radical emission as well as shifting of reaction zone towards the air injection port. This may be due to higher concentration of OH* radicals in the flame. In premixed mode as air and fuel are uniformly mixed and injected from the

air injection port the reaction zone is mostly confined along the air jet as shown in Figure 6.11. This effect is enhanced with higher amount of hydrogen addition (8wt%, case 6, Table 6.1) at equivalence ratio of 0.8. Similar to non-premixed cases, shifting of reaction zone towards the air injection port is expected to increase the residence time available for CO conversion and hence with hydrogen addition lower CO emissions are expected. The conversion of CO to CO₂ is further enhanced due to higher OH^{*} radical concentrations with addition of hydrogen to methane fuel [Derek, D. R., 2007]. As the reaction zone for 0wt% hydrogen addition (case 4, see Table 6.1) is just above the bottom of combustor, high temperature gases will be present in vicinity of bottom regions of the combustor; this can be observed from higher glow near to bottom region of combustor wall shown in Figure 6.9(h).

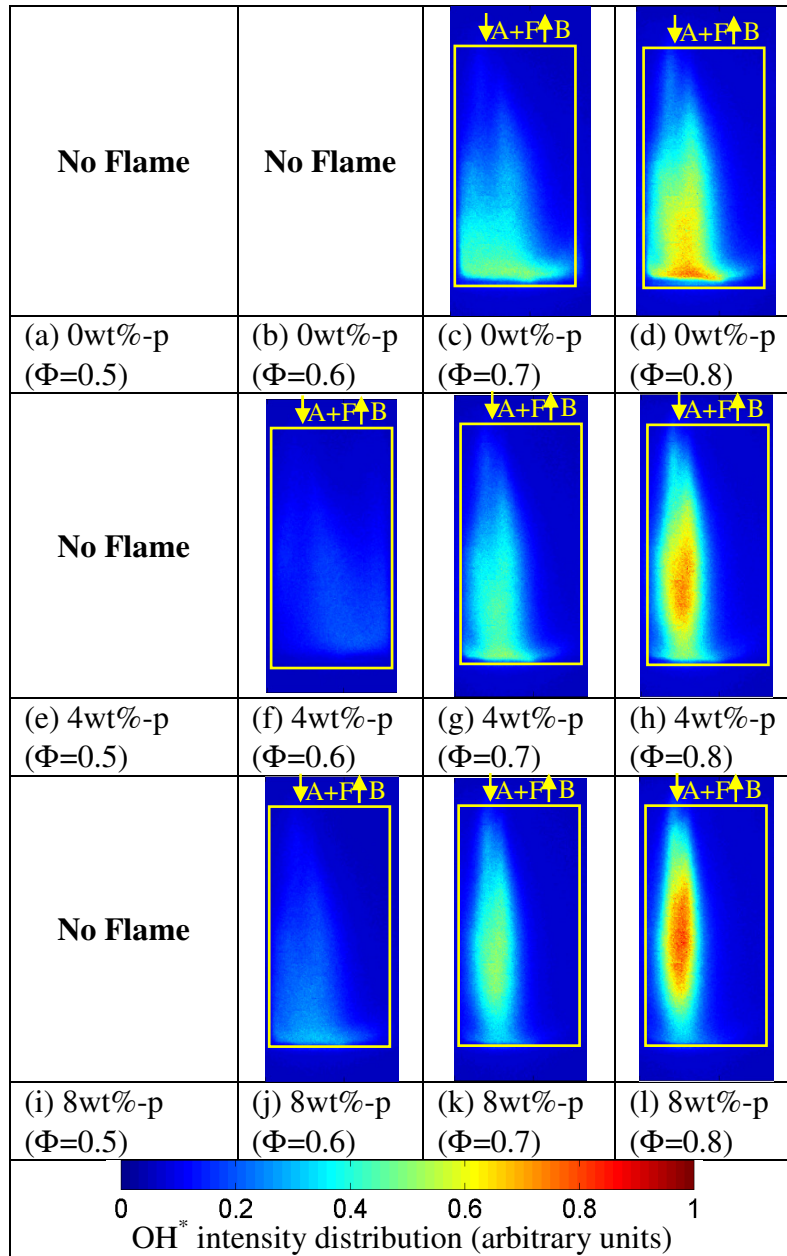


Figure 6.11 OH* distribution of premixed mode for (a-d) 0wt% H_2 , (e-h) 4wt% H_2 , and (i-l) 8wt% H_2 (A=Air, B=Burned gases, F=Fuel).

6.4.4 NO and CO Emissions

Perfectly stirred reactor calculations were performed using GRI 3.0 mechanism [Smith, G. P., *et al.*]. It was suggested in a previous investigation that GRI mechanism is well-suited for modelling combustion of methane with hydrogen addition [Jackson, G. S., *et al.*, 2003]. Residence time is assumed to be 6ms for all the

cases based on the gas density at equivalence ratio of 0.8 and calculated from equation 2.5). It may be noted that for non-reacting and perfectly stirred reactor case, the residence time is about 31ms; however for reacting condition the gas density is lower hence the residence time is also lower (see equation 2.5). NO emission levels corrected to 15% O₂ in exit gas stream for the perfectly stirred reactor mode for 0-8wt% of hydrogen addition to methane is shown in Figure 6.12(a). From Figure 6.12(a) it can be observed that NO emission level increases slightly with the addition of hydrogen to methane fuel. This suggests that hydrogen addition results in slight increase in NO emissions at same equivalence ratio possibly due to higher associated flame temperature (see Table 6.1).

The CO emission level corrected to 15% O₂ in the exit gases for perfectly stirred reactor case is shown in Figure 6.12(b). From the figure it can be inferred that the CO emission level are lower with hydrogen enrichment of the fuel. This can be attributed to lower carbon content in the fuel with hydrogen enrichment as well as higher concentration of OH* radicals and higher flame temperatures to enhance conversion of CO to CO₂ [Derek, D. R., 2007].

NO emission level for non-premixed mode for 0-8wt% of hydrogen addition to methane is shown in Figure 6.12(a). In all three cases very low NO levels (single digit) are observed. Lowest NO levels are observed for pure methane (case 1, see Table 6.1) where the NO level was found to be only about 4ppm at $\Phi=0.7$. With addition of hydrogen for non-premixed configuration cases 2, 3, (see Table 6.1) the NO emission levels are higher as compared to the pure methane case. This may be due to smaller ignition delay time for hydrogen enriched fuel case as compared to

pure methane fuel case [Cheng, R. K. and Oppenheim, A. K., 1984]. Due to smaller ignition delay time the fuel/oxidizer mixture can react earlier without uniform mixing of the fuel and oxidizer. From Table 6.1 it can be observed that with addition of hydrogen the fuel injection velocity increases to result in faster mixing of fuel in the oxidizer. However, for the present case it is possible that the reduction in ignition delay is much more significant as compared to increase in mixing of fuel. Hence this results in overall increase in the hotspot regions and higher NO emissions for hydrogen enriched fuel case.

The CO emission level in exit gases for non-premixed CDC combustor is shown in Figure 6.12(b). It can be observed that addition of hydrogen to methane fuel reduces the amounts of CO levels. This can be attributed to higher residence time of the burned gases as well as higher OH^* radical concentration for cases with hydrogen addition, see discussion for Figure 6.10. The conversion of CO to CO_2 is slower as compared to other species and hence residence time has significant effect on the CO levels. Lower CO levels can also be expected with addition of hydrogen to methane due to lower carbon content in the fuel. Furthermore the CO levels for non-premixed mode is significantly lower as compared to the perfectly stirred reactor case, and this can be attributed to higher residence time available for the reverse flow geometry of CDC combustor, see discussion for Figure 6.8.

NO emission levels for premixed mode (cases 4-6, see Table 6.1) are shown in Figure 6.12(c). The effect of hydrogen addition to methane on NO emission levels is indistinguishable. In all the cases very low NO emissions are obtained (~1ppm). It may be noted that for premixed case ignition delay time does not play a significant

role as compared to non-premixed case. In non-premixed cases the reactants are expected to mix uniformly prior to ignition, thus avoiding any hot spot regions. As in premixed case reactants are already thoroughly mixed at the point of entry to combustor, NO emissions will mostly be governed by the adiabatic flame temperature.

CO emission level for the premixed mode (cases 4-6, see Table 6.1) is shown in Figure 6.12(d). Similar to non-premixed case CO emission levels are lower with the addition of hydrogen to methane. This may be due to higher residence time as well as higher concentration of OH^* radical and higher temperatures for the cases with hydrogen addition (see discussion corresponding to Figure 6.11). Lower carbon content with addition of hydrogen to methane is also expected to reduce CO emissions. CO emission levels are lower than both non-premixed mode and calculations from perfectly stirred reactor.

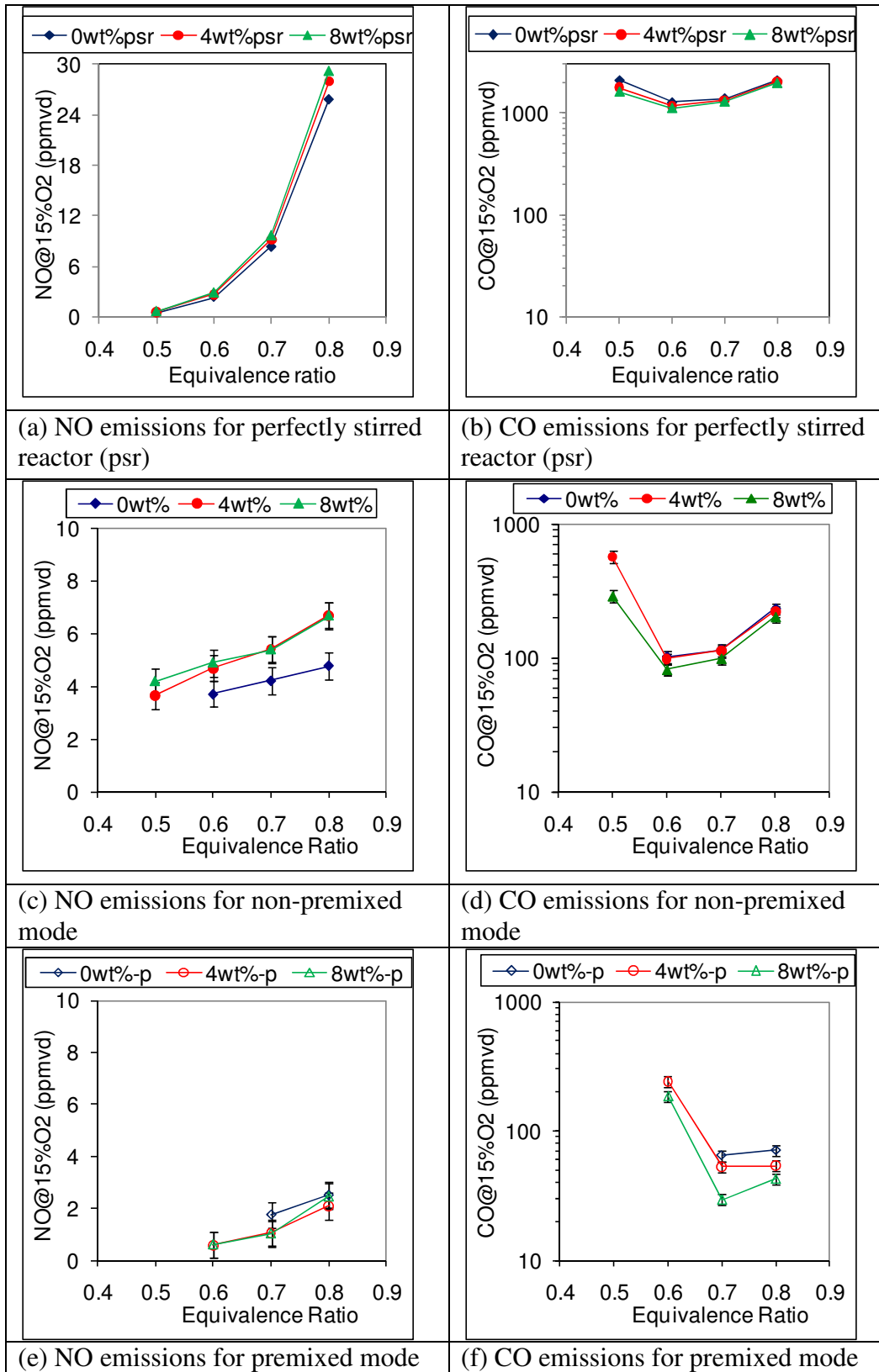


Figure 6.12 NO and CO emissions for (a-b) perfectly stirred reactor, (c-d) non-premixed mode and (e-f) premixed mode.

6.4.5 Lean Operational Limit

Wider stability limits (lower lean operational limit) is desirable to achieve higher turndown ratio for part-load gas turbine operation as well as operation of combustor at low adiabatic flame temperatures to minimize NO_x emissions. Lean operational limit for six cases (see Table 6.1) and for perfectly stirred reactor is shown in Figure 6.13. To obtain lean operational limit air flow rate was slowly increased at constant heat load until blowoff occurred. For perfectly stirred reactor case lean operational limit was obtained at the equivalence ratio where blowoff occurred.

From the figure it can be noted that with hydrogen addition, lean operational limit is extended for both premixed and non-premixed CDC modes. Calculations for perfectly stirred reactor also suggest extension of lean operational limit with hydrogen addition. Lowest lean operational limit ($\Phi=0.37$) for the combustor was obtained for 8wt% hydrogen addition in non-premixed mode (case 3, see Table 6.1). The operational limits for premixed mode of operation were higher as compared to the non-premixed case and the highest limit ($\Phi=0.6$) was obtained for 0wt% hydrogen addition (case 4, see Table 6.1). Hence it can be inferred that addition of hydrogen can be used to extend the lean operational limit for the combustor.

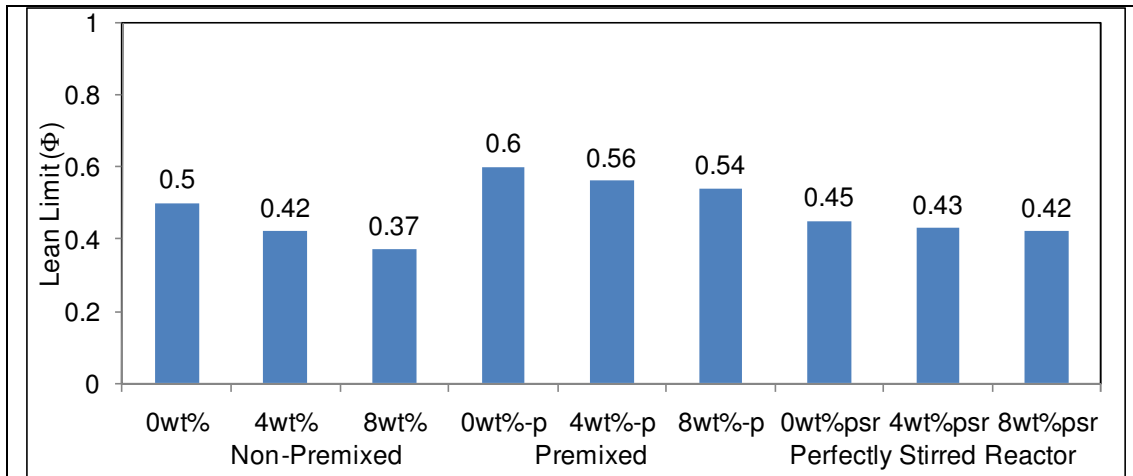


Figure 6.13 Lean operational limit with different amount of hydrogen addition to methane fuel.

6.5 Conclusions

Five different flowfield configurations, including one premixed mode and four non-premixed modes, have been examined in this chapter at thermal intensity of $57\text{MW/m}^3\text{-atm}$. Configurations where fuel was injected in cross-flow produced lower pollutant emissions possibly due to faster fuel/oxidizer mixing. Experimental studies show ultra low NO emissions for both premixed and non-premixed flow configurations (2 ppm for “RP”, 3 ppm for “RC1” at $\Phi=0.7$). Low CO emissions were observed for the premixed flow configurations, “RP” (96ppm at $\Phi=0.7$) as well as the non-premixed configuration “RC1” (57ppm, $\Phi=0.7$). As the fuel injection location was shifted downwards, away from air injection for reverse-cross flow configuration, NO and CO emissions increased possibly due to reduced mixing as well as lower residence time for the gases. Higher turndown could be achieved by changing the fuel injection location as the lean operational limit was extended when the fuel injection location was shifted down. Under investigated conditions, reverse-cross flow non-premixed configuration “RC1” showed better promise to achieve

lower NO as well as CO emissions and favourable combustion characteristics that are closer to the colorless distributed combustion (CDC) regime.

Configuration “RC1” was further investigated at thermal intensity of $85\text{MW/m}^3\text{-atm}$ for the effect of addition of hydrogen to methane fuel. Numerical simulations suggest that significant recirculation of gases was present and maximum recirculation was limited due to the confinement. Residence time calculation suggests that CDC combustor can result in lower CO emissions as compared to perfectly stirred reactor case due to lower associated residence time. Experimental studies show ultra low NO emissions for both non-premixed and premixed flow configurations (1ppm for premixed and 4ppm for non-premixed, $\Phi=0.7$). CO emissions in both premixed and non-premixed cases were lower as compared to the calculated values for perfectly stirred reactor. Addition of hydrogen to methane resulted in increase in NO emissions in the non-premixed case. CO emissions decreased significantly with addition of hydrogen for both premixed and non-premixed modes. Addition of hydrogen extended the operational limits of the CDC combustor.

Chapter 7 : Ultra-High Thermal Intensity (53-198MW/m³-atm)

From Chapter 6 it was noted that reverse cross-flow geometry shows promise to achieve ultra-low NO and CO emissions. The down selected reverse-cross flow geometry has been investigated in this chapter to obtain the combustion characteristics of CDC combustor. Two different geometry sizes were investigated with thermal intensity variation from 53-85MW/m³-atm for the first geometry and 156-198MW/m³-atm for the other geometry. The air injection diameter is increased to 5D/3 as compared to D used in previous investigation (see Chapter 5 and 6) to minimize pressure loss across the combustor. Air flow rate is kept constant while varying the fuel flow rate to simulate different power settings of gas turbine combustor operation. It may be noted that in previous investigations (see Chapter 4, 5 and 6) fuel flow rate (hence the heat load as well as thermal intensity) was kept constant while air flow rate was varied to change the equivalence ratio. Pressure fluctuations inside the combustor have been measured to obtain stability characteristics of the combustor. Pressure drop across the combustor as well as heat loss from the combustor has been reported. Global reaction zone features as well as reaction zone location using OH* chemiluminescence imaging has been included. The flowfield in non-reacting flow condition has been obtained using particle image velocimetry (PIV) technique.

7.1 Experimental Set Up (53-85MW/m³-atm)

Figure 7.1 show a photograph and schematics of the CDC combustor examined here. The depth of the combustor is 1inch, length is 3inch and width is 1.5inch. The

combustor operates at thermal intensity range of 53-85MW/m³-atm at equivalence ratios of 0.5-0.8. The heat load varied from 3.91-6.25kW for equivalence ratio variation of 0.5-0.8 with constant air flow rate. The combustor was of rectangular cross section with good optical access to provide detailed combustion diagnostics. Air was injected from the exit side as shown in Figure 7.1 and fuel was either injected in cross-flow in non-premixed condition (Figure 7.1(c)) or thoroughly mixed with the combustion air in novel premixed condition (Figure 7.1(d)). Air could be preheated using an electrical heater up to 600K air preheat temperature. The fuel was injected at normal temperature condition.

The premixed flame mode was expected to provide minimum thermal NO_x and hence it can be considered as a baseline case for comparison with the non-premixed cases. It may be noted that the configuration discussed here cannot be started directly can then be transitioned to the CDC mode of combustor operation. so that a pilot flame is required (not shown here) for the initial heat up period, which

For the given operating condition, the time and length scales are calculated based on the air jet exit characteristics.

Length scale (Air):

$$\text{Kolmogorov length scale} = l_k = l_0 (Re_{l_0}^{-3/4}) = 0.019mm$$

$$\text{Integral length scale} = l_0 = \frac{d_{jet}}{10} = 0.794mm =, d_{jet} = 5/16inch$$

$$\text{Turbulence Reynolds number} = Re_{l_0} = \frac{\rho v_{rms} l_0}{\mu} = 143.23$$

$$\text{Root-mean-square fluctuating velocity} = v_{rms} = \frac{V_{mean}}{10} = 9.2m/s, \text{ assuming } 10\% \text{ turbulence intensity, } V_{mean} = 92m/s$$

Length scale (Fuel):

$$\text{Kolmogorov length scale} = l_k = l_0 (Re_{l_0}^{-3/4}) = 0.007 \text{ mm}$$

$$\text{Integral length scale} = l_0 = \frac{d_{jet}}{10} = 0.159 \text{ mm}, d_{jet} = 1/16 \text{ inch}$$

$$\text{Turbulence Reynolds number} = Re_{l_0} = \frac{\rho v_{rms} l_0}{\mu} = 57.36$$

$$\text{Root-mean-square fluctuating velocity} = v_{rms} = \frac{V_{mean}}{10} = 6.1 \text{ m/s}, \text{ assuming } 10\%$$

$$\text{turbulence intensity, } V_{mean} = 61 \text{ m/s}$$

Mixing time scale (Air):

$$\text{Integral time scale} = \tau_{flow} = \frac{l_0}{v_{rms}} = 0.086 \text{ ms}$$

$$\text{Kolmogorov time scale} = \tau_k = \frac{\tau_{flow}}{Re_{l_0}^{1/2}} = 0.007 \text{ ms}$$

Mixing time scale (Fuel):

$$\text{Integral time scale} = \tau_{flow} = \frac{l_0}{v_{rms}} = 0.026 \text{ ms}$$

$$\text{Kolmogorov time scale} = \tau_k = \frac{\tau_{flow}}{Re_{l_0}^{1/2}} = 0.003 \text{ ms}$$

Chemical time scale (Premixed):

$$\text{Laminar flame speed} = S_L = 0.44 \text{ m/s}, T_u = 600 \text{ K}, \Phi = 0.5, O_2 = 21\%, \text{ CHEMKIN}$$

$$\text{Laminar flame thickness} = \delta_L = \frac{2k}{\rho_u c_p S_L} = 0.514 \text{ mm}, T_{avg} = 1160 \text{ K}$$

$$\text{Chemical time scale} = \tau_{flow} = \frac{\delta_L}{S_L} = 1.168 \text{ ms}$$

Damkohler number (Premixed):

$$Da = \frac{\tau_{flow}}{\tau_{chem}} = 0.07$$

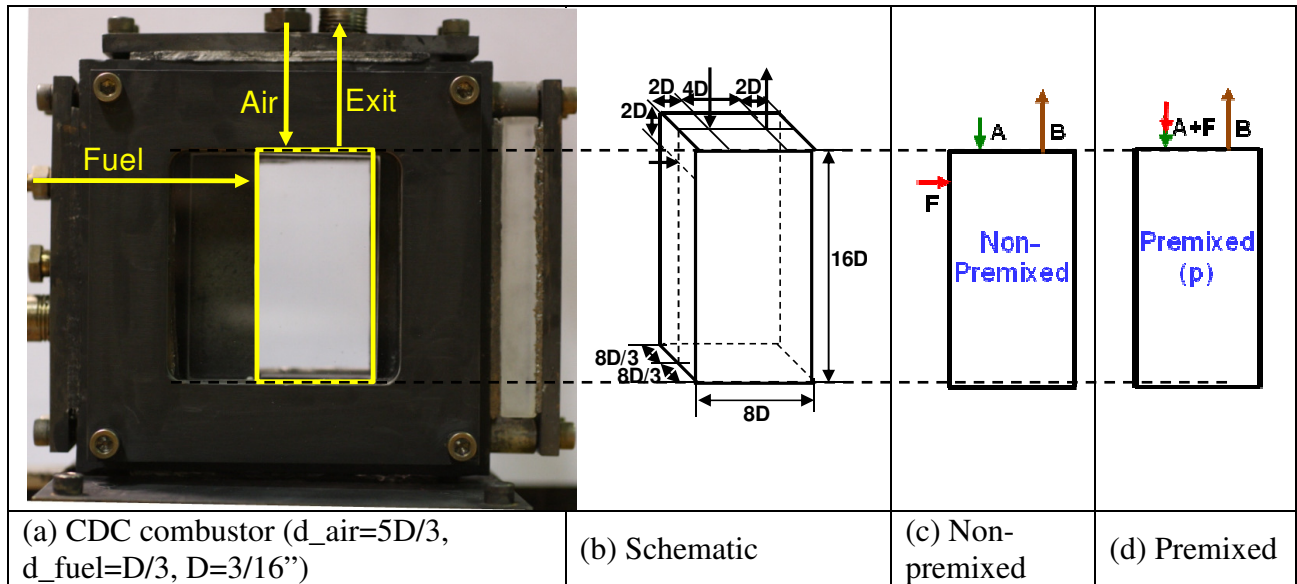


Figure 7.1 (a) photograph (b) schematic (c) non-premixed and (d) premixed mode for high thermal intensity ($53\text{-}85\text{MW/m}^3\text{-atm}$) CDC combustor.

The combustor was operated at a heat load of $3.91\text{-}6.25\text{kW}$ for equivalence ratio variation from $0.5\text{-}0.8$, at a high thermal intensity of $53\text{-}85\text{MW/m}^3\text{-atm}$ using methane as the fuel. Methane was injected at ambient temperature of 300K and air was injected at both ambient temperature of 300K and higher temperature of 600K to investigate the effect of air preheat temperature. The operating pressure was 1atm . The inlet fuel injection velocity varied from about $61\text{-}97\text{m/s}$ and this allowed for equivalence ratio to vary from 0.8 to 0.5 .

The combustor was allowed to run for about 20minutes in each configuration before taking the experimental data. Gas analyzer was used to obtain NO and CO emission level, see Appendix G for further details. The emission readings were observed to stabilize within 3 minutes for any change in experimental condition (here change in equivalence ratio for the same configuration). The experiments were repeated at least three times for each configuration and the uncertainty was estimated to be about $\pm 0.5\text{ppm}$ for NO and $\pm 10\%$ for CO emissions. The chemiluminescence

intensity from OH^* radicals in the flame was obtained using an ICCD camera coupled with a narrow band interference filter (OH^* at 307 nm) with camera f-stop setting of f-8, exposure time of 100ms and gain of 100 for all the conditions.

The experimental setup for particle image velocimetry experiments is shown in Figure 7.2(a). It may be noted that for PIV set-up the depth of combustor used is 1.5inch (see Figure 7.2(a) instead of 1inch as shown in Figure7.1(b)). The details of PIV setup is listed in Table 7.1. Width of view of the camera is 1.25inch for combustor width of 1.5inch. Smaller width of view is used to minimize reflection of laser sheet from the combustion walls so as to avoid its interference with the acquired images. The height of view was about 0.9inch so that the camera needs to be shifted along the length of the combustor to acquire complete flowfield data in the combustor. Alumina powder was used as the seed particle with particle size of about $3\mu\text{m}$. The seeder is schematically shown in Figure 7.2(b). Alumina powder was heated using an electric heating tape to about 200°C for about 2hours to remove moisture and minimize agglomeration of the alumina powder. High velocity air jet of about 170m/s from a hole of 1/16inch was introduced under the seed bed, as shown in Figure 7.2(b), to obtain a steady and uniform seeding. Combustion air was mixed with the seeding air as shown in Figure 7.2(b) with seed air flowrate of about 15% of the combustion air flowrate. The quartz windows were heated using propane torch as shown in Figure 7.2(c) to avoid deposition of alumina powder on the windows. Alumina powder was observed to have high tendency to deposit on the quartz windows which interfered to acquire good quality images. Heating of quartz windows provided a potent solution to minimize deposition of alumina powder on the quartz

windows possibly due to thermophoresis effect [Sung, C. J., *et al.*, 1994]. The effect of hot windows on the flowfield was not quantified in the present work. The laser sheet beam had a thickness of about 1mm and was used to illuminate the seed particles in the flow. The laser pulse frequency was 5Hz and pulse separation of 2μs was used to resolve high velocity regions. Interrogation window size of 48×48pixels was used to give spatial resolution of about 1.13×1.13mm. It may be noted that the Kolmogorov scales as calculated in section 7.1 is much smaller than the spatial resolution of PIV. The time response of particles following the flow is calculated as given in equation 7.1 for high particle to gas density ration case [Melling, A., 1997, Picano, F., *et al.*, 2010, Stella, A., *et al.*, 2001].

$$\frac{dU_p}{dt} = -\left(\frac{1}{\tau_p}\right)(U_p - U_f) \quad (\text{equation 7.1})$$

$$\text{characteristic particle time scale} = \tau_p = \frac{d_p^2 \rho_p}{18\mu}$$

$$\rho_p = \text{particle density}$$

$$d_p = \text{particle diameter}$$

$$\mu = \text{gas dynamic viscosity}$$

Piezoelectric dynamic pressure transducer is used to measure pressure fluctuations inside the combustor. The set-up for measurement of the dynamic pressure fluctuations is shown in Figure 7.2(d). A 3/16inch diameter ceramic tube with 3inch length was used to connect the combustion chamber with pressure transducer. The pressure transducer was water cooled (arrangement not shown here) to avoid damage from overheating during operation in combusting conditions. The data acquisition rate was about 10kHz and 100 thousand samples were acquired for a duration of 10s.

Fast Fourier Transform (FFT) was used to transfer the data from time domain to frequency domain and while reporting the data graphically, resolution of 10Hz was used to achieve better visibility. Thermocouple (B type) with wire diameter of 200 μ m was used to measure the temperature of the exhaust gases. The estimated error from radiation losses as well as uncertainty due to repeatability was about $\pm 10\%$. The exhaust gas temperature was used to quantify the heat loss from the combustor. Pressure drop across the combustor was measured using a digital pressure gauge having piezo-resistive pressure sensing element. The experiments were repeated at least three times for each operational point and the uncertainty was estimated to be about $\pm 10\%$ for pressure drop across the combustor.

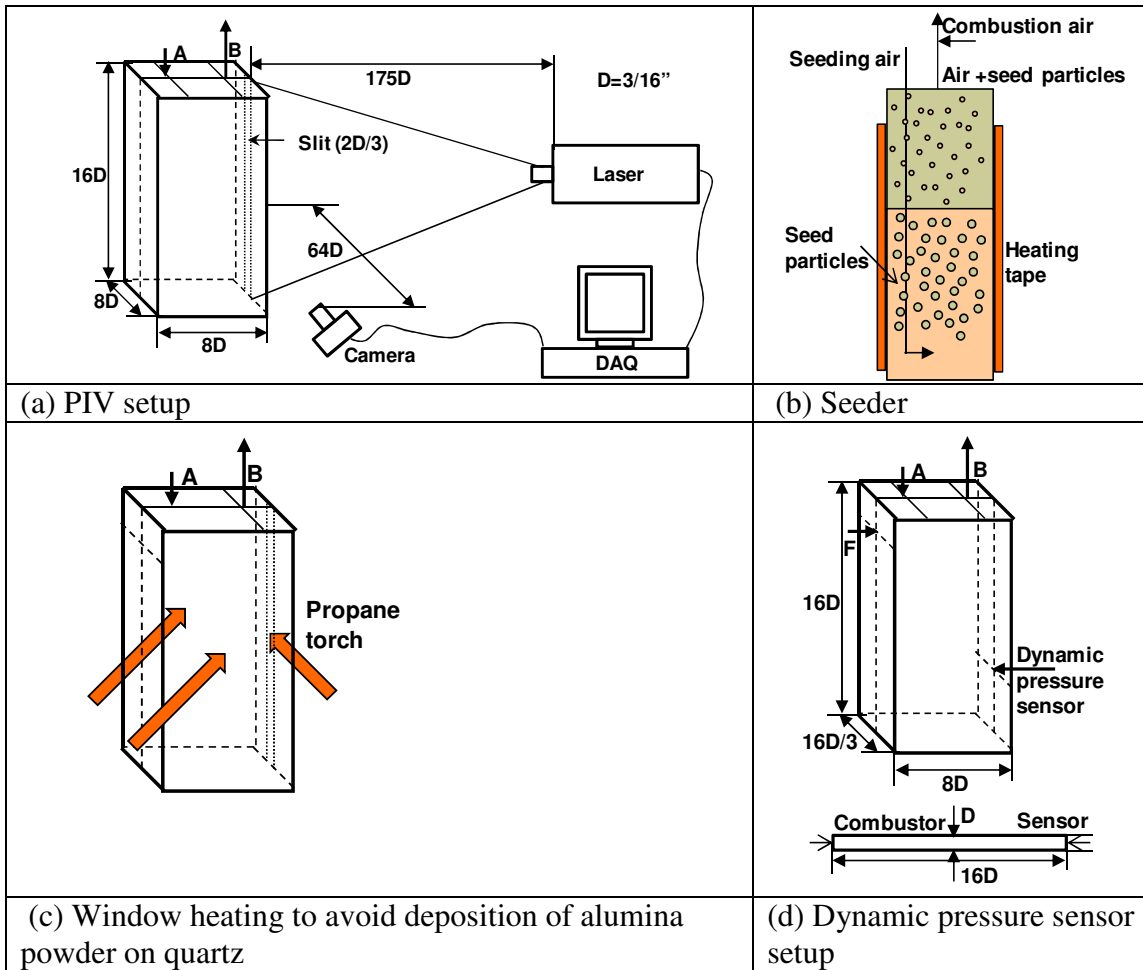


Figure 7.2 (a-c) PIV and (d) dynamic pressure sensor set-up for CDC combustor.

Table 7.1 Parameters for PIV experiment.

Seed particles	Alumina
Particle Size	3 μ m
Characteristic particle time scale	0.1ms
Acquisition rate	5Hz
Pulse separation	2 μ s
Q-switch delay	140 μ s
Laser sheet thickness	~1mm
Interrogation window	48 \times 48pixel
Spatial resolution	1.13 \times 1.13mm
Camera resolution	1360 \times 1036pixels
Width of view	1.25inch
Height of view	0.9inch
Lens focal length	60mm
f-stop setting	2.8
Seeding air	20SLPM
Combustion air	117SLPM

7.2 Results and Discussion

7.2.1 Flowfield Characteristics

Figure 7.3 shows velocity contour plots for velocity along the length (V_{mean}) and velocity along the width (U_{mean}) of the combustor and the velocity magnitude vector plot. The total area of view was about 2.75inch in length and 1.25inch in width. A distance of 1/8inch from all sides was eliminated to avoid any interference from the laser sheet reflection from the walls. From Figure 7.3(a) and (c) it can be observed that the air jet decays along the length of the combustor and reverses its direction to

escape from the exit located on the top side of the combustor. Very low velocity region is present on the right side of the air jet. The velocity contour and vector plot suggests that air accelerates just near the combustor exit and velocity increases from less than 3m/s to about 18m/s at the exit. From the Figure 7.3(b) it can be noted that the air jet splits into two parts after reaching the bottom portion of the combustor and recirculate from both left and right side of the air jet. This may be the reason for low velocity region on the right side of the air jet for the velocity data obtained from the experiments as shown in Figure 7.3(a).

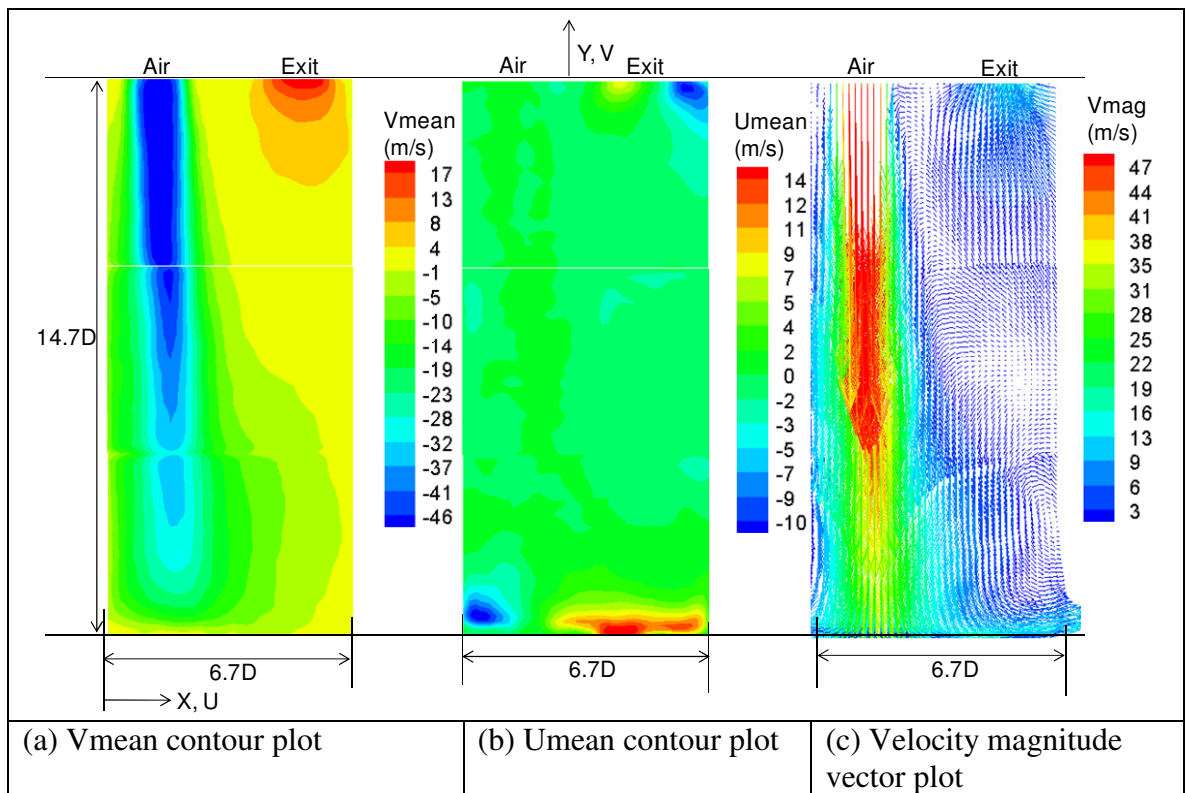


Figure 7.3 (a-b) Velocity contour plot and (b) vector plot obtained from PIV experiments, $T_{air}=300K$.

Figure 7.4 shows the fluctuating velocity along the length (V_{rms}) and width (U_{rms}) of the combustor. From the figure one can observe that high turbulence levels are present near the outer periphery of air jet in the shear region. The figure also

suggests that injection of fuel in this high turbulence region may result in faster mixing and hence reduce the pollutant emission from the combustor. V_{rms} values were observed to be higher than the U_{rms} values suggesting that the assumption of isotropic turbulence may not be valid for the present case.

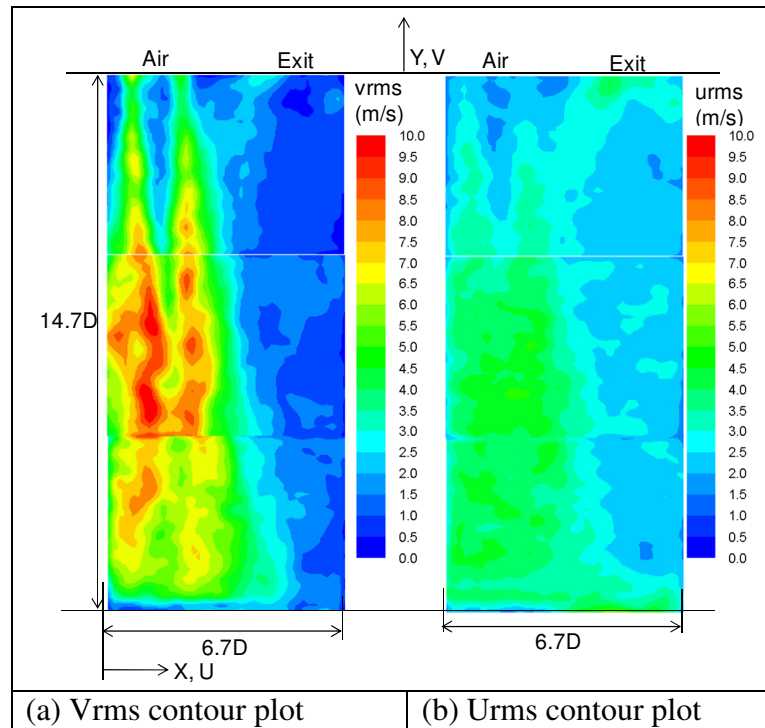


Figure 7.4 Fluctuating velocity contour plots obtained from PIV experiments, $T_{air}=300K$.

7.2.2 Global Pictures

Global reaction zone photographs for both non-premixed and premixed modes for the CDC combustor are shown in Figure 7.5. The air injection temperature for these cases was 600K. Almost colorless flames are observed for both non-premixed and premixed modes of combustor operation. In non-premixed mode bluish region near the region of fuel injection could be observed suggesting the presence of reaction zone. With decrease in equivalence ratio one can observe that the bluish reaction zone moves closer to the left combustor wall suggesting faster decay of fuel jet. This may

be due to lower momentum of fuel jet at lower equivalence ratio. Almost colorless reaction zones are observed for the premixed flow modes where higher glow from combustor walls could be observed with increase in equivalence ratio due to higher associated flame temperatures.

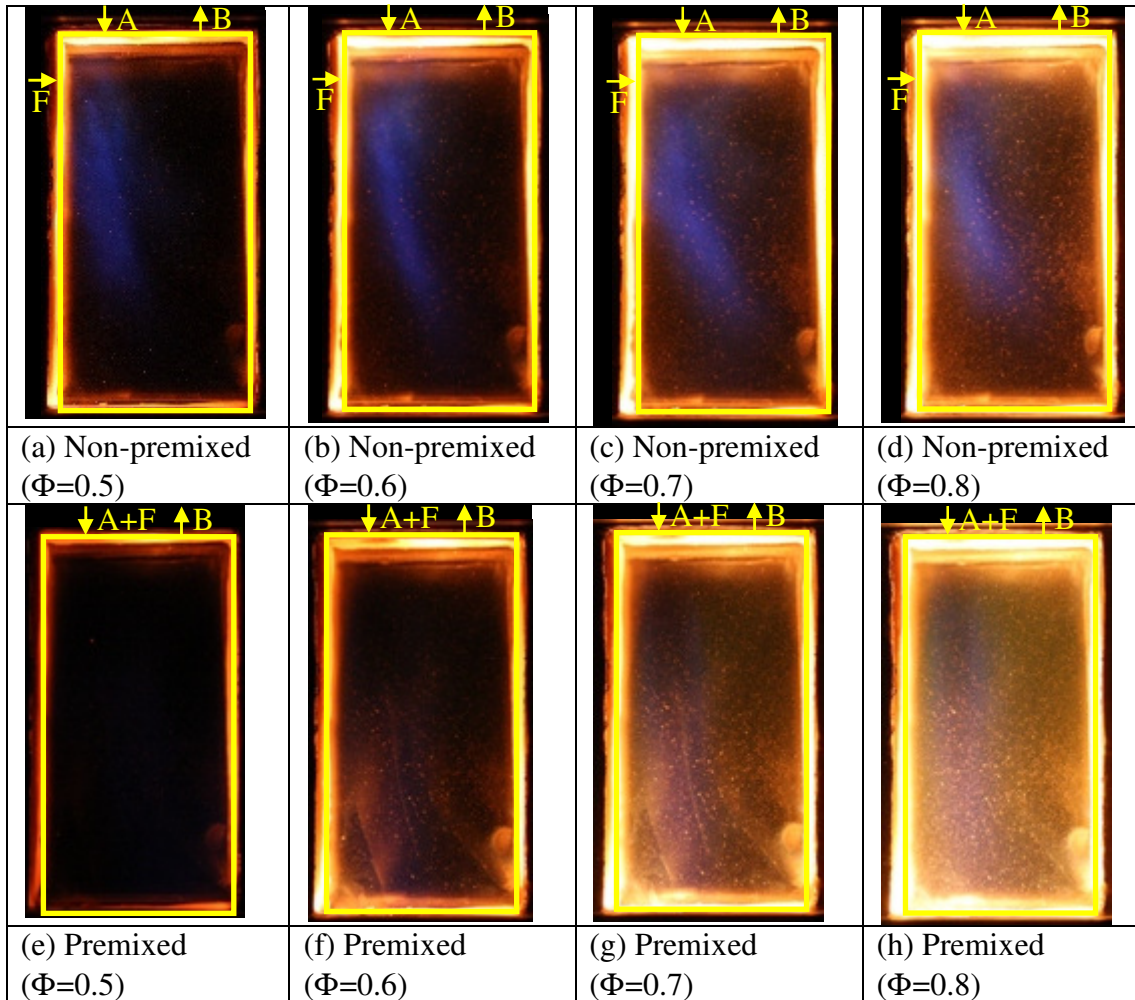


Figure 7.5 Global pictures for the CDC combustor.

7.2.3 OH^* Distribution

The OH^* distribution for both non-premixed and premixed flow mode is shown in Figure 7.6 with the air injection temperature of 600K. For non-premixed mode the reaction zone is observed to be present near the fuel injection jet, as observed from

the global flame images from Figure 7.5. With decrease in equivalence ratio the reaction zone is observed to slightly move towards the left wall of the combustor, suggesting faster decay of fuel jet (see Figure 7.6(a-d)). Higher OH^* intensity is observed with increase in equivalence ratio. The OH^* distribution for premixed mode is shown in Figure 7.6(e-h) and the reaction zone is present near the air jet. As the equivalence ratio is increased the OH^* intensity also increases as observed for the non-premixed case. For non-premixed case the OH^* intensity is much higher as compared to the premixed mode of operation suggesting that the mixing could be further enhanced to achieve more distributed reaction zone.

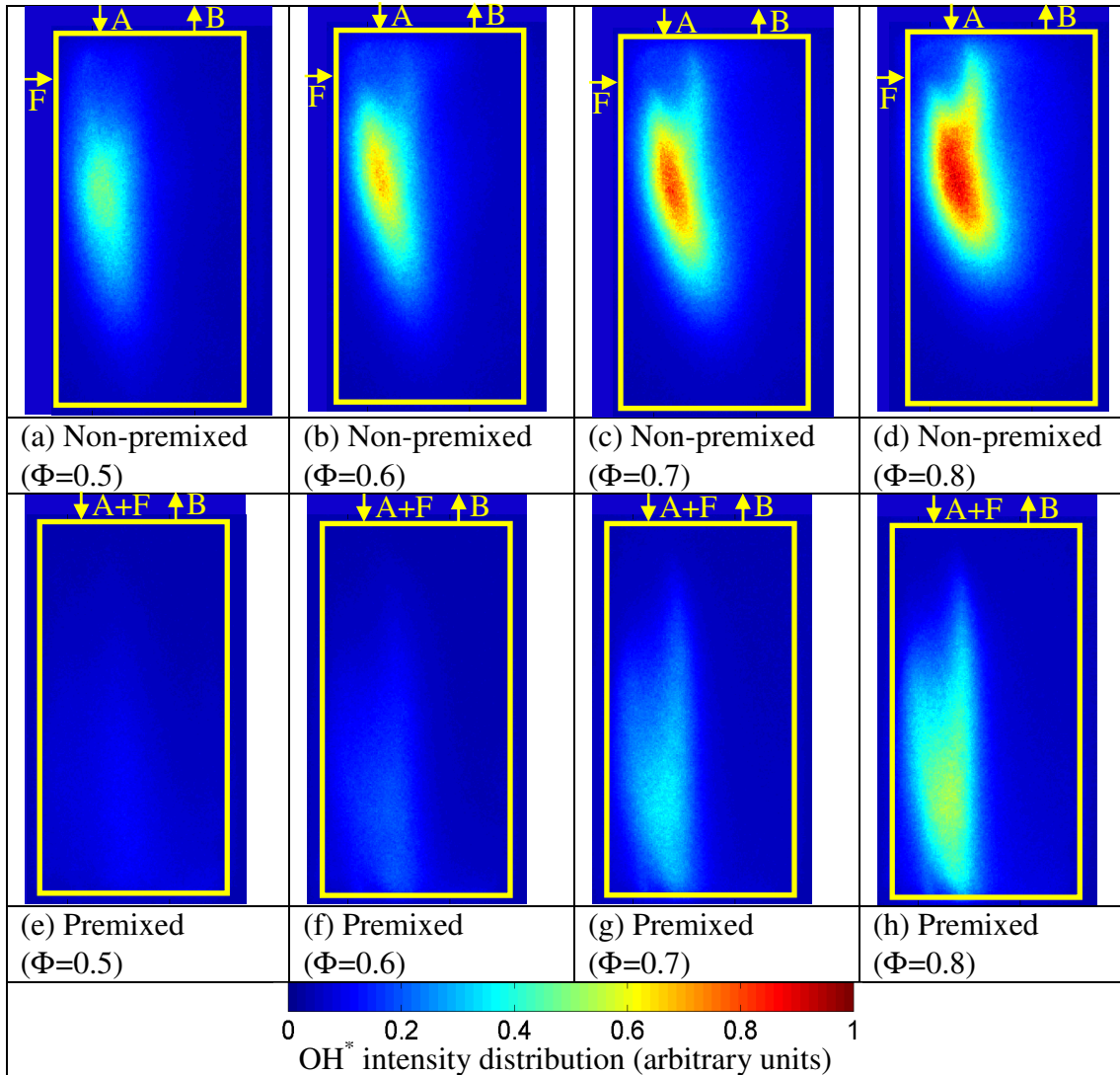


Figure 7.6 OH* chemiluminescence images for CDC combustor for (a-d) non-premixed, (e-h) premixed (A=Air, B=Burned gases, F=Fuel).

7.2.4 Emissions of NO and CO

NO emission levels corrected to 15% O₂ in exit gases for both non-premixed and premixed flow modes for the volume distributed combustion is shown in Figure 7.7(a). At higher temperature zones ($T > 1800\text{K}$) thermal mechanism is the major contributor to the total NO formation. The distributed reactions mostly suppress the formation of NO through thermal mechanism due to uniform thermal field in the entire combustion zone and avoidance of high temperature regions.

Lowest NO levels are observed for the premixed mode where the NO level was found to be only about 1ppm at equivalence ratio of 0.5 with air injection temperature of 600K. Theoretically premixed combustion mode should have minimal hot spot region resulting in the lowest NO level. For the non-premixed configurations the NO emission level is about 4ppm for air injection temperature of 600K at equivalence ratio of 0.5. For the cases with air injection temperature close to ambient conditions NO level of about 2ppm and 5ppm for premixed and non-premixed modes respectively was obtained at rather high equivalence ratio of 0.7. Increase in air preheat temperature significantly increased the NO levels at a given equivalence ratio, however increase in air preheat temperature extends the lean limit, so that the combustor could be operated at much lower equivalence ratios to provide lower NO levels.

The CO emission level corrected to 15% O₂ in the exit gases for the CDC combustor is shown in Figure 7.7(b). It can be observed that premixed modes produced lower CO levels as compared to non-premixed modes. Effect of air preheat temperature is minimal on CO emissions. Very low CO levels (about 30ppm) were obtained for air preheat temperature of 600K and equivalence ratio of 0.5 for both non-premixed and premixed modes of combustor operation.

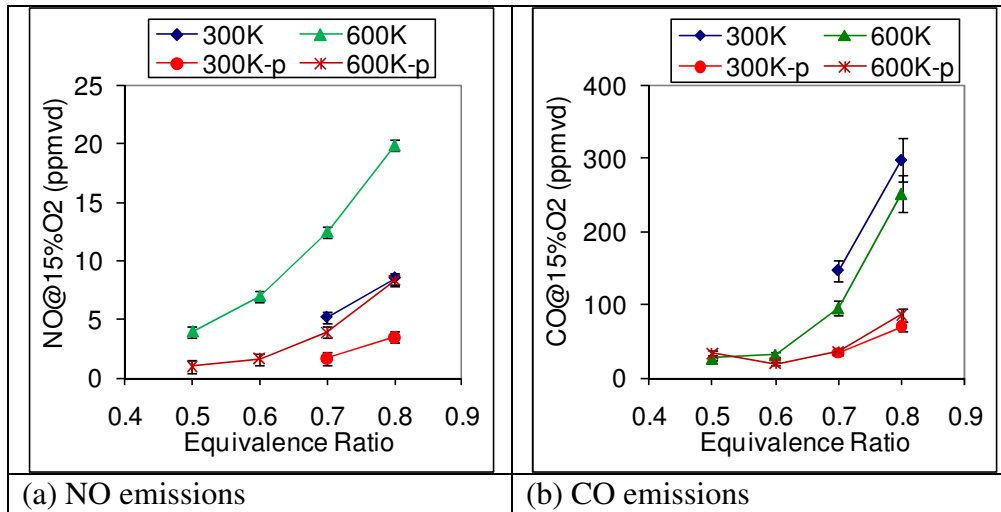


Figure 7.7 (a) NO and (b) CO emissions in non-premixed and premixed conditions (-p denotes premixed) for $T_{air}=300K$ and $600K$.

7.2.5 Dynamic Pressure Fluctuations

Lower pressure fluctuations are desirable to minimize damage to combustor hardware. Dynamic pressure fluctuations were recorded for both premixed and non-premixed flow conditions and the results are presented in Figure 7.8. The pressure fluctuations with only air flowing through the combustor are also included. For all the cases air preheat temperature of 600K are used. From Figure 7.8 one can note the presence of very low level of pressure fluctuations for both reacting and non-reacting flow conditions. For both the cases pressure fluctuations less than 0.025% of mean pressure were recorded suggesting very smooth operation of the combustor. This is much lower as compared to the industrially accepted value of 1.5%. The pressure fluctuation level in reacting flow condition is slightly higher than the pressure fluctuation level in non-reacting flow condition, as expected. With increase in equivalence ratio the pressure fluctuation level was observed to increase. The results suggest that over the range of operating conditions very smooth operation of the CDC combustor can be realized.

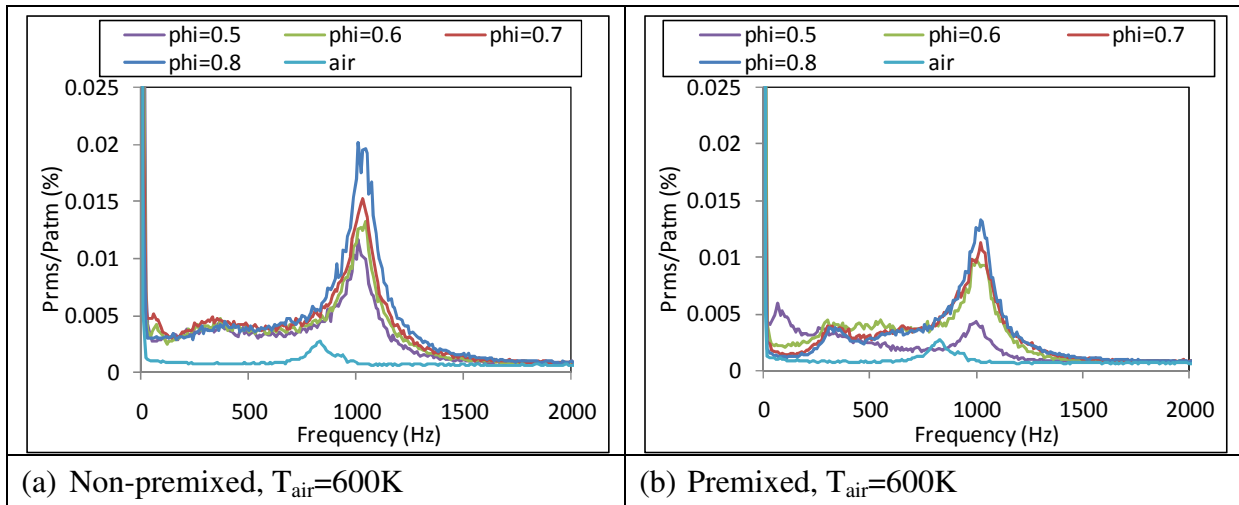


Figure 7.8 Dynamic pressure response for (a) non-premixed and (b) premixed mode.

7.2.6 Pressure Loss, Heat Loss and Lean Limit

Lower pressure loss is desirable to achieve higher efficiency from the gas turbines. Generally pressure loss of less than 5% of inlet total pressure is considered acceptable across the combustor. Pressure loss across the CDC combustor for non-premixed condition with air preheat temperature of 600K was measured and is presented in Figure 7.9(a). From the figure it can be noted that pressure loss of less than 5% can be achieved at the most desirable operating condition (at an equivalence ratio of 0.5). Pressure loss is observed to increase with equivalence ratio possibly due to higher heat addition at higher equivalence ratios. Pressure loss obtained from CFD simulations (see Figure 7.9(c)) in cold flow condition at air inlet temperature of 600K is about 3% and in reacting flow condition at equivalence ratio of 0.8 is about 5%.

Heat loss from the combustor was quantified by measuring the exhaust temperature using a 200 μ m size B type thermocouple. Gas turbine combustors ideally operates in adiabatic flow condition, hence the estimation of heat losses gives the operational behaviour of the combustor. The results presented in Figure 7.9(a) reveals that the heat losses are less than 15% of the total heat load.

Wider stability limits (lower lean flammability limit) is desirable to achieve higher turndown ratio for part-load gas turbine operation. Lean flammability limit for both premixed and non-premixed condition as well as effect of the preheat temperature is shown in Figure 7.9(b). To obtain lean limit air flow rate was slowly increased at constant heat load until blowoff occurred. Lean limit was observed to extend with increase in air preheat temperature, for example for non-premixed flow condition the lean limit extended from 0.58 to 0.44 with increase in air preheat temperature from 300K to 600K. Even though, the air preheat temperature increases NO emissions at a given equivalence ratio due to higher associated flame temperatures, lower NO levels could be achieved by operating the combustor leaner. The lean limit for non-premixed flow mode is very close to the premixed flow mode suggesting that the combustor is having characteristics closer to the premixed mode of operation even when operating in non-premixed mode.

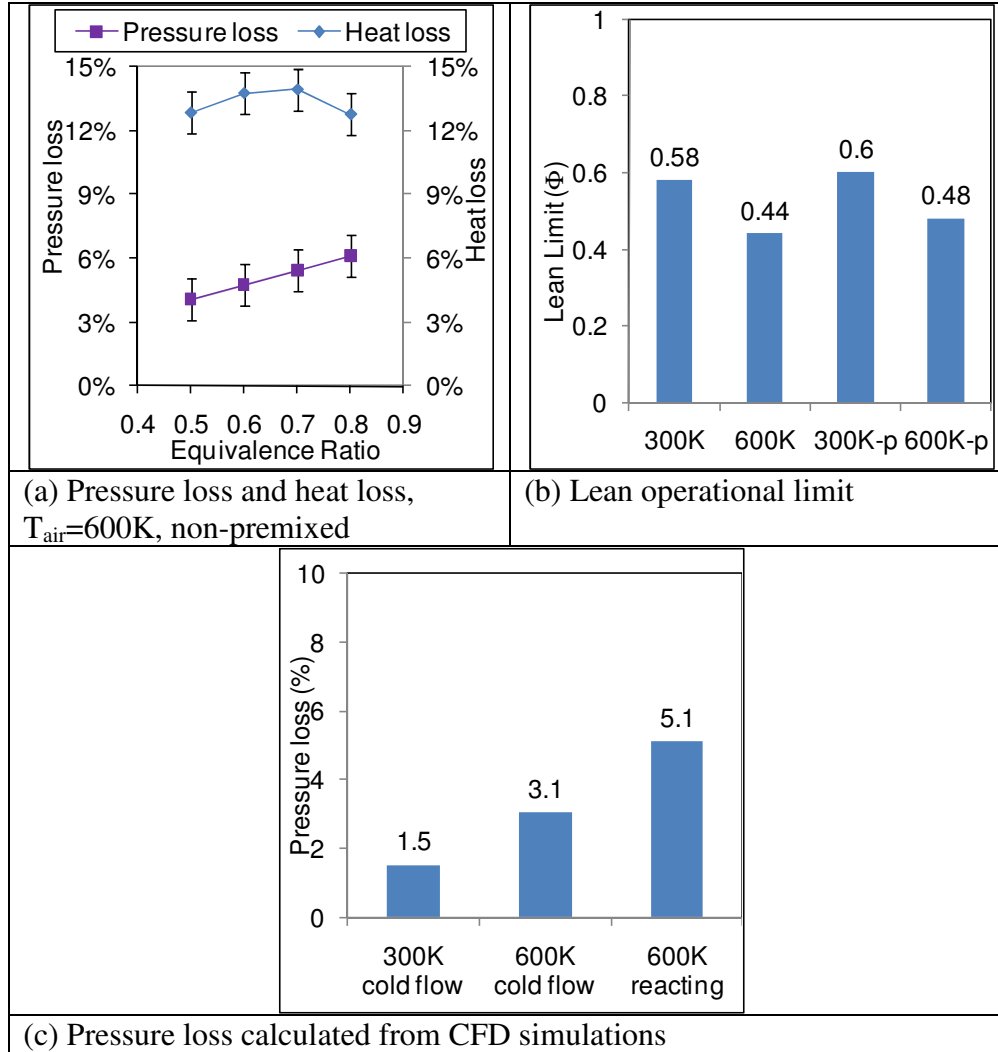


Figure 7.9 (a) Pressure loss and heat loss and (b) lean operational limit for $T_{air}=600K$ in non-premixed mode and (c) pressure loss obtained form CFD simulations.

7.3 Experimental Set Up (156-198MW/m³-atm)

Further increase in thermal intensity was achieved by reducing the length as well as width of combustor (see Figure 7.10) as compared to previous case (see Figure 7.1) for the reverse cross-flow geometry. It may be noted that width of the combustor was reduced to help alleviate zones on the left side of air jet and from the right side of the combustor. The region on left side of the air jet was observed to recirculate the gases which could be detrimental to combustor performance (see Figure 7.3). This reduction in volume allows the combustor to operate at ultra-high thermal intensity

range of $156\text{-}198\text{MW/m}^3\text{-atm}$ for equivalence ratio variation of $0.55\text{-}0.7$ and heat load variation of $4.3\text{-}5.47\text{kW}$. The fuel injection location was shifted towards the air injection location (see Figure 7.10(b)) to enhance mixing as compared to the geometry examined earlier (see Figure 7.1(b)) Air injection velocity was 92m/s at air injection temperature of 600K and fuel injection velocity varied from $67\text{-}85\text{m/s}$ to result in equivalence ratio variation from $0.55\text{-}0.7$. Both non-premixed mode in reverse cross flow configuration (see Figure 7.10(c)) and premixed mode in reverse flow configuration (see Figure 7.10(d)) were investigated at atmospheric conditions.

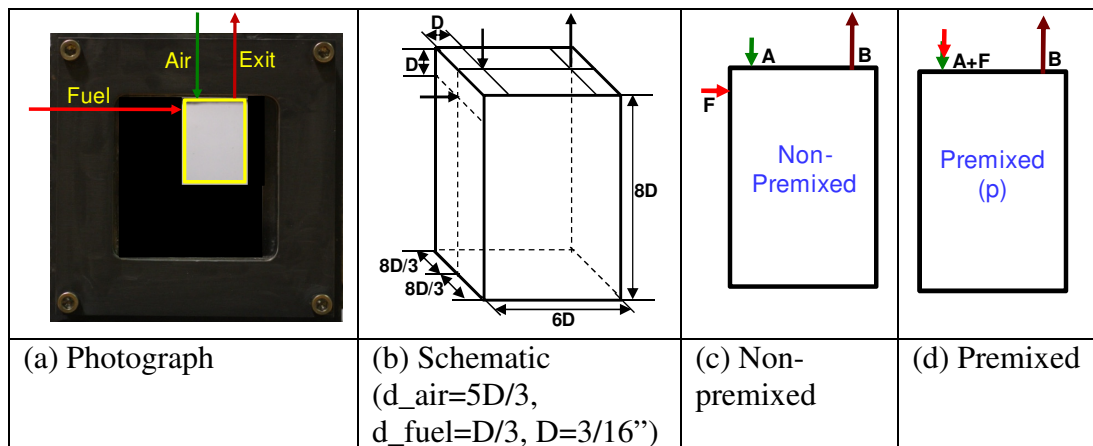


Figure 7.10 (a) Photograph (b) schematic (c) non-premixed and (d) premixed mode for ultra-high thermal intensity ($156\text{-}198\text{MW/m}^3\text{-atm}$) CDC combustor.

Gas analyzer was used to obtain NO and CO emission level, see Appendix G for further details. The emission readings were observed to stabilize within 3 minutes for any change in experimental condition (here change in equivalence ratio for the same configuration). The experiments were repeated at least three times for each configuration and the uncertainty was estimated to be about $\pm 0.5\text{ppm}$ for NO and $\pm 10\text{ppm}$ for CO emissions.

7.4 Results and Discussion

7.4.1 NO and CO emissions

The emission levels of NO and CO for this ultra-high thermal intensity combustor are presented in Figure 7.11. It can be observed that at equivalence ratio of 0.6, corresponding to thermal intensity of $170\text{MW/m}^3\text{-atm}$, the combustor produced 8ppm NO in non-premixed mode and 3ppm in premixed mode, and about 100ppm CO in both the modes. It may be noted at such high thermal intensity of $144\text{MW/m}^3\text{-atm}$ the NO emission level was 52ppm and CO emission level was 520ppm for the trapped vortex combustor [Hsu, K. Y., *et al.*,1998]. This suggests good performance of the designed CDC combustor even at such high thermal intensities.

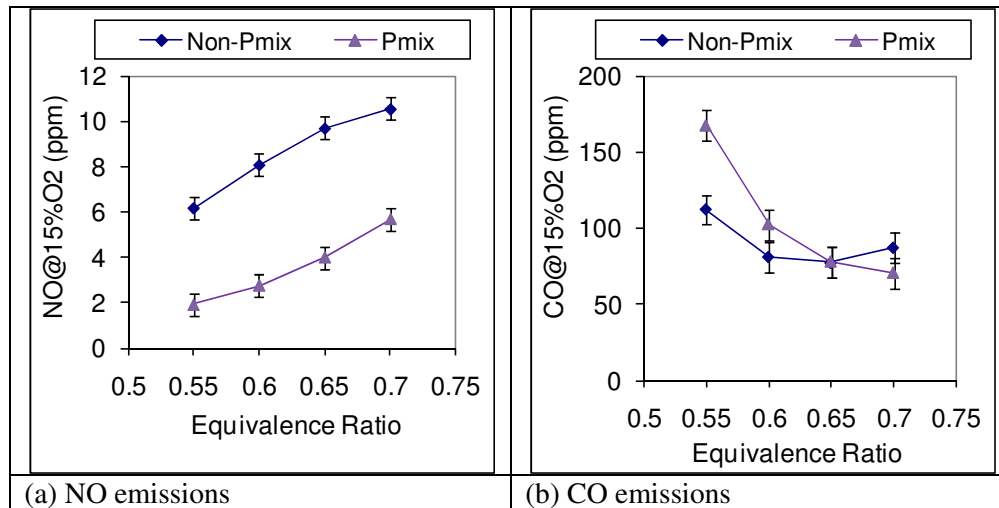


Figure 7.11 (a) NO and (b) CO emissions in non-premixed and premixed modes.

7.4.2 Fuel Dilution Effects

A fuel dilution effect on combustion performance in the non-premixed mode is investigated for high thermal intensity CDC combustor. The geometry is same as shown in Figure 7.10(c). Table 7.2 shows the operating conditions for the present investigation. Investigation is performed as equivalence ratio of 0.6 at constant heat

load of 4.7kW. Methane is diluted with nitrogen (case 3, Table 7.2), carbon dioxide (case 4, Table 7.2) and air (case 5, Table 7.3) while maintaining the same methane flow rate. The lower heating value of the fuel is about 20MJ/kg-K with fuel dilution. Fuel dilution with nitrogen simulates lower heating value fuel combustion and dilution with carbon dioxide simulates mixing of fuel with exit gases. Fuel dilution with air could be easily implemented in combustion systems by mixing fuel with the air. It may be noted that for fuel dilution with air the air/fuel ratio in the fuel stream is 1.5 and the corresponding equivalence ratio is 11.45. This equivalence ratio is much greater than the rich flammability limit of methane ($\Phi=1.64$, Turns, S. R., 2000) and hence it alleviates possibility of flashback from the fuel line. The overall equivalence ratio due to addition of air in methane is 0.57 for case5 instead of 0.6 for all other cases, however for sake of comparison the case with dilution with air is also denoted with having equivalence ratio of 0.6. The square root of momentum ratio “r” as used in equation 2.4 for jet penetration in cross flow is also included in the table. $r < 2$ for the cases investigated here suggests rapid decay of fuel jet and faster mixing (see Figure 2.6).

Table 7.2 Different cases for the effect of fuel dilution ($\Phi=0.6$, $170\text{MW}/\text{m}^3\text{-atm}$).

Case#	Fuel	CH ₄ (wt.%)	LHV (MJ/kg-K)	V _{fuel} (m/s)	V _{air} (m/s)	$r = \left(\frac{\rho_i \times v_i^2}{\rho_c \times v_c^2} \right)^{\frac{1}{2}}$	T _{adiabatic} (K)
1	CH ₄	100	50	73	92	0.93	1893
2	CH ₄ -pmix	100	50	-	98	-	1893
3	CH ₄ +N ₂	40	20	135	92	1.48	1841
4	CH ₄ +CO ₂	40	20	112	92	1.47	1838
5	CH ₄ +Air	40	20	133	92	1.48	1842

Figure 7.12 shows NO and CO emissions for the effect of fuel dilution effect in non-premixed condition. The combustor operates at thermal intensity of $170\text{MW}/\text{m}^3$ -

atm at this operational point. From the figure it may be noted that NO emission level was about 8ppm in non-premixed mode and about 3ppm in premixed flow mode. However with addition of diluents such as air, nitrogen or carbon-dioxide the NO emission level decreases further, and as low as 1.5ppm of NO could be achieved with dilution with carbon-dioxide. Very low NO emission levels were also observed by Dally, B. B., *et al.*, 2004 and diluting methane to up to fuel mass fraction of about 0.15 resulted in NO_x emission of less than 1ppm even in non-premixed mode. It may be noted that with addition of diluents in the present work the adiabatic flame temperature decreases by about 50K and this also helps to reduce the NO emission level. Figure 7.12(b) shows the CO emission level for different cases investigated here and from the figure it can be noted that with addition of air and nitrogen as diluents the CO emission level increases only slightly however addition of carbon-dioxide in the fuel stream increases the CO emission level significantly. From Figure 7.12 it can be noted that NO emission level close to premixed flow mode could be achieved by addition of small amount of air to the fuel stream and this could be beneficial in practical application of the combustors. This results in only slight increase in CO emission level.

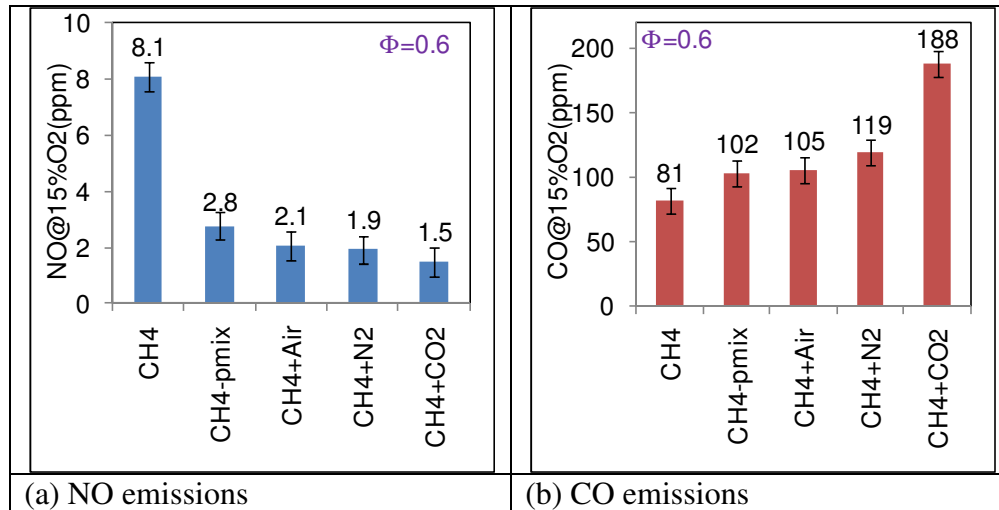


Figure 7.12 (a) NO and (b) CO emission levels for the effect of fuel dilution.

7.5 Operation with Liquid Fuel (170MW/m³-atm)

Ethanol was tested in both direct injection and in premixed-prevaporized mode at ultra-high thermal intensity of 170MW/m³-atm. The results are presented here at equivalence ratio of 0.6 and at fixed heat load of 4.7kW. The supply system of ethanol is shown in Appendix G. The fuel was injected directly in the combustion chamber (see Figure 7.10) from a port size of 0.0125inch in the direct injection mode. It may be noted that no atomizer was used in the present investigation. The fuel injection velocity was about 2.6m/s and the fuel jet was sheared and mixed due to strong cross-flowing air jet. In the premixed-prevaporized mode the fuel was injected at an upstream location and proper vaporization and mixing is expected due to high temperature air stream (600K in the present case). The air injection temperature was 600K in both the modes. Initially, the combustor was transitioned to CDC mode operating on gaseous fuel (methane) then slowly liquid fuel was injected and gaseous fuel flow rate was reduced to finally operate on liquid fuel mode. It may be noted that the fuel injection tube was maintained at much lower temperature because of cooling

due to fuel flow flowing through the tube. This avoided any problems related to coking of fuel and resulting in choking of the fuel.

Gas analyzer was used to obtain NO and CO emission level, see Appendix G for further details. The emission readings were observed to stabilize within 3 minutes for any change in experimental condition (here change in equivalence ratio for the same configuration). The experiments were repeated at least three times for each configuration and the uncertainty was estimated to be about ± 0.5 ppm for NO and ± 20 ppm for CO emissions.

The results for NO and CO emissions for direct injection (“DI”) and premixed-prevaporized (“PP”) mode of operation is shown in Figure 7.13. From the figure it may be noted that very low NO and CO emissions are obtained in both direct-injection as well as premixed-prevaporized combustion modes. CO emission levels are higher (about 200ppm) as compared to emission levels corresponding to the gaseous fuel operation (about 100ppm, see Figure 7.12). Operation of liquid fuel in direct injection mode shows promise to further extend the scope of CDC technology to high thermal intensity aircraft engine combustors that uses kerosene based liquid fuels.

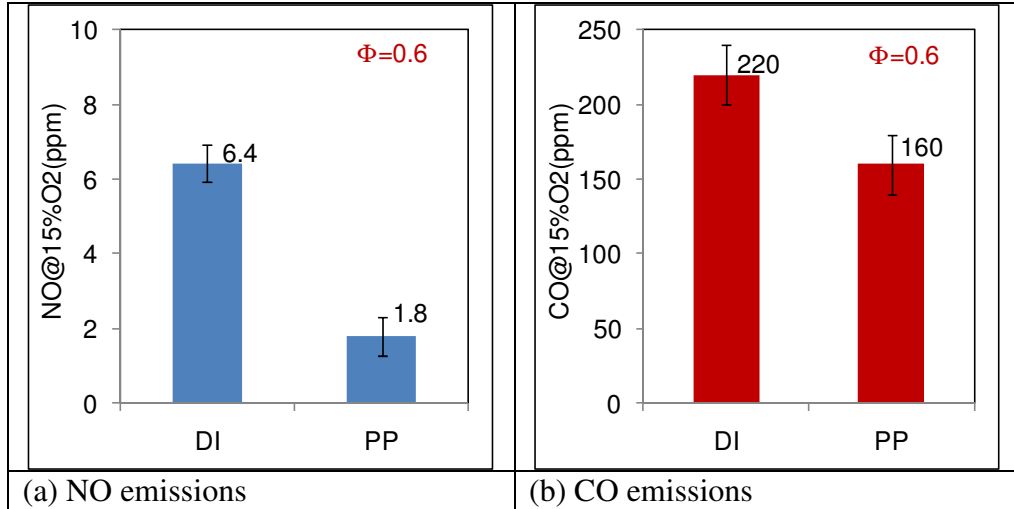


Figure 7.13 (a) NO and (b) CO emission levels with liquid (ethanol) fuel operation in direct injection (DI) and premixed prevaporized (PP) modes.

7.7 Effect of Thermal Intensity

The role of thermal intensity variation on operation of CDC combustor is investigated by comparing different reverse flow geometries operating at a thermal intensity range from 5 to 198MW/m³-atm in premixed flow mode. The geometries compared are shown in Figure 7.14 and corresponding heat load, inlet velocity, air injection diameter and inlet temperature are also included.

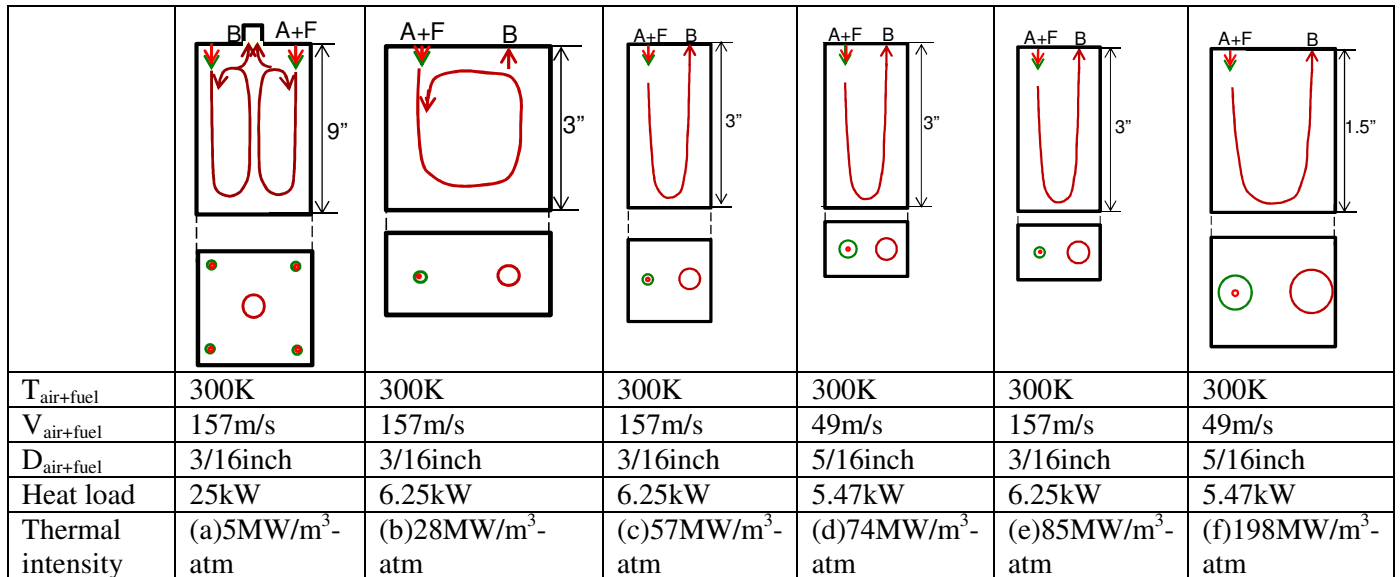


Figure 7.14 Reverse flow configurations investigated for thermal intensity range from 5-198MW/m³-atm.

Figure 7.15 shows the NO and CO emissions at equivalence ratio of 0.7 for the range of thermal intensity investigated here in premixed mode. From the figure it can be noted that the NO emissions are very less (less than 3ppm) for all the cases however there is significant variation in CO emissions. NO emission increases with increase in thermal intensity and this may be due to relatively lower heat losses at higher thermal intensity resulting in higher gas temperatures and subsequently higher NO emissions. At thermal intensity of $5\text{MW/m}^3\text{-atm}$ CO emission is only 10ppm and it increases to 64ppm at thermal intensity of $28\text{MW/m}^3\text{-atm}$ and to 96ppm at thermal intensity of $57\text{MW/m}^3\text{-atm}$. It may be noted that the air injection temperature, velocity as well as the injection diameter is same for these three cases. This increase in CO is possibly due to lower associated residence time at higher thermal intensities (see Figure 2.7). The average residence time for different combustors in reacting flow condition is shown in Figure 7.16(a) and from the figure it can be noted that the residence time decreases from 76 to 6.7ms with increase in thermal intensity from 5 to $57\text{MW/m}^3\text{-atm}$.

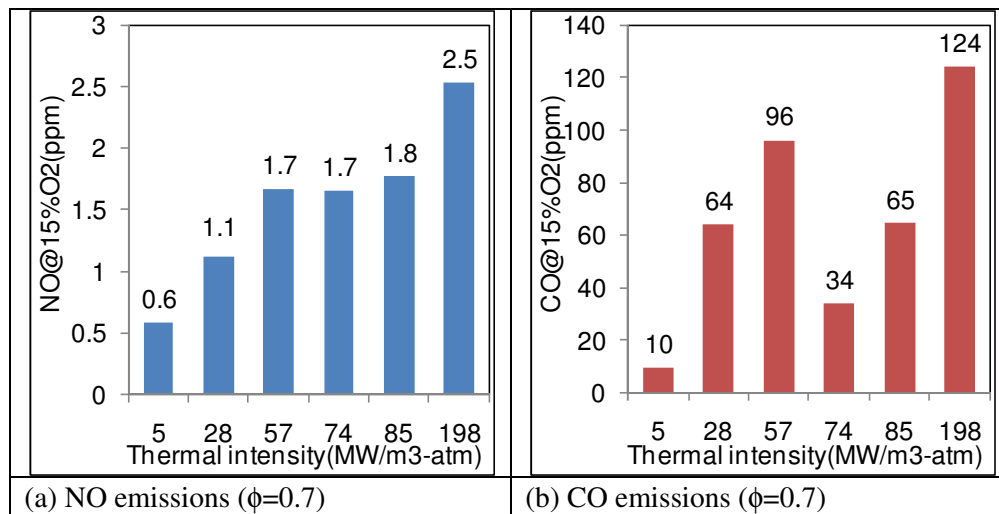


Figure 7.15 (a) NO and (b) CO emissions for premixed flow mode corresponding to thermal intensity range of $5\text{-}198\text{MW/m}^3\text{-atm}$, equivalence ratio = 0.7.

However, interesting trend is observed with respect to CO emission as the thermal intensity is increased to $85\text{MW/m}^3\text{-atm}$ (see Figure 7.14(e)) from $57\text{MW/m}^3\text{atm}$ (see Figure 7.14(c)). In this case even though the residence time decreases to 4.5ms from 6.7ms the CO emission decreases to 65 ppm from 96ppm. At higher thermal intensity the effect of confinement is expected to play an important role on the flowfield inside the combustor. The confinement ratio (ratio of air injection diameter and confinement depth) for different combustors is presented in Figure 7.16(b). It can be observed that as the thermal intensity is increased from 57 to $85\text{MW/m}^3\text{-atm}$ the confinement ratio increases from 0.13 to 0.19. At thermal intensity of $5\text{MW/m}^3\text{-atm}$ the confinement ratio was only 0.03 and the jets will behave closer to a free jet. From Figure 2.9 we can observe that at confinement ratio of about 0.1 the jet decay is very similar to the free jet decay however as the confinement ratio is increased to 0.2 and 0.3 the jet decay is much more rapid. This suggests that as the confinement ratio is increased the jet decay is very fast and this may result in anchoring of reaction zone closer to the air injection location.

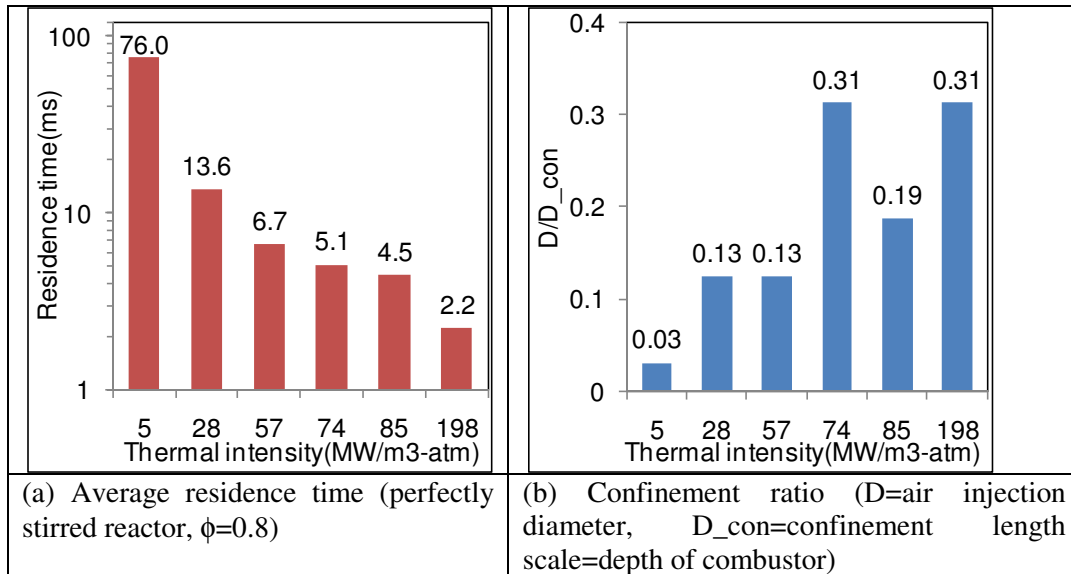


Figure 7.16 (a) Average residence time in reacting condition (b) confinement ratio for thermal intensity range from 5-198MW/m³-atm.

Location of reaction zone was obtained from the OH* chemiluminescence imaging technique and the results are presented in Figure 7.17 these two cases. Moving of reaction zone towards the air injection location for higher thermal intensity case of 85MW/m³-atm as compared to the thermal intensity case of 57MW/m³-atm can be observed. This shifting of reaction zone may result in longer residence time available for the hot gases before escaping from the combustor and result in lower CO emissions.

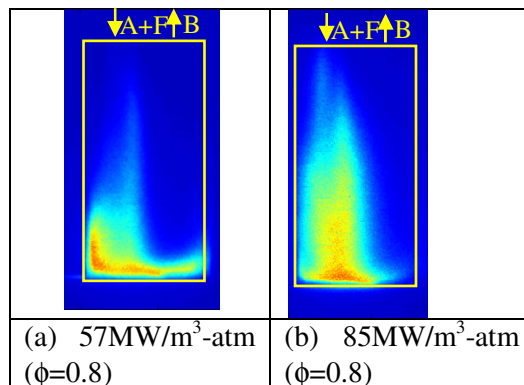


Figure 7.17 OH* distribution at thermal intensity of (a) 57MW/m³-atm and (b) 85MW/m³-atm.

Hence with careful design of the combustor lower CO emissions could be achieved even at higher thermal intensities. With increase in air injection diameter (see Figure 7.14(d) and (f)) the confinement ratio is further increased to 0.3 and this result in lower CO emission (34ppm at thermal intensity of $74\text{MW}/\text{m}^3\text{-atm}$). Hence increasing the air injection diameter can prove beneficial to not only reduce the pressure drop across the combustor but also to move reaction zone closer to air injection location and increase the residence time inside the combustor. Comparing the case of combustor operating at thermal intensity of 74 and $198\text{MW}/\text{m}^3\text{-atm}$ (see Figure 7.14(d) and (f) respectively) we observe that CO emission increases from 34ppm to 124ppm respectively. It can be noted that for these two cases the confinement ratio is same of about 0.31 and hence increase in thermal intensity resulted in smaller residence time (2.2ms as compared to 4.5ms) and hence higher CO emissions.

The residence time characteristics for the combustors shown in Figure 7.14 are presented in Figure 7.18. It may be noted that the combustors are labeled in this figure based on thermal intensity calculated at equivalence ratio of 0.8 and only air flow is considered in cold flow conditions. The case labeled “85-5/16” corresponds to Figure 7.14(d) and case labeled as “227-5/16” correspond to Figure 7.14(f). From the figure it may be noted that with increase in thermal intensity higher fraction of tracer having lower residence time is present (see Figure 7.18(b)). For these combustors the air injection diameter is 3/16inch. With increase in air injection diameter to 5/16 inch from 3/16 inch interesting trend is observed in Figure 7.18(d). Even with same flow rate, the fraction of tracer having lower residence time is higher for smaller air

injection diameter and this may result in lower CO level even at same thermal intensity which was observed in Figure 7.15 suggesting significant reduction of CO from 65ppm to 34ppm with slight change in thermal intensity from 85 to 74ppm respectively.

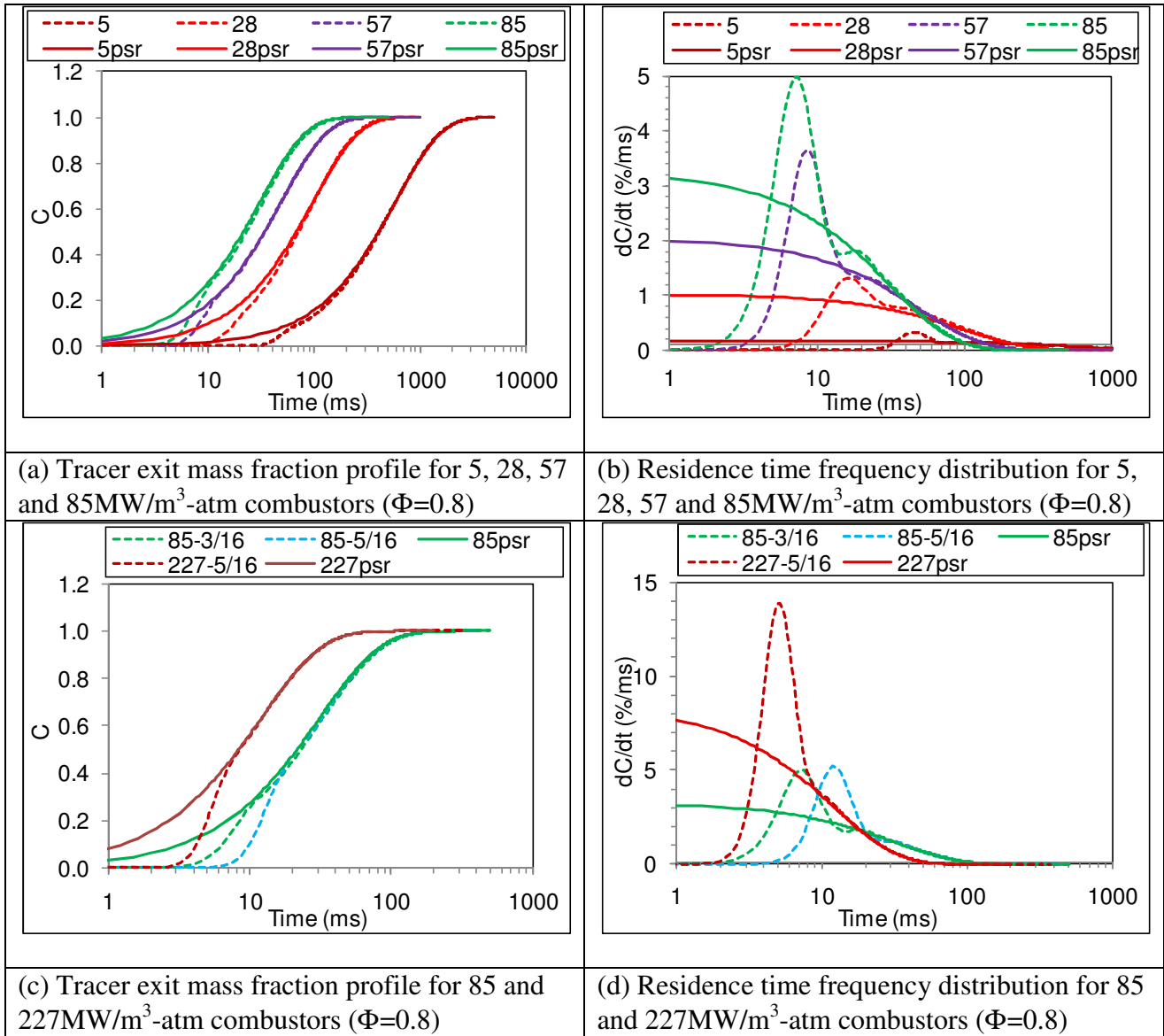


Figure 7.18 Residence time characteristics for the reverse flow combustors investigated.

7.7 Conclusions

Reverse cross flow geometry, including a premixed mode and a non-premixed mode, has been examined at thermal intensity in the range of 53-85MW/m³-atm and 156-198MW/m³-atm. Such high thermal intensity is much higher than that used in contemporary current day land based gas turbine combustors. The combustor operating at thermal intensity range of 53-85MW/m³-atm was operated at air preheat temperature of 300K and 600K. Particle image velocimetry technique was used to obtain the flowfield characteristics for geometry operating at thermal intensity range of 53-85MW/m³-atm in cold flow conditions. Experimental data suggest that the gases recirculate from both sides of the air jet. Experimental data show ultra low NO emissions for both premixed and non-premixed flow configurations (1ppm for novel premixed and 4ppm for non-premixed at $\Phi=0.5$, $T_{\text{air}}=600\text{K}$). Low CO emissions were observed for both premixed and non-premixed flow modes (about 30ppm at $\Phi=0.5$). Almost colorless reaction zones were observed in both non-reacting and reacting flow conditions. Very low pressure fluctuations (<0.025%) were obtained in both reacting and non-reacting flow conditions suggesting very smooth operation of the distributed CDC combustor. Pressure loss of less than 5% and heat loss of about 15% were recorded. Further investigation of mixing of fuel with air will provide insights to further reduce NO_x and CO emissions.

The combustor operating at ultra-high thermal intensity range of 156-198MW/m³-atm produced NO emission level of about 8ppm in non-premixed mode and 3ppm in premixed mode ($\Phi=0.6$). CO emission level of about 100ppm is produced in both the modes. Dilution of fuel with inert gases and air resulted in significant reduction in

NO emissions (from 8ppm to 2ppm) in non-premixed mode. The combustor was also tested with liquid fuel (ethanol) at thermal intensity of $170\text{MW/m}^3\text{-atm}$ and very low NO emission of 6ppm in direct-injection mode and 2ppm in premixed-prevaporized was obtained. CO emission was about 200ppm in both the modes. This suggests very good performance even at such high thermal intensities and shows promise to develop CDC combustors at ultra high thermal intensities with enhanced performance with application to aircraft engines. Comparing reverse flow configurations from thermal intensity of $5\text{-}198\text{MW/m}^3\text{-atm}$ revealed that careful design of CDC combustor can result in lower CO emissions even at high thermal intensity such that the reaction zone is anchored closer to the air injection location to give higher residence time.

Chapter 8 : Summary

Development of colorless distributed combustion (CDC) for gas turbine application requires careful examination on the role of various input and operational parameters to achieve ultra-low NO_x emission and stable combustion operating at ultra-high thermal intensity. In this dissertation various flowfield configurations, such as forward flow, reverse flow with fuel injection from same side of air injection, opposite side of air injection, in cross flow and premixed flow modes were investigated for a range of thermal intensity extending from 5 to $198\text{MW/m}^3\text{-atm}$.

Figure 8.1(a) shows the thermal intensities and Figure 8.1(b) shows the length scale of selected combustors that have been investigated in this dissertation with the range of thermal intensity investigated extending from 5 to $170\text{MW/m}^3\text{-atm}$. It may be noted that for operation at ultra-high thermal intensity ($156\text{-}198\text{MW/m}^3\text{-atm}$) the most desirable operational point was at equivalence ratio of 0.6 at thermal intensity of $170\text{MW/m}^3\text{-atm}$. The flowfield configuration as well as the corresponding equivalence ratio is also included in the graph. Both non-premixed and premixed flow modes are included in the plots. The length scale of the investigated combustors varies from 9inch for low thermal intensity ($5\text{MW/m}^3\text{-atm}$) combustor to 1.5inch for ultra-high thermal intensity ($156\text{-}198\text{MW/m}^3\text{-atm}$) combustor.

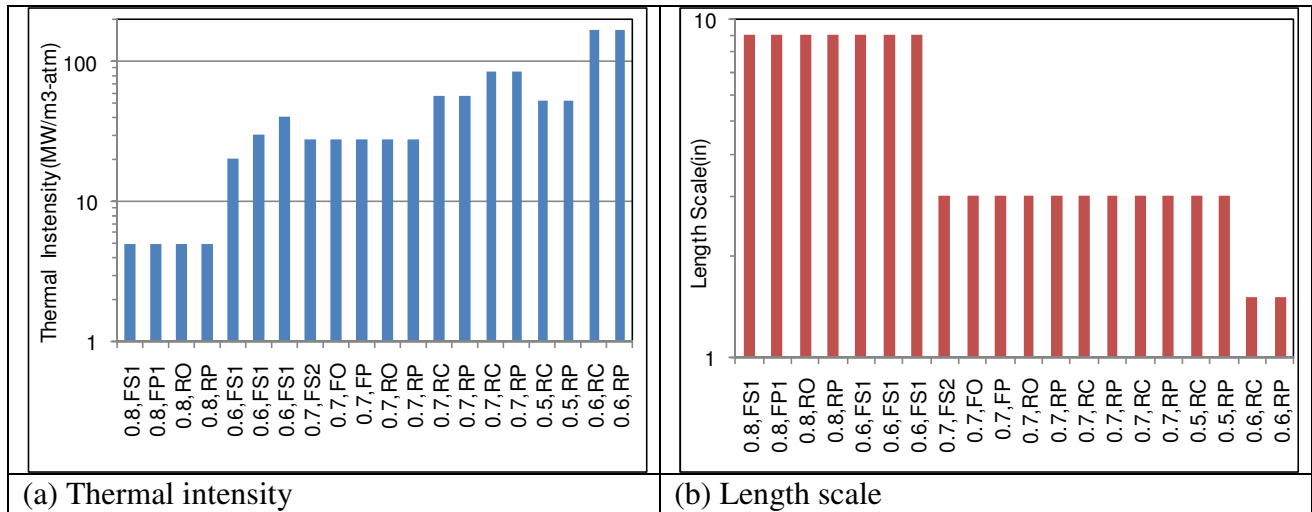


Figure 8.1 Thermal intensity and length scale for various combustors investigated in the present work.

Figure 8.2 shows the NO and CO emission level for the selected combustors. It can be observed that ultra-low NO emissions (about 1ppm) were observed for premixed mode and the non-premixed combustion modes also reveal single digit NO emissions. CO emissions for most of the combustor geometries and configuration are less than 100ppm.

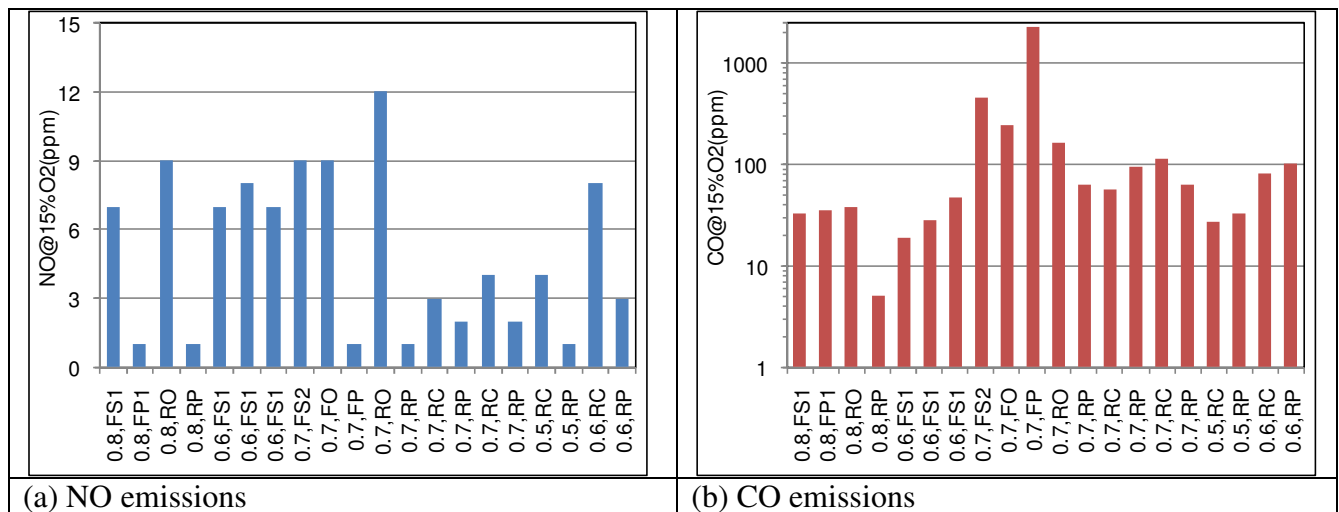


Figure 8.2 NO, CO emissions for various combustors investigated in the present work.

Figure 8.3 shows the heat load for the CDC combustors. Heat load of 25kW was used for combustor with length of 9 inch and lower heat loads were used for smaller combustors.

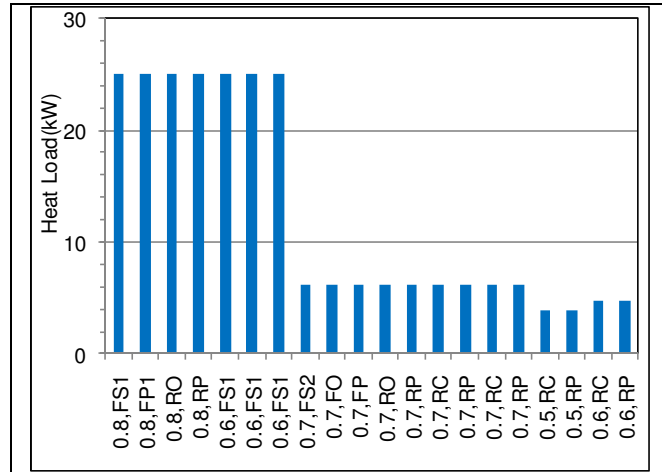


Figure 8.3 Heat load for various combustors investigated in the present work.

Initially investigations were performed at thermal intensity of $5\text{MW}/\text{m}^3\text{-atm}$. It was found from numerical investigation that reverse flow configuration resulted in higher fraction of gases having higher residence time even though the average residence time was noted to be independent of the flow configuration. This was supported by experimental investigation that revealed that reverse flow configuration resulted in lower CO emission levels on premixed flow mode. Effect of air and fuel injection diameter was investigated for a forward flow configuration “FS1” at thermal intensity of $5\text{MW}/\text{m}^3\text{-atm}$ and it was observed that the fuel injection diameter had minimal effect on NO and CO emissions. However, with increase in air injection diameter, both the NO and CO emissions increased significantly suggesting that the air jet is the dominant jet and governs the flowfield and mixing inside the combustor as increase in air injection diameter considerably increases the mixing time scales (D/U).

The thermal intensity was increased for forward flow configuration “FS1” and investigations were performed at thermal intensity of 20, 30 and 40MW/m³-atm. It was observed numerically that operation of combustor at higher thermal intensity (20-40MW/m³-atm) results in lower residence time and lower gas recirculation and hence it poses problem of stabilizing combustion and results in higher CO emissions with increase in thermal intensity. This was also supported by experimental investigation where higher CO emissions were observed at higher thermal intensity. A simpler combustor having only one air and fuel injection port was investigated at thermal intensity of 28MW/m³-atm in both non-premixed and premixed modes.

The thermal intensity was then increased to 57MW/m³-atm and reverse cross-flow configuration was observed to give most desirable performance. Fuel injection in cross-flow resulted in faster mixing between fuel and oxidizer and hence this resulted in lower NO and CO emissions. Further reduction in volume resulted in thermal intensity of 85MW/m³-atm. At thermal intensity of 85MW/m³-atm the effect of hydrogen addition to methane fuel was investigated and it was observed that with addition of hydrogen the NO emission increased slightly, CO emissions decreased significantly and the lean stability limits were extended.

The selected geometry which operated in reverse cross-flow configuration at thermal intensity range of 53-85MW/m³-atm was further investigated. In non-premixed mode this configuration resulted in very low NO (about 4ppm) and CO (about 30ppm) as well as less than 5% pressure loss across the combustor. In premixed flow mode this configuration resulted in only 1ppm of NO and about 30ppm of CO emissions. The root mean square pressure fluctuations were less than

0.025% suggesting very stable combustion. This is very low as compared to those in current engines (typical value = 1.5%). Almost colorless reaction zones were observed in both non-premixed and premixed flow modes and the reaction zone was observed to be present in cross flow near the fuel injection location in non-premixed mode. The thermal intensity at the most desirable operational point was $53\text{MW/m}^3\text{-atm}$.

Further reduction in volume of the combustor in reverse cross-flow configuration resulted in ultra-high thermal intensity range of $156\text{-}198\text{MW/m}^3\text{-atm}$ and combustor operated at thermal intensity of $170\text{MW/m}^3\text{-atm}$ at desirable operating point with NO emissions of 8ppm and 3ppm in non-premixed and premixed mode respectively. CO emission level was about 100ppm in both the modes. Dilution of fuel with inert gas as well as air resulted in significant reduction in NO emissions in non-premixed mode (from 8ppm to 2ppm). This geometry was also tested with liquid fuel (ethanol) and very low NO emission of 6ppm in direct-injection mode and 2ppm in premixed-prevaporized mode was obtained. CO emission level was 200ppm in both the modes. This shows promise for extension of this technology to aircraft engine application utilizing liquid fuel. The details of operating performance of combustor at thermal intensity of 53 and $170\text{MW/m}^3\text{-atm}$ are given in Figure 8.4.

A summary of combustor performance operating in various configurations at range of thermal intensities investigated in this dissertation is given in Table F.2 of the Appendix F. The combustors are arranged in increasing order of thermal intensity.

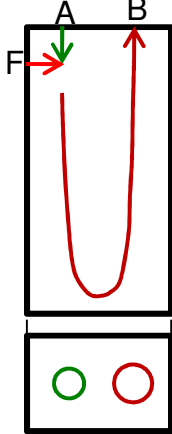
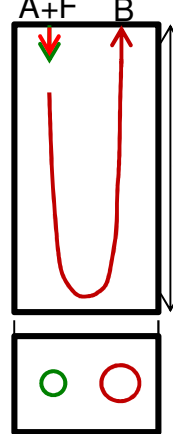
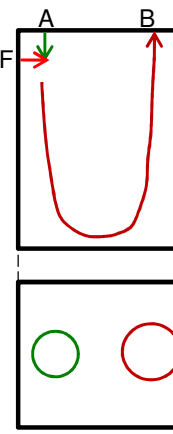
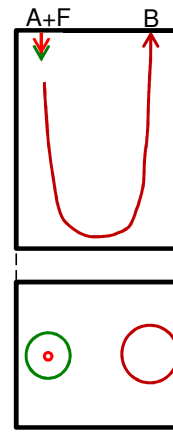
Downselected Geometry, "Reverse Cross-Flow"				
	RC	RP	RC	RP
Thermal Intensity	$53\text{MW/m}^3\text{-atm}$	$53\text{MW/m}^3\text{-atm}$	$170\text{MW/m}^3\text{-atm}$	$170\text{MW/m}^3\text{-atm}$
Heat load	3.91kW	3.91kW	4.7kW	4.7kW
Fuel	Methane	Methane	Methane	Methane
Pressure	1atm	1atm	1atm	1atm
Air Velocity	92m/s	97m/s	92m/s	98m/s
Fuel Velocity	61m/s	-	73m/s	-
Air diameter	7.9mm	7.9mm	7.9mm	7.9mm
Fuel diameter	1.6mm	-	1.6mm	-
$\tau_{\text{air}}(D/U)$	0.086ms	0.082ms	0.086ms	0.081ms
$\tau_{\text{fuel}}(D/U)$	0.026ms	-	0.024ms	-
Air Temperature	600K	600K	600K	600K
Fuel Temperature	300K	-	300K	-
NO@15%O ₂	4ppm ($\Phi=0.5$)	1ppm ($\Phi=0.5$)	8ppm ($\Phi=0.6$)	3ppm($\Phi=0.6$)
CO@15%O ₂	27ppm ($\Phi=0.5$)	34ppm ($\Phi=0.5$)	81ppm ($\Phi=0.6$)	102ppm($\Phi=0.6$)
Pressure drop	<5%	<5%	-	-
Prms	<0.025%	0.025%	-	-

Figure 8.4 Selected combustor geometry and operational parameters among the combustors investigated in the present work.

The contribution of this dissertation is systematic development of high thermal intensity CDC combustor for ultra-low NO and CO emissions from thermal intensity of 5 to $198\text{MW/m}^3\text{-atm}$. Design guidelines have been outlined that can be very useful while designing a gas turbine combustor operating on CDC technology. Detailed investigation of various flowfield configurations at range of thermal intensity is reported and this experimental data base can be very useful while designing practical combustor as well as to validate numerical models.

Chapter 9 : Conclusions and Recommendations for Future Work

9.1 Conclusions

Design and development of a CDC combustor for high thermal intensity application requires careful examination of critical parameters such as gas recirculation, flowfield configuration, fuel/oxidizer mixing and confinement effects to achieve desirable combustion characteristics. By systematic design of the combustor ultra-low emissions of NO and CO were demonstrated up to ultra-high thermal intensity of $198\text{MW/m}^3\text{-atm}$. This thermal intensity is an order of magnitude higher than the thermal intensity of a state of the art land based gas turbine combustor ($15\text{MW/m}^3\text{-atm}$). Direct injection of air and fuel in the combustion chamber at high velocity was employed and no flame stabilizer such as swirler or bluff body was used in the present work. Simple computational fluid dynamics as well as chemical kinetic computations were performed to help in designing the combustor as well as to understand the experimental results. The experimental database reported in this dissertation could also serve as a database to develop and validate computational models to predict combustion characteristics of CDC combustors. Following conclusions can be drawn based on the work performed in this dissertation that can be useful for designing a high thermal intensity CDC combustor.

9.1.1 Effect of Flowfield Configuration

Both reverse and forward flow configurations were investigated and it was observed that reverse flow configuration resulted in significantly lower CO emissions as compared to a forward flow configuration. This is because of favorable residence

time distribution characteristics for reverse flow configuration as compared to forward flow configuration. Reverse flow configuration was observed to have lower fraction of gases having smaller residence time this results in more conversion of CO to CO₂ and results in lower CO emissions. It was observed that the average residence time inside the combustor was independent of the flow configurations and it only depended on the combustor volume. In forward flow configuration favorable residence time distribution could be obtained by positioning the air injection ports away from the line of exit to ensure longer path for the gases before escaping the combustor and hence resulting in better conversion of CO to CO₂.

9.1.2 Effect of Air and Fuel Injection Diameter

Effect of air and fuel injection port size was investigated for a forward flow configuration and it was noted that the fuel injection diameter had minimal effect on the emission however increase in air injection diameter significantly increased emissions of both NO and CO. The reason for this is attributed to slower turbulent mixing for larger air injection diameter resulting in more hot spot regions and hence higher emissions. The air jet is the dominant jet with an order of magnitude higher jet momentum as compared to the fuel jet hence the air jet governs the flowfield as well as turbulent mixing inside the combustor. On the other hand smaller air injection diameter results in larger pressure loss due to higher inlet velocity and hence appropriate selection of air injection diameter is required to achieve lower pressure loss as well as lower emissions.

9.1.3 Fuel/Oxidizer Mixing

Faster fuel/oxidizer mixing was observed to be critical to reduce both NO and CO emissions. Entrainment of fuel jet in the strong air jet was observed to be insufficient to achieve lower emissions for high thermal intensity application. Injection of fuel in cross-flow with respect to the high velocity air jet resulted in faster mixing of fuel jet in the hot and diluted oxidizer and minimizes the emissions. Injection of fuel in cross-flow and closer to the air jet results in anchoring of reaction zone away from the exit and hence increases the residence time to further improve conversion of CO to CO₂. Reverse cross-flow configuration was observed to result in minimum NO as well as CO emissions because to faster mixing of fuel and well as favorable residence time characteristics.

9.1.4 Effect of Thermal Intensity

Reduction in combustor volume to increase thermal intensity was investigated for a forward flow configuration and higher thermal intensity was observed to reduce gas recirculation as well as reduce the residence time of the gases inside the combustor. Higher thermal intensity had minimal effect on NO emissions however it significantly increased the CO emissions due to lower residence time. Interestingly, it was observed that lower CO emissions could be achieved even at high thermal intensity if the reaction zone is anchored away from the exit to maximize the time available for conversion of CO to CO₂. Investigations were performed in reverse flow configurations and for larger confinement ratio (ratio of jet diameter to the confinement length scale) the air jet was observed to decay faster and have smaller fraction of gases having lower residence time. This suggests that smaller confinement

length scale can result in anchoring of reaction zone away from the combustor exit and result in lower CO emissions even at higher thermal intensity and this was supported experimentally. Moreover, larger air jet diameter can be beneficial not only to minimize the pressure loss but also to achieve more favorable residence time characteristics and hence achieve lower CO emissions and this was also observed experimentally.

9.1.5 Effect of Hydrogen Addition to Methane

Addition of hydrogen to methane fuel was investigated in reverse cross-flow configurations and this resulted in slight increase in NO emissions, significant decrease in CO emissions and extension of lean operational limit. This suggests that lower NO emissions could be achieved with lower CO emissions by operating combustor at leaner condition. The reaction zone was observed to move closer to the fuel injection location with addition of hydrogen due to lower ignition delay time of hydrogen enriched fuel. This may be the reason for slightly higher NO emissions because of ignition of fuel before proper mixing with the oxidizer for hydrogen enriched fuel. Lower CO emissions are due to lower carbon content in the fuel as well as larger residence time for hot gases due to shifting of reaction zone away from the exit for hydrogen enriched fuel.

9.1.6 Effect of Air Preheat Temperature

Higher preheat temperature was investigated in reverse cross-flow mode. It was observed that increase in air preheat temperature increased NO emissions significantly but had minimal effect on CO emissions. Increasing the air injection

temperature significantly extended the lean operational limit hence lower NO and CO emissions were achieved by operating the combustor at leaner condition.

9.1.7 Fuel Dilution Effects

Dilution of methane with air as well as inert gases such as nitrogen or carbon-dioxide resulted in significant reduction in NO emission in non-premixed condition and NO emissions almost equal to the premixed mode were achieved. This suggests that lower heating value fuel could be successfully used in a CDC combustor with ultra-low NO_x emissions. Dilution of fuel with small amount of air such that the fuel stream is much above the rich flammability limit of fuel to avoid problem of flashback could be used as a viable option to significantly reduce the NO_x emissions. CO emissions were observed to increase significantly with carbon-dioxide dilution. Reverse cross-flow configuration was used for this investigation.

9.1.8 Operation with Liquid Fuel

Operation with liquid fuel (ethanol) was successfully demonstrated at ultra-high thermal intensity in both premixed-prevaporized as well as direct injection mode. Ultra-low emission of NO was observed in both the modes. No atomizer was used for introducing fuel in the combustor and the liquid fuel was directly injected using a tube with appropriate velocity. Reverse cross-flow configuration was used and due to fast shearing of fuel jet in direct injection mode resulted in stable reaction zone as well as low pollutant emissions.

9.2 Recommendations for Future Work

Colorless distributed combustion (CDC) shows remarkable potential for further development and implementation in gas turbine combustors. However, in depth research is still required to gain insight on the fundamental process of combustion of fuel in hot and diluted conditions under high thermal intensity conditions. Improved design and testing is essential to transfer the technology for practical gas turbine applications. Recommendation for future work is suggested below:

9.2.1 Detailed Species and Temperature Distribution

Detailed reaction zone structure, species and temperature distribution can be obtained using advanced non-intrusive optical diagnostic techniques such as planar laser induced fluorescence (PLIF) for characterization of turbulent combustion regimes in both premixed and non-premixed combustion modes. NO formation regions could be identified and novel techniques could be used to further reduce the pollutant emissions.

9.2.2 Quantification of Relevant Time Scales

Ignition delay and mixing time scales can be quantified and it can be confirmed that the mixing time scales are lower than ignition delay time scales. This will ensure that the fuel/oxidizer mixture burns due to spontaneous ignition after a uniform mixture is achieved as well as it will provide understanding to further improve the combustor design to achieve even lower emissions.

9.2.3 Flowfield in Reacting Condition

Particle image velocimetry technique can be used to obtain flowfield in the reacting flow condition to understand the gas recirculation as well as mixing characteristics inside the combustor. Deposition of alumina powder on the quartz windows posed a challenge to have desirable optical access through the combustor. The particles deposit on the quartz windows possibly due to the thermophoretic effects and novel techniques needs to be implemented to avoid deposition of particles.

9.2.4 Improved Fuel/Oxidizer Mixing

Fuel/oxidizer mixing could be further enhanced by considering novel ideas such as implementation of forced pulsations in the fuel stream. Fuel dilution effects were investigated in the present dissertation and it was observed that small amount of air addition to the fuel stream (much above the rich flammability limit to avoid flashback) could result in substantial reduction in NO emission level in non-premixed mode. This technique could be further explored to achieve ultra-low emission levels.

9.2.5 Characterization of Dynamic Performance

The dynamic stability of the combustor could be investigated in detail and the combustor can be characterized based on the dynamic response at lean operation. Pressure oscillations could be measured to understand the interaction of heat release oscillations with natural modes of the combustor. Forced pulsations from fuel or air streams could be used to understand the effect of perturbations on the dynamic stability of the combustor. This could be useful for understanding combustor behavior in real operating conditions.

9.2.6 Scaling of CDC Combustor

Scaling-up of CDC combustor from laboratory scale to practical combustors poses many challenges such as to maintain similar turbulent mixing time scales, achieve sufficient mixing at large scale, achieving dynamic stability as well as desired pressure drop while maintaining similar ultra-low emissions and high thermal intensity. For practical implementation of the CDC technology for gas turbine engines, extensive scaling studies and demonstration is essential. A brief scaling approach is presented in Appendix D.

9.2.7 Liquid Fuel Operation

In the present dissertation the focus of combustor development was on land based power plants where natural gas is used as a fuel. Sample results with liquid fuel utilization in CDC combustor has been included in this dissertation. However, development of CDC technology for liquid fuel operation poses additional challenges of complicated physics of atomization, evaporation and then combustion to achieve even lower emission levels. Operation of CDC combustor using liquid fuel hence requires detailed investigation of each of these physical phenomenon as well as examination of fuel chemistry so as to achieve reactions in distributed regime with minimal hot spot regions. In initial investigation with liquid fuel in this dissertation for premixed-prevaporized fuel as well as direct-injection of fuel showed encouraging results. Further investigation of liquid fuel atomization using coaxial air or swirling air could be used to further enhance the fuel preparation and reduce emission level. Detailed investigation of atomization and evaporation characteristics could form a major portion of the research along with carefully tailored direct injection of liquid

fuel inside the combustor. The operation could be extended to biofuels and heavy fuels to achieve the goal of carbon neutral power production and extend the fuel flexibility.

9.2.8 Application to Aircraft Engines

The combustors for aircraft engines operate at thermal intensity of about $150\text{MW}/\text{m}^3\text{-atm}$ using kerosene based fuels. The length scales for these combustors are about 6-10inches. A brief scaling analysis for scaling up of the CDC combustor from 1.5inch to 4inch is given in Appendix D. This combustor could be installed in the laboratory setting with thermal load of about 75kW and the validity of scaling analysis could be tested. In the present dissertation thermal intensity up to $198\text{MW}/\text{m}^3\text{-atm}$ was investigated, however the potential of operation of CDC combustor can be tested to thermal intensities above $200\text{MW}/\text{m}^3\text{-atm}$. This will result in significant benefits of reducing hardware costs while operating with very small sized combustors. For these combustors the residence time will be less than 2ms. These ultra compact combustors would be useful to reduce overall weight of the gas turbine system and resulting in significant benefits especially for aerospace applications.

9.2.9 Elevated Pressure Operation

Land based gas turbine combustors operate at elevated pressures at about 15atm. At these pressures the combustion chemistry can be very different as compared to normal pressure condition even though the aerodynamics might be similar. Hence, investigation of CDC operation at elevated pressure condition will give useful insight

while designing a practical gas turbine combustor. The aircraft engines will operate at about 40atm at take-off and about 10atm during cruise and hence operation for range of pressure could be tested and used for different applications.

9.2.10 Part Load Operation

From investigation in this dissertation it was observed that the operational window was narrow where both NO and CO emission were low. However, the gas turbine combustors operate at part load conditions depending on the demand fluctuation and the operation between 50-100% load conditions is desirable. Aircraft combustors have even more different and demanding requirements ranging from taxi, takeoff climb, cruise, approach and landing and different operating conditions require different power level from the combustor which may range from 20-100%. It may be noted that different part load condition also alters the thermal intensity of the combustor. Extension of operational window for CDC combustor could be pursued to increase the applicability of CDC combustors to practical engines. Further research is required to understand relight capability of CDC combustor in case of blow-off during combustor operation. Hence, further design enhancements to achieve reliable relight capability are required.

Appendix A - List of Papers

List of journal and conference papers published based on the work presented in this dissertation is given below.

A. 1 Journal Papers

- J.1 Arghode, V. K. and Gupta, A. K., “Effect of Flow Field for Colorless Distributed Combustion (CDC) for Gas Turbine Combustion”, *Applied Energy*, Vol. 87, 2010, pp. 1631-1640.
- J.2 Arghode, V. K. and Gupta, A. K., “Development of High Intensity CDC Combustor for Gas Turbine Engines”, *Applied Energy*, Vol. 88, 2011, pp. 963-973.
- J.3 Arghode, V. K. and Gupta, A. K., “Investigation of Forward Flow Configuration for Colorless Distributed Combustion for Gas Turbine Application”, *Applied Energy*, Vol. 88, 2011, pp. 29-40.
- J.4 Arghode, V. K. and Gupta, A. K., “Investigation of Reverse Flow Configuration for Colorless Distributed Combustion for Gas Turbine Application”, *Applied Energy*, Vol. 88, 2011, pp. 1096-1104.
- J.5 Arghode, V. K. and Gupta, A. K., “Hydrogen Addition Effects on Methane-Air Colorless Distributed Combustion Flames”, *International Journal of Hydrogen Energy*, Vol. 36, 2011, pp. 6292-6302.
- J.6 Arghode, V. K., Gupta, A. K. and Bryden, K. M., “High Intensity Colorless Distributed Combustion for Ultra Low Emissions and Enhanced Performance”, *Applied Energy*, **(In Press 2011)**.
- J.7 Arghode, V. K., Khalil, A. E. E. and Gupta, A. K., “Fuel Dilution and Liquid Fuel Operational Effects on Ultra-High Thermal Intensity Distributed Combustor”, *Applied Energy*, **(Submitted 2011)**.
- J. 8 Arghode, V. K., Khalil, A. E. E. and Gupta, A. K., “Role of Thermal Intensity on Operational Characteristics and Ultra-Low Emission Distributed Combustion”, *Applied Energy*, **(In Preparation 2011)**.

A. 2 Conference Papers

- C.1 Arghode, V. K. and Gupta, A. K., “Numerical Simulations of Gas Recirculation for CDC Combustor”, *7th High Temperature Air Combustion and Gasification International Symposium, Phuket, Thailand, 13-16 January, 2008.*
- C.2 Arghode, V. K., Gupta, A. K. and Yu, K. H., “Colorless Distributed Combustion (CDC): Effect of Flowfield Configuration”, *47th AIAA Aerospace Sciences Meeting, Orlando, Florida, 5-8 January, 2009.*
- C.3 Arghode, V. K. and Gupta, A. K., “Effect of Confinement on Colorless Distributed Combustion for Gas Turbine Engines”, *45th AIAA/ASME/SAE/ASEE Joint Propulsion Conference and Exhibit, Denver, Colorado, 2-5 August, 2009.*
- C.4 Arghode V. K. and Gupta A. K., “Investigation of Fuel/Air Mixing Characteristics in a CDC Combustor”, *19th International Symposium on Airbreathing Engines, Montreal, Canada, 7-11 September, 2009.*
- C.5 Arghode, V. K., Gupta, A. K. and Yu, K. H., “Investigation of Non-Premixed and Premixed Distributed Combustion for GT Application”, *48th AIAA Aerospace Sciences Meeting, Orlando, Florida, 4-7 January, 2010.*
- C.6 Arghode, V. K. and Gupta, A. K., “Investigation of Distributed Combustion for Gas Turbine Application: Forward Flow Configuration”, *ASME 2010 Power Conference, Chicago, Illinois, 13-15 July, 2010.*
- C.7 Arghode, V. K. and Gupta, A. K., “Investigation of Distributed Combustion for Gas Turbine Application: Reverse Flow Configuration”, *46th AIAA/ASME/SAE/ASEE Joint Propulsion Conference, Nashville, Tennessee, 25-28 July 2010.*
- C.8 Arghode, V. K. and Gupta, A. K., “Hydrogen Addition Effects on Methane-Air Colorless Distributed Combustion Flames”, *49th AIAA Aerospace Sciences Meeting, Orlando, Florida, 4-7 January, 2011.*
- C.9 Arghode, V. K., Gupta, A. K. and Bryden, K. M., “High Intensity Colorless Distributed Combustion for Ultra Low Emissions and Enhanced Performance”, *46th AIAA/ASME/SAE/ASEE Joint Propulsion Conference, San Diego, California, 1-3 August, 2011.*
- C.10 Arghode, V. K., Khalil, A. E. E. and Gupta, A. K., “Fuel Dilution Effects on High Thermal Intensity CDC Combustor”, *50th AIAA Aerospace Sciences Meeting, Orlando, Tennessee, 9-12 January, 2012.*

List of other journal and conference papers published by Arghode, V. K. *et al.*

A. 3 Other Journal Papers

- OJ.1 Arghode, V. K., Kumar, A., Sundarraj, S. and Dutta, P., “Computational Modeling of GMAW Process for Joining Dissimilar Aluminum Alloys”, *Numerical Heat Transfer, Part A: Applications*, v 53, p 432-455, 2008.
- OJ.2 Kim, H. S., Arghode, V. K., Linck, M., B. and Gupta, A., K., “Hydrogen Addition Effects in a Confined Swirl-Stabilized Methane-Air Flame”, *International Journal of Hydrogen Energy*, v 34, p 1054-1062, 2009.
- OJ.3 Kim, H. S., Arghode, V. K. and Gupta, A., K., “Flame Characteristics of Hydrogen-Enriched Methane-Air Premixed Swirling Flames”, *International Journal of Hydrogen Energy*, v 34, p 1063-1073, 2009.
- OJ.4 Kim, H. S., Arghode, V. K. and Gupta, A. K., “Combustion Characteristics of a Lean Premixed LPG-Air Combustor”, *International Journal of Hydrogen Energy*, v 34, p 1045-1053, 2009.
- OJ.5 Arghode, V. K. and Gupta, A. K., “Jet Characteristics from a Submerged Combustion System”, *Applied Energy*, (**In Press 2011**).
- OJ.6 Khalil, A. E. E., Arghode, V. K. and Gupta A., K., “Low Calorific Value Fuelled Distributed Combustion With Swirl For Gas Turbine Applications”, *Applied Energy*, (**Submitted 2011**).
- OJ.7 Khalil, A. E. E., Arghode, V. K. and Gupta A. K., “High Temperature Air Combustion; Challenges and Achievements”, *Applied Energy*, (**In Preparation 2011**).

A. 4 Other Conference Papers

- OC.1 Arghode, V. K., Kumar, A. and Dutta, P., “Modelling of Transport Phenomena in Welding of Dissimilar Aluminium Alloys”, *Invited Paper, 8th International Seminar on Numerical Analysis of Weldability, 25-27 September 2006, Gratz, Seggau, Austria*.
- OC.2 Kim, H. S., Arghode, V. K. and Gupta, A. K., “Flame Characteristics of Hydrogen-Enriched Methane-Air Premixed Swirling Flames”, *45th AIAA Aerospace Sciences Meeting, 8-11 January 2007, Reno, Nevada*.
- OC.3 Kim, H. S., Arghode, V. K., Gupta, A. K., “Hydrogen Addition Effects on Swirl Stabilized Methane Flame”, *ASME Design Engineering Technical Conferences and Computers and Information in Engineering Conference, 4-7 September 2007, Las Vegas, Nevada*.

- OC.4 Arghode, V. K., Gupta, A. K. and Yu, K. H., “Effect of Nozzle Exit Geometry on Submerged Jet Characteristics in Underwater Propulsion”, *46th AIAA Aerospace Sciences Meeting, 7-10 January 2008, Reno, Nevada.*
- OC.5 Tsukamoto, K., Arghode, V. K., Oshima, N. and Gupta, A., K., “Numerical Investigation of Methane- Air Premixed Swirling Flame”, *6th International Energy Conversion Engineering Conference, 28-30 July 2008, Cleveland, Ohio.*
- OC.6 Khalil, A. E. E., Arghode, V. K. and Gupta A. K., “Colorless Distributed Combustion (CDC) with Swirl for Gas Turbine Application”, *ASME Power Conference, 13-15 July 2010, Chicago, Illinois.*
- OC.7 Khalil, A. E. E., Arghode, V. K. and Gupta A. K., “Distributed Combustion with Swirl for Gas Turbine Application”, *49th AIAA Aerospace Sciences Meeting, 4-7 January 2011, Orlando, Florida.*

Appendix B - Centerline Jet Velocity Decay

Centerline velocity decay of a turbulent jet exiting in ambient condition is given in equation B.1. The correlation constants from different references are given in Table B.1 and plotted in Figure B.1. It can be noted that there is a wide range of velocity decay obtained from the correlations. For comparison purposes correlation given by Hussein 1 has been used in this dissertation. Accurate matching of the velocity profile with predicted numerical simulations is not aimed for in the dissertation, instead the correlation is used as general guideline for comparison and understanding the flowfield characteristics.

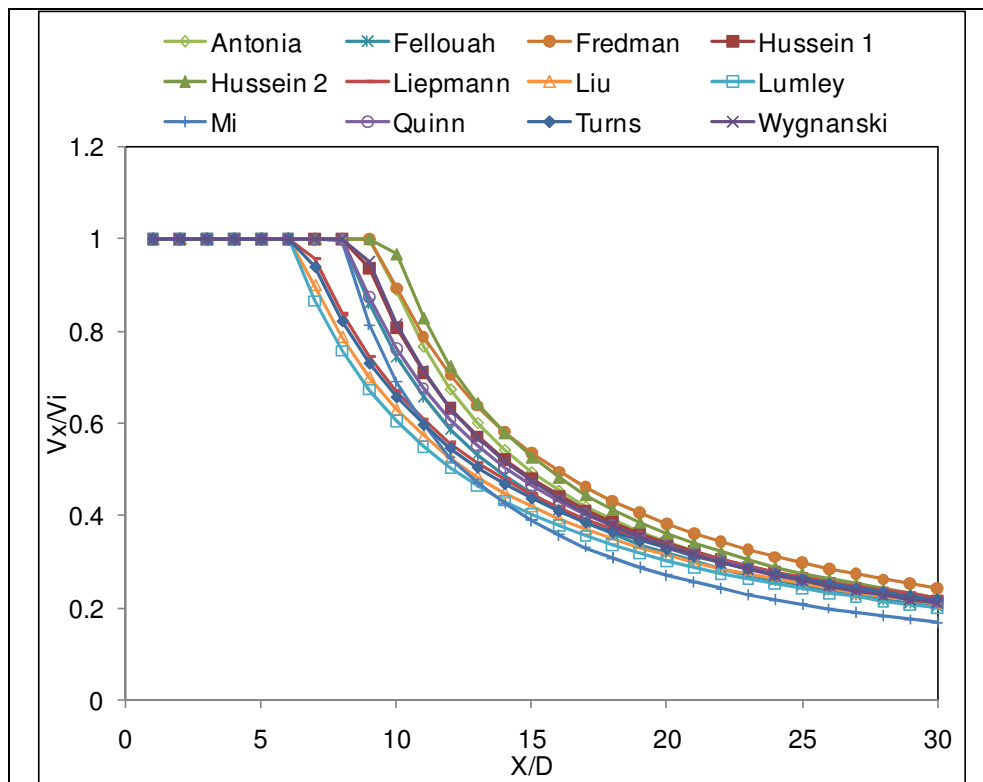


Figure B.1 Centerline jet velocity decay plots using different correlations in literature.

$$\frac{V_x}{V_i} = \frac{B_u}{(x/D - x_0/D)} \quad (\text{equation B.1})$$

V_x = Centerline jet velocity

V_i = Initial jet velocity

x = Distance along the jet centerline

x_0 = Virtual origin

D = Jet diameter

Table B.1 Correlation constants for centerline velocity decay of a free jet.

Reference	B_u	x_0/D
Antonia, 2002	5.99	2.15
Fellouah, 2009	6.7	2.5
Ferdman, 2000	6.7	2.5
Hussein 1, 1994	5.9	2.7
Hussein 2, 1994	5.8	4
Liepmann, 1994	6.7	0
Liu, 1997	6.3	0
Lumley, 1993	6.06	0
Mi, 2007	4.48	3.5
Quinn, 2006	5.99	2.15
Turns, 2000	6.575	0
Wynanski, 1969	5.7	3

Appendix C - CFD Simulations of Free Jet

Grid refinement study was performed for two mesh sizes of 26K and 120K as shown in Figure C.1. The coarse mesh (26K) is similar to the mesh used for 3D numerical simulations in the dissertation. The refined mesh took much more time to converge (10x) and hence it was unsuitable for numerical computation for 3D geometry investigated in the dissertation.

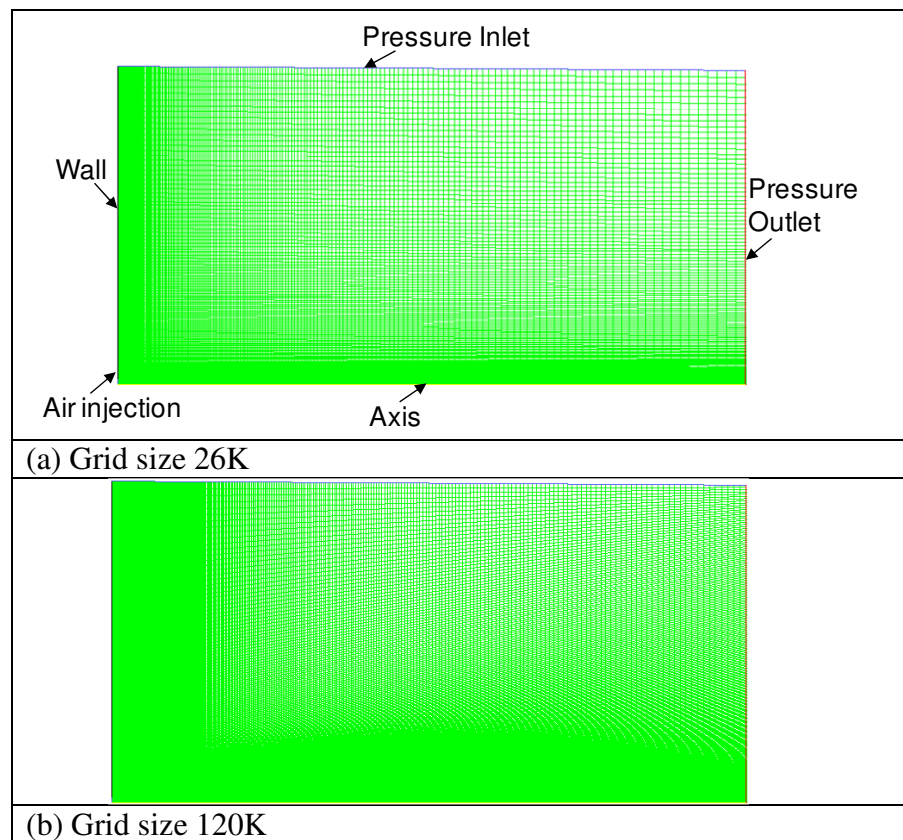


Figure C.1 Mesh used for simulations (2D axisymmetric, diameter=64D, length=64D, air injection diameter=D, D=3/16”).

The result of grid refinement study is presented in Figure C.2(a). Inlet jet velocity is 128m/s with inlet turbulence intensity of 5%. Realizable k-e model is used for the simulations. Correlation used for comparison is from [Hussein 1, 1994, see table B1].

From the figure it can be observed that for refined mesh the velocity decay is slightly delayed as compared to the coarse mesh however the difference is not significant.

The effect of air inlet velocity is shown in Figure C.2(b). Coarse mesh is used for the simulations. Inlet turbulence intensity was 5% and realizable k-e model was used for the simulations. From the figure it can be noted that the velocity decay is not independent of inlet velocity for the CFD simulations. The velocity decay is delayed for higher inlet velocity. This suggests that the turbulence model is not able to capture the Reynolds number independence of free jet decay.

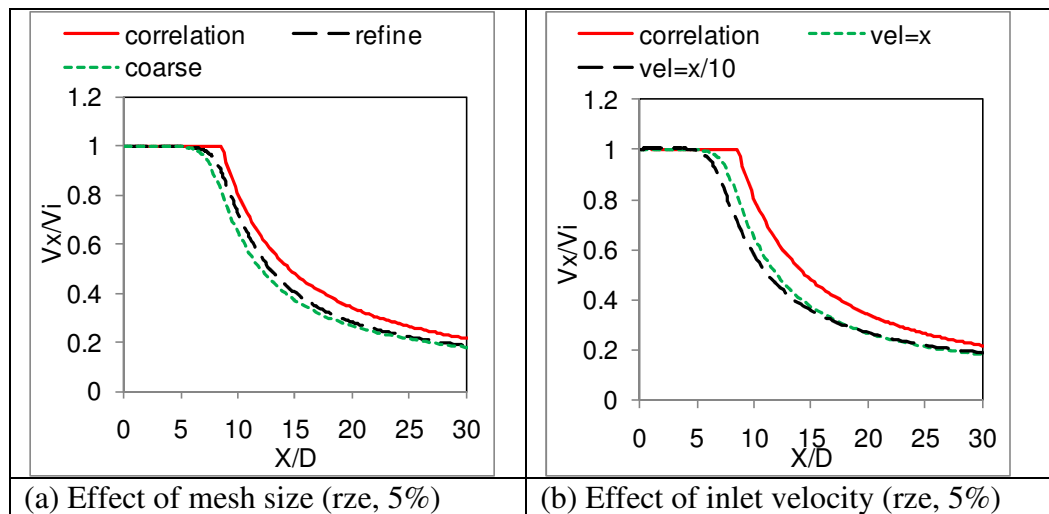


Figure C.2 Effect of (a) grid size and (b) inlet velocity, k-e realizable model, turbulent intensity=5%, inlet velocity $x=128\text{m/s}$.

Effect of inlet turbulence intensity is shown in Figure C.2(a). Realizable k-e model was used for simulation with air injection velocity of 128m/s . It can be noted that the inlet turbulence intensity has significant effect on the velocity decay profile and lower turbulence intensity significantly delay the velocity decay. In the dissertation inlet turbulence intensity of 5% has been used. Figure C.2(b) shows the effect of turbulence model on velocity decay and it can be noted that realizable k-e model results in slightly delayed decay of centerline velocity as compared to standard (ske)

k-e model. In the dissertation realizable k-e model is used instead of standard k-e model. For this simulation inlet turbulence intensity of 5% and inlet velocity of 128m/s was used.

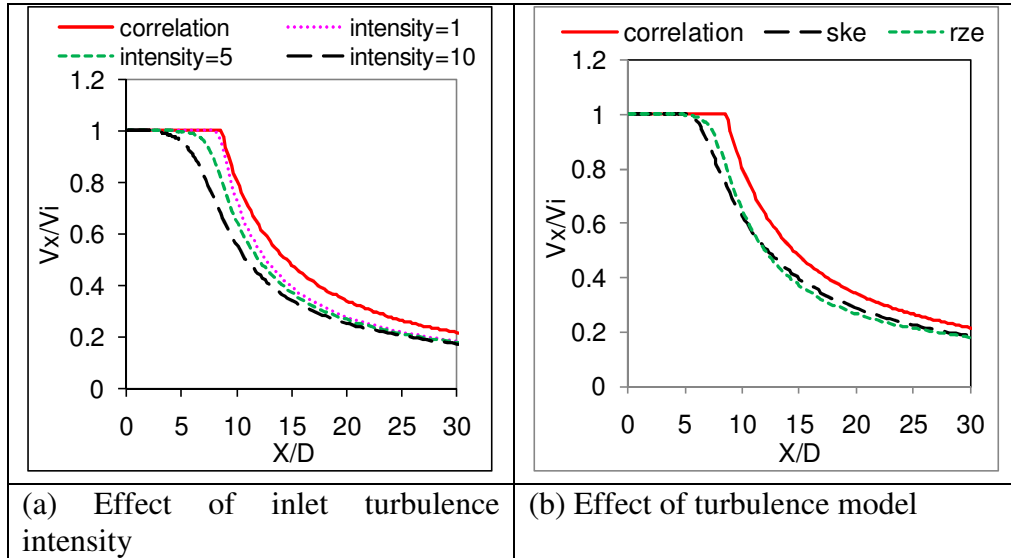


Figure C.3 Effect of inlet turbulence intensity and turbulence models.

Appendix D – Scaling of CDC Combustor

Scaling studies of CDC combustor is performed for implementation of CDC combustors in practical gas turbines. The scaling factor was calculated to be 11765:1 in terms of heat load where a conventional combustor can releases close to 48000kW of energy through combustion. Different approaches have been discussed in Kumar, S., *et al.*, 2005, which include constant velocity (CV) and constant residence time approach (CRT) and these approaches have been summarized in Table D.1.

As observed from Table D.1, CV approach leads to increase in mixing time and significant decrease in thermal intensity, whereas CRT approach resulted in very high velocity which will result in unacceptable levels of pressure drop across the combustor. However thermal intensity and mixing time is constant for CRT approach. In Cole's approach the velocity is increased significantly and this does not seem to be a feasible solution for scaling a CDC combustor. In Kumar, S., *et al.*, 2005, approach the geometry was scaled based on the CRT approach and the number of air and fuel injection ports were increased to maintain constant mixing time.

In the present scaling approach the geometry of CDC combustor is scaled so as to fit practically in a gas turbine combustor. The scaled combustor can is a cylindrical volume which operates in reverse cross-flow mode as shown in Table D.2. The gases exit from the central region whereas the combustion air enters the combustor from the periphery. Fuel is injected in cross-flow as shown in Table D.2. It may be noted that the scaled combustor is essentially similar to the CDC combustor investigated experimentally. Most of the parameters were preserved in the scaling however the thermal intensity reduced to about $21\text{MW/m}^3\text{-atm}$ from $53\text{MW/m}^3\text{-atm}$ and the

turbulent mixing time increased by almost an order of magnitude. Higher mixing time may lead to lower mixing rates and lead to higher NO_x, CO emissions and this issue needs to be tested while practically implementing the combustor.

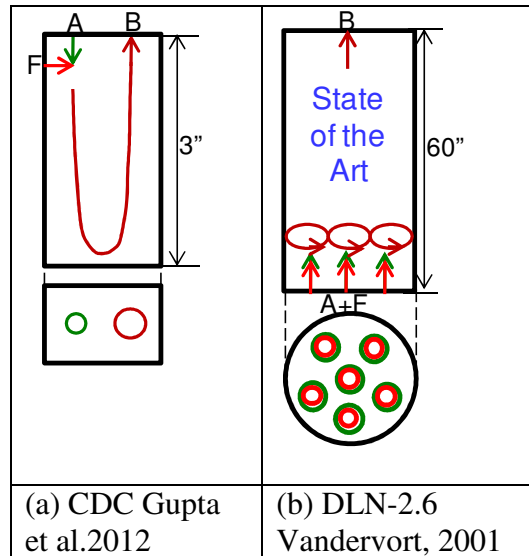


Figure D.1 Scaling of CDC combustor.

- $Q = (H2/P2)/(H1/P1)$
- H2, H1 = heat load
- P2, P1 = operating pressure
- CV = constant velocity
- CRT = constant residence time

Table D.1 Different scaling approach.

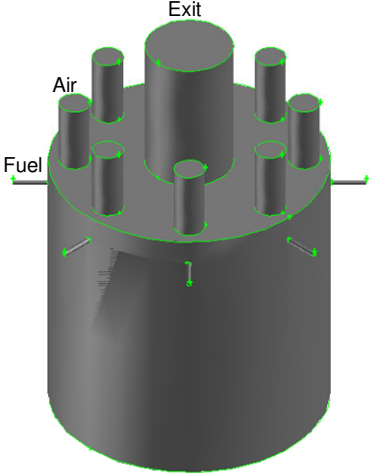
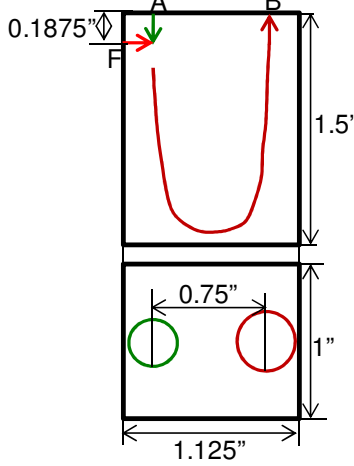
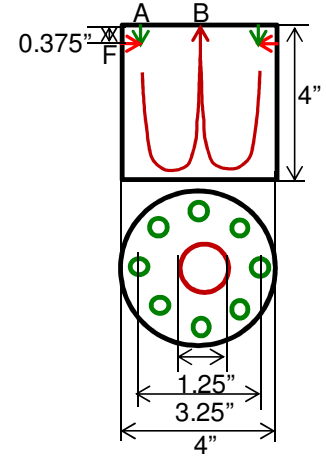
Scaling approach (Kumar, S., <i>et al.</i> , 2005)	Geometric scaling	Velocity scaling	τ_{mixing} (D/U)	Intensity
CV	$\sim Q^{1/2}$	$\sim \text{Constant}$	$\sim Q^{1/2}$	$\sim Q^{-1/2}$
CRT	$\sim Q^{1/3}$	$\sim Q^{1/3}$	$\sim \text{Constant}$	$\sim \text{Constant}$
Cole	$\sim Q^{1/4}$	$\sim Q^{1/2}$	$\sim Q^{-1/4}$	$\sim Q^{1/4}$
Sudarshan	$\sim Q^{1/3}$	$\sim \text{Constant}$	$\sim \text{Constant}$	$\sim \text{Constant}$
Present	$\sim Q^{1/3}$	$\sim \text{Constant}$	$\sim Q^{1/3}$	$\sim \text{Constant}$

Table D.2 Parameters of high thermal intensity scaled combustor.

Thermal Intensity	53MW/m ³ -atm	19MW/m ³ -atm
Heat load	3.91kW ($\Phi=0.5$)	46000kW ($\Phi=0.5$)
Fuel	Methane	Natural gas
Pressure	1atm	16atm
Air Velocity	92m/s	92m/s
Fuel Velocity	61m/s	61m/s
Exit Velocity	160m/s	165m/s
Air Temperature	600K	600K
Fuel Temperature	300K	300K
Exit temperature	1500K	1500K
D_{air}	0.3125inch	3inch
D_{fuel}	0.0625inch	0.6inch
$\tau_{air}(D/U)$	0.086ms	0.83ms
$\tau_{fuel}(D/U)$	0.026ms	0.25ms
D_{exit}	0.375inch	10inch
# air, fuel holes	1, 1	8, 8
L/D_{air}	9.6	10

Scaling of the ultra-high thermal intensity CDC combustor is given in Table D.3. Aircraft engines operate at thermal intensity of about $150\text{MW/m}^3\text{-atm}$ with residence time in the range of 2-3ms. The length scale of such combustors is about 6-10inch. In the present study the combustor is scaled from 1.5inch to 4inch and heat load is scaled from 4.7kW to 75 kW. These flowrates could be handled in laboratory settings and hence will be useful for providing valuable data while further scaling up of CDC combustor for land based gas turbine application. The air and fuel injection diameters are chosen for easy access of the fittings available commercially. The scaled combustor could also be operated for ethanol fuel and corresponding parameters for ethanol fuel is also presented in the table. It may be noted that while scaling up of CDC combustor from the thermal intensity decreased from $170\text{MW/m}^3\text{-atm}$ to $92\text{MW/m}^3\text{-atm}$. However it may be noted that the turbulent mixing time was maintained very close to the small scale CDC combustor.

Table D.3 Parameters of ultra-high thermal intensity scaled combustor.

			
Thermal Intensity	170MW/m ³ -atm	92MW/m ³ -atm	92MW/m ³ -atm
Heat load	4.7kW ($\Phi=0.6$)	75kW ($\Phi=0.6$)	75kW ($\Phi=0.6$)
Fuel	Methane	Propane	Ethanol
Pressure	1atm	1atm	1atm
Air Velocity	92m/s	92m/s	86m/s
Fuel Velocity	73m/s	52m/s	1.7m/s
Exit Velocity	170m/s	245m/s	245m/s
Air Temperature	600K	600K	600K
Fuel Temperature	300K	300K	300K
Exit temperature	1600K	1600K	1600K
D _{air}	0.3125inch	0.4375inch	0.4375inch
D _{fuel}	0.0625inch	0.0625inch	0.0225inch
$\tau_{air}(D/U)$	0.086ms	0.120ms	0.129ms
$\tau_{fuel}(D/U)$	0.026ms	0.030ms	-
D _{exit}	0.375inch	1.25inch	1.25inch
# air, fuel holes	1, 1	8, 8	8, 8
L/D _{air}	9.6	9.1	9.1

Appendix E – Equilibrium and Perfectly Stirred Reactor Calculations

Equilibrium calculations were performed to obtain values of NO and CO emissions as well as adiabatic flames temperatures at different equivalence ratios for methane air combustion at normal and elevated initial temperature and normal pressure. The values are summarized in Table E.1 and E.2. It may be noted that at equivalence ratio of 0.7 the adiabatic flame temperature is about 1850K which is close the thermal NO formation region and hence operation leaner than equivalence ratio of 0.7 is desired at normal temperature operation.

The NO and CO plots (see Figure E.1) suggests that much higher NO levels are obtained from equilibrium calculations, however, it may be noted that equilibrium calculations does not consider the chemical kinetics and only thermodynamics is considered. With limited time available in the combustor the NO emissions are expected to be limited by the residence time in the combustor. Similarly CO emissions from equilibrium calculations suggests very low values at leaner condition (<0.6) however due to limited time available in practical combustor CO will not get converted to CO_2 completely and higher CO emissions are expected at limited residence time.

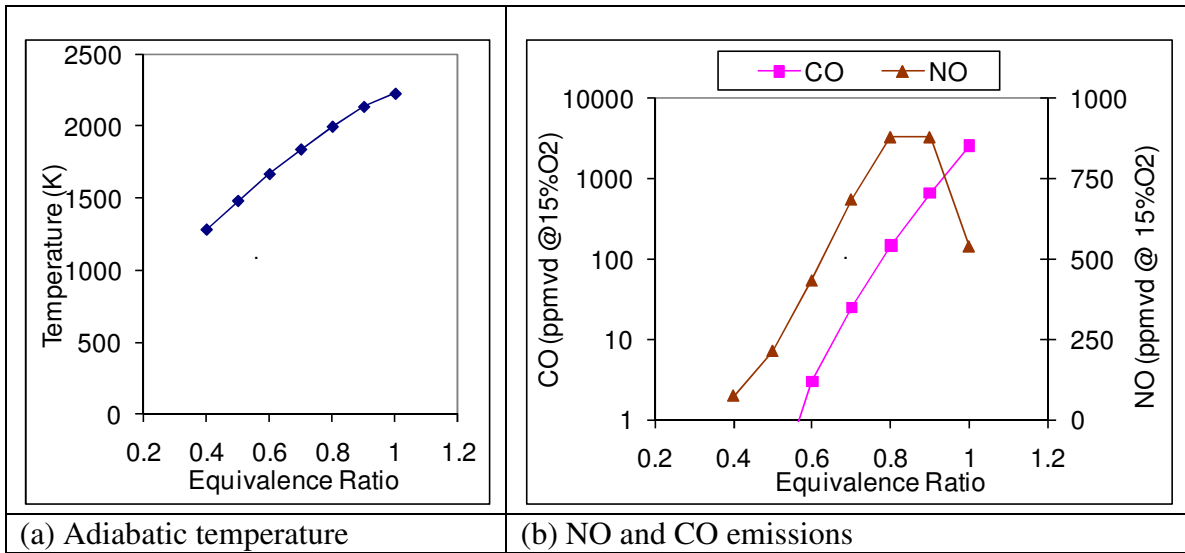


Figure E.1 (a) Adiabatic flame temperature, (b) NO and CO emissions from equilibrium calculations.

Table E.1 Equilibrium calculations for methane air combustion ($T_{in}=300K$).

Equilibrium Calculations for Methane+Air, $T_{in}=300K$					
Phi	Tadiabatic (K)	O ₂ (vol. %)	CO ₂ (vol. %)	CO (ppm) @ 15%O ₂	NO (ppm) @ 15%O ₂
0.4	1280	13.14%	4.38%	0	75
0.5	1480	11.04%	5.54%	0	214
0.6	1666	8.87%	6.72%	3	433
0.7	1838	6.64%	7.92%	25	685
0.8	1996	4.39%	9.10%	147	879
0.9	2134	2.23%	10.12%	663	879
1	2225	0.57%	10.50%	2563	539

Table E.2 summarizes the equilibrium values for NO and CO at air preheat temperature of 600K. It may be noted that at higher preheat temperature the adiabatic flame temperature, CO and NO emission level is also higher.

Table E.2 Equilibrium calculations for methane air combustion ($T_{in}=600K$).

Equilibrium Calculations for Methane+Air, $T_{in}=600K$					
Phi	Tadiabatic (K)	O2 (vol. %)	CO2 (vol. %)	CO (ppm) @ 15%O2	NO (ppm) @ 15%O2
0.4	1527	13.09%	4.38%	1	856
0.5	1717	10.95%	5.54%	9	1376
0.6	1893	8.74%	6.70%	61	1837
0.7	2053	6.50%	7.84%	278	2113
0.8	2192	4.31%	8.85%	945	2106
0.9	2301	2.37%	9.50%	2537	1777
1	2366	0.94%	9.52%	5641	1189

Perfectly stirred reactor calculations were performed at residence time of 20ms and the results are presented in Figure E. 2 and Table E.3. From the figure and table we can observe that the NO emission level is much lower than the equilibrium value and CO emission level is much higher than the equilibrium values. We can also note that the contribution of thermal NO decreases significantly at lower equivalence ratios (0.5, 0.6). This suggests that the role of other mechanisms such as prompt and N_2O mechanism is significantly in this operating condition.

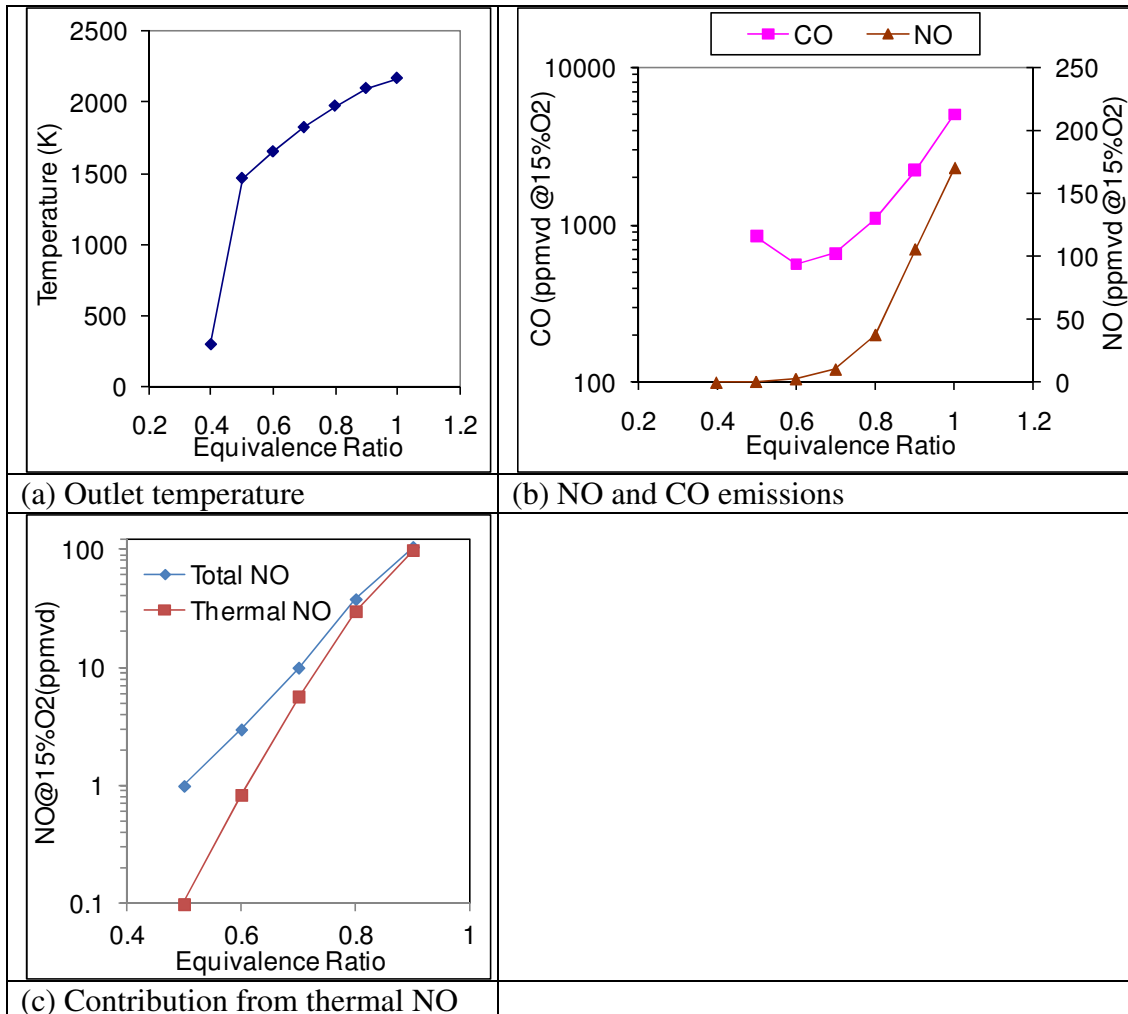


Figure E.2 (a) Outlet temperature, (b) NO and CO emissions from perfectly stirred reactor calculations.

Table E.3 Perfectly stirred reactor calculations for methane air combustion ($T_{in}=300K$, $T_{res}=20ms$).

Perfectly Stirred Reactor Calculations for Methane+Air						
Phi	Tout (K)	O2 (vol. %)	CO2 (vol. %)	CO (ppm @ 15%O2)	NO (ppm @ 15%O2)	Contribution of Thermal NO (%)
0.4	300	20.15	0.00	0	0	0
0.5	1461	11.14	5.38	848	1	10
0.6	1649	8.97	6.59	563	3	28
0.7	1817	6.80	7.74	662	10	57
0.8	1966	4.64	8.80	1097	38	79
0.9	2087	2.61	9.62	2230	105	94
1	2166	1.03	9.76	5035	169	115

The effect of pressure and temperature on NO and CO emissions is shown in Figure E.3. residence time of 15ms is used for these computations. From the figure we can observe that with increase in pressure NO emissions increases at higher equivalence ratios but decreases at lower equivalence ratios. At higher equivalence ratio the contribution from thermal NO is higher and this may be the reason for higher NO. CO emissions decreases significantly at higher pressure and this may be because of faster reaction rates to convert CO to CO₂. Higher inlet temperature also results in higher NO emissions possibly due to increased contribution from thermal mechanism. CO emissions also increase at higher temperature possibly due to higher dissociation of CO₂ to CO at higher temperatures.

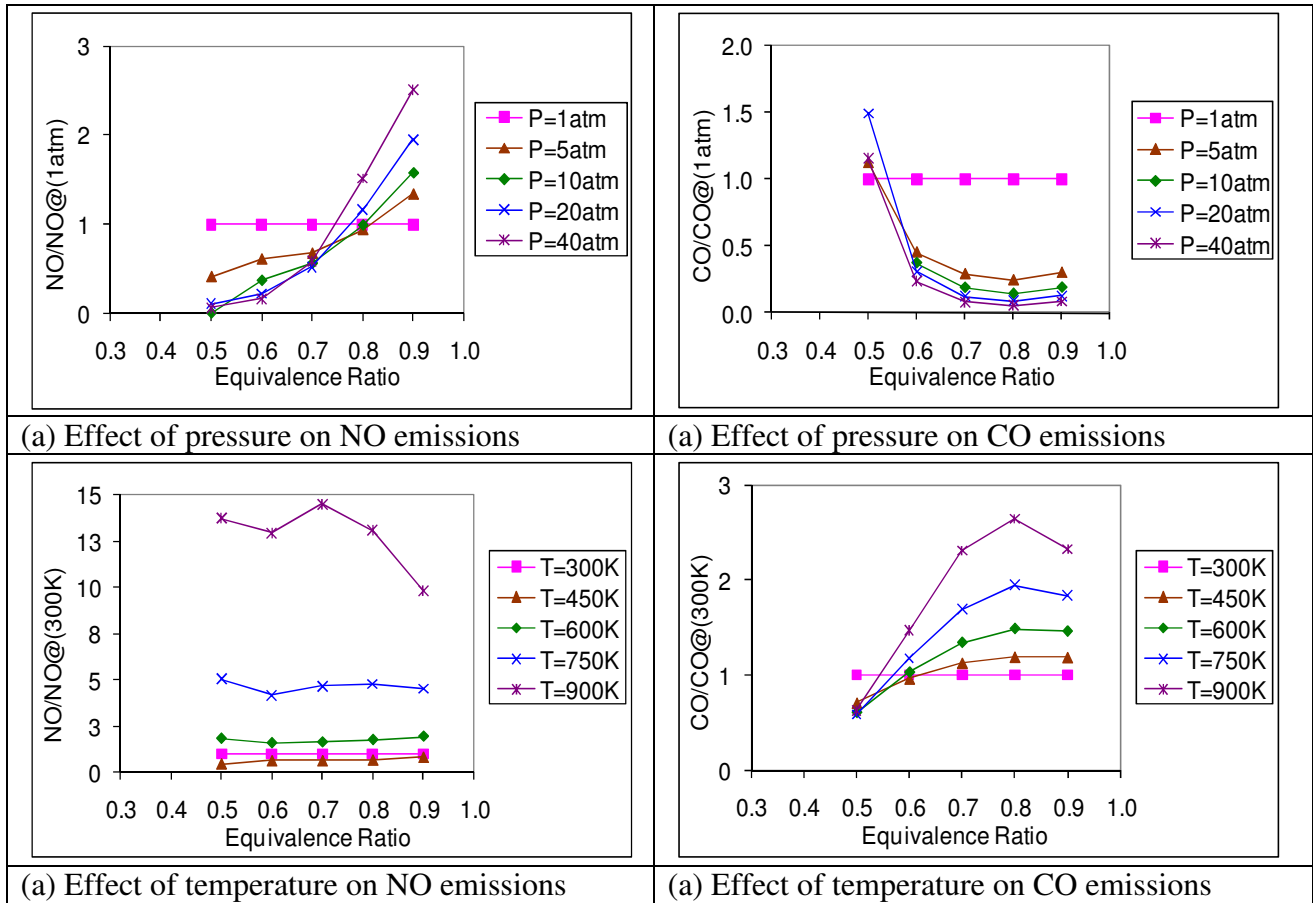


Figure E.3 (a,b) Effect of pressure and (c,d) effect of temperature on NO and CO emissions from perfectly stirred reactor calculations.

Appendix F – Operational Characteristics of Low Emission Combustors

Table F.1 Combustor geometries reported in literature.

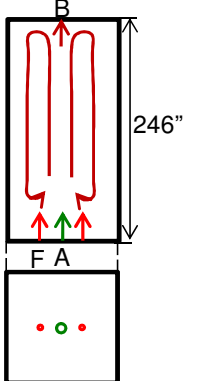
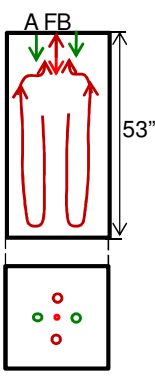
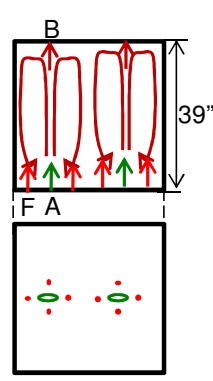
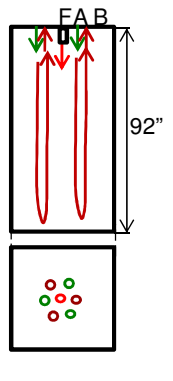
				
	(1)MILD, Weber <i>et al.</i> , IFRF, 2005	(2)FLOX, Colorado <i>et al.</i> , U Antioquia, 2010	(3)HiTAC, Gupta <i>et al.</i> , NFK, 2003	(4)FLOX, Wunning <i>et al.</i> , WS GmbH, 1997
Configuration	FS	RS	FS	RS
Thermal Intensity	0.02MW/m ³ -atm	0.05MW/m ³ -atm	0.06MW/m ³ -atm	0.07MW/m ³ -atm
Heat load	580kW	20kW	58kW	200kW
Fuel	Natural gas	Natural gas	Natural gas	Natural gas
Pressure	1atm	1atm	1atm	1atm
Air Velocity	85m/s	79m/s	74m/s	-
Fuel Velocity	100m/s	81m/s	40m/s	-
Air Diameter	124mm	24.4mm	29.1mm	-
Fuel Diameter	11.3mm	3.2mm	2.7mm	-
$\tau_{air}(D/U)$	1.46ms	0.309ms	0.393ms	-
$\tau_{fuel}(D/U)$	0.113ms	0.040	0.068ms	-
Air Temperature	1600K	810K	1400K	1100K
Fuel Temperature	300K	300K	300K	300K
NO _x @15%O ₂	9ppm($\Phi=1$)	1ppm($\Phi=0.8$)	44ppm ($\Phi=0.8$)	11ppm ($\Phi=0.9$)
CO@15%O ₂	< 10ppm($\Phi=1$)	<10ppm($\Phi=0.8$)	-	-

Table F.1 Combustor geometries reported in literature (contd...).

	(5)HiTAC, Gupta <i>et al.</i> , NFK, 2003	(6)HiTAC, Gupta <i>et al.</i> , NFK, 2003	(7)FODI, Sobiesiak <i>et al.</i> , Queen's, 1998	(8)FODI, He <i>et al.</i> , Queen's, 2008
Configuration	FS	FO	FS	RS
Thermal Intensity	$0.1\text{MW}/\text{m}^3\text{-atm}$	$0.1\text{MW}/\text{m}^3\text{-atm}$	$0.1\text{MW}/\text{m}^3\text{-atm}$	$0.1\text{MW}/\text{m}^3\text{-atm}$
Heat load	350kW	350kW	368kW	32kW
Fuel	Natural gas	Natural gas	Natural gas	Natural gas
Pressure	1atm	1atm	1atm	1atm
Air Velocity	-	-	145m/s	118m/s
Fuel Velocity	-	-	51m/s	41m/s
Air Diameter	-	-	19.1mm	12.7mm
Fuel Diameter	-	-	6.35mm	5.4mm
$\tau_{\text{air}}(D/U)$	-	-	0.131ms	0.107ms
$\tau_{\text{fuel}}(D/U)$	-	-	0.125ms	0.132ms
Air Temperature	1400K	1400K	650K	324K
Fuel Temperature	300K	300K	300K	288K
$\text{NO}_x @ 15\%\text{O}_2$	9ppm ($\Phi=0.8$)	8ppm($\Phi=0.8$)	12ppm($\Phi=0.8$)	3ppm($\Phi=0.6$)
$\text{CO}@ 15\%\text{O}_2$	<10ppm ($\Phi=0.8$)	10ppm($\Phi=0.8$)	-	34ppm($\Phi=0.6$)

Table F.1 Combustor geometries reported in literature (contd...).

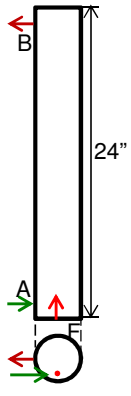
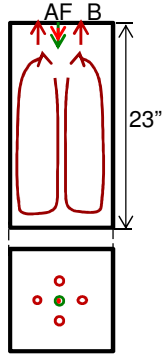
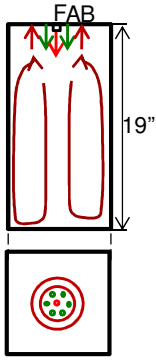
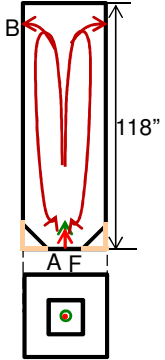
				
	(9)PAWC, Yetter <i>et al.</i> , Princeton, 2000	(10)MILD, Mi <i>et al.</i> , U. Ad. 2009	(11)MILD, Dally <i>et al.</i> , U. Ad., 2004	(12)FLOX, Xing <i>et al.</i> , UST China, 2007
Configuration	SWIRL	RS	RS	FS (coaxial)
Thermal Intensity	0.1MW/m ³ -atm	0.2MW/m ³ -atm	0.2MW/m ³ -atm	0.3MW/m ³ -atm
Heat load	0.54kW	10kW	7kW	1000kW
Fuel	Methane	Natural gas	Methane	Natural gas
Pressure	1atm	1atm	1atm	1atm
Air Velocity	17m/s	21m/s	85m/s	-
Fuel Velocity	1m/s	10m/s	15m/s	63m/s
Air Diameter	11.2mm	4.4mm	5mm	-
Fuel Diameter	4.8mm	7.2mm	4 mm	-
$\tau_{air}(D/U)$	0.658ms	0.210ms	0.059ms	-
$\tau_{fuel}(D/U)$	4.8ms	0.720ms	0.267ms	-
Air Temperature	300K	723K	1352K	300K
Fuel Temperature	300K	293K	300K	300K
NO _x @15%O ₂	5ppm($\Phi=0.1$)	1ppm($\Phi=0.8$)	7ppm ($\Phi=0.8$)	26ppm($\Phi=0.9$)
CO@15%O ₂	225ppm($\Phi=0.1$)	<10ppm($\Phi=0.8$)	-	<10ppm($\Phi=0.9$)

Table F.1 Combustor geometries reported in literature (contd...).

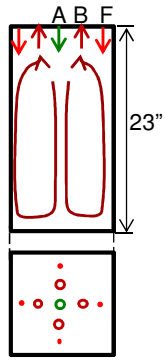
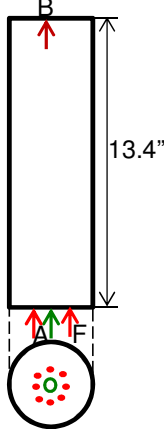
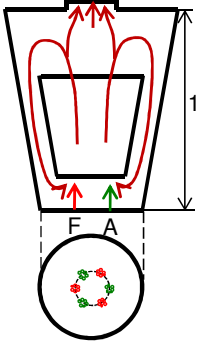
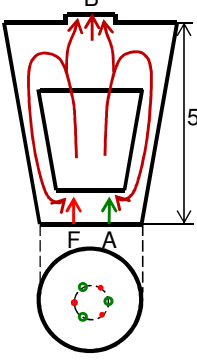
				
	(13)MILD, Szego <i>et al.</i> , U. Ad., 2009	(14)FLOX, Verissimo <i>et al.</i> , TU Lisbon, 2011	(15)HILE, Kumar <i>et al.</i> , IISc, 2005	(16)HILE, Kumar <i>et al.</i> , IISc, 2002
Configuration	RS	FLOX	FS	FS
Thermal Intensity	0.3MW/m ³ -atm	3.8MW/m ³ -atm	5.6MW/m ³ -atm	10MW/m ³ -atm
Heat load	15kW	10kW	150kW	3kW
Fuel	Natural gas	Methane	LPG	LPG
Pressure	1atm	1atm	1atm	1atm
Air Velocity	20m/s	96m/s	95m/s	79m/s
Fuel Velocity	40m/s	6.2m/s	243m/s	60m/s
Air Diameter	26.6mm	10mm	5mm	2mm
Fuel Diameter	2mm	2mm	0.7mm	0.5mm
$\tau_{\text{air}}(D/U)$	1.33ms	0.104ms	0.052ms	0.025ms
$\tau_{\text{fuel}}(D/U)$	0.05ms	0.323ms	0.003ms	0.008ms
Air Temperature	723K	973K	300K	300K
Fuel Temperature	293K	300K	300K	300K
NO _x @ 15%O ₂	14ppm ($\Phi=0.8$)	4ppm($\Phi=0.9$)	7.5ppm ($\Phi=1$)	4ppm ($\Phi=0.9$)
CO@ 15%O ₂	<100ppm ($\Phi=0.8$)	12ppm($\Phi=0.9$)	2900ppm ($\Phi=1$)	2200ppm ($\Phi=0.9$)

Table F.1 Combustor geometries reported in literature (contd...).

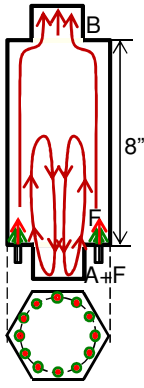
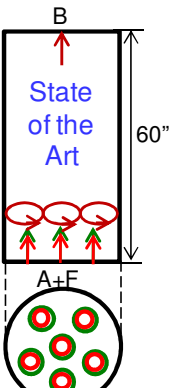
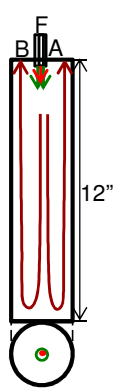
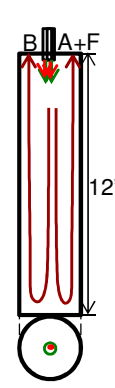
				
	(17)FLOX, Luckerath <i>et al.</i> , DLR, 2008	(18)DLN-2.6, Vandervort, 2001	(19)SPRF, Bobba <i>et al.</i> , GA-Tech, 2008	(20)SPRF, Bobba <i>et al.</i> , GA-Tech, 2008
Configuration	FS (coaxial)	SWIRL (Premixed)	RS (coaxial)	RP
Thermal Intensity	14MW/m ³ -atm	15MW/m ³ -atm	20MW/m ³ -atm	20MW/m ³ -atm
Heat load	475kW	46000kW	20kW	20kW
Fuel	Natural gas	Natural gas	Natural gas	Natural gas
Pressure	20atm	16atm	1atm	1atm
Air Velocity	160m/s	70m/s	110m/s	120m/s
Fuel Velocity	78m/s	-	30m/s	-
Air Diameter	4.5mm	-	6.35mm	6.35mm
Fuel Diameter	1mm	-	4.7mm	-
$\tau_{air}(D/U)$	0.028ms	-	0.058ms	0.053ms
$\tau_{fuel}(D/U)$	0.013ms	-	0.157ms	-
Air Temperature	735K	631K	450K	450K
Fuel Temperature	300K	-	450K	-
NO _x @ 15%O ₂	1ppm ($\Phi=0.4$)	<9ppm ($\Phi=0.4$)	1ppm ($\Phi=0.5$)	1ppm ($\Phi=0.5$)
CO@ 15%O ₂	<10ppm ($\Phi=0.4$)	<10ppm ($\Phi=0.4$)	<10ppm ($\Phi=0.5$)	<10ppm ($\Phi=0.5$)

Table F.1 Combustor geometries reported in literature (contd...).

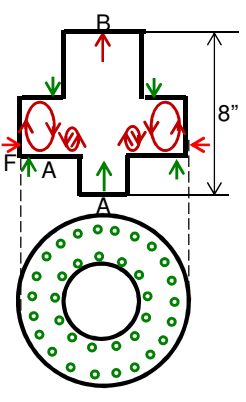
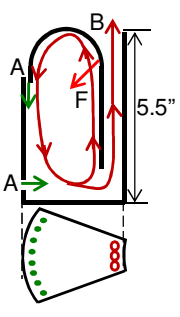
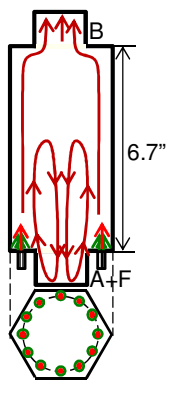
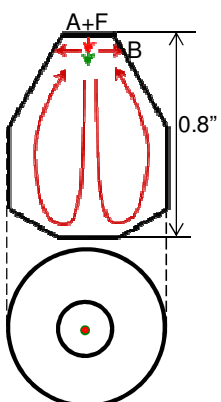
				
	(21)RQL/TVC, Straub <i>et al.</i> , NETL, 2005	(22)TVC, Melo <i>et al.</i> , Technion, 2009	(23)FLOX, Lammel <i>et al.</i> , DLR, 2010	(24)JSR, Shuman <i>et al.</i> , UWashington, 2000
Configuration	RO	RO	FP	RP
Thermal Intensity	20MW/m ³ -atm	25MW/m ³ -atm	68MW/m ³ -atm	90MW/m ³ -atm
Heat load	700kW	32kW	750 kW	0.85kW
Fuel	Natural gas	Methane	Natural gas	Natural gas
Pressure	10atm	1atm	7atm	6.5atm
Air Velocity	-	75m/s	90m/s	80m/s
Fuel Velocity	-	83m/s	-	-
Air Diameter	-	4mm	12mm	1.4mm
Fuel Diameter	-	1mm	-	-
$\tau_{air}(D/U)$	-	0.053ms	0.133ms	0.018ms
$\tau_{fuel}(D/U)$	-	0.012ms	-	-
Air Temperature	644K	300K	673K	573K
Fuel Temperature	300K	300K	-	-
NO _x @15%O ₂	40ppm ($\Phi=0.5$)	6ppm ($\Phi=0.5$)	10ppm($\Phi=0.63$)	3ppm($\Phi=0.6$)
CO@15%O ₂	<10ppm ($\Phi=0.5$)	500ppm ($\Phi=0.5$)	<10ppm($\Phi=0.63$)	50ppm($\Phi=0.6$)

Table F.1 Combustor geometries reported in literature (contd...).

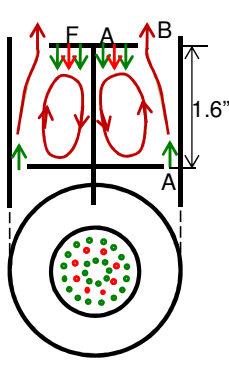
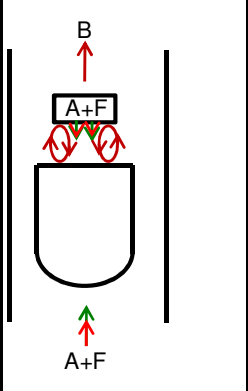
		
	(25)TVC, Hsu <i>et al.</i> , AFRL, 1998	(26)AVC, Edmonds <i>et al.</i> , NETL, 2008
Configuration	RS	RP
Thermal Intensity	144MW/m ³ -atm	-
Heat load	30kW	1000kW
Fuel	Propane	Natural gas
Pressure	1atm	10atm
Air Velocity	48m/s	81m/s
Fuel Velocity	17m/s	-
Air Diameter	2.29mm	-
Fuel Diameter	1.75mm	-
$\tau_{\text{air}}(D/U)$	0.048ms	-
$\tau_{\text{fuel}}(D/U)$	0.103ms	-
Air Temperature	300K	603K
Fuel Temperature	300K	-
NO _x @15%O ₂	52ppm ($\Phi=0.2$)	4ppm($\Phi=0.55$)
CO@15%O ₂	520ppm ($\Phi=0.2$)	<10ppm ($\Phi=0.55$)

Table F.2 Combustor geometries investigated by Arghode, V. K. and Gupta, A. K.

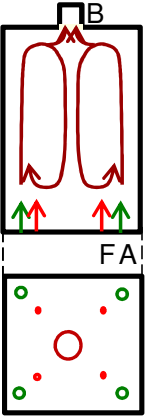
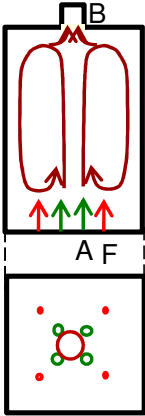
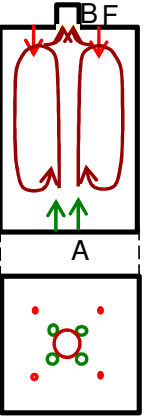
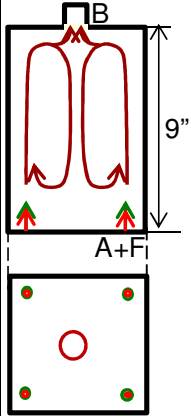
				
	(1)CDC, Gupta <i>et al.</i> , UMD, 2010	(2)CDC, Gupta <i>et al.</i> , UMD, 2010	(3)CDC, Gupta <i>et al.</i> , UMD, 2010	(4)CDC, Gupta <i>et al.</i> , UMD, 2010
Configuration	FS	FS	FO	FP
Thermal Intensity	$5\text{MW}/\text{m}^3\text{-atm}$	$5\text{MW}/\text{m}^3\text{-atm}$	$5\text{MW}/\text{m}^3\text{-atm}$	$5\text{MW}/\text{m}^3\text{-atm}$
Heat load	25kW	25kW	25kW	25kW
Fuel	Methane	Methane	Methane	Methane
Pressure	1atm	1atm	1atm	1atm
Air Velocity	128m/s	128m/s	128m/s	139m/s
Fuel Velocity	97m/s	97m/s	97m/s	-
Air Diameter	4.8mm	4.8mm	4.8mm	4.8mm
Fuel Diameter	1.6mm	1.6mm	1.6mm	-
$\tau_{\text{air}}(D/U)$	0.038ms	0.038ms	0.038ms	0.035ms
$\tau_{\text{fuel}}(D/U)$	0.016ms	0.016ms	0.016ms	-
Air Temperature	300K	300K	300K	300K
Fuel Temperature	300K	300K	300K	-
NO@15%O ₂	7ppm($\Phi=0.8$)	3ppm($\Phi=0.8$)	6ppm ($\Phi=0.8$)	1ppm($\Phi=0.8$)
CO@15%O ₂	33ppm($\Phi=0.8$)	289ppm($\Phi=0.8$)	204ppm ($\Phi=0.8$)	35ppm($\Phi=0.8$)

Table F.2 Combustor geometries investigated by Arghode, V. K. and Gupta, A. K. (contd...).

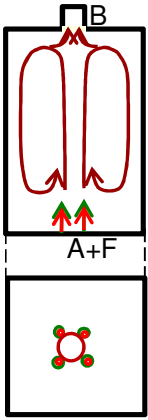
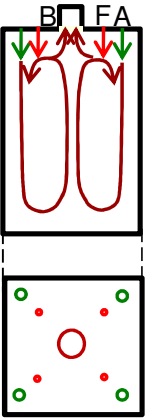
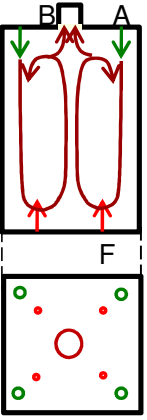
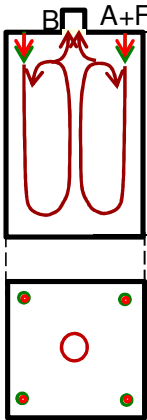
				
	(5)CDC, Gupta <i>et al.</i> , UMD, 2010	(6)CDC, Gupta <i>et al.</i> , UMD, 2010	(7)CDC, Gupta <i>et al.</i> , UMD, 2010	(8)CDC, Gupta <i>et al.</i> , UMD, 2010
Configuration	FP	RS	RO	RP
Thermal Intensity	5MW/m ³ -atm	5MW/m ³ -atm	5MW/m ³ -atm	5MW/m ³ -atm
Heat load	25kW	25kW	25kW	25kW
Fuel	Methane	Methane	Methane	Methane
Pressure	1atm	1atm	1atm	1atm
Air Velocity	139m/s	128m/s	128m/s	139m/s
Fuel Velocity	-	97m/s	97m/s	-
Air Diameter	4.8mm	4.8mm	4.8mm	4.8mm
Fuel Diameter	-	1.6mm	1.6mm	-
$\tau_{air}(D/U)$	0.035ms	0.038ms	0.038ms	0.035ms
$\tau_{fuel}(D/U)$	-	0.016ms	0.016ms	-
Air Temperature	300K	300K	300K	300K
Fuel Temperature	-	300K	300K	-
NO@15%O ₂	2ppm ($\Phi=0.8$)	11ppm($\Phi=0.8$)	9ppm ($\Phi=0.8$)	1ppm($\Phi=0.8$)
CO@15%O ₂	663ppm($\Phi=0.8$)	208ppm($\Phi=0.8$)	38ppm ($\Phi=0.8$)	5ppm($\Phi=0.8$)

Table F.2 Combustor geometries investigated by Arghode, V. K. and Gupta, A. K. (contd...).

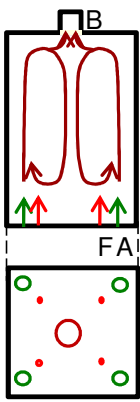
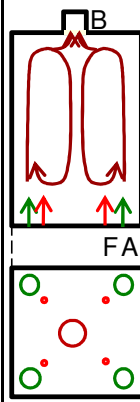
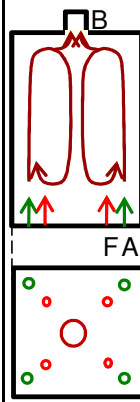
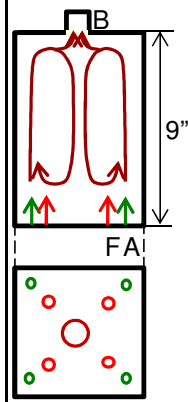
				
	(9)CDC, Gupta <i>et al.</i> , UMD, 2010	(10)CDC, Gupta <i>et al.</i> , UMD, 2010	(11)CDC, Gupta <i>et al.</i> , UMD, 2010	(12)CDC, Gupta <i>et al.</i> , UMD, 2010
Configuration	FS1	FS1	FS1	FS1
Thermal Intensity	$5\text{MW/m}^3\text{-atm}$	$5\text{MW/m}^3\text{-atm}$	$5\text{MW/m}^3\text{-atm}$	$5\text{MW/m}^3\text{-atm}$
Heat load	25kW	25kW	25kW	25kW
Fuel	Methane	Methane	Methane	Methane
Pressure	1atm	1atm	1atm	1atm
Air Velocity	46m/s	24m/s	128m/s	128m/s
Fuel Velocity	97m/s	97m/s	24m/s	11m/s
Air Diameter	mm	mm	4.8mm	4.8mm
Fuel Diameter	1.6	1.6mm	mm	-
$\tau_{\text{air}}(D/U)$	0.173ms	0.463ms	0.038ms	0.038ms
$\tau_{\text{fuel}}(D/U)$	0.016	0.016ms	0.132ms	0.433ms
Air Temperature	300K	300K	300K	300K
Fuel Temperature	300K	300K	300K	300K
NO@15%O ₂	11ppm ($\Phi=0.8$)	15ppm($\Phi=0.8$)	7ppm ($\Phi=0.8$)	8ppm($\Phi=0.8$)
CO@15%O ₂	98ppm($\Phi=0.8$)	145ppm($\Phi=0.8$)	47ppm ($\Phi=0.8$)	70ppm($\Phi=0.8$)

Table F.2 Combustor geometries investigated by Arghode, V. K. and Gupta, A. K. (contd...).

	(13)CDC, Gupta <i>et al.</i> , UMD, 2011	(14)CDC, Gupta <i>et al.</i> , UMD, 2011	(15)CDC, Gupta <i>et al.</i> , UMD, 2011	(16)CDC, Gupta <i>et al.</i> , UMD, 2011	(17)CDC, Gupta <i>et al.</i> , UMD, 2011
Configuration	FS	FO	FP	RO	RP
Thermal Intensity	28MW/m ³ - atm	28MW/m ³ - atm	28MW/m ³ - atm	28MW/m ³ - atm	28MW/m ³ - atm
Heat load	6.25kW	6.25kW	6.25kW	6.25kW	6.25kW
Fuel	Methane	Methane	Methane	Methane	Methane
Pressure	1atm	1atm	1atm	1atm	1atm
Air Velocity	146m/s	146m/s	157m/s	146m/s	157m/s
Fuel Velocity	97m/s	97m/s	-	97m/s	-
Air Diameter	4.8mm	4.8mm	4.8mm	4.8mm	4.8mm
Fuel Diameter	1.6mm	1.6mm	-	1.6mm	-
$\tau_{air}(D/U)$	0.033ms	0.033ms	0.031ms	0.033ms	0.031ms
$\tau_{fuel}(D/U)$	0.016ms	0.016ms	-	0.016ms	0.016ms
Air Temperature	300K	300K	300K	300K	300K
Fuel Temperature	300K	300K	-	300K	-
NO@15%O ₂	9ppm ($\Phi=0.7$)	9ppm ($\Phi=0.7$)	2ppm ($\Phi=0.7$)	12ppm ($\Phi=0.7$)	1ppm ($\Phi=0.7$)
CO@15%O ₂	465ppm ($\Phi=0.7$)	250ppm ($\Phi=0.7$)	2282ppm ($\Phi=0.7$)	163ppm ($\Phi=0.7$)	64ppm ($\Phi=0.7$)

Table F.2 Combustor geometries investigated by Arghode, V. K. and Gupta, A. K. (contd...).

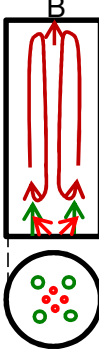
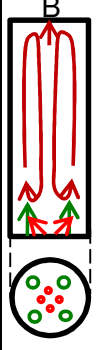
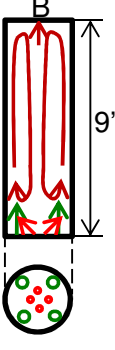
			
	(18)CDC, Gupta <i>et al.</i> , UMD, 2011	(19)CDC, Gupta <i>et al.</i> , UMD, 2011	(20)CDC, Gupta <i>et al.</i> , UMD, 2011
Configuration	FS	FS	FS
Thermal Intensity	20MW/m ³ -atm	30MW/m ³ -atm	40MW/m ³ -atm
Heat load	25kW	25kW	25kW
Fuel	Methane	Methane	Methane
Pressure	1atm	1atm	1atm
Air Velocity	171m/s	171m/s	171m/s
Fuel Velocity	97m/s	97m/s	97m/s
Air Diameter	4.8mm	4.8mm	4.8mm
Fuel Diameter	1.6mm	1.6mm	1.6mm
$\tau_{\text{air}}(D/U)$	0.028ms	0.028ms	0.028ms
$\tau_{\text{fuel}}(D/U)$	0.016ms	0.016ms	0.016ms
Air Temperature	300K	300K	300K
Fuel Temperature	300K	300K	300K
NO@15%O ₂	7ppm ($\Phi=0.6$)	8ppm($\Phi=0.6$)	7ppm ($\Phi=0.6$)
CO@15%O ₂	19ppm ($\Phi=0.6$)	28ppm($\Phi=0.6$)	48ppm ($\Phi=0.6$)

Table F.2 Combustor geometries investigated by Arghode, V. K. and Gupta, A. K. (contd...).

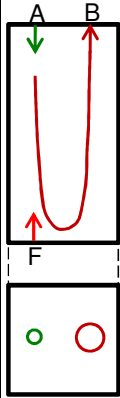
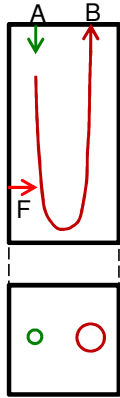
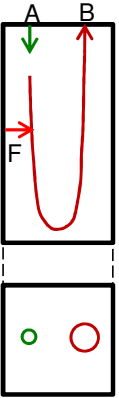
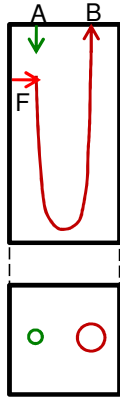
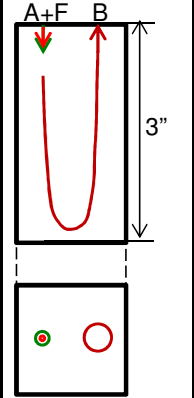
					
	(21)CDC, Gupta <i>et al.</i> , UMD, 2011	(22)CDC, Gupta <i>et al.</i> , UMD, 2011	(23)CDC, Gupta <i>et al.</i> , UMD, 2011	(24)CDC, Gupta <i>et al.</i> , UMD, 2011	(25)CDC, Gupta <i>et al.</i> , UMD, 2011
Configuration	RO	RC	RC	RC	RP
Thermal Intensity	57MW/m^3 - atm	57MW/m^3 - atm	57MW/m^3 - atm	57MW/m^3 - atm	57MW/m^3 - atm
Heat load	6.25kW	6.25kW	6.25kW	6.25kW	6.25kW
Fuel	Methane	Methane	Methane	Methane	Methane
Pressure	1atm	1atm	1atm	1atm	1atm
Air Velocity	146m/s	146m/s	146m/s	146m/s	157m/s
Fuel Velocity	97m/s	97m/s	97m/s	97m/s	-
Air Diameter	4.8mm	4.8mm	4.8mm	4.8mm	4.8mm
Fuel Diameter	1.6mm	1.6mm	1.6mm	1.6mm	-
$\tau_{\text{air}}(D/U)$	0.033ms	0.033ms	0.0338ms	0.033ms	0.031ms
$\tau_{\text{fuel}}(D/U)$	0.016ms	0.016ms	0.016ms	0.016ms	-
Air Temperature	300K	300K	300K	300K	300K
Fuel Temperature	300K	300K	300K	300K	-
NO@15%O ₂	9ppm ($\Phi=0.7$)	6ppm ($\Phi=0.7$)	3ppm ($\Phi=0.7$)	3ppm ($\Phi=0.7$)	2ppm ($\Phi=0.7$)
CO@15%O ₂	202ppm ($\Phi=0.7$)	203ppm ($\Phi=0.7$)	131ppm ($\Phi=0.7$)	57ppm ($\Phi=0.7$)	97ppm ($\Phi=0.7$)

Table F.2 Combustor geometries investigated by Arghode, V. K. and Gupta, A. K. (contd...).

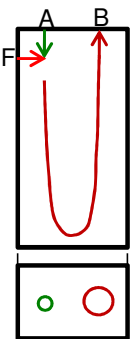
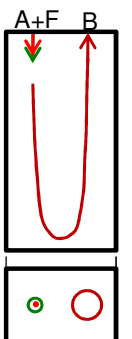
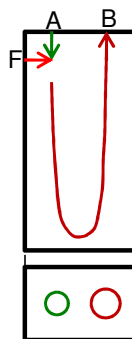
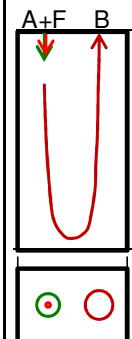
				
	(26)CDC, Gupta <i>et al.</i> , UMD, 2012	(27)CDC, Gupta <i>et al.</i> , UMD, 2012	(28)CDC, Gupta <i>et al.</i> , UMD, 2012	(29)CDC, Gupta <i>et al.</i> , UMD, 2012
Configuration	RC	RP	RC	RP
Thermal Intensity	85MW/m ³ -atm	85MW/m ³ -atm	74MW/m ³ -atm	74MW/m ³ -atm
Heat load	6.25kW	6.25kW	5.47kW	5.47kW
Fuel	Methane	Methane	Methane	Methane
Pressure	1atm	1atm	1atm	1atm
Air Velocity	146m/s	157m/s	46m/s	49m/s
Fuel Velocity	97m/s	-	85m/s	-
Air Diameter	4.8mm	4.8mm	7.9mm	7.9mm
Fuel Diameter	1.6mm	-	1.6mm	-
$\tau_{\text{air}}(D/U)$	0.033ms	0.031ms	0.172ms	0.164ms
$\tau_{\text{fuel}}(D/U)$	0.016ms	-	0.019ms	-
Air Temperature	300K	300K	300K	300K
Fuel Temperature	300K	-	300K	-
NO@15%O ₂	4ppm ($\Phi=0.7$)	2ppm($\Phi=0.7$)	5ppm ($\Phi=0.5$)	2ppm ($\Phi=0.5$)
CO@15%O ₂	115ppm ($\Phi=0.7$)	64ppm($\Phi=0.7$)	147ppm ($\Phi=0.7$)	34ppm ($\Phi=0.7$)

Table F.2 Combustor geometries investigated by Arghode, V. K. and Gupta, A. K. (contd...).

	(30)CDC, Gupta <i>et al.</i> , UMD, 2012	(31)CDC, Gupta <i>et al.</i> , UMD, 2012	(32)CDC, Gupta <i>et al.</i> , UMD, 2012	(33)CDC, Gupta <i>et al.</i> , UMD, 2012
Configuration	RC	RP	RC	RP
Thermal Intensity	53MW/m ³ -atm	53MW/m ³ -atm	170MW/m ³ -atm	170MW/m ³ -atm
Heat load	3.91kW	3.91kW	4.7kW	4.7kW
Fuel	Methane	Methane	Methane	Methane
Pressure	1atm	1atm	1atm	1atm
Air Velocity	92m/s	97m/s	92m/s	98m/s
Fuel Velocity	61m/s	-	73m/s	-
Air Diameter	7.9mm	7.9mm	7.9mm	7.9mm
Fuel Diameter	1.6mm	-	1.6mm	-
$\tau_{air}(D/U)$	0.086ms	0.082ms	0.086ms	0.081ms
$\tau_{fuel}(D/U)$	0.016ms	-	0.024ms	-
Air Temperature	600K	600K	600K	600K
Fuel Temperature	300K	-	300K	-
NO@ 15%O ₂	4ppm ($\Phi=0.5$)	1ppm ($\Phi=0.5$)	8ppm ($\Phi=0.6$)	3ppm($\Phi=0.6$)
CO@ 15%O ₂	27ppm ($\Phi=0.7$)	33ppm ($\Phi=0.7$)	81ppm ($\Phi=0.6$)	102ppm($\Phi=0.6$)

Appendix G – Experimental Apparatus

Line diagram for the CDC test facility is shown in Figure G.1. Different diagnostics and air/flow measurement system are also included in the figure.

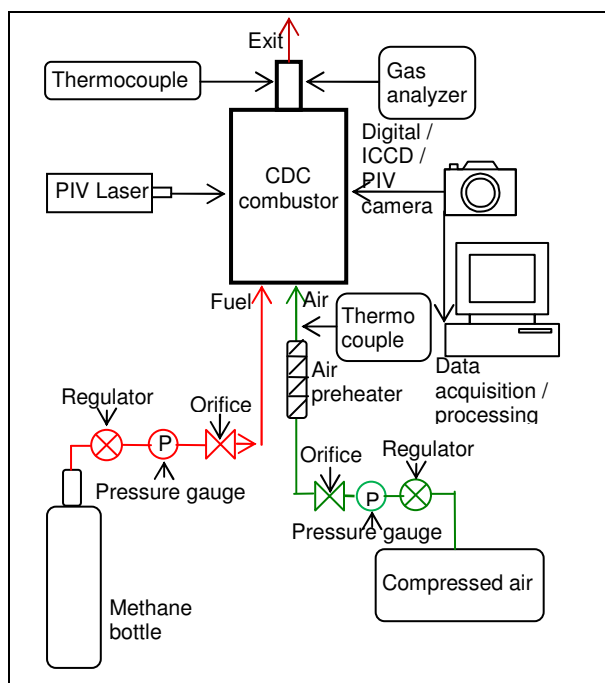


Figure G.1 Line Diagram of CDC test facility.

G.1 Air/Fuel Flowrate Measurement

Air compressor (Ingersol Rand SSR EP 100) was used to pressurize the air and store in a tank. This tank was connected with air supply line for the combustion system. The air was compressed up to a maximum pressure of 110psig in the tank and compressor automatically turns on and off to maintain the pressure between 95 and 110psig in the tank. Methane was supplied from compressed bottles. The supplied methane was chemically pure (ME-CP300, Airgas Inc.) with composition of greater than 99% methane. Both air and fuel flow rates were measured using choked flow orifice systems. Precision stainless steel orifices were used to choke the flow of the

gases and upstream pressure was controlled to supply the required mass flow rate of gases (Okeef Controls Co.). The upstream pressure was controlled using pressure regulators to maintain a steady pressure and avoid oscillations in pressure due to compressor turning on and off periodically. The upstream pressure for both air and fuel was maintained between ± 0.2 psi of the desired pressure. Upstream pressure was measured using a piezoresistive digital pressure gauge (DPG1000B-100G, Omega Inc.) with accuracy of ± 0.25 psi. It was ensured that the downstream pressure was lower than the pressure required to choke the flow based on the upstream pressure.

The mass flowrate of gases was obtained from well known equation for mass flowrate through a choked nozzle. The input parameters are orifice area, upstream pressure and properties of the gases. The equation is given in equation below in equation G.1:

$$M_{gas} = C_v \times \frac{M_w P_{upstream}}{R_u T_{upstream}} \times A \times V_{sonic} \times \left[\left(\frac{2}{\gamma+1} \right)^{\frac{\gamma+1}{\gamma-1}} \right]^{1/2} \quad (\text{equation G.1})$$

M_{gas} = mass flow rate of gas

C_v = discharge coefficient

$P_{upstream}$ = upstream absolute pressure of gas (Pa)

$T_{upstream}$ = upstream absolute temperature of gas (K)

R_u = universal gas constant (8314J/mol-K)

M_w = molecular weight of the gas

A = Orifice area (m^2)

V_{sonic} = Sonic velocity of gas at temperature of $T_{upstream}$ (m/s)

γ = specific heat ratio of the gas

It was ensured that the downstream pressure ($P_{downstream}$) was lower than the pressure required for choking based on the upstream pressure, see equation G.2. It may be noted that the pressure oscillation in the combustion chamber does not affect the flow rates of gases as the flow is choked and the pressure information cannot travel upstream.

$$P_{downstream} \leq P_{upstream} \left(\frac{2}{\gamma+1} \right)^{\frac{\gamma}{\gamma-1}} \quad (\text{equation G.2})$$

The uncertainty of air and fuel flow rates is estimated to be about $\pm 2\%$.

G.2 Air Preheater

A 5kW electric heater (Thermal Devices Inc.) is used to preheat the air to a desired temperature. The desired power supplied to the heater can be adjusted using a power control module and potentiometer to supply desired voltage to the heater. To preheat the air to 600K approximately 50% power was required (2.5kW).

G.3 Temperature Measurement

The air preheat temperature was measure using a K-type thermocouple with sheath size of 1/16inch with exposed bead (Omega Inc.). The thermocouple bead was placed in high velocity preheated air stream (about 92m/s) to maximize heat transfer and minimize the temperature difference between the thermocouple bead and the flowing gases. The exhaust gas temperature was measured using a B-type thermocouple with wire size of 200 μ m (Omega Inc.). The thermocouple bead was placed in the high velocity exit flow (about 170m/s) to maximize heat transfer to the thermocouple bead and minimize the temperature difference between the thermocouple bead and the flowing gases. The error in temperature measurement due to radiation heat transfer

was not compensated and the error was estimated to be less than 20K [Bradley, D. and Matthews, K. J., 1968]. The manufacturer specified error for the thermocouple is less than $\pm 5K$.

G.4 Global Imaging

Global reaction zone imaging was performed using a digital SLR camera (Canon EOS 40D) with resolution of 3888pixel \times 2592pixel (10.1megapixel). For a set of images same exposure time, f-stop setting and the same distance from the combustor is used so that the images could be compared for light intensity. No post processing of images for changing brightness/contrast was implemented.

G.5 Chemiluminescence Imaging

Chemiluminescence is the emission of light as a result of chemical reaction. The light is emitted when a molecule from electronically excited state decays to lower energy level. The wavelength of radiation depends on the type of molecule and for the present case OH^* chemiluminescence imaging is used where the wavelength of radiation is about 307nm. As the excited OH^* radical is only observed in reaction zone this can be used as a flame marker [Gaydon, A. G., 1974, 1979]. To obtain chemiluminescence intensity distribution in the CDC combustor, an intensified charged coupled device (ICCD) is used with a narrow band pass filter with central wavelength of 307nm and bandwidth of 10nm. This allows only light near wavelength of 307nm to pass through the camera. For a set of experiments same exposure time, gain, f-stop setting and same distance of camera from the combustor is used so that the light intensity could be compared. The camera is focused sharply to obtain precise location of the reaction zone inside the combustor. The

camera had resolution of 576pixel × 384pixels (0.2megapixel) and was equipped with 105mm Nikon lens.

G.6 Gas Analyzer

Exit gas analysis system is shown in Figure G.2. Exit gas from the combustor is drawn using a pump through a water cooled sampling probe. The sampling probe is cooled to freeze the chemistry of the gases and avoid errors associated with composition changes occurring in the sampling probe. The gas sample is passed through a desiccant filled container to absorb moisture from the gas sample. The desiccant is indicating drierite which changes color from blue to pink when its absorbing efficacy has decreased. The dry gas sample is supplied to a portable gas analyzer Horiba – PG250 for online gas analysis. The flowrate of sample gas is about 0.4SLPM. The response time for NO, O₂ and CO is within 45 seconds. The repeatability is ±0.5ppm for NO, ±0.25vol% for O₂ and ±5ppm for CO. The gas analyzer for NO, O₂ and CO was calibrated with standard calibration gas frequently.

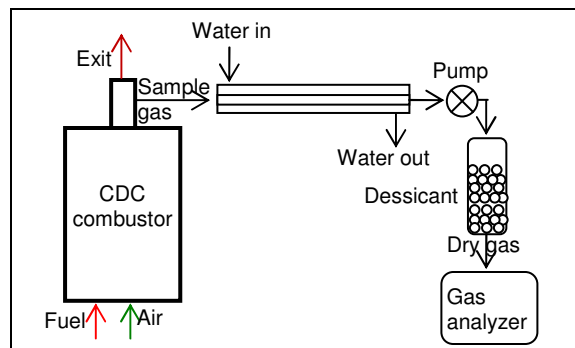
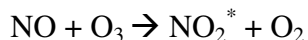


Figure G.2 Exit gas sampling system.

The gas analyzer has different measurement systems to obtain NO, O₂ and CO levels.

G.6.1 NO analyzer

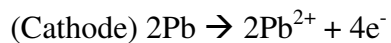
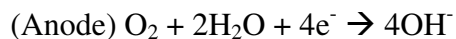
NO level is measured using chemiluminescence method. In this method ozone gas (O_3) is introduced to the sample gas and part of nitric oxide (NO) in the sample react with ozone to form nitrogen dioxide (NO_2). Part of this formed NO_2 will be in the excited state (NO_2^*) and when it returns to normal state it emits light (chemiluminescence).



The emitted light is detected by a photodiode and the output signal is calibrated for a known concentration of NO in a gas mixture.

G.6.2 O₂ analyzer

O_2 level is measured using galvanic cell method. In this method precious metal Au is used for anode, non-metal Pb is used for cathode and KOH is used for electrolyte. By connecting a suitable load resistance to the electrodes, gas passes through the permeable membrane, and oxygen inside is oxidized by the anode.



The electromotive force generated by these reactions is measured and calibrated for a known O_2 concentration in a gas mixture.

G.6.3 CO analyzer

CO level is measured using non-dispersive infrared method. In this method the infrared radiation absorbed by the measured component is calibrated with the

concentration of the gas. In this technique both sample gas and zero gas (with 0%CO) is passed through the test section alternatively and in fixed amount and after fixed interval of time. The infrared light radiated from the source is passed through the test section and enters the detector. Hence, in each cycle of switching sample gas and the zero gas the light intensity recorded by the detector fluctuates. This fluctuation is converted into electric signal and calibrated for a known CO concentration in a gas mixture.

G.7 Particle Image Velocimetry

G.7.1 PIV Laser

The laser sheet was obtained from a 200mJ dual cavity Nd:YAG laser system (Gemini 200-15, New Wave research Inc.). The wavelength of the light was 532-nm for both the cavities. The laser pulses from the cavities were controlled separately by a timing hub. The light emitted by the cavities was passed through a series of reflectors which allowed beams from both the cavities to pass through a single aperture. The laser pulse from each cavity had beam diameter of about 5mm. The pulses were passed through a focusing lens with a focal length of 500mm. The final lens in the optical set up was a cylindrical lens, which caused the round beam to spread out into a two-dimensional sheet. The result was a triangular sheet of laser light with an included angle of approximately 30 degrees. The thickness of the sheet decreased with increasing distance from the cylindrical lens, and reached a minimum thickness of about 1 mm at a distance of about 500mm from the cylindrical lens. For the purposes of the current investigation, the sheet was oriented vertically, as was the experimental flow. The laser sheet was trimmed using a metal plate and only the laser

sheet length required to illuminate the flow field inside the combustor was allowed to pass through.

The flashlamp power for each cavity was tuned in order to ensure that each cavity emitted the same pulse energy during operation. The energy of each pulse was controlled by adjustment of a global Q-switch setting, which determined the period of time during each pulse when the cavities could effectively emit. The duration of each pulse was approximately 3-5 ns.

G.7.2 PIV Camera

A 1360pixel \times 10361pixel resolution (1.4megapixel) monochrome camera was used to capture the images (IDT 1400DE). The camera was equipped with 60 mm Nikon lens. The camera direction was perpendicular to the laser sheet and f-stop setting was set to minimum of 2.8 so as to allow maximum light to enter the camera.

G.7.3 Seeder

An entrained flow seeder was designed to seed combustion air with alumina powder. A schematic of the seeder is shown in Figure G.3. High velocity air jet (about 170m/s) was injected under the seed bed as shown in Figure G.3(a). This resulted in separation and entrainment of alumina powder in the seeding air. Generally about 15% of total combustion air is used for seeding. The combustion air was mixing with seeding air and particles as shown in Figure G. 3(b). The diameter of the tube was increase to 1inch to minimize deposition of alumina powder on walls of tube and achieve steady seed particles flow.

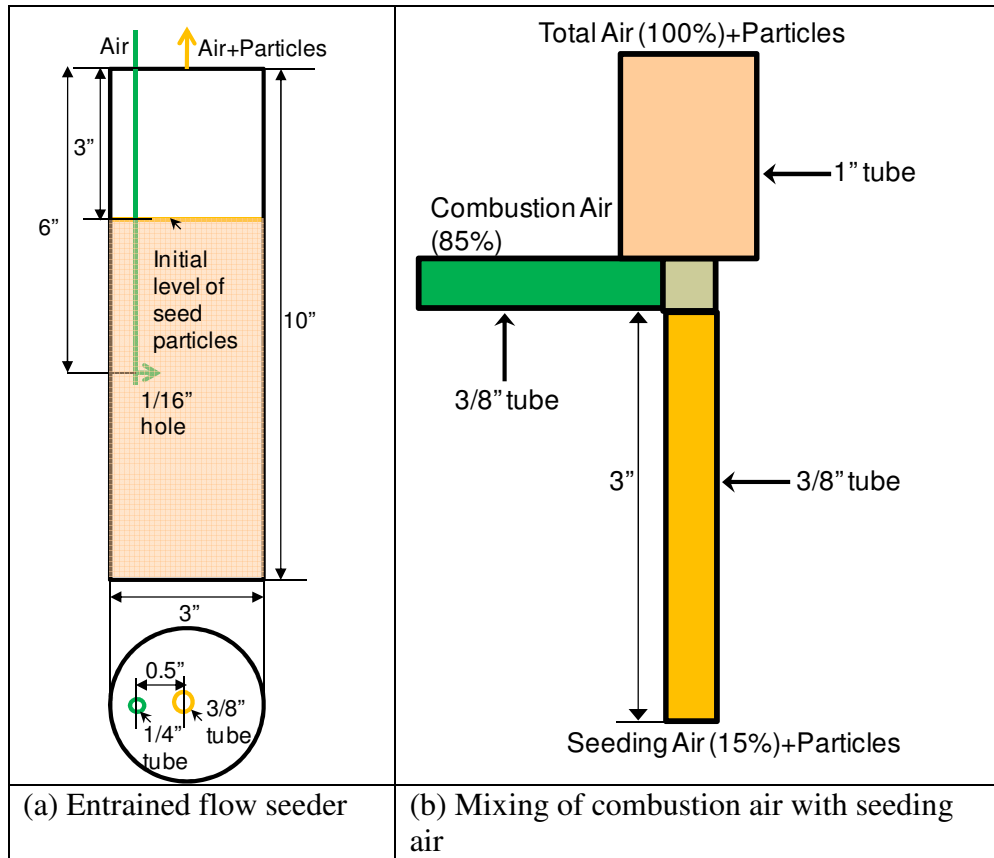


Figure G.3 Entrained flow seeding system for alumina particles used for PIV experiments.

G.8 Dynamic Pressure Sensor

A Kistler piezoelectric pressure transducer (211B5) with maximum allowable pressure of 100psi was used to measure dynamic pressure measurements. The threshold of detect ability for this sensor is 0.001psi. The transducer was installed in a water cooled adaptor to avoid damage to the electronics inside the sensor due to high temperature. The signals were passed through a coupler (5134B1) and the filtered and amplified signals were then transferred to data acquisition card (IOtech, personal DAQ/3000). The signals were acquired at sampling rate of 10kHz and 100K samples were recorded. FFT was performed in Matlab software and the spectrum was plotted with moving average of 10Hz.

G.9 Liquid Supply System

Small diameter tube was used to calibrate the liquid flow rate based on the pressure drop across the tube as given in equation G.2. Ethanol at high pressure was supplied to the tube by using compressed air which is supplied to the ethanol tank as shown in Figure G.4. The pressure at the inlet of the tube can be changed using a pressure regulator.

$$\text{Pressure drop} = \Delta P = \lambda \times \frac{L}{D} \times \rho \times \frac{V^2}{2} \quad (\text{equation G.2})$$

$$\lambda = \frac{64}{Re}$$

$$Re = \frac{\rho \times V \times D}{\mu}$$

Re =Reynolds number

V =Velocity through tube

D =Inner diameter of tube

ρ =Density of liquid

μ =Dynamic viscosity of the liquid

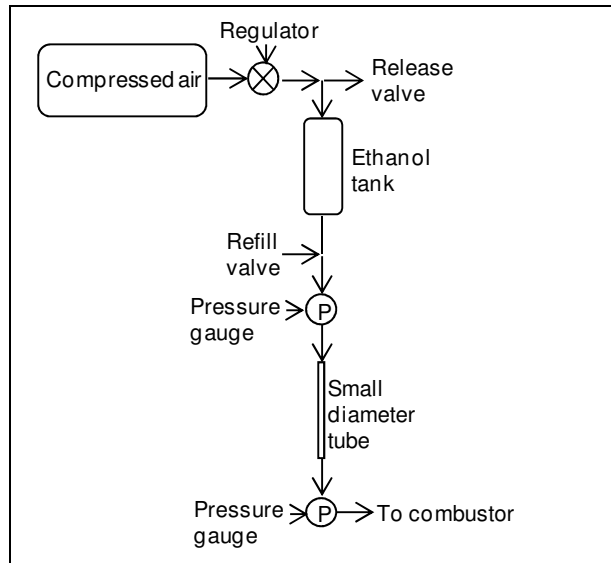


Figure G.4 Liquid fuel supply system.

G.10 Ignition and Initial Heating of the Combustor

The CDC modes investigated in this dissertation cannot be started directly, initially a conventional flame is stabilized inside the combustor and then slowly air and fuel flowrates are increased in the CDC mode. Once the combustion is stabilized in CDC mode the flow of air and fuel to the conventional flame is stopped or the conventional flame is withdrawn and replaced by ceramic plug to avoid any aerodynamic flow distortions. Ignition system used in the present dissertation is shown in Figure G.5. For low thermal intensity combustor ($5\text{MW}/\text{m}^3\text{-atm}$, see Chapter 4), combustion is started in diffusion flame mode “D” by igniting the mixture using an electric stun gun (200 kV, Street Wise Security Products SW-200). Once the combustion in diffusion mode is stabilized the igniter rods are withdrawn to avoid any flow distortions. For high thermal intensity combustor ($28\text{-}198\text{MW}/\text{m}^3\text{-atm}$, see Chapter 5-7) a 3kW propane torch (Bernzomatic, BZ8250HT) is ignited and inserted in the CDC combustor. Then the fuel and air flowrates for CDC mode are slowly increased to stabilize combustion in CDC mode. Once combustion is stabilized in

CDC mode the propane torch is withdrawn and a ceramic plug is inserted in the hole to avoid flow distortions. It may be noted that due to high back pressure propane torch could not sustain combustion with only one exit and a secondary exit is initially opened to reduce the back pressure. Once the flow is stabilized in CDC mode the secondary exit is closed using a ceramic plug to avoid flow distortions.

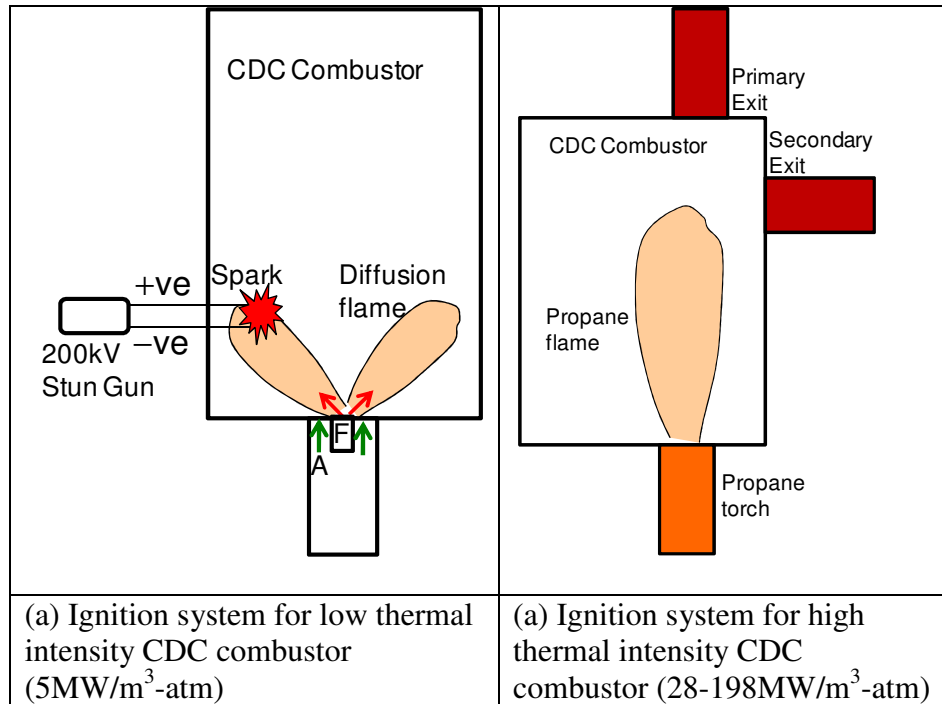


Figure G.5 Ignition system and initial heating for the CDC combustor.

Appendix H – Combustor Assembly

This section presents the design of ultra-high thermal intensity ($156\text{-}198\text{MW/m}^3\text{-atm}$) combustor and the scaled ultra-high thermal intensity combustor ($92\text{MW/m}^3\text{-atm}$).

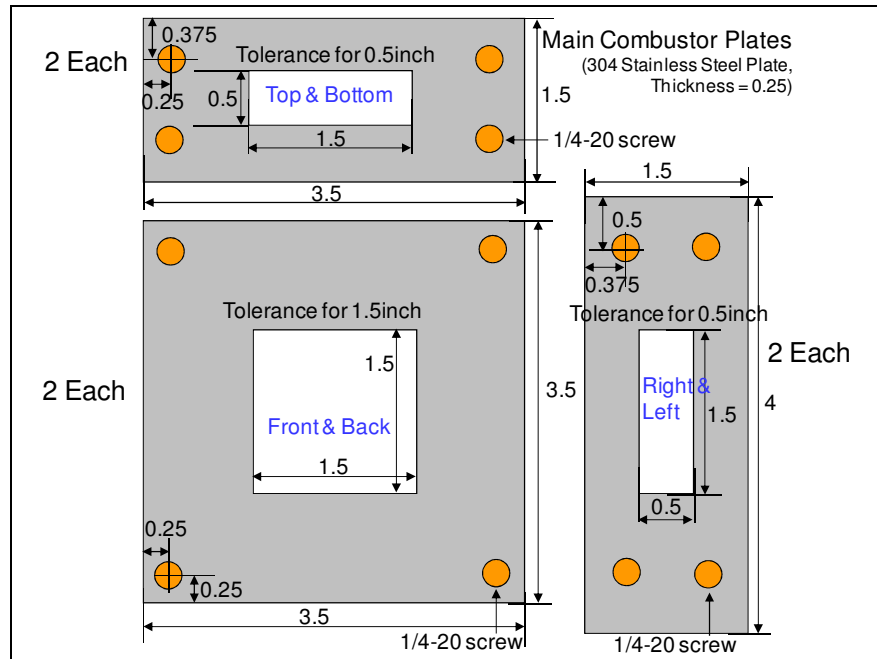
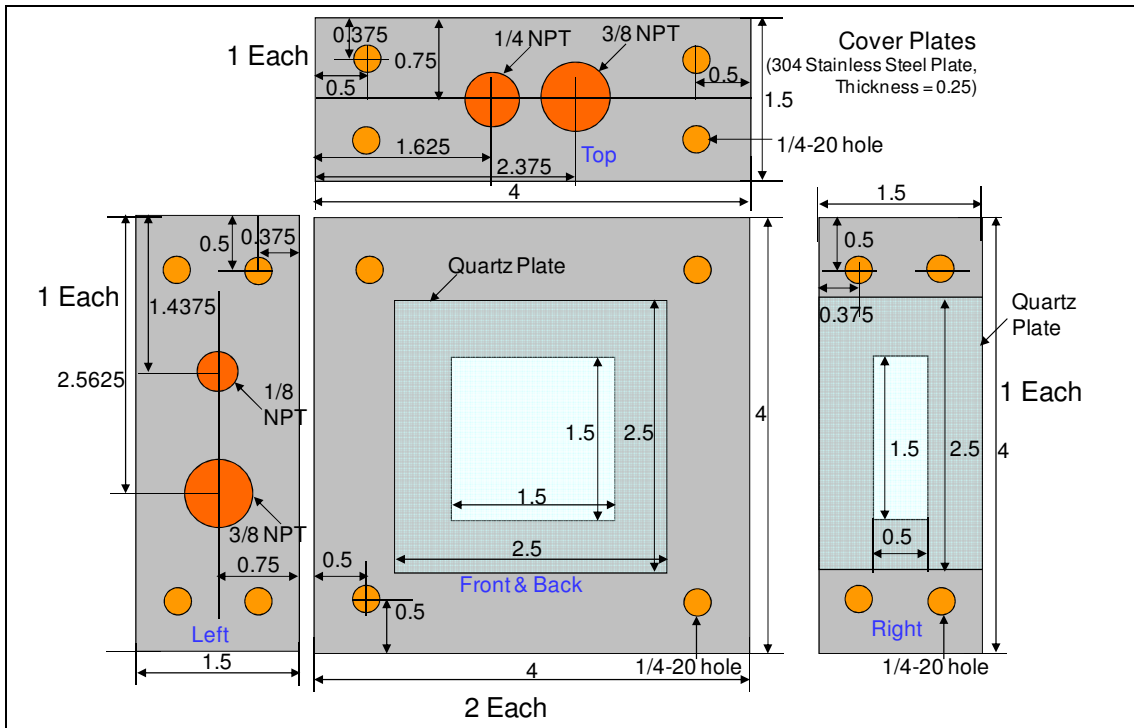
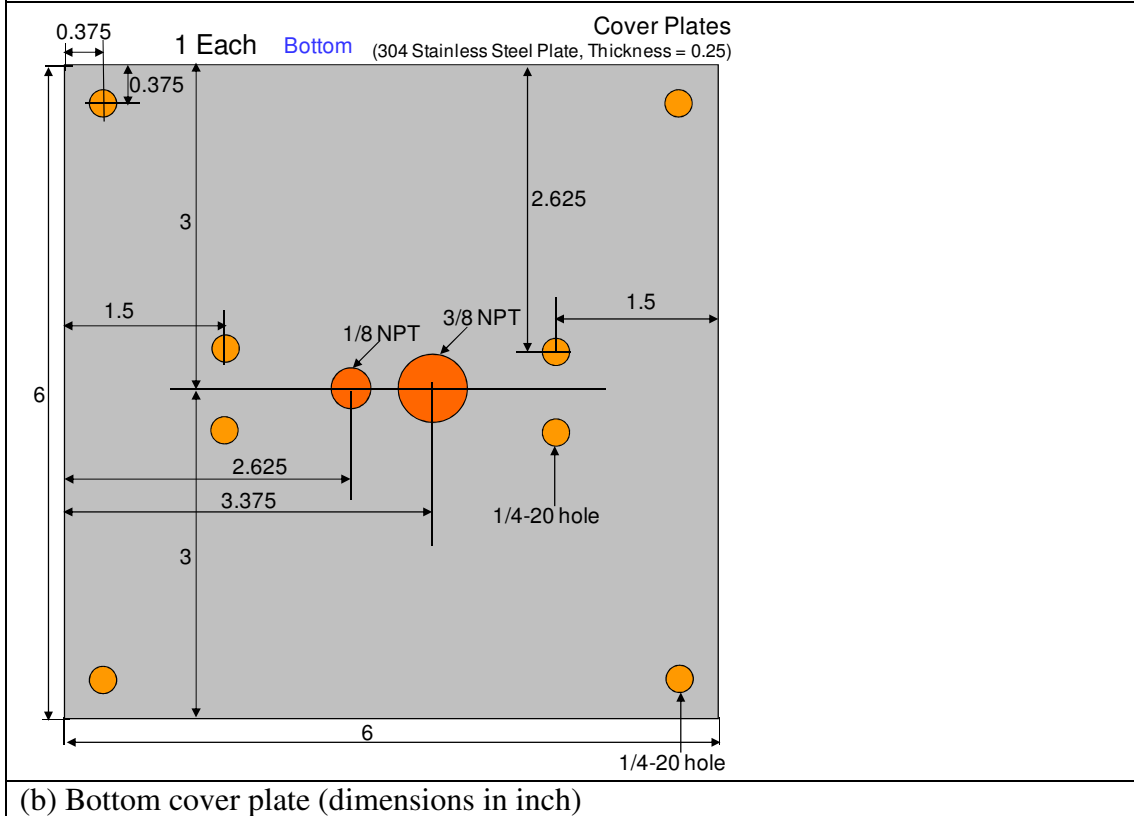


Figure H. 1 Main combustor plates (dimensions in inch).



(a) Top, left, right front and back cover plates (dimensions in inch)



(b) Bottom cover plate (dimensions in inch)

Figure H. 2 Combustor cover plates (dimensions in inch).

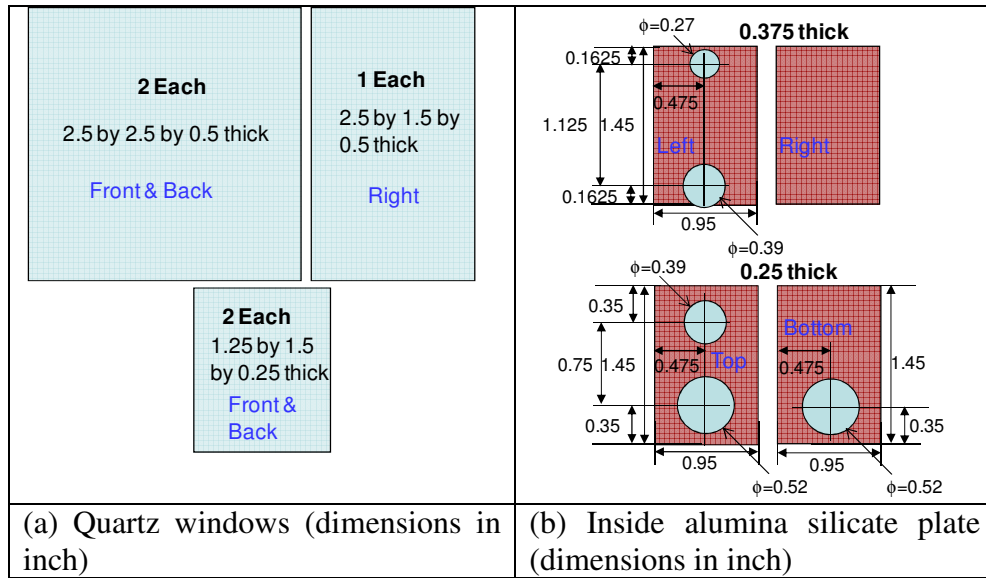


Figure H. 3 Quartz and alumina silicate plates (dimensions in inch).

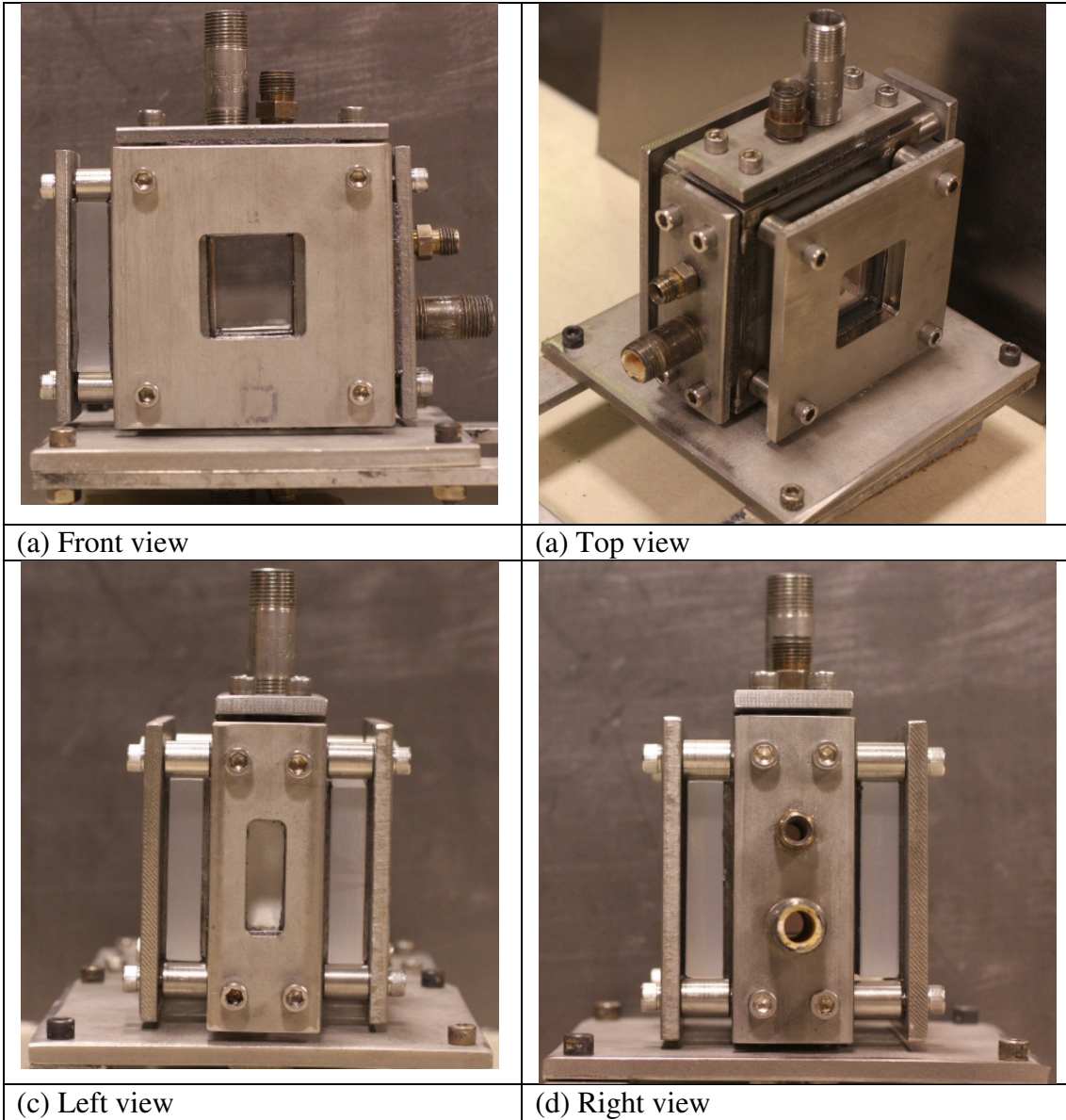
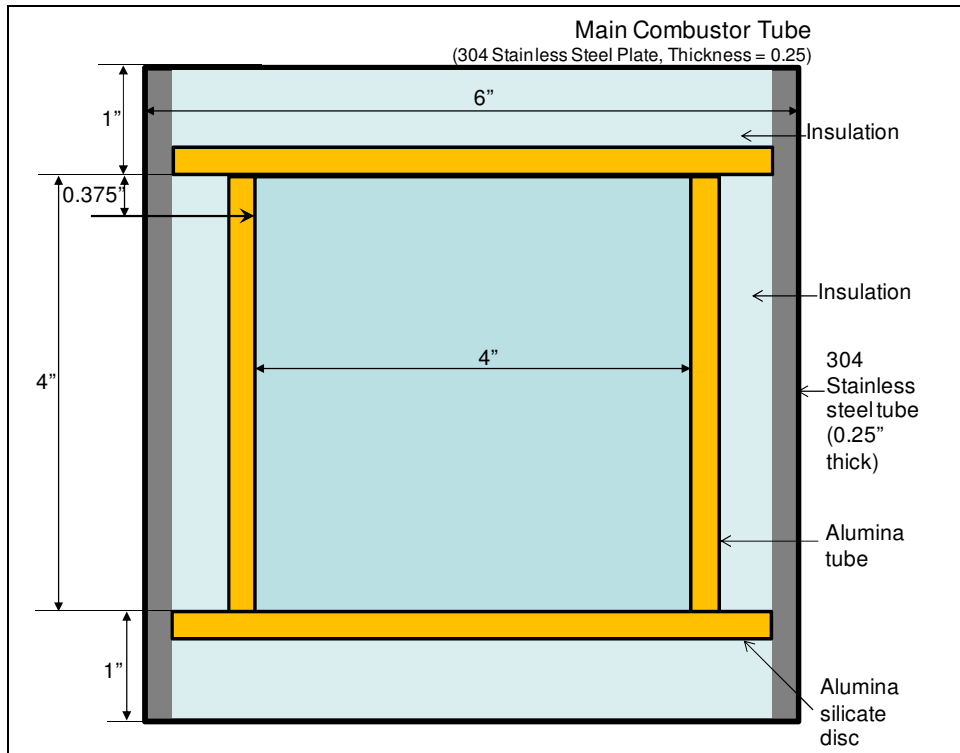
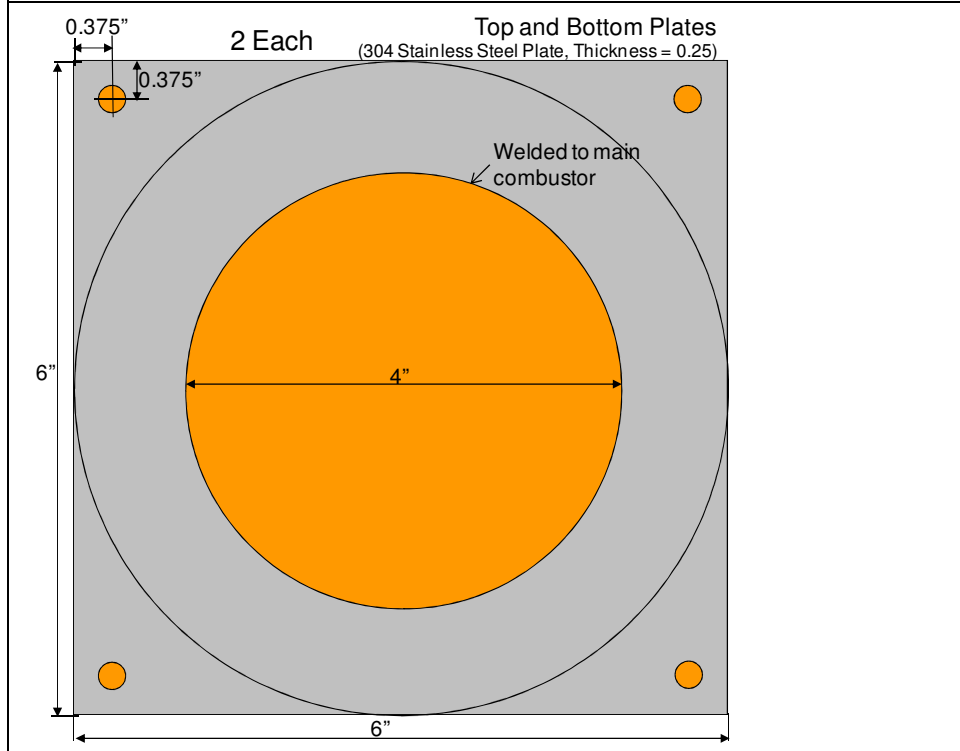


Figure H. 4 Photographs of ultra high thermal intensity CDC combustor (156-198MW/m³-atm)

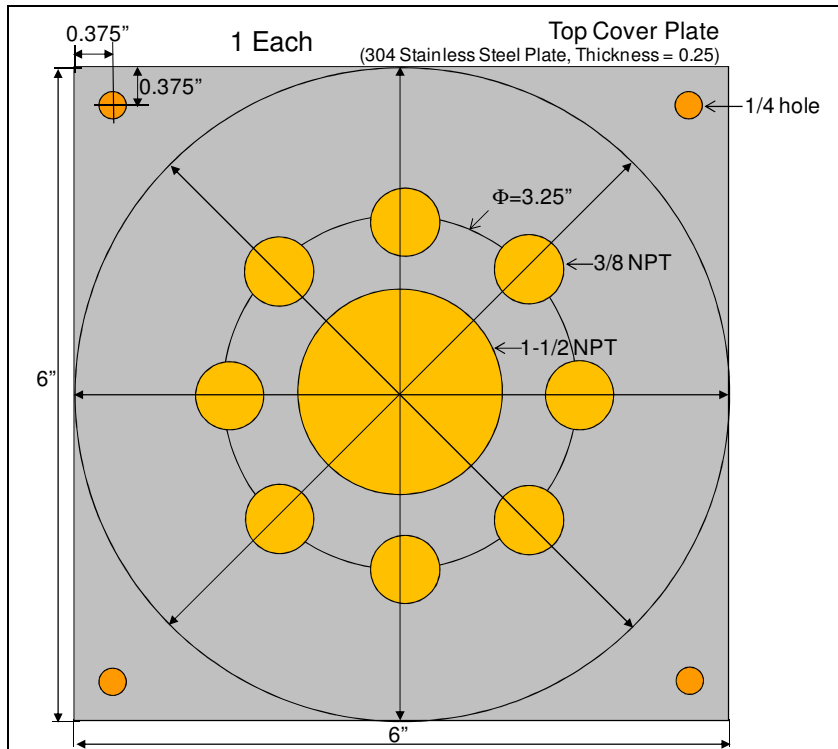


(a) Main combustor tube

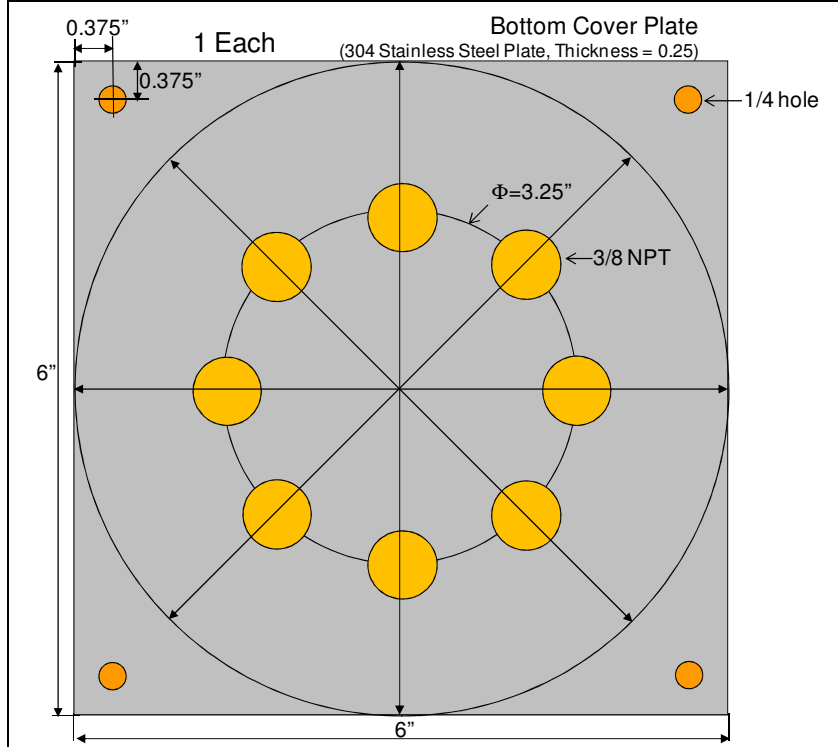


(b) Top and bottom plates

Figure H. 5 Main combustor tube and top and bottom plates.



(a) Top cover plate



(b) Bottom cover plate

Figure H. 6 Main combustor tube and top and bottom plates.

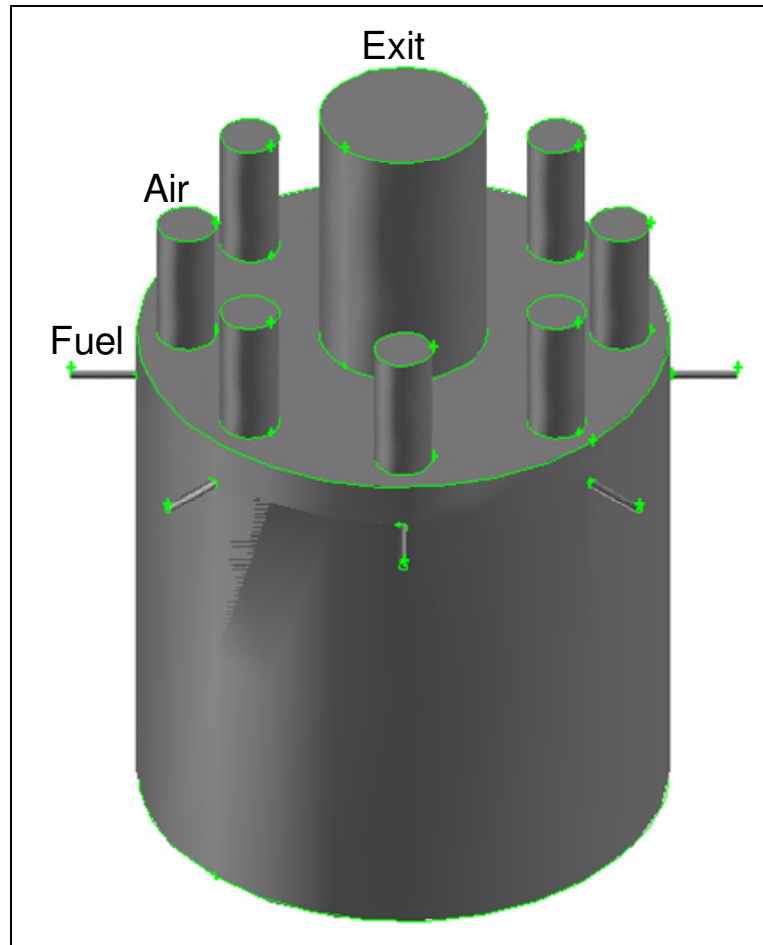


Figure H. 7 Scaled ultra-high thermal intensity CDC combustor ($93\text{MW}/\text{m}^3\text{-atm}$).

References

Combustion

Derek, D. R., "Lean Combustion - Technology and Control", *Elsevier*, 2007.

Gaydon, A. G., "Spectroscopy of Flames", *Chapman and Hall, London*, 1974

Gaydon, A. G., "Flames, Their structure, Radiation and Temperature". *Chapman and Hall, London*, 1979

Li, S. C. and Williams, F. A., "Reaction Mechanisms for Methane Ignition", *Journal of Engineering for Gas Turbines and Power*, Vol. 124, 2002, pp. 471-480.

Smith, G. P., Golden, D. M., Frenklach, M., Moriarty, N. W., Eiteneer, B., Goldenberg, M., Bowman, C. T., Hanson, R. K., Song, S., Gardiner, W. C., Lissianski, V. V. and Qin, Z., http://www.me.berkeley.edu/gri_mech/.

Turns, S. R., "An Introduction to Combustion", *McGraw-Hill*, 2000.

Flameless Oxidation (FLOX)

Colorado, A. F., Herrera, B. A., Amell, A. A., "Performance of a Flameless Combustion Furnace using Biogas and Natural Gas", *Bioresource Technology*, Vol. 101, 2010, pp. 2443-2449.

Lammel, O., Schutz, H., Schmitz, G., Luckerath, R., Stohr, M., Noll, B., Aigner, M., Hase, M., Krebs, W., "FLOX[®] Combustion at High Power density and High Flame Temperatures", *Journal of Engineering for Gas Turbines and Power*, Vol. 132, 2010, pp. 121503-1-10

Luckerath, R., Meier, W. and Aigner, M., "FLOX[®] Combustion at High Pressure with Different Fuel Compositions", *Journal of Engineering for Gas Turbines and Power*, Vol. 130, 2008, pp. 011505-1-7.

Lupant, D., Pesenti, B., Evrard, P. and Lybaert, P., "Numerical and Experimental Characterization of a Self-Regenerative Flameless Oxidation Burner Operation in a Pilot-Scale Furnace", *Combustion Science and Technology*, Vol. 179, 2007, pp. 437-453.

Plessing, T., Peters, N. and Wunning, J. G., "Laseroptical Investigation of Highly Preheated Combustion with Strong Exhaust Gas Recirculation", *Proceedings of the Combustion Institute*, Vol. 27, 1998, pp. 3197-3204.

Verissimo, A. S., Rocha, A. M. A. and Costa, M., “Operational, Combustion and Emission Characteristics of a Small Scale Combustor”, *Energy and Fuels*, Vol. 25, 2011, pp. 2469-2480.

Wunning, J., “Industrial Burner with Low NO_x Emissions”, *US Patent# 5570679*, 1996.

Wunning, J. G. and Wunning, J. A., “Combustion Chamber with Flameless Oxidation”, *US Patent# 7062917*, 2006.

Wunning, J. A. and Wunning, J. G., “Flameless Oxidation to Reduce Thermal NO-Formation”, *Progress in Energy and Combustion Science*, Vol. 23, 1997, pp. 81-94.

Xing, X., Wang, B., and Lin, Q., “Structure of Reaction Zone of Normal Temperature Air Flameless Combustion in a 2 ton/h Coal-Fired Boiler Furnace”, *Journal of Power and Energy*, Vol. 221, 2007, pp. 473-480.

Fuel/Oxidant Direct Injection(FODI)

He, Y., “Flameless Combustion of Natural Gas in the SJ/WJ Furnace”, *PhD Dissertation-Queen’s University*, 2008.

Sobiesiak, A., Rahbar, S. and Becker, H. A., “Performance Characteristics of the Novel Low-NO_x CGRI Burner for Use with High Air Preheat”, *Combustion and Flame*, Vol. 115, 1998, pp. 93-125.

Besik, F. K., Rahbar, S., Becker, H. A., Sobiesiak, A., “Low NO_x Burner”, *US Patent# 5772421*, 1998.

Gas Turbine Combustion

Lefebvre, A. H., “Gas Turbine Combustion”, *Taylor and Francis*, 1999.

Lieuwen, T. and Yang, V., “Combustion Instabilities in Gas Turbine Engines”, *Progress in Astronautics and Aeronautics*, Vol. 210, 2005.

National Energy Policy, “Reliable, Affordable, and Environmentally Sound Energy for America’s Future,” Report of the National Energy Policy Development Group, May, 2001.

Vandervort, C. L., “9 ppm NO_x/CO Combustion System for “F” Class Industrial Gas Turbines”, *Journal of Engineering for Gas Turbines and Power*, Vo. 123, 2001, pp. 317-321.

Vincent, E. T., "The Theory and Design of Gas Turbines and Jet Engines", *McGraw-Hill Book Co.*, 1950.

Environmental Protection Agency Federal Register, "Standards of Performance for Stationary Combustion Turbines; Final Rule", Vol. 71, 2006, pp. 38481-38506.

High Intensity Low Emission (HILE)

Kumar, S., "Computational and Experimental Studies on Flameless Combustion of Gaseous Fuels", *Phd Dissertation-Indian Institute of Science*, 2007.

Kumar, S., Paul, P. J. and Mukunda, H. S., "Investigations of the Scaling Criteria for a Mild Combustion Burner", *Proceedings of the Combustion Institute*, Vol. 30, 2005, pp. 2613-2621.

Kumar, S., Paul, P. J., and Mukunda, H. S., "Studies on a New High-Intensity Low-Emission Burner", *Proceedings of the Combustion Institute*, Vol. 29, 2002, pp. 1131-1137.

High Temperature Air Combustion (HiTAC)

Choi, G-M. and Katsuki, M., "New Approach to Low Emission of Nitric Oxides from Furnaces using Highly Pre-Heated Air Combustion", *Journal of the Energy Institute*, Vol. 73, 2000, pp. 18-24.

Gupta, A. K., "Thermal Characteristics of Gaseous Fuel Flames using High Temperature Air", *Journal of Engineering for Gas Turbines and Power*, Vol. 126, 2004, pp. 9-19.

Gupta, A. K., Bolz, S. and Hasegawa, T., "Effect of Air Preheat Temperature and Oxygen Concentration on Flame Structure and Emission", *Journal of Energy Resources Technology*, Vol. 121, 1999, pp. 209-216.

Lille, S., Blasiak, W. and Jewartowski, M., "Experimental Study of the Fuel Jet Combustion in High Temperature and Low Oxygen Content Exhaust Gases", *Energy*, Vol. 30, 2005, pp. 373-384.

Mortberg, M., "Study of Gas Jet Burning in Low Oxygen Content and High Temperature Oxidizer", *PhD Dissertation-Royal Institute of Technology*, 2005.

Mortberg, M., Blasiak, W. and Gupta, A. K., "Combustion of Normal and Low Calorific Fuels in High Temperature and Oxygen Deficient Environment", *Combustion Science and Technology*, Vol. 178., 2006, pp. 1345-1372.

Mortberg, M., Blasiak, W. and Gupta, A. K., "Experimental Investigation of Flow Phenomena of a Single Fuel Jet in Cross-Flow During Highly Preheated Air Combustion Conditions", *Journal of Engineering for Gas Turbines and Power*, Vol. 129, 2007, pp. 556-564.

Tsuji, H., Gupta, A.K., Hasegawa, T., Katsuki, M., Kishimoto, K., and Morita, M., "High Temperature Air Combustion: From Energy Conservation to Pollution Reduction", *CRC Press*, 2003.

Yang, W., and Blasiak, W., "Chemical Flame Length and Volume in Liquified Propane Gas Combustion using High-Temperature and Low-Oxygen-Concentration Oxidizer", *Energy and Fuels*, Vol. 18, 2004, pp. 1329-1335.

Hydrogen Addition to Methane Fuel

Cheng, R. K., Oppenheim, A. K., "Autoignition in Methane-Hydrogen Mixtures", *Combustion and Flame*, Vol. 58, 1984, pp. 125-139.

Jackson, G. S., Sai, R., Plaia, J. M., Boggs, C. M., Kiger, K. T., "Influence of H₂ on the Response of Lean Premixed CH₄ Flames to High Strained Flows", *Combustion and Flame*, Vol. 132, 2003, pp. 503-511.

Kim, H. S., Arghode, V. K., Gupta, A. K., "Flame Characteristics of Hydrogen-Enriched Methane-Air Premixed Swirling Flames", *International Journal of Hydrogen Energy*, Vol. 34, 2009, pp. 1063-1073.

Kim, H. S., Arghode, V. K., Linck, M. B., Gupta, A. K., "Hydrogen Addition Effects in a Confined Swirl-Stabilized Methane-Air Flame", *International Journal of Hydrogen Energy*, Vol. 34, 2009, pp. 1054-1062.

Jet Stirred Reactor (JSR)

Rutar, T., Malte, P. C., "NO_x Formation in High-Pressure Jet Stirred Reactors with Significance to Lean-Premixed Combustion Turbines", *Journal of Engineering for Gas Turbines and Power*, Vol. 124, 2002, pp. 776-783.

Shuman, T. R., "NO_x and CO Formation for Lean-Premixed Methane-Air Combustion in a Jet-Stirred Reactor Operated at Elevated Pressure", *PhD Dissertation-University of Washington*, 2000.

Forney, L. J., Nafia, N., "Turbulent Jet Reactors: Mixing Time Scales", *Chemical Engineering Research and Design*, Vol. 76, 1998, pp. 728-736.

Moderate and Intense Low Oxygen Dilution (MILD)

Cavaliere, A. and de Joannon, M., “Mild Combustion”, *Progress in Energy and Combustion Science*, Vol. 30, 2004, pp. 329-366.

Cavigiolo, A., Galbiati, M. A., Effuggi, A., Gelosia, D. and Rota R., “Mild Combustion in a Laboratory-Scale Apparatus”, *Combustion Science and Technology*, Vol. 175, 2003, pp. 1347-1367.

Dally, B. B., Riesmeier, E. and Peters, N., “Effect of Fuel Mixture on Moderate and Intense Low Oxygen Dilution Combustion”, *Combustion and Flame*, Vol. 137, 2004, pp. 418-431.

Dally, B. B., Karpetis, A. N. and Barlow, R. S., “Structure of Turbulent Non-Premixed Jet Flames in a Diluted Hot Coflow”, *Proceedings of the Combustion Institute*, Vol. 29, 2002, pp. 1147-1154.

Derudi, M., Villani, A., and Rota, R., “Sustainability of Mild Combustion of Hydrogen-Containing Hybrid Fuels”, *Proceedings of the Combustion Institute*, Vol. 31, 2007, pp. 3393-3400.

Effuggi, A., Gelosa, D., Derudi, M. and Rota, R., “Mild Combustion of Methane-Derived Fuel Mixtures: Natural Gas and Biogas”, *Combustion Science and Technology*, Vol. 180, 2008, pp. 481-493.

Mi, J., Li, P., Dally, B. B. and Craig, R. A., “Importance of Initial Momentum Rate and Air-Fuel Premixing on Moderate or Intense Low Oxygen Dilution (MILD) Combustion in a Recuperative Furnace”, *Energy and Fuels*, Vol. 23, 2009, pp. 5349-5356.

Ozdemir, I. B. and Peters, N., “Characteristics of the Reaction Zone in a Combustor Operating at Mild Combustion”, *Experiments in Fluids*, Vol. 30, 2001, pp. 683-695.

Szego, G. G., “Experimental and Numerical Investigation of a Parallel Jet MILD Combustion Burner System in a Laboratory-scale Furnace”, *PhD Dissertation-The University of Adelaide*, 2010.

Szego, G. G., Dally, B. B. and Nathan, G. J., “Operational Characteristics of a Parallel Jet MILD Combustion Burner System”, *Combustion and Flame*, Vol. 156, 2009, pp. 429-438.

Szego, G. G., Dally, B. B., and Nathan, G. J., “Scaling of NO_x Emissions from a Laboratory-Scale Mild Combustion Furnace”, *Combustion and Flame*, Vol. 154, 2008, pp. 281-295.

Weber, R., Smart, J. P., and vd Kamp, W., “On the (MILD) Combustion of Gaseous, Liquid, and Solid Fuels in High Temperature Preheated Air”, *Proceedings of the Combustion Institute*, Vol. 30, 2005, pp. 2623-2629.

Particle Image Velocimetry

Melling, A., “Tracer Particles and Seeding for Particle Image Velocimetry”, *Measurement Science and Technology*, Vol. 8, 1997, pp. 1406-1416.

Picano, F., Battista, F., Troiani, G., and Casciola, C. M., “Dynamic of PIV seeding Particles in Turbulent Premixed Flames”, *Experiments in Fluids*, Vol. 50, 2010, pp. 433-454.

Stella, A., Guj, G., Kompenhans, J., Raffel M. and Richard H., “Application of Particle Image Velocimetry to Combusting Flows: Design Considerations and Uncertainty Assessment”, *Experiments in Fluids*, Vol. 30, 2001, pp. 167-180.

Sung, C. J., Law, C. K. and Axelbaum, R. L., “Thermophoretic Effects on Seeding Particles in LDV Measurements of Flames”, *Combustion Science and Technology*, Vol. 99, 1994, pp. 119-132.

Pollutant Emission

Correa, S. M., A review of NO_x Formation Under Gas-Turbine Combustion Conditions, *Combustion Science and Technology*, Vol. 87, 1992, pp. 329-362.

Fenimore, C. P., “Formation of Nitric Oxide in Premixed Hydrocarbon Flames”, *Proceedings of the Combustion Institute*, Vol. 13, 1971, pp. 373-380.

Miller, J. A. and Bowman C. T., Mechanisms and Modeling of Nitrogen Chemistry in Combustion. *Progress in Energy and Combustion Science*, Vol. 15, 1989, pp. 287–338.

Princeton Axysymmetric Whirl Combustor (PAWC)

Yetter, R. A., Glassman, I., Gabler, H. C., “Asymmetric Whirl Combustion: A New Low NO_x Approach”, *Proceedings of the Combustion Institute*, Vol. 28, 2000, pp. 1265-1272.

Glassman, I., Yetter, R. and Sivo, J. A., “Axymmetric Whirl Combustor”, *US Patent# 5307621*, 1994.

Stagnation Point Reverse Flow (SPRF)

Bobba, M. K., “Flame Stabilization and Mixing Characteristics in a Stagnation Point reverse Flow Combustor”, *PhD Dissertation-Georgia Institute of Technology*, 2007.

Bobba, M. K., Gopalakrishnan, P., Periagaram, K. and Seitzman, J. M., "Flame Structure and Stabilization Mechanisms in a Stagnation-Point Reverse-Flow Combustor", *Journal of Engineering for Gas Turbines and Power*, Vol. 130, 2008, pp. 031505-1-8.

Gopalakrishnan, P., "Effects of the Reacting Flowfield on Combustion Processes in a Stagnation Point Reverse Flow Combustor", *PhD Dissertation-Georgia Institute of Technology*, 2008.

Gopalakrishnan, P., Bobba, M. K. and Seitzman, J. M., "Controlling Mechanisms for Low NO_x Emissions in a Non-Premixed Stagnation Point Reverse Flow Combustor", *Proceedings of the Combustion Institute*, Vol. 31, 2007, 3401-3408.

Zinn, B. T., Neumeier, Y., Seitzman, J. M., Jagoda, J. and Hashmonay, B., "Stagnation Point Reverse Flow Combustor for a Combustion System", *US Patent# 7168949*, 2007.

Trapped Vortex Combustor (TVC)

Bruno, C., Losurdo, M., "The Trapped Vortex Combustor: An Advanced Combustion Technology for Aerospace and Gas Turbine Applications", *Advanced Combustion and Aerothermal Technologies*, Vol. 6, 2007, pp. 365-384.

Edmonds, R. G., Williams, J. T, Steele, R. C., Straub, D. L., Casleton, K. H., Bining, A., "Low NO_x Advanced Vortex Combustor", *Journal of Engineering for Gas Turbine and Power*, Vol. 130, 2008, pp. 1-4.

Hsu, K. Y., Goss, L. P., Roquemore, W. M., "Characteristics of a Trapped-Vortex Combustor", *Journal of Propulsion and Power*, Vol. 14, 1998, pp. 57-65.

Hui, W., Chen, Q., Shao, W., Zhang, Y., Wang, Y., Xiao, Y., "Combustion of Hydrogen in an Experimental Trapped Vortex Combustor", *Journal of Thermal Science*, Vol. 18, 2009, pp. 256-261.

Kendrick, D., Lawlor, S. P. and Steele, R. C., "Trapped Vortex Combustor", *US Patent# 7003961*, 2006.

Melo, M. J., Sousa, J. M. M., Costa, M., Levy, Y., "Experimental Investigation of a Novel Combustor Model for Gas Turbines", *Journal of Propulsion and Power*, Vol. 25, 2009, pp. 609-617.

Straub, D. L., Casleton, K. H., Lewis, R. E., Sidwell, T. G., Maloney, D. J., Richards, G. A., "Assessment of Rich-Burn, Quick-Mix, Lean-Burn Trapped Vortex Combustor

for Stationary Gas Turbines”, *Journal of Engineering for Gas Turbines and Power*, Vol. 127, 2005, pp. 36-41.

Temperature Measurement

Bradley, D., Matthews, K. J., “Measurement of High Gas Temperatures with Fine Wire Thermocouples”, *Journal of Mechanical Engineering Science*, Vol. 10, 1968, pp. 299-305.

Turbulent Jets

Fellouah, H., Ball, C. G. and Pollard, A., “Reynolds Number Effects within the Development Region of a Turbulent Round Free Jet”, *International Journal of Heat and Mass Transfer*, Vol. 52, 2009, pp. 3943-3954.

Ferdman, E., Otugen, M. V. and Kim, S., “Effect of Initial Velocity Profile on the Development of the Round Jet”, *Journal of Propulsion and Power*, Vol. 16, 2000, pp. 676-686.

Grandmaison, E. W., Yimer, I., Becker, H. A. and Sobiesiak, A., “The Strong-Jet/Weak-Jet Problem and Aerodynamic Modeling of the CGRI Burner”, *Combustion and Flame*, Vol. 114, 1998, pp. 381-396.

Han, D. and Mungal, M. G., “Direct Measurement of Entrainment in Reacting/Nonreacting Turbulent Jets”, *Combustion and Flame*, Vol. 124, 2001, pp. 370-386.

Han, D., Orozco, V. and Mungal, M. G., “Gross-Entrainment Behaviour of Turbulent Jets Injected Obliquely into a Uniform Crossflow”, *AIAA Journal*, Vol. 38, 2000, pp. 1643-1649.

Hussein, H. J., Capp, S. P. and George, W. K., “Velocity Measurements in a High-Reynolds-Number, Momentum-Conserving, Axisymmetric, Turbulent Jet”, *Journal of Fluid Mechanics*, Vol. 258, 1994, pp. 31-75.

Liepmann, D., Gharib, M., Vorticity and entrainment dynamics of near-surface jets, American Society of Mechanical Engineers, *Fluids Engineering Division - Free-Surface Turbulence*, Vol. 181, pp. 53-58, 1994.

Liu, H., Winoto, S. H. and Shah, D. A., “Velocity Measurements within Confined Turbulent Jets: Application to Cardiovascular Regurgitation”, *Annals of Biomedical Engineering*, Vol. 25, 1997, pp. 939-948.

- Mi, J., Kalt, P., Nathan, G. J. and Wong, C. Y., "PIV Measurements of a Turbulent Jet Issuing from Round Sharp-Edged Plate" *Experiments in Fluids*, Vol. 42, 2007, pp. 625-637.
- Panchapakesan, N. R. and Lumley, J. L., "Turbulence Measurements in Axisymmetric Jets of Air and Helium", *Journal of Fluid Mechanics*, Vol. 246, 1993, pp. 197-223.
- Papadopoulos, G. and Pitts, W. M., "A Generic Centerline Velocity Decay Curve for Initially Turbulent Axisymmetric Jets", *Journals of Fluids Engineering*, Vol. 121, 1999, pp. 80-85.
- Papadopoulos, G. and Pitts, W. M., "Scaling the Near-Field Centerline Mixing Behavior of Axisymmetric Turbulent Jets", *AIAA Journal*, Vol. 36, 1998, pp. 1635-1642.
- Quinn, W. R., "Upstream Nozzle Shaping Effects on near Field Flow in Round Turbulent Free Jet", *European Journal of Mechanics, B/Fluids*, Vol. 25, 2006, pp. 279-301.
- Rajaratnam, N., "Turbulent Jets", *Elsevier*, 1976.
- Ricou, F. P. and Spalding, D. B., "Measurements of Entrainment by Axisymmetrical Turbulent Jets", *Journal of Fluid Mechanics*, Vol. 11, 1961, pp. 21-32.
- Shih, T-H., Liou, W. W., Shabbir, A., Yang, Z. and Zhu, J., "A New $k-\varepsilon$ Eddy Viscosity Model for High Reynolds Number Turbulent Flows", Vol. 24, 1995, pp. 227-238.
- Singh, G., Sundararajan, T. and Shet, U. S. P., "Entrainment and Mixing Studies for a Variable Density Confined Jet", *Numerical Heat Transfer, Part-A*, Vol. 35, 1999, pp. 205-223.
- Wynanski, I. and Fiedler, H., "Some Measurements in the Self-Preserving Jet", *Journal of Fluid Mechanics*, Vol. 38, 1969, pp. 577-612.
- Xu, G. and Antonia, R. A., "Effect of Different Initial Conditions on a Turbulent Round Free Jet", *Experiments in Fluids*, Vol. 33, 2002, pp. 677-683.
- Yang, W. and Blasiak, W., "Flame Entrainments Induced by a Turbulent Reacting Jet using High-Temperature and Oxygen-Deficient Oxidizer", *Energy and Fuels*, Vol. 19, 2005, pp. 1473-1483.
- Yimer, I., Becker, H. A. and Grandmaison, E. W., "The Strong-Jet/Weak-Jet Problem: New Experiments and CFD", *Combustion and Flame*, Vol. 124, 2001, pp. 481-502.